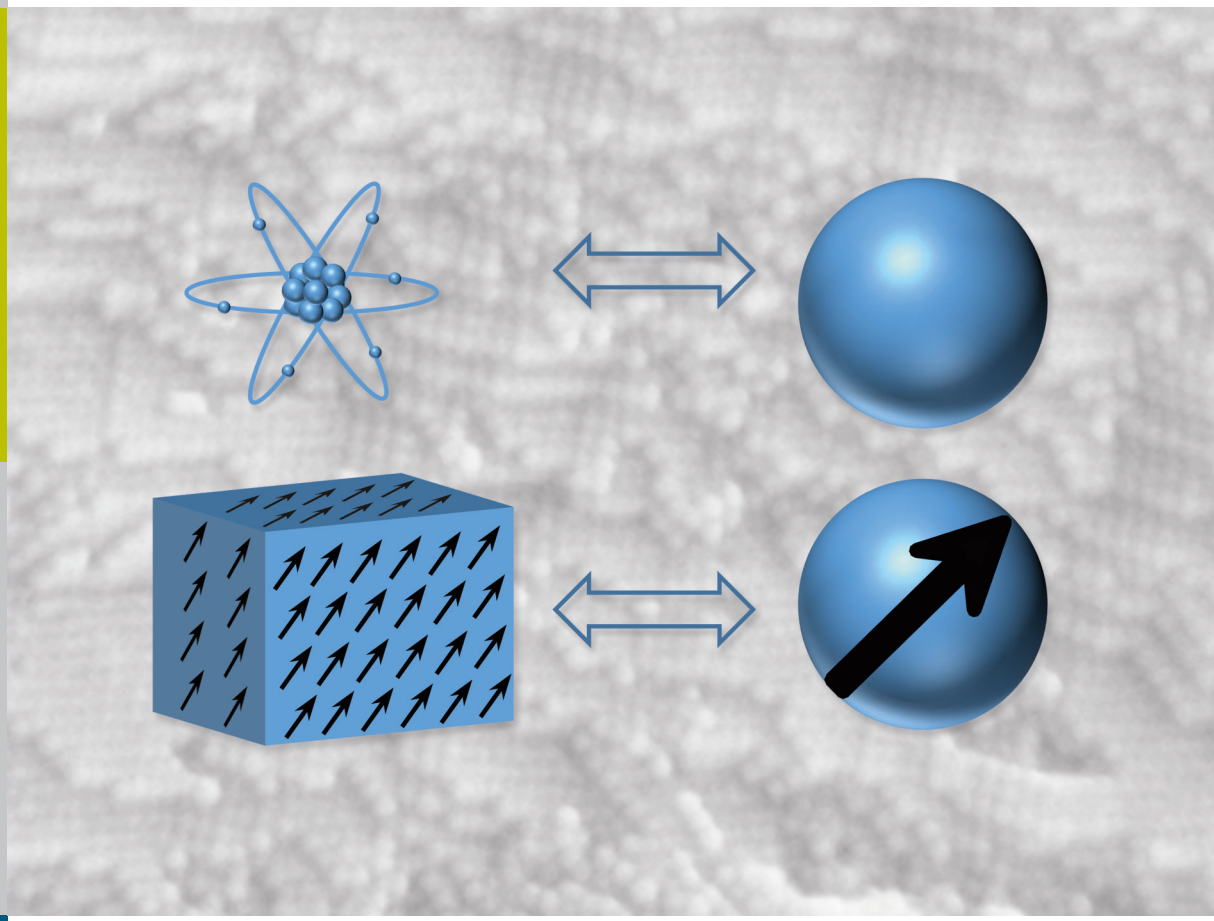
Magnetic Proximity Effects in Nanoparticle Composite Systems and Macrocrystals

Genevieve Wilbs



Member of the Helmholtz Association

Schlüsseltechnologien / Key Technologies
Band / Volume 142
ISBN 978-3-95806-233-7

JÜLICH FORSCHUNGSZENTRUM

Schriften des Forschungszentrums Jülich
Reihe Schlüsseltechnologien / Key Technologies Band / Volume 142

Forschungszentrum Jülich GmbH
Peter Grünberg Institute (PGI)
Scattering Methods (PGI-4 / JCNS-2)

Magnetic Proximity Effects in Nanoparticle Composite Systems and Macrocrystals

Genevieve Wilbs

Schriften des Forschungszentrums Jülich
Reihe Schlüsseltechnologien / Key Technologies Band / Volume 142

ISSN 1866-1807 ISBN 978-3-95806-233-7

Bibliographic information published by the Deutsche Nationalbibliothek.
The Deutsche Nationalbibliothek lists this publication in the Deutsche
Nationalbibliografie; detailed bibliographic data are available in the
Internet at http://dnb.d-nb.de.

Publisher and Distributor: Forschungszentrum Jülich GmbH
Zentralbibliothek
52425 Jülich
Tel: +49 2461 61-5368
Fax: +49 2461 61-6103
Email: zb-publikation@fz-juelich.de
www.fz-juelich.de/zb

Cover Design: Grafische Medien, Forschungszentrum Jülich GmbH

Printer: Grafische Medien, Forschungszentrum Jülich GmbH

Copyright: Forschungszentrum Jülich 2017

Schriften des Forschungszentrums Jülich
Reihe Schlüsseltechnologien / Key Technologies, Band / Volume 142

D 82 (Diss. RWTH Aachen University, 2017)

ISSN 1866-1807
ISBN 978-3-95806-233-7

The complete volume is freely available on the Internet on the Jülicher Open Access Server (JuSER)
at www.fz-juelich.de/zb/openaccess.



This is an Open Access publication distributed under the terms of the Creative Commons Attribution License 4.0,
which permits unrestricted use, distribution, and reproduction in any medium, provided the original work is properly cited.

Abstract

Assemblies of magnetic nanoparticles are of major interest for future applications e.g. in spintronic devices, high density data storage systems or biomedical applications. The reason is not only the obvious miniaturization, but also their novel properties emerging only at the nanoscale. Hence, arranging nanoparticles like atoms in a crystal enables the fabrication of a new class of materials. To gain in-depth understanding of these systems, it is necessary to investigate them on all length scales.

The present work provides a novel and extensive contribution to the understanding of the self-assembly of iron oxide nanoparticle superstructures and their influence on polarizable matrix materials. Through the investigation of the samples at all stages of preparation, a comprehensive picture of the unique phenomena observed at the end is derived. For this purpose, oleic acid coated iron oxide nanoparticles were deposited on silicon substrates by spincoating to manufacture two-dimensional arrangements. Hereby, the influence of several parameters has been investigated and optimized. Afterwards, the organic surfactant shell was removed by oxygen plasma treatment. This process has been studied in detail, because it initiates a phase transformation that significantly influences the magnetic properties of the system (e.g. by reducing the blocking temperature). Thin palladium or platinum films were then respectively deposited to create a matrix material. Aside from magnetometry measurements, first order reversal curves were obtained in cooperation with the Max-Planck-Institute for Intelligent Systems, both revealing that the matrix materials significantly influence the inter-particle interaction and vice versa. However, only by performing x-ray magnetic circular dichroism experiments at the Advanced Photon Source of the Argonne National Laboratory, it could be evidenced unambiguously that platinum can be polarized by an oxide. Additionally, these systems were investigated concerning their electrical transport properties, whereby several nanoparticle phenomena could be observed.

Another highlight of this work is the successful preparation of three-dimensional iron oxide nanoparticle assemblies on length scales of > 1000 μm by carefully adjusting the parameters of a newly developed centrifuge assisted sedimentation method. Extensive SEM studies combined with magnetometry and sophisticated SAXS experiments resulted in a comprehensive overview on the morphology and magnetism of these so-called 'macrocrystals', as well as on the nanoparticle arrangement inside them. Like this, highly correlated systems with a macroscopic expansion could be manufactured. Finally, a nanoparticle/palladium multilayer was prepared. It demonstrates that the polarization and magnetoresistance effects found in the two-dimensional systems can only partially be transfered to three dimensional assemblies. In conclusion, this work shows how two- and three-dimensional nanoparticle assemblies can be prepared, how their properties are modified at different stages of preparation and how a polarizable matrix material influences the particles and vice versa.

Zusammenfassung

Aufgrund ihrer zukünftigen Einsatzmöglichkeiten z.B. in spintronischen Geräten, Datenspeichern mit hoher Speicherdichte oder biomedizinischen Anwendungen, sind wechselwirkende Anordnungen magnetischer Nanopartikel von großem Interesse. Das liegt nicht nur an der offensichtlichen Miniaturisierung, sondern vor allem auch an neuartigen Eigenschaften, die nur auf der Nanoskala auftreten. Daher ermöglicht die Anordnung von Nanopartikeln analog zu Atomen in einem Kristall die Erzeugung einer völlig neuen Materialklasse. Um ein tiefgreifendes Verständnis dieser Systeme zu gewinnen, sind Untersuchungen auf allen Längenskalen notwendig.

Die vorliegende Arbeit bietet einen neuartigen und umfangreichen Beitrag zum Verständnis der Selbstorganisation von Eisenoxidnanopartikeln zu Superstrukturen und ihrem Einfluss auf polarisierbare Matrixmaterialien. Durch die Analyse der Proben nach jedem Präparations-schritt entsteht ein umfassendes Bild der einzigartigen Phänomene, die am Ende beobachtet werden können. Zu diesem Zweck wurden ölsäurebeschichtete Eisenoxidnanopartikel durch Rotationsbeschichtung auf ein Siliziumsubstrat aufgetragen, wodurch ein zweidimensionales System erzeugt wurde. Dabei wurde der Einfluss verschiedener Parameter untersucht und optimiert. Anschließend wurde die organische Partikelhülle durch die Behandlung mit einem Sauerstoffplasma entfernt. Dieser Prozess wurde detailliert untersucht, da er eine Phasenumwandlung initiiert, die einen signifikanten Einfluss auf die magnetischen Eigenschaften des Systems hat (z.B. durch Reduktion der Blockingtemperatur). Danach wurde jeweils dünne Platin- und Palladiumschichten aufgetragen, um das Matrixmaterial zu erzeugen. Neben Magnetometriemessungen wurden sogenannte 'First Order Reversal' Kurven in Kooperation mit dem Max-Planck-Institut für Intelligente Systeme gemessen. Beides zeigte eine signifikante Beeinflussung der Nanopartikel durch das jeweilige Matrixmaterial und umgekehrt. Mit Hilfe von zirkulären, magnetischen Röntgendichroismusmessungen, die an der Advanced Photon Source im Argonne National Laboratory durchgeführt wurden, konnte darüberhinaus die Polarisation von Platin durch das Eisenoxid eindeutig nachgewiesen werden. Zusätzlich wurden diese Systeme bezüglich ihres elektrischen Transportverhaltens untersucht, wobei diverse Nanopartikelphänomene beobachtet werden konnten.

Einen weiteren Aspekt dieser Arbeit bildet die erfolgreiche Präparation von dreidimensionalen Eisenoxidnanopartikelanordnungen, die gößer als 1000 μm sind, durch sorgfältiges Einstellen der Parameter einer neu entwickelten Zentrifugationsmethode. Umfangreiche Rasteelektronenmikroskopiestudien in Kombination mit Magnetometrie und Kleinwinkelröntgenstreuexperimenten führten zu einem umfassenden Überblick bezüglich der Morphologie und dem Magnetismus dieser sogenannten 'Makrokristalle', sowie der Anordnung der Nanopartikel darin. Auf diese Weise konnten magnetisch wechselwirkende Systeme mit makroskopischer Ausdehnung erzeugt werden. Schließlich wurde ein Nanopartikel/Palladium Mehrschichtsystem erzeugt, mit dessen Hilfe demonstriert werden konnte, dass die Polarisations- und magnetoresistiven Effekte, die in zweidimensionalen Systemen beobachtet wurden, nur teilweise auf dreidimensionale Assemblierungen übertragbar sind. Zusammenfassend kann man also festhalten, dass diese Arbeit nicht nur zeigt, wie zwei- und dreidimensionale Nanopartikelassemblierungen erzeugt werden, sondern auch, wie sich ihre Eigenschaften während der einzelnen Präparationsschritte verändern und wie sie eine polarisierbare Matrix beeinflussen und umgekehrt.

Contents

1 Introduction **1**
- 1.1 Motivation . . . 1
- 1.2 Concept . . . 1
- 1.3 Current State of Research . . . 2

2 Theoretical Background **3**
- 2.1 The Iron Oxides . . . 3
  - 2.1.1 Magnetite . . . 3
  - 2.1.2 Maghemite . . . 4
  - 2.1.3 Wustite . . . 4
- 2.2 Basics of Solid State Magnetism . . . 5
  - 2.2.1 Magnetic Moment . . . 5
  - 2.2.2 Magnetic Interactions . . . 6
  - 2.2.3 Anisotropy . . . 10
  - 2.2.4 Classification of Magnetic Materials . . . 11
  - 2.2.5 Nanomagnetism . . . 17
- 2.3 Self-Assembly . . . 21
  - 2.3.1 Van der Waals Interaction . . . 21
  - 2.3.2 Magnetic Interaction in Nanoparticle Systems . . . 22
  - 2.3.3 Steric Repulsion . . . 23
  - 2.3.4 Capillary Forces . . . 23
  - 2.3.5 Attractive Depletion Force . . . 24
  - 2.3.6 Entropy . . . 25
  - 2.3.7 Other Forces . . . 26
- 2.4 Scattering . . . 26
  - 2.4.1 Reciprocal Space . . . 26
  - 2.4.2 Diffraction . . . 27
  - 2.4.3 X-ray and Synchrotron Radiation . . . 31
- 2.5 Electrical Transport . . . 32
  - 2.5.1 Models of Electrical Conduction . . . 32
  - 2.5.2 Thin Film Conductivity . . . 33
  - 2.5.3 Magnetoresistance . . . 33

3 Experimental Methods and Instruments **37**
- 3.1 Magnetometry . . . 37
  - 3.1.1 Vibrating Sample Magnetometer . . . 37
  - 3.1.2 Superconducting Quantum Interference Device . . . 38
  - 3.1.3 Measurement Procedures . . . 39
- 3.2 Magneto Optical Kerr Effect . . . 41

3.3 First Order Reversal Curves . . . 42
3.3.1 The Preisach Model . . . 42
3.3.2 Measurement procedure . . . 43
3.3.3 Data Evaluation . . . 43
3.4 Resistivity . . . 45
3.5 X-Ray Powder Diffraction . . . 46
3.6 Small Angle X-Ray Scattering . . . 47
3.7 Grazing Incindence Small Angle X-ray Scattering . . . 50
3.8 X-ray Absorption Spectroscopy . . . 52
3.8.1 EXAFS . . . 53
3.8.2 XANES . . . 53
3.9 X-ray Magnetic Circular Dichroism . . . 53
3.9.1 Transition Probabilities . . . 54
3.9.2 Sum Rules . . . 55
3.9.3 Experimental Setup . . . 55
3.9.4 Data Treatment . . . 56
3.10 Scanning Electron Microscopy . . . 58
3.11 Coating . . . 59
3.12 Plasma Etching . . . 60

4 Two Dimensional Systems 61
4.1 Sample Description . . . 61
4.1.1 Self-assembly . . . 62
4.1.2 Magnetic Properties . . . 64
4.2 Sub-monolayer Fabrication . . . 66
4.3 Plasma Treatment . . . 68
4.3.1 Reference Sample . . . 68
4.3.2 Oleic Acid Removal . . . 70
4.3.3 Phase Transformation . . . 70
4.4 Polarization Effects . . . 75
4.5 Magnetoresistance Effects . . . 82
4.5.1 Measurements in van der Pauw Geometry . . . 82
4.5.2 Measurements on Hall Bar Structures . . . 85
4.5.3 Influence of Nanoparticle Size . . . 87
4.6 Conclusion . . . 89

5 Three Dimensional Systems 93
5.1 Nanoparticle Description . . . 93
5.2 Macrocrystal Preparation . . . 99
5.3 Macrocrystal Morphology . . . 101
5.3.1 Batch O1 . . . 101
5.3.2 Batch O2 . . . 109
5.4 Nanoparticle Arrangement . . . 113
5.4.1 Influence of Size Distribution . . . 113
5.4.2 Influence of Centrifugation Parameters . . . 115
5.4.3 Influence of Surfactants . . . 126
5.5 Magnetic Properties . . . 129
5.6 Polarization and Magnetoresistance Effects . . . 131

5.7 Conclusion 135

6 Summary and Outlook **137**

A Nanoparticle Data Sheet Ocean NanoTech **139**

B Sample List 2D **141**

C Magnetometry **143**

D SEM Images of Macrocrystals **145**

List of Figures **199**

List of Tables **209**

List of Acronyms **211**

List of Symbols **213**

Bibliography **221**

Acknowledgement **231**

1 Introduction

1.1 Motivation

Magnetic nanoparticle assemblies have moved into the focus of intense research activities due to their potential use as building blocks for high density data storage systems, spintronic devices, refrigeration or biomedical applications [1–4]. They exhibit novel optical, magnetic and electrical properties that are caused by size effects like quantum mechanically discrete energy states, superparamagnetism or surface plasmons [5–7]. Thanks to rapid developments in chemical synthesis, several characteristics like size and shape have become tunable for a broad range of materials [8].

Nevertheless, arranging nanoparticles in a desired configuration remains challenging: It is well known which phenomena contribute to the assembling process and the single mechanisms are also mostly well understood. But the complex interplay and huge variety of interactions make predictions about the outcome of a process and the overall understanding difficult.

However, if a nanoparticle assembly is successfully manufactured, it can exhibit extraordinary properties due to inter-particle interactions. Moreover, its characteristics can be tuned by embedding the system in specific matrix materials. In this way, an artificial material can be designed that exhibits a combination of properties that cannot be achieved by conventional substances.

1.2 Concept

The scope of this thesis is, on the one hand, the self-assembly of iron oxide nanoparticles to obtain two- and three-dimensional arrangements. On the other hand, it is investigated how the nanoparticles interact with each other and how they influence a polarizable matrix material.

Chapter 2 provides general information about the material system, magnetism and self-assembly. In addition, the basics of scattering theory and electrical transport are outlined as basis for the corresponding measurements. In chapter 3 the methods for sample preparation are described. Furthermore, all the instruments and measurement techniques that are used to investigate the samples are introduced. Chapter 4 is about two-dimensional nanoparticle assemblies and provides an in-depth study of their properties. Additionally, it is shown how these samples can be embedded into a polarizable matrix material and how matrix and particles influence each other. In chapter 5 these considerations are transfered to a three-dimensional system. A summary and outlook finally concludes this thesis in chapter 6.

1.3 Current State of Research

By now, the properties of individual magnetic nanoparticles are relatively well understood: The monodomain state was already investigated in 1959, where Bean and Livingston found a magnetic behavior at elevated temperatures, that is comparable to the Langevin paramagnetism of moment-bearing atoms but with a 10^6 times larger magnetic moment (so-called 'superspin'). They also defined the term 'superparamagnetism' [9]. Several studies concerning the switching behavior then demonstrated that the superspin can also be blocked below a specific temperature [10–14]. In 2009 Guimaraes et al. could also explain the formation of the monodomain state below a critical volume in general by employing energetic considerations [15].

After these aspects were understood, research activities concerning nanoparticle assemblies began to increase significantly. Several studies on systems with varying interaction strength led to the definition of four different systems. Assemblies without interaction are purely superparamagnetic, and for systems that exhibit non-negligible interactions that are nevertheless too weak to cause any collective behavior, the term 'modified superparamagnetism' was created. Fully frustrated, random superspins with a sufficiently strong interaction form a superspin glass and if the interaction is strong enough to arrange the superspins like atoms in a ferromagnet, this is referred to as 'superferromagnetism' [16–19]. Hereby, it is often assumed that the interaction is either of dipolar [20–23] or RKKY exchange character [24]. Various attempts have been made to achieve ordered systems with a macroscopic coherence length e.g. by surface functionalization or assisted self-assembly [25, 26]. However, as far as we know, there has been no success yet in manufacturing assemblies beyond the mesoscopic length scale.

Apart from the investigation of nanoparticle assemblies themselves, massive interest also arose in tuning the physical and chemical properties by matrix materials. Most studies focus on core/shell nanoparticles [27–33], but there are also approaches concerning capping [34], adsorption [35], interacting substrates [36] and embedding [35]. Among all the phenomena that are found in these systems, the polarization of platinum is especially relevant for this thesis. Several authors could demonstrate this effect using metallic nanostructures [37, 38], but as far as we know, all attempts using an oxide failed so far [39].

2 Theoretical Background

2.1 The Iron Oxides

Iron is a magnetic material that is malleable, ductile and strong. It is thus not surprising that it is known best as the metal that gave us tools and weapons. Furthermore, this white, shiny substance [40] is the second most abundant metal on earth. Nonetheless, it is rarely found as pure material in nature due to its rapid reaction with hydrogen and oxygen to form seventeen different configurations of hydroxides and oxides [41, 42]. Three of them, namely magnetite, maghemite and wustite are relevant for this thesis and will be discussed in detail below. The corresponding phase diagram is shown in figure 2.1.

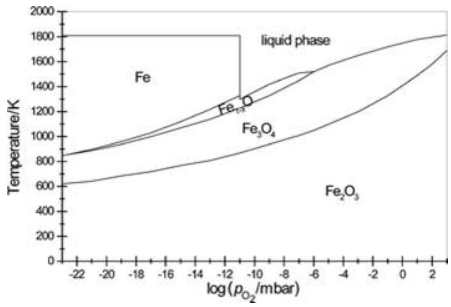


Figure 2.1: Phase diagram of the iron-oxygen system, reprinted with permission from [43].

2.1.1 Magnetite

Magnetite (Fe_3O_4) can easily be found in rocks and is the magnetic material known longest by mankind [44]. It is often referred to as lodestone and finds applications e.g. in spintronics, environmental research [45] or pigments due to its black color and good water solubility [46]. The crystal structure can be described by an inverse spinel with 32 O^{2-}, 8 Fe^{2+} and 16 Fe^{3+} ions in the unit cell (figure 2.2 a): The oxygen ions are aligned along the [111] direction of a Cubic Close Packing (CCP) structure (a = 0.839 nm) that forms octahedral and tetrahedral sites.

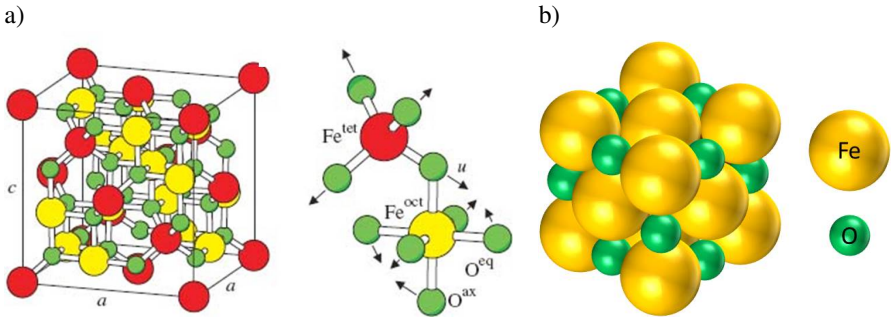


Figure 2.2: a) Inverse spinel (reprinted with permission from [48]) and b) rocksalt structure of wustite. Red and yellow spheres represent tetrahedrally and octahedrally coordinate iron ions, respectively. Green spheres are oxygen ions.

While the former are occupied by divalent and half of the trivalent ions, the latter are filled with trivalent ions only [47]. This leads to a ferrimagnetic behavior below the Curie temperature T_C = 858 K due to an antiparallel orientation of octahedrally and tetrahedrally coordinated ions [48]. While the magnetic moments of the trivalent iron ions cancel each other out, the moments of the remaining divalent ions yield a net magnetic moment of (9 μ_B - 4 μ_B) = 5 μ_B (M_s = 480·10^3 A/m) [49]. At low temperatures the material is insulating, but a charge ordering mechanism at the Verwey temperature T_V = 122 K leads to a phase transition which causes semi-metallic properties above this temperature [48].

2.1.2 Maghemite

Calcination of bulk magnetite at 570 K yields a red-brown substance called maghemite (Fe_2O_3) [46], that is applicable in medicine, magnetic recording or sensor technology [50]. Like magnetite it exhibits an inverse spinel structure (a = 0.834) with 32 O^{2-} ions, but the iron valency is different: 21 $\frac{1}{3}$ Fe^{3+} occupy all the tetrahedral and 13 ⅓ octahedral sites, leaving 2 ⅔ octahedrally coordinated vacancies. The material is also ferrimagnetic below its Curie Temperature T_C = 820 K [51], but has a slightly lower saturation magnetization M_s = 420·10^3 A/m [52].

2.1.3 Wustite

Wustite (FeO) is a material barely found in nature (e.g. as black substance in rocks [53]), because at atmospheric pressure it is stable above 840 K only. Nevertheless, non stoichiometric Fe_xO can be obtained by quenching the material to room temperature. This leads to a metastable mixed crystal that contains magnetite-like building blocks [54–56] and can be used e.g. as precursor for the synthesis of other iron oxides. Depending on the temperature and pressure, different compositions (x = 0.84 to 0.95) can be found, that form a rock salt structure (figure 2.2 b) with different lattice parameters (a = 0.428 nm to 0.431 nm) [53, 57, 58]. If the material is cooled below the Néel temperature T_N = 198 K, it becomes anitferromagnetic with the spins within the (111) plane being parallel to each other and antiparallel to adjacent layers [58].

2.2 Basics of Solid State Magnetism

2.2.1 Magnetic Moment

Every electron is inter alia characterized by a magnetic quantum number m_l and a spin quantum number m_s. These correspond, respectively, to an orbital angular momentum $\vec{L}$ and a spin angular momentum $\vec{S}$ as follows:

$$\overrightarrow{m_s} = -g_e \vec{S} \frac{\mu_B}{\hbar} \tag{2.1}$$

$$\overrightarrow{m_l} = -g \vec{L} \frac{\mu_B}{\hbar} \tag{2.2}$$

Where μ_B is the Bohr magneton, g ≈ 1 is the Landé factor and $g_e \approx 2$ gives the spin-g-factor [57, 59]. If an atom contains more than a single electron, three distinct coupling energies have to be considered for the calculation of the total angular momentum $\vec{J}$: Between the orbital angular momenta of single electrons (W_{l_i,l_k}), between the spins of single electrons (W_{s_i,s_k}) and between spin and orbital angular momenta (W_{l_i,s_i}). For W_{l_i,l_k}, $W_{s_i,s_k} \gg W_{l_i,s_i}$, single orbital angular momenta $\vec{l}$ and spins $\vec{s}$, respectively, couple to a total orbital angular momentum $\vec{L}$ and total spin $\vec{S}$, before they are summed up to the total angular momentum $\vec{J}$ (L-S coupling):

$$\vec{L} = \sum_i \vec{l_i} \tag{2.3}$$

$$\vec{S} = \sum_i \vec{s_i} \tag{2.4}$$

$$\vec{J} = \vec{L} + \vec{S} \tag{2.5}$$

$$|\vec{X}| = \sqrt{X(X+1)}\hbar \qquad \vec{X} = \vec{L}, \vec{S}, \vec{J} \tag{2.6}$$

For the other case (W_{l_i,l_k}, $W_{s_i,s_k} \ll W_{l_i,s_i}$), the orbital angular momenta and spins of every single electron couple to a total angular momentum $\vec{j}$ first, before they are added up to the total angular momentum of the whole electron shell $\vec{J}$ [60]:

$$\vec{j_i} = \vec{l_i} + \vec{s_i} \tag{2.7}$$

$$\vec{J} = \sum_i \vec{j_i} \tag{2.8}$$

The respective (paramagnetic effective) magnetic moment[1] μ represents the basic building block of solid state magnetism [61]:

$$\mu = -g_{(J,L,S)}\,\mu_B\sqrt{J(J+1)} \tag{2.9}$$

$$g_{(J,L,S)} = 1 + \frac{J(J+1) + S(S+1) - L(L+1)}{2J(J+1)} \qquad \text{(for L-S coupling)} \tag{2.10}$$

For bulk material consisting of a huge number of atoms, the magnetic moment $\vec{M}$ per unit volume V is then given by [57]:

$$\vec{M} = \frac{\vec{\mu}}{V} \tag{2.11}$$

If an external magnetic field $\vec{H}$ is applied, the material reacts by an additional magnetization, which is in case of a linear magnetic material given by:

$$\vec{M} = \chi\vec{H} \tag{2.12}$$

The constant of proportionality χ represents the magnetic susceptibility. The combination of macroscopic (external field) and microscopic (orbital currents in atoms / molecules and electronic spin) aspects causing magnetic fields finally leads to the magnetic induction $\vec{B}$:

$$\vec{B} = \mu_0(\vec{H} + \vec{M}) = \mu\mu_0\vec{H} \tag{2.13}$$

$$\mu = 1 + \chi \tag{2.14}$$

Where μ_0 and μ give the permeability of vacuum and matter, respectively [59].

2.2.2 Magnetic Interactions

If the total angular momentum $\vec{J}$ of an atom is different to zero, the respective magnetic moment (cf. equation 2.9) interacts with the magnetic moment of the atom next to it what results in several ordering phenomena. Before their discussion in section 2.2.4, the relevant types of interaction are presented.

Dipole-Dipole Interaction

From electrodynamics it is known that the interaction energy between two magnetic dipoles $\vec{\mu}_1$ and $\vec{\mu}_2$ separated by $\vec{r}$ is given by

$$E = \frac{\mu_0}{4\pi r^3}\left(\vec{\mu_1}\cdot\vec{\mu_2} - \frac{3}{r^2}(\vec{\mu_1}\cdot\vec{r})(\vec{\mu_2}\cdot\vec{r})\right). \tag{2.15}$$

[1] to be distinguished from the ordered moment for $T \to 0$

For individual atoms, the magnitude of the magnetic moment is usually in the order of several Bohr magnetons μ_B and they have a distance of several Ångstrøms to the next. For parallel alignment, this leads to a value of approximately

$$E = -\frac{2\mu_0\mu_B^2}{4\pi r^3} \approx 1.6 \cdot 10^{-23} J \approx 100\ \mu eV \tag{2.16}$$

which corresponds to a temperature of 1.2 K. Since the phenomena shown in section 2.2.4 are also found at room temperature, they must be caused by another effect [59].

Exchange Interaction

Except for metallic ferromagnetism, most magnetic ordering phenomena can be explained by the quantum mechanical exchange interaction. The model describes electrons by wave functions and is based on the Coulomb interaction (repulsive force between charged particles that have the same sign) as well as the Pauli exclusion principle. A distinction is made between direct and indirect exchange [59]:

Direct Exchange

Direct exchange is found if neighboring orbitals overlap sufficiently: Within a certain region of space around an electron the probability of finding another electron with the same spin orientation is close to zero due to the Pauli exclusion principle. This is referred to as exchange-correlation hole [59].

The wave function describing such a two-electron system consists of a spatial part $\Psi(r_1, r_2)$ and a spin part χ [62]. In total it has to be antisymmetric due to the fermionic nature of electrons. Hence, one part always has to exhibit the opposite symmetry than the other:

$$\Psi_S = \Psi^{sym}(\vec{r}_1, \vec{r}_2)\chi^{antisym} \tag{2.17}$$

$$\Psi_T = \Psi^{antisym}(\vec{r}_1, \vec{r}_2)\chi^{sym} \tag{2.18}$$

For the spin part, two symmetric eigenstates are obvious, namely $|\uparrow\uparrow\rangle$ and $|\downarrow\downarrow\rangle$. The other possible states $|\uparrow\downarrow\rangle$ and $|\downarrow\uparrow\rangle$ are neither symmetric nor antisymmetric themselves, but symmetry can be constructed by linear combinations:

$$\chi^{sym} = \frac{1}{\sqrt{2}}\left(|\uparrow\downarrow\rangle + |\downarrow\uparrow\rangle\right) \tag{2.19}$$

$$\chi^{antisym} = \frac{1}{\sqrt{2}}\left(|\uparrow\downarrow\rangle - |\downarrow\uparrow\rangle\right) \tag{2.20}$$

Since there is in total only one antisymmetric χ, this forms a singlet state (Ψ_S) in combination with $\Psi^{sym}(\vec{r}_1, \vec{r}_2)$, and a triplet state Ψ_T is given by $\Psi^{antisym}(\vec{r}_1, \vec{r}_2)$ together with one of the three possible symmetric spin wave functions. By applying a suitable Hamilton operator $\widehat{H}$, the energy difference between these states can be calculated:

$$E_S = \int \Psi_S^* \widehat{H} \Psi_S d\vec{r}_1 d\vec{r}_2 \tag{2.21}$$

$$E_T = \int \Psi_T^* \widehat{H} \Psi_T d\vec{r}_1 d\vec{r}_2 \tag{2.22}$$

$$E_S - E_T = 2 \int \Psi_a^*(\vec{r}_1) \Psi_b^*(\vec{r}_2) \widehat{H} \Psi_a(\vec{r}_2) \Psi_b(\vec{r}_1) d\vec{r}_1 d\vec{r}_2 = 2J \tag{2.23}$$

Where J is referred to as exchange integral. It shows, that the singlet and triplet state, having different positional wave functions due to the Pauli principle, are unequal in energy which is caused by the Coulomb interaction. For parallel (antiparallel) spin alignment the triplet (singlet) state must be energetically favorable, leading to J > 0 (J < 0) [59].

Using a parametrization of equation 2.23 the Hamilton operator can be rewritten as effective Hamiltonian which consists of a constant C and a spin dependent part $\widehat{H}^{spin}$:

$$\widehat{H} = \frac{1}{4}(E_S + 3E_T) - 2J\vec{S_1} \cdot \vec{S_2} = C + \widehat{H}^{spin} \tag{2.24}$$

The generalization to a many-body system by adding up interactions between all neighboring atoms is known as Heisenberg Hamiltonian [63]:

$$\widehat{H} = -2 \sum_{i>j} J_{ij} \vec{S_i} \cdot \vec{S_j} \tag{2.25}$$

Kinetic Exchange

Aside from the process described above, long range order can also be caused by electron hopping which is described by the Hubbard model: It considers electrons with spin $\frac{1}{2}$ (orientation $\sigma = \uparrow$ or $\downarrow$) that can move on a regular grid according to the Pauli principle. The corresponding Hamiltonian

$$\widehat{H} = -t \sum_{\langle ij \rangle, \sigma} \left(c_{i\sigma}^+ c_{j\sigma} + c_{j\sigma}^+ c_{i\sigma} \right) + U \sum_i (n_{i\uparrow} n_{i\downarrow}) = \widehat{H}_t + \widehat{H}_U \tag{2.26}$$

consists of the kinetic energy given by $\widehat{H}_t$ and the Coulomb energy described by $\widehat{H}_U$. The operator $c_{i\sigma}$ removes an electron with spin σ from lattice site i and $c_{j\sigma}^+$ creates an electron with the same spin at j whereby the sum considers neighboring sites $i < j$ only. The hopping amplitude $t > 0$ is a measure for the energy gain due to delocalization and the Coulomb energy U gives the energy that is required if two electrons occupy the same lattice site. Hence, for $U \ll t$ the model describes a metallic material, while for $U \gg t$ the material is a Mott-Hubbard insulator.

If neighboring orbitals are both occupied, hopping and thus energy gain is possible only for antiparallel spin orientation due to the Pauli exclusion principle. This leads to antiferromagnetic coupling (figure 2.3a). But for lattice sites that provide two degenerate energy levels, an electron will preferably perform a hopping process to the empty orbital, if it is oriented parallel

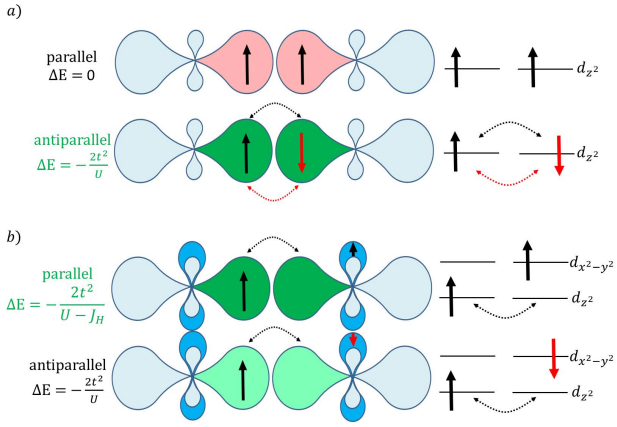


Figure 2.3: Energy gain due to hopping if a) neighboring lattice sites are both occupied, or b) every lattice site provides two degenerate energy levels and the considered one is empty. Green orbitals allow for electron hopping (darker green corresponds to larger energy gain), red orbitals not. According to [59].

to the other electrons. This is caused by the 1^{st} Hund's rule which states that maximum spin is energetically favorable (figure 2.3b).

Indirect Exchange

In transition metal oxides, two metal ions are usually separated by an intermediate oxygen ion. The kinetic interaction on one side of the oxygen ion influences the other side, what can cause long range order. Two different mechanisms are distinguished:

If neighboring metal ions exhibit the same valence state, only virtual hopping is possible. This so-called "super exchange" is exemplarily shown for manganese oxide in figure 2.4: For a 180° interaction between two filled (a) or two empty orbitals (b), it is energetically favorable for the metal ions to align antiparallel. But for a 180° interaction between a filled and an empty orbital (c), or for a 90° interaction between two filled orbitals (not shown here), parallel orientation is favorable. These configurations are found in most transition metal oxides with only one valance state and are referred to as Goodenough-Kanamori-Anderson rules.

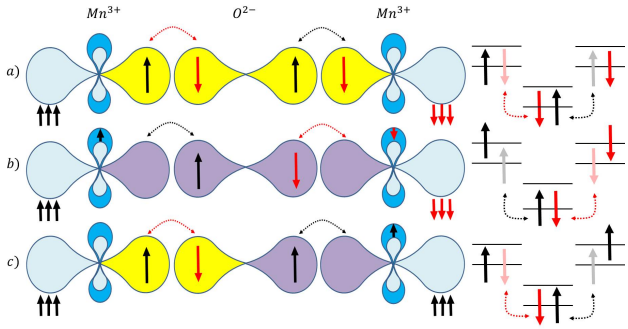


Figure 2.4: Super exchange interaction in manganese oxide for different geometries: Depending on the configuration, either antiparallel (a,b) or parallel (c) arrangement is energetically favorable. Yellow (purple) orbitals correspond to an antiparallel (parallel) coupling between oxygen and manganese, according to [59].

If the metal ion is present in two different valence states, real hopping becomes possible: For parallel alignment, changing the lattice site does not require an excitation energy and leads to energy gain due to delocalization. This process is called "double exchange" and is exemplarily shown for manganese oxide in figure 2.5 [59].

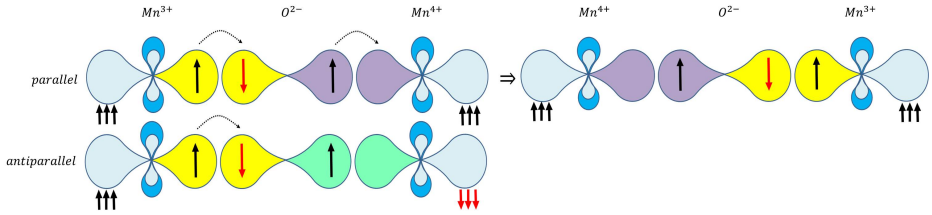


Figure 2.5: Double exchange interaction in manganese oxide: For parallel arrangement of manganese ions hopping is possible without excitation energy, according to [59].

2.2.3 Anisotropy

If single magnetic moments are embedded in a periodic lattice[2], the wave functions of neighboring moments exhibit different overlap energies for varied orbital moment orientations [64]. This causes **magnetocrystalline anisotropy** with so-called easy axes, along which the material can be more easily magnetized than along other directions. Hence, the system has an additional energy term which depends on the angle θ between the favored direction and the magnetic moment. For uniaxial anisotropy, this can be described by

$$E_{MC}^{uni} = K_1 V \sin^2\theta + K_2 \sin^4\theta \tag{2.27}$$

[2]Even though this simple model is based on localized magnetic moments, it is also utilized for metallic band magnets.

Where K_1 and K_2 are the anisotropy constants. If the system exhibits cubic anisotropy, three different axes can be identified. These are usually not equal in energy leading to a primary, secondary and tertiary axis. In spherical coordinates, the corresponding energy is

$$E_{MC}^{cubic} = K_1 \left(\frac{1}{4} sin^2\theta \sin^2 2\Phi + \cos^2\theta \right) \sin^2\theta + \frac{K_2}{16} \sin^2 2\Phi \sin^2 2\theta + ... \tag{2.28}$$

Where θ and Φ are the polar and azimuthal angle between the favored direction and the magnetic moment, respectively. The magnetocrystalline anisotropy energy is usually larger in a lattice with low symmetry than in highly symmetrical systems. Aside from these effects mainly arising from spin-orbit coupling [63], preferred directions can also be caused by dipolar interactions: This so-called **shape anisotropy** originates from the slow decrease in dipolar interaction as a function of the distance ($\propto r^{-3}$) in a finite body. Summation over all pairs of moments converges slowly and the dipolar field experienced by a certain moment considerably depends on the moments at the sample boundary [65]. This can e.g. keep the magnetization of thin films in the plane, what can be described by

$$E_{shape}^{film} = \frac{1}{2} \mu_0 M^2 \cos^2\theta \tag{2.29}$$

Where M is the magnetization and θ gives the angle between the magnetic moment and the film normal [63]. Another example are elongated particles, where the demagnetization factors parallel ($N_\parallel$) and perpendicular ($N_\perp$) to the long symmetry axis yield different values. The corresponding energy can be estimated using the ellipticity κ and the angle Ψ between the long symmetry axis and the magnetization direction [64]:

$$E_{shape}^{particle} = \frac{1}{2}(N_\perp - N_\parallel)\mu_0 V M_s^2 \sin^2\psi \tag{2.30}$$

$$N_\parallel = \frac{1}{\kappa^2 - 1} \left(\frac{\kappa}{2\sqrt{\kappa^2 - 1}} \ln \left(\frac{\kappa + \sqrt{\kappa^2 - 1}}{\kappa - \sqrt{\kappa^2 - 1}} \right) - 1 \right) \tag{2.31}$$

$$N_\perp = \frac{\kappa}{2(\kappa^2 - 1)} \left(\kappa - \frac{1}{2\sqrt{\kappa^2 - 1}} \ln \left(\frac{\kappa + \sqrt{\kappa^2 - 1}}{\kappa - \sqrt{\kappa^2 - 1}} \right) \right) \tag{2.32}$$

But anisotropy can also be caused by broken translation symmetry, e.g. at the particle surface, where the number of nearest neighbors is reduced. This leads to **surface anisotropy** which can e.g. favor an out-of-plane magnetization direction. This effect competes with the volume anisotropy, but it is usually comparably small and therefore often neglected [64].

2.2.4 Classification of Magnetic Materials

The magnetic susceptibility χ introduced in section 2.2.1 is a useful measure on how a material can be magnetized if it is exposed to an external field. Hence, several phenomena are identified using its value and temperature dependency:

Paramagnetism

It was already shown that electrons possess a permanent magnetic moment due to their orbital movement and their spin. In a magnetic field these begin to align while thermal motion counteracts this effect. Since the alignment results in a net positive magnetization, the related susceptibility has to be positive as well (c.f. equation 2.12):

$$\chi_{para} > 0 \tag{2.33}$$

For localized electrons (atomic paramagnetism) two different cases are possible [59]: If the electron shell is partially filled, it is a semi-classical mechanism, where the spin orientation is assumed to be quantized while the thermodynamics are treated classically using Boltzmann statistics. Hence, this so-called Langevin-paramagnetism is temperature dependent. But paramagnetism is also found in materials with entirely filled shells: Even though the total angular momentum is zero for the ground state, perturbation theory allows a mixing of exited states that can possess a finite magnetic moment into the ground state. This leads to a finite, temperature independent paramagnetism that can be found in all materials. However, this so-called van-Vleck-paramagnetism is relevant for vanishing ground states only and is therefore usually neglected [63].

Furthermore, paramagnetism can be caused by the spin of itinerant electrons in a metal. This so-called Pauli-paramagnetism is temperature independent. While the Langevin-paramagnetism is a rather large effect ($\chi_{para}^{Langevin} = 10^{-3\ldots-2}$), the Pauli- and van-Vleck-paramagnetism are usually comparably small[3] ($\chi_{para}^{Pauli} = \chi_{para}^{vanVleck} = 10^{-6\ldots-5}$) [59].

Diamagnetism

The phenomenon of diamagnetism is often qualitatively explained using classical physics: It is assumed, that a magnetic field applied to an atom with no net magnetic moment generates small currents inside the atom by induction. According to Lenz's law, these currents counteract their cause leading to induced magnetic moments that are aligned antiparallel to the external field. The resulting susceptibility is negative and temperature independent:

$$\chi_{dia} < 0 \tag{2.34}$$

But even though this approach is entirely wrong because diamagnetism is a pure quantum mechanical effect, the magnetic moment calculated using QM is in agreement with the classical result [66].

In general, diamagnetic behavior can be found in both, materials with entirely filled shells (Larmor-diamagnetism) and in metals with itinerant electrons (Landau-Diamagnetism), but the susceptibility value is comparably small ($\chi_{dia} = 10^{-6\ldots-5}$) [59]. An overview is given in table 2.1.

[3] Nevertheless, in molecular crystals the van-Vleck-paramagnetism can sometimes exceed the Langevin-paramagnetism [63].

	Paramagnetism	**Diamagnetism**
Localized electrons	Spin and orbital angular momentum of partially filled shells $Langevin - paramagnetism$ $\chi^{Lang} = \frac{C}{T} = \frac{N\mu_0\mu^2}{V3k_BT}$	
	Spin and orbital angular momentum of excited states in atoms with entirely filled shells $vanVleck - paramagnetism$ $\chi^{vV} = \frac{2\mu_0\mu_B^2 N}{V} \sum_{n=1,2,...} \frac{\lvert<n\rvert L_z + g_e S_z \rvert 0>\rvert^2}{E_n - E_0}$	Orbital angular momentum of atoms with entirely filled shells $Larmor - diamagnetism$ $\chi^{Lar} = -\frac{\mu_0 N e^2}{6m_e V} Z_a r_a^2$
Conduction electrons	Spin $Pauli - paramagnetism$ $\chi^P = \frac{3N\mu_0\mu_B^2}{2E_F}$	Orbital angular momentum $Landau - diamagnetism$ $\chi^{Land} = -\frac{\mu_0 k_F e^2}{12\pi^2 m_e} = -\frac{1}{3}\chi^P$

Table 2.1: Classification of magnetic effects, where C is the Curie constant and T is the temperature. N is the number of atoms, μ_0 and μ represent the vacuum and magnetic permeability, respectively. V is the volume and k_B the Boltzmann constant. e and m_e give the electronic charge and mass, respectively. Z_a describes the number of electrons and r_a is the ionic radius. μ_B is the Bohr magneton and g_e is the electronic g-factor. E_n and E_0 represent the energy of the excited and ground state, respectively and E_F is the Fermi energy [59].

Collective Magnetism

In section 2.2.2 several magnetic interactions operating between magnetic moments of solids were presented. These can produce different types of magnetic ground states of which some are temperature dependent. Examples are ferromagnetism where magnetic moments align parallel or antiferromagnetism where adjacent magnetic moments are oriented antiparallel to each other. Their susceptibility can be fitted to the Curie-Weiss-law:

$$\chi \propto \frac{1}{T - \theta} \tag{2.35}$$

Where θ represents the Weiss temperature which is zero for a truly paramagnetic material, positive for ferromagnets ($\theta = T_C$) and negative in antiferromagnets without frustration ($\theta = -T_N$). The corresponding Curie temperature T_C and Néel temperature T_N are the critical values above which the materials become paramagnetic. While experimentally determined data often meets the calculated value of the former quite well, the latter can be very different. This is due to several simplifications in the underlying model [63].

Ferromagnetism

As shown in section 2.2.2 ferromagnetism (i.e. parallel spin alignment) is found in materials with a positive exchange constant. But at sample edges e.g. the magnetic field diverges what leads to demagnetizing fields that cost the energy $\frac{B^2}{2\mu_0}\left[\frac{J}{m^3}\right]$. This can be avoided by breaking the material into domains as shown in figure 2.6 a. On the other hand, this is also related to energy costs, because the magnetization has to rotate between domains, so that a component will lie along the hard axis. The domain wall formation is therefore a balance between the energy cost for their formation and the cost of demagnetizing fields [63].

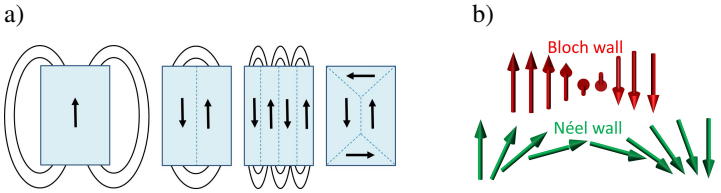


Figure 2.6: a) Domain formation and stray field reduction in ferromagnetic materials. b) Illustration of spin rotation within Bloch and Néel walls.

The width of these domain walls is also a balance, but between exchange and anisotropy energies: The larger the angle between two exchange coupled spins in a ferromagnet, the higher is the corresponding energy cost. Hence, the total rotation of 90° or 180° is distributed on N minor rotations. On the other hand, every single spin which is not parallel to the easy axis has a component along the hard axis, which is not energetically favorable. Thus, the energy per interface area of a domain wall σ_w contains a contribution from exchange interaction (tending to expand the wall) and anisotropy (tending to tighten the wall):

$$\sigma_w = \frac{JS^2\pi^2}{Na^2} + \frac{NKa}{2} \tag{2.36}$$

Where J is the exchange integral and S is the spin. The interatomic distance is given by a and K is the anisotropy constant. The equilibrium configuration delivers the domain wall width δ by applying $d\sigma_w/dN = 0$:

$$\delta = Na = \pi S\sqrt{\frac{2J}{Ka}} \tag{2.37}$$

Depending on the dimensionality, either Bloch walls, where the magnetization rotates through the plane (bulk), or Néel walls, where it turns within the plane (thin films) are found (c.f. figure 2.6 b) [63].

When the magnetic moment is recorded as function of the applied magnetic field, ferromagnetic materials exhibit hysteretic behavior. This is either caused by coherent / incoherent spin rotation or domain wall movement (figure 2.7 a). For the latter, domains that are energetically favorable grow at the expense of others (this process is reversible) until they are pinned at defects. If the magnetic field is further increased above a critical value, domain wall movement suddenly continues and the change becomes irreversible. These so-called Barkhausen jumps are shown in the inset of figure 2.7 b [67, 68].

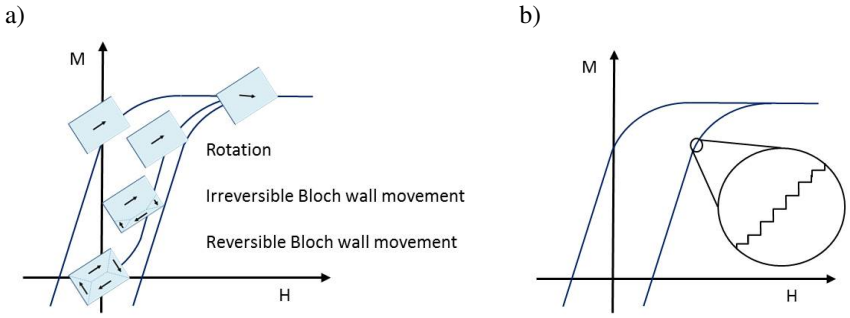


Figure 2.7: a) Illustration of the physical origin of ferromagnetic hysteresis loops. b) Barkhausen jumps.

Antiferromagnetism

If the exchange constant is negative, the spins of next neighbors will align antiparallel to each other causing antiferromagnetism. This situation can be interpreted as two interpenetrating, antiparallel, ferromagnetic sub-lattices that completely cancel each other (figure 2.8).

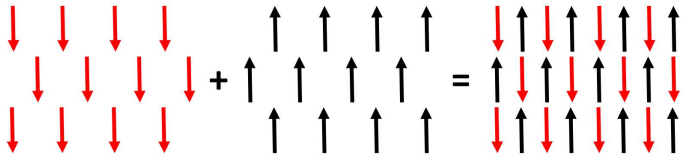


Figure 2.8: Illustration of antiferromagnetic order by two interpenetrating ferromagnetic sub-lattices.

If a magnetic field is applied perpendicular to the anisotropy axis, both sub-lattices will turn by a small angle in opposite directions leading to a net magnetic moment (figure 2.9 a). This is possible even for small fields. But for magnetic fields that are parallel to the anisotropy axis, the spins will not cant until a critical value is reached. Then, one sub-lattice will either change its direction by 180° (spin-flip) or both spins will change to a completely new configuration where they exhibit the same angle towards the field direction (spin-flop, figure 2.9 b) [59].

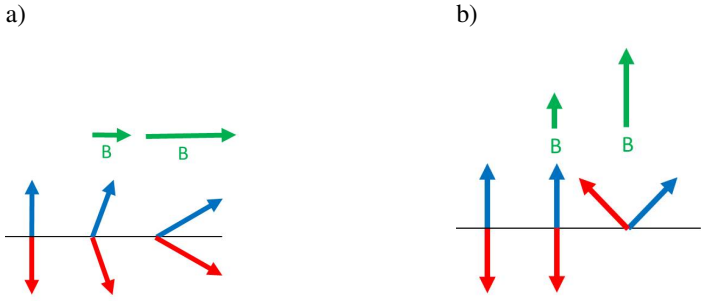


Figure 2.9: a) Antiferromagnetic spin canting if a magnetic field is applied perpendicular to the anisotropy axis. b) Spin-flop process for magnetic fields applied parallel to the anisotropy axis.

Ferrimagnetism

Similar to antiferromagnetic materials, ferrimagnetic systems exhibit two interpenetrating, ferromagnetic sub-lattices. However, they do not completely compensate each other, leading to a net magnetic moment. This is e.g. possible if the sub-lattice moment lengths are different, or if they are not exactly antiparallel to each other. Since the spontaneous magnetization is different for the sub-lattices due to distinct molecular fields, the overall magnetization behavior can be very complex. The susceptibility can therefore often not be described by a simple Curie-Weiß law, though a well defined Curie temperature can be found [59, 63].

Spin glass

If materials exhibit competitive relations between exchange interactions (e.g. for random anisotropies or RKKY interactions) and some kind of randomness (e.g. site- or bond-randomness) they can form a spin glass. These systems are dynamically disordered at elevated temperatures, but if they are cooled below a critical value, the independent spins begin to build up correlated units. Interactions become more long ranged but stay random to some extent ("cooperative freezing"): The system freezes into one of its many ground states, which is metastable and has a slow relaxation behavior [63]. This leads to several interesting phenomena, like e.g. the aging process (c.f. section 3.1.3) [59].

Itinerant Ferromagnetism

In a metallic ferromagnet such as Fe, Co or Ni, the magnetic moment and the ferromagnetic order are caused by the spin of itinerant conduction electrons. Hence, a model based on exchange interaction that was derived for localized spin systems can only be applied in a very limited way [69]. A better description is given by band-ferromagnetism that can be motivated using molecular field theory: it assumes that all spins experience the same average exchange field $\lambda\vec{M}$ caused by all their neighbors. The electron gas in a metal can be magnetized by this molecular field according to the Pauli-paramagnetism χ_P mentioned above. In turn, the resulting magnetization is responsible for the molecular field. Hence, this positive feedback mechanism ("chicken-and-egg scenario") can lead to spontaneous magnetization if the resulting state is energetically favorable: flipping spin-down electrons with energies from $(E_F - \delta E)$ to E_F transfers them to the spin-up band with energies from E_F to $(E_F + \delta E)$. The corresponding kinetic energy change ΔE_{KE} equals the product of the number of moved electrons and their energy increase δE:

$$\Delta E_{KE} = \frac{1}{2} g(E_F)\delta E \cdot \delta E = \frac{1}{2} g(E_F)(\delta E)^2 \tag{2.38}$$

Where $g(E_F)$ is the density of states at the Fermi edge. The energy of the molecular field ΔE_{PE} is given by:

$$\Delta E_{PE} = -\int_0^M \mu_0(\lambda M')dM' = -\frac{1}{2}\mu_0\lambda M^2 \tag{2.39}$$

Assuming the magnetic moment of every electron is 1 μ_B, the magnetization M is

$$M = \mu_B(n_\uparrow - n_\downarrow) = \mu_B \left(\left[\frac{1}{2}(n + g(E_F)\delta E) \right] - \left[\frac{1}{2}(n - g(E_F)\delta E \right] \right) = \mu_B g(E_F)\delta E \tag{2.40}$$

Hence, the total energy change ΔE can be written as

$$\Delta E = \Delta E_{KE} + \Delta E_{PE} = \frac{1}{2} g(E_F)(\delta E)^2 \left(1 - U g(E_F)\right) \tag{2.41}$$

Where $U = \mu_0 \lambda \mu_B^2$ is a measure for the exchange energy. Since spontaneous magnetization is possible only if the energy reduction by the molecular field outweighs the energy cost for spin flipping (i.e. $\Delta E < 0$), equation 2.41 implies the necessity of

$$U g(E_F) \geq 1 \tag{2.42}$$

This so-called Stoner criterion shows that ferromagnetism in metals mainly requires strong exchange interaction and a large density of states at the Fermi level [63].

2.2.5 Nanomagnetism

Table 2.2 demonstrates that several characteristic lengths are in the same order of magnitude as the dimensions of nanomaterials. This gives rise to several surface- and finite-size-effects which cause numerous extraordinary properties and an interesting dynamic behavior [15]. However, this section will focus on the main concepts like the single domain state, magnetic anisotropy and supermagnetic states only.

Property	Length scale [nm]
Interatomic distance	10^{-1}
Fermi wavelength	$10^{-1} - 10^2$
Electron mean free path	$1 - 10^2$
Spin diffusion length	$10 - 10^2$
Exchange interaction range	$10^{-1} - 1$
RKKY interaction range	$10^{-1} - 10$
Domain size	$10 - 10^4$
Domain wall width	$1 - 10^2$
Critical diameter for superparamagnetism	$1 - 10^2$

Table 2.2: Examples for several characteristic length scale ranges, according to [15].

Single Domain Nanoparticles

As shown in section 2.2.4, ferromagnetic materials are often divided into domains because the energy loss due to domain wall formation is much smaller than energy gain by stray field

reduction. But if the sample size is reduced, the former becomes more costly compared to the latter. Hence, a critical radius R_c can be defined, below which the single domain state becomes energetically favorable: the energy for the monodomain state of a spherical particle of radius r is given by

$$E_{mono} = \frac{2}{9}\mu_0 \pi M^2 r^3 \tag{2.43}$$

and the energy cost for a 90° or 180° domain wall (c.f. figure 2.10) corresponds to

$$E_{wall}^{90°} = 2\pi r^2 \sigma_w^{90°} \tag{2.44}$$

$$E_{wall}^{180°} = \frac{1}{9}\mu_0 \pi M^2 r^3 + \pi \sigma_w^{180°} \tag{2.45}$$

Where σ_w is the energy cost of a wall per unit area (c.f. equation 2.36). For $E_{mono} < E_{wall}$ domain wall formation becomes energetically unfavorable leading to

$$R_c < \frac{9\sigma_w}{\mu_0 M^2} \tag{2.46}$$

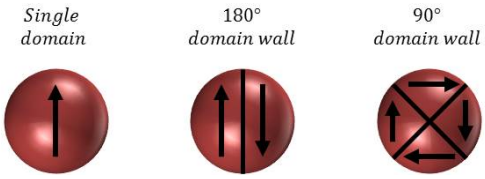


Figure 2.10: Examples for magnetization configurations in spherical ferromagnetic nanoparticles.

Supermagnetic States

In the previous section it was shown that nanoparticles can exhibit a monodomain state under specific conditions. Assuming strong exchange interaction and neglecting spin canting effects due to surface anisotropy, all spins within such a particle can be summed up to a so-called "superspin". In nanoparticle assemblies, these superspins can interact and cause order or frustration leading to systems that are reminiscent of a conventional spin glass or ferromagnetic system [64]:

Superparamagnetism

A model describing non-interacting single domain nanoparticles was developed by Stoner and Wohlfarth in 1948. They assumed magnetization reversal by coherent rotation only and neglected curling and buckling (figure 2.11), which also implies that surface anisotropy is negligible. The energy of such a particle is then given by

$$E = E_{MC} + E_{shape} - \mu_0 H M_s V \cos(\alpha - \theta) \tag{2.47}$$

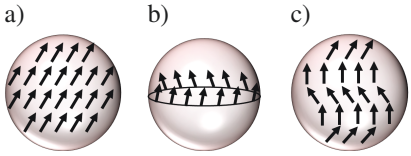


Figure 2.11: Illustration of possible magnetization reversal modes in single-domain nanoparticles: a) Coherent rotation occurs if all moments rotate in unison and always point into the same direction. b) For curling the spins are gradually wound up and in c) the buckling mode the spin structure is gradually compressed, according to [64].

where the last term denotes the Zeeman energy. θ is the angle between the superspin moment and the magnetocrystalline anisotropy axis. The angle between the latter and the applied magnetic field $\vec{H}$ is given by α. By considering only one effective anisotropy axis as mentioned before, equation 2.47 simplifies to

$$E = KV \sin^2\theta - \mu_0 H M_s V \cos(\alpha - \theta). \tag{2.48}$$

By plotting this function in dependency of the angle between superspin and anisotropy axis, one finds two minima at 0° and 180° that are separated by the energy barrier $\Delta E = KV$ (figure 2.12). A magnetic field can lead to a favored direction, but in zero-field the orientations are energetically degenerate. Here, the superspin either flips between the two possible orientations if the thermal energy $E_{th} = k_B T$ is larger than the barrier, or it is frozen in one direction for low E_{th}. For the reason that ΔE is very small for nanoparticles, the former is the more common case. These dynamics can be portrayed by the Néel-Brown model which describes the probability p for superspin reversal by an Arrhenius law and gives the characteristic relaxation time τ:

$$\tau = \tau_0 \exp\left(\frac{KV}{k_B T}\right) \propto \frac{1}{p} \tag{2.49}$$

Where $\tau_0 = 10^{-12}...10^{-9}$ s (depending on the applied field and temperature) gives the elementary spin flip time. By assuming a barrier height of e.g. 315 K one finds relaxation times between 10^{-9} s and 10^{+18} s at 300 K and 5 K, respectively. This enormous range has to be kept in mind by performing measurements because they also have their specific time scale. Hence, the so-called blocking temperature T_B is defined where the time scale of the measurement procedure τ_m and the superspin reversal τ match:

$$T_B = \frac{KV}{k_B \ln(\tau_m/\tau_0)} \tag{2.50}$$

This temperature can be found using measurements according to the ZFC protocol described in section 3.1.3 by estimating the temperature at maximum magnetization. In addition, the size distribution can be evaluated by comparing this measurement to the FC curve: while the peak position in the ZFC curve is characteristic for the overall averaged relaxation time, in the FC curve larger particles will block earlier upon cooling than the average size. Hence, the curves will split at higher temperatures for broader size distributions.

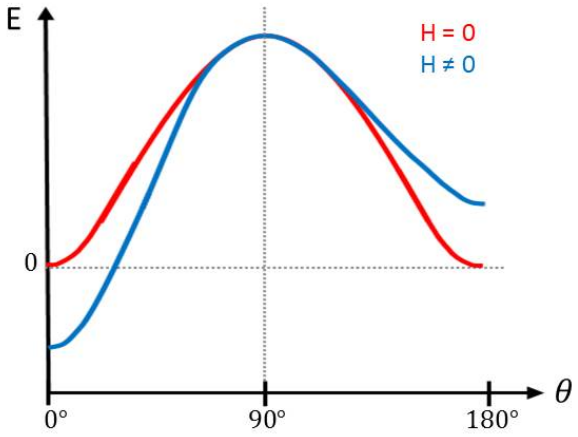


Figure 2.12: Energy of a single-domain nanoparticle in dependency of the angle θ between the superspin and the anisotropy axis, according to the Stoner-Wohlfarth model for zero applied field (red) and a magnetic field with $h = \frac{\mu_0 H M_s}{2K} = 0.2$ (blue), according to [64].

Finally, it should be mentioned that the blocking temperature is also reduced with increasing external fields, because they lower the energy barrier [64].

Superspin Glass

A disordered assembly of single-domain nanoparticles with frustrated interparticle interaction is comparable to spin glasses as described in section 2.2.4. For the reason that superspins align instead of atomic ones, it is referred to as superspin glass (SSG).

To furnish proof that a system exhibits such behavior, several measurement procedures are possible: if e.g. the magnetization is measured upon cooling while a magnetic field is applied, the curve will exhibit a dip below the glass temperature which can be qualitatively identified using a ZFC measurement[4].

Another feature found in glassy systems only is aging. It can be probed by memory effect measurements as outlined in section 3.1.3 (ZFC protocol with inserted aging stop below the blocking temperature). During the waiting time a superspin glass system will relax into an energetically favorable state leading to a reduced magnetic moment. Due to the enormous range of time scales found in spin glasses, this has no influence on the states at all other temperatures below and above the stopping temperature [64].

Superferromagnetism

As the name implies, a superferromagnetic system consists of strongly interacting nanoparticle-superspins that are aligned in parallel within a certain region of space (domain). But despite their similar appearance, conventional and super FM have different origins: usually, nanoparticles are coated by a surfactant shell to avoid agglomeration by steric repulsion. This leads to distances of several tens of Ångstrøms what makes exchange (the cause for conventional FM)

[4] Here it coincides with the blocking temperature.

negligible ($E \approx 10mK$). But due to the large magnetic moment of superspins, dipolar interaction (which is negligible in conventional FM) becomes significant, as will be shown in section 2.3.2. Hence, this effect is also referred to as dipolar FM [64].

2.3 Self-Assembly

Self-assembly is an ever-present phenomenon found in nature at any length scale: beginning with atoms arranging in crystal structures over several weather phenomena up to galaxy formation. But although interactions in bulk materials are as well understood as molecular forces, the description of effects emerging at the nanoscale remains problematic: neither scaling down the former, nor scaling up the latter, meets the results found for nanomaterials sufficiently and no consistent model is known so far due to the enormous amount of aspects influencing the process. Hence, for every individual system one has to decide which interactions dominate for the particular shape, size, separation and external parameters [47]. This section will focus on the main microscopic (van der Waals interaction, magnetic interactions in nanoparticle systems, steric repulsion), mesoscopic (capillary forces, attractive depletion force) and macroscopic effects (entropy) that are relevant for this thesis.

2.3.1 Van der Waals Interaction

In atoms, molecules and even bulk materials positive and negative charges perform random motions. These electromagnetic fluctuations cause (mostly) attractive forces that are summarized by the term van der Waals interaction. It can be quantified by several theoretical models, like e.g. the Hamaker integral approximation where the potential U_{vdW} is calculated by taking three phenomena into account that all scale with r^{-6}:

$$U_{vdW} = \frac{C^{Keesom} + C^{Debye} + C^{London}}{r^6} = \frac{C_{vdW}}{r^6} \tag{2.51}$$

Where r is the distance between the considered atoms or molecules [47]. The first term is the Keesom interaction which describes the polarization of a permanent dipole by another one:

$$C^{Keesom} = \frac{u_1^2 u_2^2}{3(4\pi\epsilon_0\epsilon_r)^2 k_B T} \tag{2.52}$$

Where u gives the orientational polarizability of dipole 1 and 2. ϵ_0 and ϵ_r are the vacuum and relative permittivity, respectively. k_B denotes the Boltzmann constant and T gives the temperature. In addition, permanent dipoles are capable of inducing dipoles in their neighborhood. This is referred to as Debye interaction:

$$C^{Debye} = \frac{u_1^2\alpha_{02} + u_2^2\alpha_{01}}{(4\pi\epsilon_0\epsilon_r)^2} \tag{2.53}$$

The electronic polarizability of the non-polar atom is given by α_0. The last term is the so-called London interaction, which is usually the dominating force. It considers the instantaneous dipole moment found in every atom due to thermal fluctuations which averages to zero over time:

$$C^{London} = \frac{3\alpha_{01}\alpha_{02}}{2(4\pi\epsilon_0\epsilon_r)^2} \cdot \frac{h\nu_1 h\nu_2}{h\nu_1 + h\nu_2} \tag{2.54}$$

Where h gives the Planck constant and ν is the orbiting frequency of the electron [70]. Pairwise summation or integration enables the description of mesoscopic, spherical objects with radius a and molar volume v:

$$U_{vdW} = \frac{C_{vdW}\pi}{3v_1v_2} \cdot \left[\frac{a_1a_2}{r^2-(a_1+a_2)^2} + \frac{a_1a_2}{r^2-(a_1-a_2)^2} + \frac{1}{2}\ln\left(\frac{r^2-(a_1+a_2)^2}{r^2-(a_1-a_2)^2}\right)\right] \tag{2.55}$$

Magnetite nanoparticles with a diameter of 10 nm e.g. exhibit a value of $U_{vdW} = 500\ k_BT$ at a distance of 0.1 nm [71]. Further models for the van der Waals interaction like e.g. the Dzyaloshinskii-Lifshitz-Pitaevskii-method which is derived from a continuum approach or the coupled-dipole model that utilizes pairwise summation, also take many-body effects into account. However, the Hamaker approximations seems to fit best for nanoparticular distances. Hence, the other models will not be discussed in this section [47].

2.3.2 Magnetic Interaction in Nanoparticle Systems

As outlined in section 2.2.5, dipole-dipole interactions between single domain nanoparticles can be very strong due to their superspin of $\mu = 10^3 - 10^5\mu_B$. The calculation of the corresponding interaction energy with equation 2.15 yields the static value. But in section 2.2.5 it was shown, that superspins perform thermally activated fluctuations, which also have to be taken into account. Hence, the total dipolar energy is

$$U_{dd} = U_{dd}^{stat} + U_{dd}^{fluc} \tag{2.56}$$

$$U_{dd}^{fluc} = -\frac{1}{3k_BT}\left(\frac{\mu_1\mu_2}{4\pi\mu_0 r^3}\right)^2 \tag{2.57}$$

Where k_B represents the Boltzmann constant and T is the temperature. r describes the nanoparticle distance and μ_0 is the vacuum permeability [47]. Depending on the nanoparticle concentration and strength of interaction, either hexagonal close packed structures (high concentration) or the formation of chains, rings and networks (low concentration) can be found due to the directional nature of the dipolar interaction.

Another aspect that has to be considered is exchange interaction. It is a very short-ranged effect and therefore becomes relevant only for extremely close packed arrangements with nanoparticle cores in close contact (i.e. without e.g. an organic shell inbetween) where the wave functions of surface atoms belonging to different particles can overlap. As described in section 2.2.2, it can lead to either parallel or antiparallel alignment [64].

2.3.3 Steric Repulsion

An undesirable effect often found in nanoparticular systems is agglomeration due to strong attractive forces trying to minimize surface energy. This can be prevented e.g. by steric repulsion: long chained molecules normally tend to become dense and short to maximize entropy, but if they are in contact with a solvent, good wetting is energetically favorable so they tend to stretch. The result is an equilibrium height h_0 balancing these two effects. By grafting one end of such molecules to the surface of nanoparticles while leaving the other one free, a brush-like structure emerges (figure 2.13) that avoids agglomeration by an intrinsic osmotic pressure. Physical properties, like the repulsive force U_s between two spherical particles with radius a_1 and a_2 separated by r can be calculated using numerical methods as the Monte-Carlo simulation:

$$U_s = \frac{2\pi a_1 a_2}{a_1 + a_2} \times \frac{\pi^2 k_B T \Gamma h_0^3}{6Nb^2} \left(-\ln u - \frac{9}{5}(1-u) + \frac{1}{3}(1-u^3) - \frac{1}{30}(1-u^6) \right) \tag{2.58}$$

$$u = \frac{r - a_1 - a_2}{2h_0} \tag{2.59}$$

Where the number of monomers with length b in the chain is given by N and the surface density of polymers is described by Γ [47].

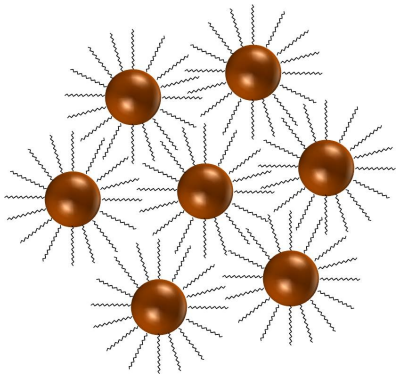


Figure 2.13: Illustration of steric stabilization.

2.3.4 Capillary Forces

If two solids are separated by a small gap that is filled with a fluid, they exhibit strong adhesive interaction. This effect was first observed in capillaries where liquids can rise against gravity. Hence, the underlying mechanism is referred to as capillary force. The phenomenon is based on the fact that surface atoms have less neighbors to interact with than atoms in the interior. The consequential net force perpendicular to the surface induces contraction and is called surface tension:

$$\sigma = \int_{-\infty}^{+\infty} (p_N - p_T)\, dz \tag{2.60}$$

Where p gives the tangential (T) and normal (N) pressure components, respectively. z is the distance to the surface. The pressure difference across such a curved liquid is described by the Young-Laplace relation:

$$\Delta p = \sigma \left(\frac{1}{r_1} + \frac{1}{r_2} \right) \tag{2.61}$$

Where the principal radii of curvature are given by r. Additionally, this surface bending leads to an increased vapor pressure (hence molecules can evaporate easier in a drop than in a film) characterized by the Kelvin equation:

$$RT \ln \left(\frac{p_0^k}{p_0} \right) = V_m \sigma \left(\frac{1}{r_1} + \frac{1}{r_2} \right) \tag{2.62}$$

Where R refers to the gas constant and V_m is the molar volume of the liquid. p_0^k and p_0 give the vapor pressure of the curved and flat surface in thermodynamic equilibrium, respectively. Finally, the wetting phenomenon has to be considered using the Young relation which gives the contact angle Θ in dependency of the interfacial tensions γ at the liquid-vapor (L), solid-vapor (S) and solid-liquid (SL) interface (figure 2.14a):

$$\gamma_L \cos \Theta = \gamma_S - \gamma_{SL} \tag{2.63}$$

Using equations 2.61, 2.62 and 2.63 the total capillary force between two spheres or a sphere and a plane can be expressed:

$$F = 2\pi l \gamma_L - \pi l^2 \Delta p \tag{2.64}$$

Where l gives the azimuthal radius as shown in figure 2.14b [72–74].

2.3.5 Attractive Depletion Force

Another example for entropy driven self-assembly can be found in dispersions containing nanoparticles with two different diameters, both with small size distribution. If the large particles approach each other, the smaller ones no longer fit in between and this space becomes accessible for the solvent molecules only (figure 2.15). This uncompensated osmotic pressure P causes an attractive force F between the large particles that can be utilized to calculate the depletion interaction potential:

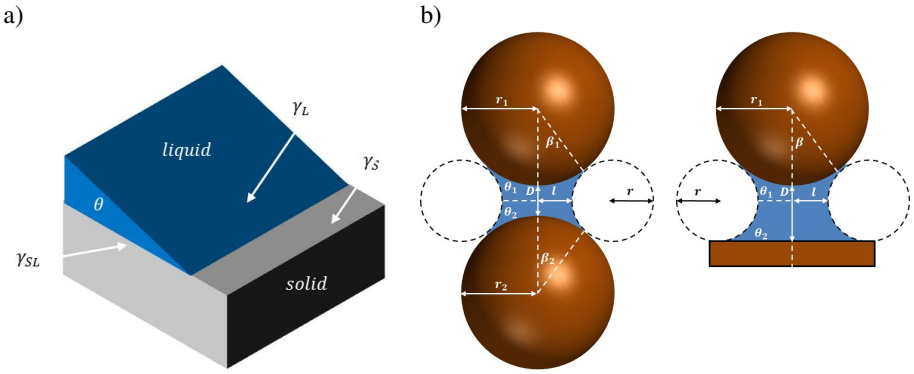


Figure 2.14: a) Illustration of the contact line for a liquid drop (blue) on a solid surface (gray) surrounded by gas. b) Meniscus formation between two bodies.

$$U_{dep} = \int_{r}^{2R_d} F(r)dr = n_B k_B T V_{ov}(r) \tag{2.65}$$

$$R_d = R + \frac{\sigma}{2} \tag{2.66}$$

$$V_{ov}(r) = \frac{4}{3}\pi R_d^3 \left[1 - \frac{3r}{4R_d} - \frac{1}{16}\left(\frac{r}{R_d}^3\right)\right] \tag{2.67}$$

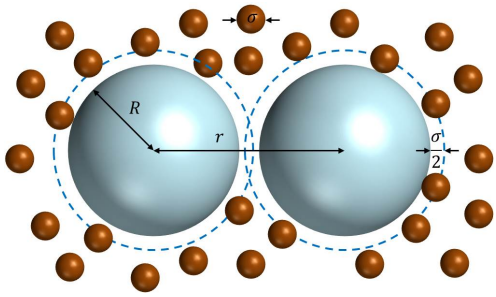


Figure 2.15: Two large spheres approaching each other and thus hindering the small ones to use the space in between. The resulting uncompensated osmotic pressure causes an attractive depletion force.

r gives the center to center distance between two large particles. The radii are given by R and $\frac{\sigma}{2}$, respectively. n_B is the total number of solutes and V_{ov} describes the overlap volume. Of course, equation 2.65 is valid only for $2R < r < 2R_d$ [75].

2.3.6 Entropy

For an entirely 'free' system without boundary conditions, entropy has to be maximized. Hence, particles in a solution usually perform random motions. Nevertheless, entropy can also cause

crystallization if the particle concentration is high enough, because an ordered phase then exhibits a lower free energy thus higher entropy. Figure 2.16 shows phase diagrams calculated for different interaction strengths: for non-interacting particles only the fluid (F) and crystal (C) state can be found with a metastable phase inbetween, where both coexist. In systems that exhibit long range order, a liquid (L) or gaseous (G) phase is also possible. For systems with rather short ranged interaction the fluid state is not possible [47].

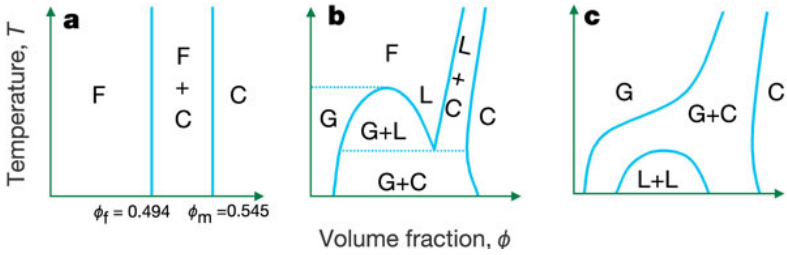


Figure 2.16: Phase diagrams for entropy driven crystallization a) without b) with long range and c) with short range interaction. The volume fraction is calculated by dividing the volume occupied by all the particles by the total volume, reprinted with permission from [76].

2.3.7 Other Forces

Aside from the phenomena described so far, several other short and long ranged forces can affect the self-assembly process. However, most of them have a rather small influence on the systems presented in this thesis. Hence, they will only be introduced briefly:

Hydrogen bonding, covalent bonds or donor-acceptor interactions are examples for so-called molecular surface forces. These attractive phenomena of short ranged nature are often used for stabilization or surface functionalization purposes [77].

Electrostatic interaction is a directional force that can either be attractive or repulsive. It is also used for nanoparticle stabilization by charging the surface using solvents with a specific pH value or charged ligand shells. While the surface charge distribution is defined by the geometry of the particle, the interaction strength depends on the dielectric constant of the solvent and the number of ions surrounding the particle [47].

Further effects like convection and friction can also affect the self-assembly process, but due to their minor influence on the systems under study they will not be discussed here.

2.4 Scattering

2.4.1 Reciprocal Space

The structure of a crystal and its symmetry plays a major role in the determination of numerous physical properties (e.g. electronic band structure or optical transparency). In real space, the arrangement of atoms is described by unit cells, which contain the smallest group of particles

that can constitute the repeating pattern of a crystal. But sometimes the concept of reciprocal space is advantageous, because it facilitates e.g. diffraction data interpretation to a large extent. For this, symmetry is described using planes of atoms. They are defined by a vector normal to the plane using the vector cross-product of two independent lattice vectors $\vec{t_1}$, $\vec{t_2}$ within the plane:

$$\vec{t_1} = U_1\vec{a} + V_1\vec{b} + W_1\vec{c} \tag{2.68}$$

$$\vec{t_2} = U_2\vec{a} + V_2\vec{b} + W_2\vec{c} \tag{2.69}$$

$$\vec{t_1} \times \vec{t_2} = (U_1V_2 - U_2V_1)\vec{a} \times \vec{b} + (V_1W_2 - V_2W_1)\vec{b} \times \vec{c} + (W_1U_2 - W_2U_1)\vec{c} \times \vec{a} \tag{2.70}$$

Where $\vec{a},\ \vec{b},\ \vec{c}$ represent basis vectors while U_1, V_1, W_1 and $U_2,\ V_2,\ W_2$ are sets of integers. For convenience, the prefactors in equation 2.70 can be replaced by the labels $h,\ k,\ l$, which are the smallest integer number triple describing the corresponding lattice plane:

$$h = (U_1V_2 - U_2V_1) \tag{2.71}$$

$$k = (V_1W_2 - V_2W_1) \tag{2.72}$$

$$l = (W_1U_2 - W_2U_1) \tag{2.73}$$

Since the cross products in equation 2.70 are useful for a general description of such a plane, they are employed as new basis vectors $\vec{a}^{\,*},\ \vec{b}^{\,*},\ \vec{c}^{\,*}$ and together with the Miller indices, they define the reciprocal lattice vector $\vec{G}$ (after normalization):

$$V = a \cdot b \times c \tag{2.74}$$

$$\vec{a}^{\,*} = \frac{2\pi}{V}\,\vec{b} \times \vec{c} \tag{2.75}$$

$$\vec{b}^{\,*} = \frac{2\pi}{V}\,\vec{c} \times \vec{a} \tag{2.76}$$

$$\vec{c}^{\,*} = \frac{2\pi}{V}\,\vec{a} \times \vec{b} \tag{2.77}$$

$$\vec{t_1} \times \vec{t_2} = h\vec{a}^{\,*} + k\vec{b}^{\,*} + l\vec{c}^{\,*} = \vec{G} \tag{2.78}$$

2.4.2 Diffraction

In general, diffraction refers to a scattering process that is assumed to be coherent (fixed phase relationship between waves of identical frequency) and elastic (wavelengths of incoming and scattered beams are identical). The requirements for suitable probes comprise a wavelength comparable to the size of the feature under study (usually interatomic distances), small absorption and minimal sample damage. Hence, the probes of choice are electrons, neutrons and X-rays.

In a typical experiment, the incoming waves are reflected from planes of atoms that are separated by a distance d as shown in figure 2.17. Constructive interference is possible only, if the

difference in path lengths of waves reflected from neighboring planes equals an integer multiple of the wavelength, what is known as Bragg's law [78]:

$$n\lambda = 2d\sin\theta \tag{2.79}$$

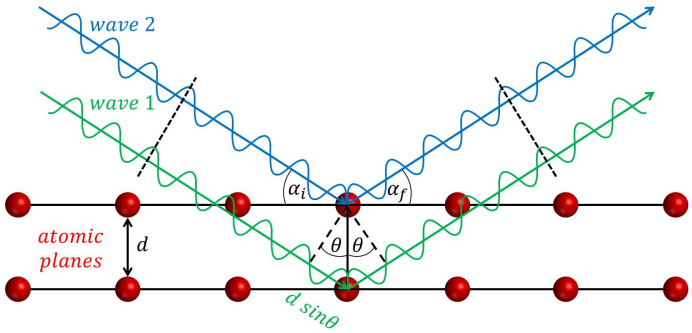


Figure 2.17: Schematic representation of Bragg's law.

But this equation contains no information about directions, which are necessary for in-depth analysis. Hence, the so-called wave vector $\vec{k}$ is introduced, to describe the incident $\vec{k_i}$ and diffracted beam $\vec{k_s}$ [79]:

$$k = |\vec{k}| = \frac{2\pi}{\lambda} \tag{2.80}$$

Using this term, it can be demonstrated that Bragg's law is equivalent to the following relation which is referred to as Laue condition:

$$\vec{k_i} - \vec{k_s} = \vec{Q} = \vec{G} \tag{2.81}$$

It shows that constructive interference is possible only, if the wave vector change caused by the scattering event (described by the scattering vector $\vec{Q}$) equals the distance between two lattice points in reciprocal space (given by the reciprocal lattice vector $\vec{G}$). For the reason that the interaction is assumed to be elastic (i.e. $|\vec{k_i}| = |\vec{k_s}|$), all reciprocal lattice points fulfilling the Laue equation are located on a sphere (so-called Ewald sphere) of radius $\frac{2\pi}{\lambda}$ around the starting point of $\vec{k_i}$ [78].

It should also be kept in mind, that powder samples correspond to a set of spherical shells in reciprocal space, hence delivering all reflections at once while for single crystals the sample has to be rotated to identify one reflection after another (c.f. figure 2.18) [80].

This demonstrates that diffraction of electromagnetic radiation or particle beams is a powerful tool for the analysis of long-range order at atomic scales. For a more rigorous description of the scattering formalism, one has to calculate the case, where the Bragg equation is not fulfilled as well. This is possible by employing the stationary wave equation in its complex exponential form:

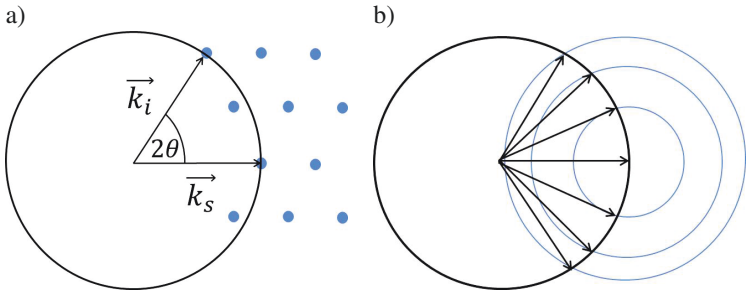


Figure 2.18: Intersection of the Ewald sphere with the reciprocal lattice for a) single crystals and b) polycrystalline powders.

$$\Psi = A \exp(i\vec{k} \cdot \vec{x}) \tag{2.82}$$

It completely characterizes a wave in space by giving its wavelength and direction (both included in the wave vector $\vec{k}$) as well as the amplitude A. A position in space is additionally given by $\vec{x}$.

Considering the generalized geometrical construction of two waves scattered at different particles shown in figure 2.19, the path length difference l can be calculated:

$$l = l_1 + l_2 = \frac{\lambda}{2\pi}\,\vec{k}_i \cdot \vec{r} - \frac{\lambda}{2\pi}\,\vec{k}_s \cdot \vec{r} = \frac{\lambda}{2\pi}\left(\vec{k}_i - \vec{k}_s\right) \cdot \vec{r} \tag{2.83}$$

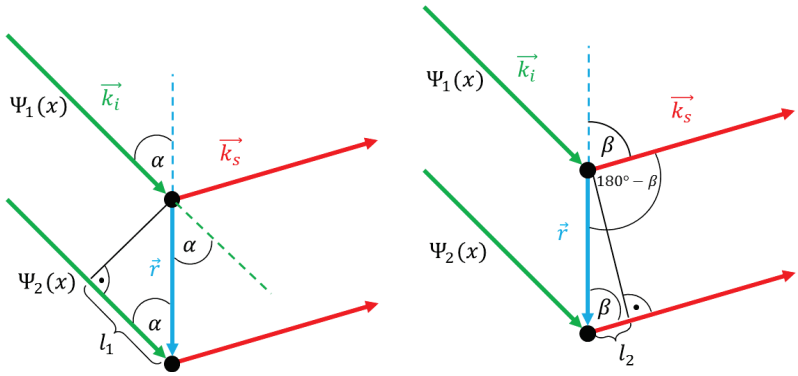


Figure 2.19: Geometrical construction for the calculation of the phase difference between two beams scattered at different particles separated by $\vec{r}$. The incoming and scattered waves are represented by the wave vectors $\vec{k}_i$ and $\vec{k}_s$, respectively.

The distance between the two particles is given by $\vec{r}$. This equation can be used to determine the total phase difference $\Delta\Phi$:

$$\Delta\Phi = \frac{2\pi}{\lambda}\, l = \left(\vec{k}_i - \vec{k}_s\right) \cdot \vec{r} = \vec{Q} \cdot \vec{r} \tag{2.84}$$

The total scattering is then given by

$$\Psi(x) = \Psi_1(x) + \Psi_2(x) = e^{i\vec{k_s}\cdot\vec{r}} + e^{i\vec{k_s}\cdot\vec{r}}e^{i\vec{Q}\cdot\vec{r}} = e^{i\vec{k_s}\cdot\vec{r}}\left(1 + e^{i\vec{Q}\cdot\vec{r}}\right) \tag{2.85}$$

The second term in the product is the so-called phase factor $F(\vec{Q})$ that gives the amplitude modification of the scattered beam:

$$F(\vec{Q}) = 1 + e^{i\vec{Q}\cdot\vec{r}} \tag{2.86}$$

It can be generalized to an ensemble of particles by simply adding up all the contributions:

$$F(\vec{Q}) = \sum_j e^{i\vec{Q}\cdot\vec{r_j}} \tag{2.87}$$

The particle positions are defined with respect to an origin $\vec{r_j}$. If different types of particles are involved, this can also be taken into account by weighting the components:

$$F(\vec{Q}) = \sum_j f_j e^{i\vec{Q}\cdot\vec{r_j}} \tag{2.88}$$

If neutrons are applied as probes, f_j is either referred to as form factor (for magnetic scattering) or scattering length (for nuclear scattering), whereas in X-ray studies it is called X-ray atomic form factor. However, in an experiment the detector can only measure the intensity I which is given by

$$I = |F(\vec{Q})|^2 = \left|\sum_j e^{i\vec{Q}\cdot\vec{r_j}}\right|^2 = \sum_{i,j} e^{i\vec{Q}\cdot(\vec{r_i}-\vec{r_j})} \tag{2.89}$$

Even though $I(\vec{Q})$ contains information about the distance between all pairs of particles $(\vec{r_i}-\vec{r_j})$, this data cannot be extracted directly, because all the information about the phase of the complex quantity $F(\vec{Q})$ is lost since I is a real positive value. This is the so-called phase problem [78].

However, these considerations neglect several aspects of the scattering process such as multiple scattering events, beam refraction when it enters and leaves the sample and primary beam extinction caused by scattering within the sample[5]. For a more general description of the scattering process, the so-called scattering cross section σ, which is proportional to the scattered intensity[6] I can be employed to calculate the double differential cross section:

$$\frac{d^2\sigma}{d\Omega dE} = \frac{n}{j d\Omega dE} \tag{2.90}$$

The number of particles per second, which are scattered under the scattering angle 2θ into the solid angle $d\Omega$ within the energy range (E...E+dE) is given by n. j is the incident beam flux

[5]This specific combination of assumptions is referred to as Born / kinematic scattering approximation.
[6]Proportionality factors depend on the detailed experiment geometry.

(particles per area and time). If the energy change is not considered, the angular dependence can be described by the differential cross section [81]:

$$\frac{d\sigma}{d\Omega} = \int_0^\infty \frac{d^2\sigma}{d\Omega dE} dE \tag{2.91}$$

2.4.3 X-ray and Synchrotron Radiation

The electromagnetic spectrum of X-rays covers energies in the range of $10^2 - 10^5$ eV and is therefore found between ultraviolet and gamma radiation. In laboratory sources, X-rays are generated by accelerating electrons towards a metallic target. Due to their rapid deceleration when they enter the material, a broad continuous spectrum of radiation called Bremsstrahlung is emitted (figure 2.20a). Its minimum wavelength corresponds to the incident electron energy. In addition, some electrons knock out core electrons. When these empty levels are subsequently filled by electrons dropping from outer shells, an X-ray photon of characteristic energy is emitted as shown in figure 2.20 b.

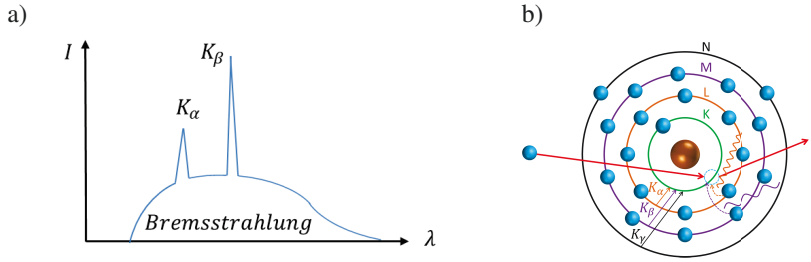


Figure 2.20: a) Schematic plot of a typical X-ray spectrum consisting of the continuous Bremsstrahlung and characteristic lines b) Illustration of electron transitions causing characteristic X-ray lines.

For diffraction experiments it is more practical to use monochromatic radiation at a fixed intensity and adjust the angle to fulfill equation 2.79 than vice versa. Hence, especially the Kα transition is relevant (electrons falling from the L to the K shell) because it can easily be used to produce monochromatic radiation by removing all the other wavelengths by absorbing filters.

In laboratory sources most of the incident energy is converted to heat which limits the maximum beam intensity to avoid target overheating. Additionally, only wavelengths corresponding to specific energy level transitions are possible. A way to overcome these problems is synchrotron radiation: when electrons are accelerated in a circular orbit, they always experience radial acceleration leading to continuous photon emission. By utilizing Bragg reflection in a monochromator crystal, any wavelength within the X-ray spectrum can be selected [78]. Even though this requires large scale facilities, such a radiation is a valuable tool for the analysis of matter due to its unique properties like polarization, high collimation and an intense continuous spectrum that enable fascinating measurement procedures like e.g. X-ray Magnetic Circular Dichroism (XMCD) or Grazing Incidence Small Angle X-ray Scattering (GISAXS) [82].

2.5 Electrical Transport

2.5.1 Models of Electrical Conduction

The Drude model of electrical conduction was the first attempt to explain the transport properties of electrons in a metallic solid. It is an application of the kinetic gas theory and assumes that the atomic cores are small and have a fixed position. The outermost electrons of every atom can, on the other hand, move independently and freely being influenced by external fields only. After a specific period of time, which solely depends on the temperature of the crystal, the electrons scatter on the atomic cores. This event is assumed to be fast and that the velocity of the electrons after the scattering process is independent of their velocity before. This model predicts the order of magnitude of the resistance of a metal well, but it fails in explaining several observations like e.g. superconductivity, the temperature dependency of thermal and electrical conductance or the dependency of the mean free path on the crystal quality [83].

These and other deficiencies of classical physics led to a revolution, namely the development of quantum mechanics. It turned out, that the Drude model violates the Pauli exclusion principle and a new model based on the Fermi-Dirac statistics was developed by Arnold Sommerfeld. It explains e.g. the temperature dependency of the thermal energy of the electron gas. In the classical (Drude) model it is assumed that a temperature increase by ΔT increases the energy of all electrons by $k_B \Delta T$ leading to values much higher than those experimentally found. However, using the Fermi-Dirac statistics, only electrons within a region of $k_B T$ around the Fermi level are affected thus predicting correct values [83].

2.5.2 Thin Film Conductivity

Conventional models for electrical transport, like those introduced in the previous section, were developed under the assumption of materials with macroscopic extension. Hence, they have to be adjusted for the investigation of samples that are confined in one (or more) dimensions. In thin film systems e.g. the electron movement is highly restricted in one direction leading to electron transport only in parallel to the plane of the layer. This leads to increased conductivity values with decreasing layer thickness. In literature, this is referred to as sheet resistance:

$$R_s = \frac{\rho}{t} \tag{2.92}$$

Where ρ is the bulk resistivity and t is the layer thickness [84]. However, real samples are rarely perfectly homogeneous with a flat surface as it is assumed by the models presented so far. Impurities, lattice defects and the structure of the material disturb the conductivity. Hence, the description by granular, electrical networks is rather appropriate. In this model, the current is assumed to either flow through contact points of or tunnels through small gaps between the grains. This leads to decreasing resistance with increasing temperature which is the opposite behavior observed for homogeneous layers, where the resistance increases with rising temperatures [85].

2.5.3 Magnetoresistance

If the resistivity of a material changes with the application of a magnetic field, this is referred to as magnetoresistance and occurs in all metals. There is a huge variety of such effects, all caused by distinctly different mechanisms. Four of them, namely Lorentz, anisotropic, spin disorder and giant magnetoresistance are relevant for the samples studied in this thesis. A schematic overview is provided in figure 2.21.

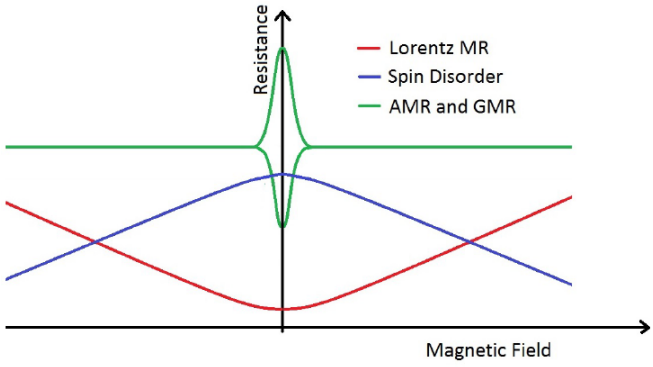


Figure 2.21: Schematic overview on the field dependency of four magnetoresistance effects that are relevant for samples studied in this thesis, taken from [86].

Relevant Magnetoresistance Effects

Lorentz Magnetoresistance and Hall Effect Magnetic fields generally exert a Lorentz force on conduction electrons leading to a curving of their trajectories. Consequently, the resistivity raises with increasing fields. Furthermore, an additional effect can be observed in narrow conductor geometries. If the conductor width is smaller than the diameter of the electron orbits, they accumulate at one side of the sample causing the so-called Hall resistance [87, 88].

Anisotropic Magnetoresistance If the resistivity change $\Delta\rho$ is positive for $I||H$ and negative for $I \perp H$, this is referred to as anisotropic magnetoresistance. It is caused by spin orbit coupling. By rotating the magnetization direction, the electron cloud about each nucleus is slightly deformed. For a transversal alignment of the current towards the field and magnetization direction, the electronic orbits are in the plane of the current leading to a small scattering cross-section. When conduction electrons travel through the lattice, they are thus less often scattered leading to decreasing resistivity values. If the current is, on the other hand, oriented parallel to the field, the electronic orbits are perpendicular to the current causing an increased scattering cross section that leads to higher resistivity values [89].

Spin Disorder Magnetoresistance In transition metals it is assumed that 3d electrons are localized at atomic sites while 4s electrons are mobile and form an itinerant band. Hereby, s and d electrons are coupled by exchange interaction. At finite temperatures, the spins of the latter perform fluctuations causing an inhomogeneous exchange potential from which the conducting s electrons are scattered. To reduce this effect, and thus the resistivity, a large magnetic field can be applied to align the d electron spins [90].

Giant Magnetoresistance The giant magnetoresistance effect is e.g. found in alternating layers of magnetic and non-magnetic metals. The film thickness hereby has to be smaller than the mean free path of the conduction electrons. If adjacent magnetic layers are coupled antiferromagnetically, a significantly higher resistance than for parallel alignment can be observed. This is caused by spin dependent scattering. The spin of the conduction electrons can either be oriented parallel or antiparallel to the magnetization direction. For the former, the scattering process is less efficient leading to a lower resistivity than for the latter. Hence, for magnetic layers with antiparallel magnetization directions, one spin orientation is massively scattered in the first layer and the other in the second layer leading to high resistance. For parallel alignment, one spin direction can easily pass through the whole system resulting in a low resistance state [89].

Kondo Effect

Decreasing temperatures generally lead to a reduction of phonons. Hence, conduction electrons in a metal are less scattered and the resistance is reduced. If the material contains impurities, this leads to additional scattering that causes a temperature independent residual resistance even at 0 K. However, for magnetic impurities the resistivity decreases with decreasing temperature only until the so-called Kondo temperature. Upon further cooling, the resistivity increases again

which is explained by spin-flip scattering. If the conduction electrons of the metal are scattered from the localized d electrons of the magnetic impurities, this can lead to spin exchange. But this is possible only for antiparallel spin orientation. Hence, conduction electrons accumulate around localized electrons that exhibit the opposite spin direction forming a polarization cloud. At low temperatures, there are less thermal fluctuations and the diameter of the polarization cloud increases. If a voltage is applied, the conduction electrons are scattered from the polarization clouds whereas a larger diameter results in a larger scattering cross section and thus an increased resistivity with decreasing temperature [91].

Further Magnetoresistance Effects

Ordinary Magnetoresistance This effect found in non-magnetic metals is very small at low fields but can become huge at high magnetic field strengths. In general, the resistivity change $\Delta\rho$ is larger for $I||H$ than for $I \perp H$ but always positive. Depending on the electron orbital structure at the Fermi surface, three cases can be distinguished [89]:

- Closed Fermi surfaces: Magnetic fields increase the cyclotron frequency of the electrons, which are confined to their orbit. At very high magnetic fields this effect saturates.
- Equal numbers of electrons and holes: Independent of the crystallographic orientation, the magnetoresistance increases with increasing magnetic fields.
- Fermi surfaces with open orbits in some crystallographic directions: The magnetoresistance saturates in the direction of closed orbits and becomes large in the direction of open orbits.

Tunnel Magnetoresistance If two ferromagnetic layers are separated by a thin, insulating barrier, conduction electrons can tunnel though the insulator thus enabling transport. Hereby, the tunneling efficiency is strongly spin dependent due to the difference in the DOS for different spin polarities between the electrodes. Hence, parallel alignment results in a high tunneling probability whereas antiferromagnetic alignment significantly reduces it [92].

Colossal Magnetoresistance Colossal magnetoresistance is a phenomenon found e.g. in mixed valence manganese oxides. These materials exhibit a perovskite structure and undergo a low temperature transition from insulating to metallic behavior, whereas the effect is observed in the metallic regime. While t_{2g} electrons of the Mn^{3+} are bound to the ion, the double exchange interaction allows e_g electrons to perform a hopping process between Mn sites of different valence states. However, this is possible only, if the two Mn core spins are parallel to each other. Hence, the resistance decreases, if they are aligned by a magnetic field [63].

Extraordinary Magnetoresistance In conductor-semiconductor hybrid systems an additional magnetoresistance effect can be observed. If a magnetic field is applied, the Hall angles converges at large field strengths towards $\pi/2$. This changes the electron trajectories in the metal thus causing a resistivity increase [93].

3 Experimental Methods and Instruments

3.1 Magnetometry

For the direct measurement of magnetic moments in a sample, either the change in force experienced or the change in magnetic flux produced can be applied. For the latter, the sample is usually moved relative to pick-up coils which are wound in gradiometer configuration to minimize the background magnetic field and cancel out any influence of static or dynamic homogeneous fields. Thereby, the magnetic flux Φ temporally changes and a voltage V is induced:

$$V = -N\left(\frac{d\Phi}{dt}\right) \tag{3.1}$$

$$\Phi = A|\vec{B}| \tag{3.2}$$

Where N is the number of turns in the pickup coil and $\vec{B}$ describes the magnetic induction. The effective area of the coil normal to $\vec{B}$ is given by A.

In order to maximize the coupling to the impedance transducer[1] and reduce inductance, magnetometers using a Superconducting QUantum Interference Device (SQUID) have coils with very few turns only. But if the setup utilizes a vibrating sample or extraction magnetometer (with the latter not being considered here), multiturn coils are used to maximize the voltage induced [94].

3.1.1 Vibrating Sample Magnetometer

For the Vibrating Sample Magnetometer (VSM) shown in figure 3.1, as it is installed in the Quantum Design Physical Property Measurement System (PPMS) used for this thesis, the sinusoidal signal of an oscillator is translated into vertical vibration with a frequency of approximately 40 Hz and 1-3 mm amplitude using a transducer assembly. The sample is centered at

[1] Analog device that couples flux change to an electronic circuit for signal processing and readout

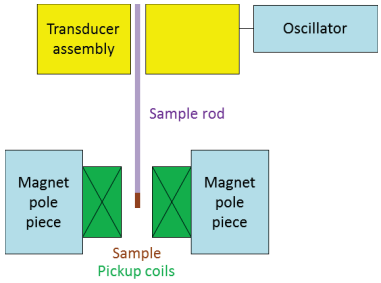


Figure 3.1: Schematic illustration of the vibrating sample magnetometer setup.

a point midway between the pickup coils to provide signal independency of position to first order. Additionally, a superconducting coil capable of generating extremely homogeneous fields is utilized for sample magnetization.

As the sample moves, the AC component of the field produced is detected by the pickup coils. They give an AC output that is measured by a lock-in amplified phase-sensitive detector, leading to a DC output proportional to the temporal flux change given by

$$V = G\sigma\omega A\cos(\omega t) \tag{3.3}$$

Where the geometric factor for the coils is described by G and the sample moment is σ. The amplitude and angular frequency of sample motion are given by A and ω, respectively [94–96].

3.1.2 Superconducting Quantum Interference Device

The SQUID technology allows for high-precision measurements of magnetic moments by combining two effects found in superconductors:

1. Flux quantization: Below the critical temperature T_c the electrons in a superconducting loop are grouped in so-called Cooper pairs [97]. Their motions are phase coherent and can therefore be described by a single wavefunction [98, 99]. If a magnetic field is applied, it changes the phase of the wavefunction. But in order to persist, the phase at an arbitrary starting point must be identical to the phase obtained when getting back to that point after traveling once around the whole loop. So a current starts to flow that creates an opposing field and changes the flux to allow the wavefunction to rejoin its own end. Thus, only discrete flux values ($n\Phi_0 = n \cdot 2.07 \cdot 10^{-15}\ Wb$ [100]) are permitted [101].

2. Josephson tunneling: If two superconductors are separated by a thin, insulating barrier ("weak link" or Josephson junction), they can couple by Cooper pair tunneling. This leads to a direct current through the barrier without any voltage drop[2]. By applying an external field, an AC voltage is induced that causes a temporal alteration of the phase difference between the superconductors. This causes an alternating current which superimposes the direct current [102].

[2] As long as the critical current is not exceeded.

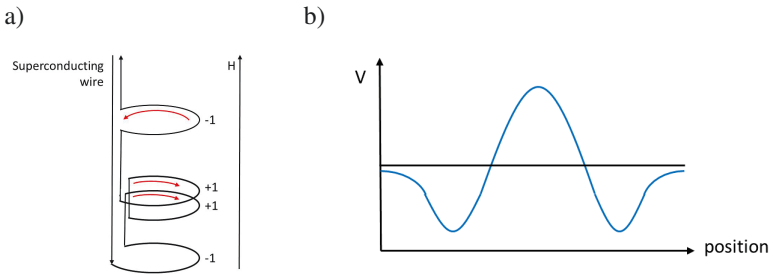


Figure 3.2: a) Pickup coil for Quantum Design MPMS systems. b) Example response curve.

A distinction is made between superconducting loops interrupted once (rf-SQUID) or twice (dc-SQUID) by a Josephson junction. In the commercially available Quantum Design Magnetic Property Measurement System (MPMS) used in this thesis, the former is installed and inductively coupled to a resonant circuit. In order to measure the magnetic moment of a sample, it is moved through a pickup coil that is designed as second-order gradiometer (figure 3.2a) to cancel out all homogeneous fields. The current is then transfered to the SQUID via superconducting wires where it induces a magnetic field that changes the flux [102]. This influences the phase, which leads to an altered impedance in the ring that changes the AC voltage in the inductively coupled circuit. This voltage change is proportional to the total applied flux and constitutes the output signal, which is plotted against position as shown in figure 3.2b (so-called response curve).The signal is then fitted on the theoretical curve of a single dipole, using the magnetic moment m(T,H) as fit-parameter [103].

3.1.3 Measurement Procedures

ZFC-FC For magnetic nanoparticles, many properties (e.g. the blocking temperature T_B) can be defined using the Zero Field Cooled (ZFC) - Field Cooled (FC) measurement procedure (figure 3.3a,b). Beginning at room temperature, the sample is cooled down in zero field to the minimum temperature considered (here 5 K). Afterwards, a small field of e.g. $\mu_0 H = 0.005$ T is applied and the magnetic moment is recorded while heating up to the maximum temperature (here 350 K), providing the so called ZFC curve.

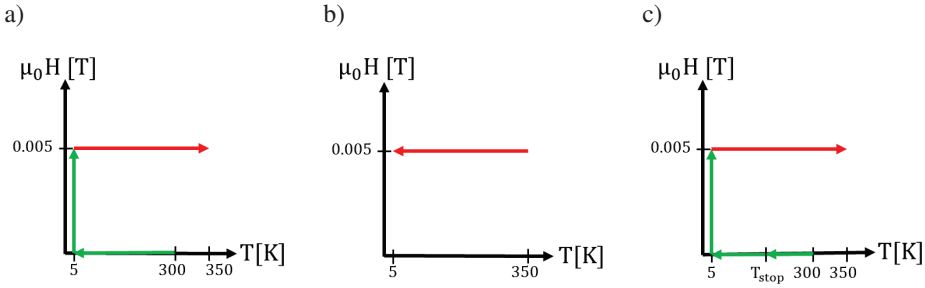


Figure 3.3: Measurement procedures for a) zero field cooling b) field cooling and c) memory effect, where red arrows mark the paths along which the magnetic moment is recorded.

Subsequently, the FC curve is obtained by cooling the sample from maximum to minimum temperature with a magnetic field applied (here $\mu_0 H = 0.005$ T) while simultaneously measuring the magnetic moment.

Memory Effect measurements are a well known technique to determine whether a sample displays superspin glass behavior. Therefore, the ZFC procedure is slightly modified by inserting an aging stop below the blocking temperature (figure 3.3c). Since the effect is found at the rising edge of the curve, it is convenient calculating the difference between this curve and a regular ZFC curve [16, 17].

Delta M In order to determine the nature of interaction between individual nanoparticles, the so-called delta-M curve can be calculated using DC Demagnetization remanence (DCD) and Isothermal Remanent Magnetization (IRM) curves. For the former, the sample is cooled down to 5 K in zero field and is then magnetized to full saturation with a large negative field (here $\mu_0 H = -1$ T). Subsequently, a small positive field (here $\mu_0 H = 0.01$ T) is applied. After 10 s delay, the remanent magnetization is measured and the procedure is repeated with a magnetic field increased by ΔH (here $\mu_0 \Delta H = 0.01$ T) until saturation is reached (figure 4.20). The IRM curve is obtained similarly, but the sample is demagnetized before starting the measurement [104, 105]. According to the Stoner-Wohlfarth theory, there is a simple relationship between the IRM and DCD curve if non-interacting particles are in a single domain state:

$$M_{DCD}(H) = M_s(H) - 2M_{IRM}(H) \tag{3.4}$$

Where M_s describes the saturation magnetization. However, in real systems a deviation from this behavior is often observed. According to Henkel, this additional term is caused by interactions between the particles [106]:

$$\Delta M(H) = 2\frac{M_{IRM}(H)}{M_s} + \frac{M_{DCD}(H)}{M_s} - 1 \tag{3.5}$$

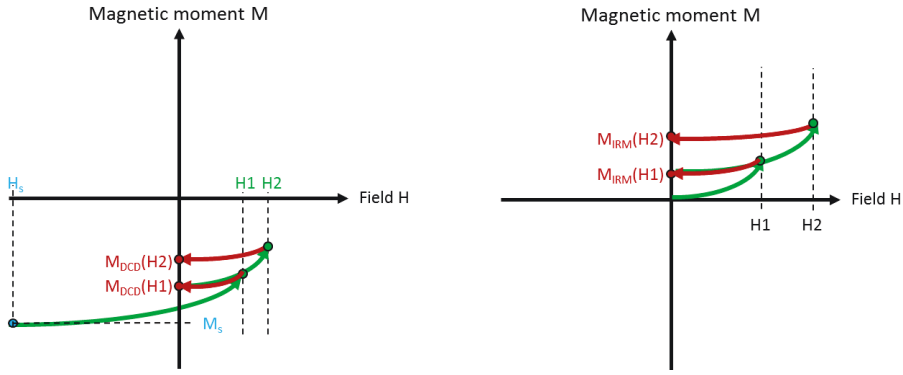


Figure 3.4: Illustration of measurement procedure for DCD (left) and IRM (right) curves.

3.2 Magneto Optical Kerr Effect

An alternative to the direct measurement of magnetic moments (c.f. section 3.1) is the Magneto-Optical Kerr Effect (MOKE) technique, which is based on magnetic circular dichrosim (cf. section 3.9) [107]. In this thesis it was performed in coorperation with the Max-Planck-Institute for Intelligent Systems, department Schütz to obtain first order reversal curves (c.f. section 3.3).

In general, laser light is first linearly polarized and then focused onto a magnetic sample. Due to exchange and spin-orbit coupling, the absorption spectra for left- and right-circularly polarized light are different. This causes a phase difference between the electric field components parallel and perpendicular to the plane of incidence (Kerr ellipticity ϵ_K) and a rotation of the polarization plane (Kerr rotation θ_K). This can be described by the complex Kerr angle Φ_K (figure 3.5) which is, in a first approximation, proportional to the magnetization of the sample:

$$\Phi_K = \theta_K + i\epsilon_K \tag{3.6}$$

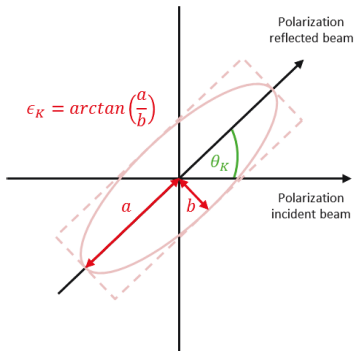


Figure 3.5: Schematic description of the Kerr rotation θ_K and ellipticity ϵ_K, which can be combined to the complex Kerr angle Φ_K.

It contains three components which are distinguished by the direction of the magnetization in relation to the plane of incidence: for the longitudinal and polar Kerr effect, the magnetization lies parallel to the plane of incidence and is either parallel or perpendicular to the sample surface, respectively. If the magnetization is neither parallel to the plane of incidence nor to the sample surface, it is referred to as transversal Kerr effect (figure 3.6) [108].

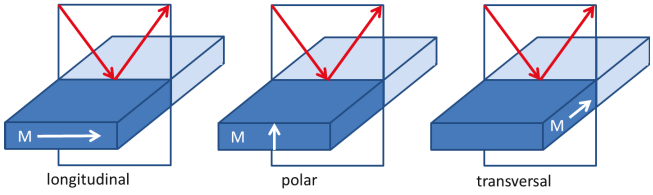


Figure 3.6: Illustration of geometric arrangement for the longitudinal, polar and transversal Kerr effect.

3.3 First Order Reversal Curves

Observing hysteresis loops is a standard technique for the characterization of magnetic samples. Figure 3.7 shows a typical major loop where two paths between saturation are possible. The state at zero field is referred to as remanence and the magnetic field required for zero magnetic moment is called coercivity H_c. The term susceptibility is defined as $\chi = \lim_{H \to 0} \frac{M(H)}{H}$ [109]. While such a measurement generally provides averaged properties only, the application of First-Order Reversal Curves (FORC) reveals insight into details of the reversal process and internal interactions [110].

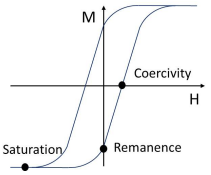


Figure 3.7: Characteristics of a typical major hysteresis loop.

3.3.1 The Preisach Model

Originally, the FORC method was based on a model developed by Preisach in 1935. He neglected contributions due to stress, temperature or frequency dependence and modeled the hysteresis loop as a set of elementary processes described by square loops, so-called hysterons (figure 3.8a). These are characterized by threshold reversal fields H_{up} and H_{down} at which the saturation magnetization switches between +1 and -1. The offset H_u from the origin is a measure for the interaction field due to surrounding neighbors acting on a specific particle. In general, this model is valid only if every minor loop starts and ends at the same point on the major hysteresis loop (wiping-out property, figure 3.8b) and if all minor loops with the same upper and lower field limits are geometrically congruent (congruency property, figure 3.8c) [111]. Since most physical systems do not fulfill these conditions, other approaches like e.g. the physical analysis model (which will be discussed below) have to be applied [109].

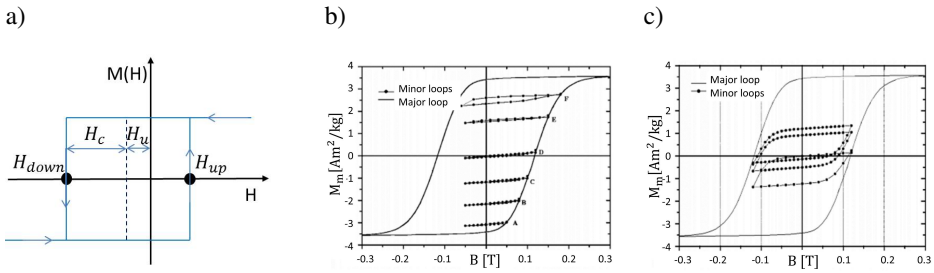


Figure 3.8: a) Graphical illustration of a hysteron displaying its threshold reversal fields H_{up}, H_{down} and offset H_u. b) Illustration of the wiping-out and c) congruency property, both reprinted with permission from [112].

3.3.2 Measurement procedure

In general, the FORC measurement aims at recording the H_u and H_c parameters for every mathematical hysteron of the system. Therefore, a family of e.g. 101 minor loops is recorded by first saturating the sample in positive direction to force all the hysterons into the "up" position. Then, a negative reversal field H_r is applied, which lies on the top branch of the major loop shortly before negative saturation. Here, some of the hysterons switch to the "down" position, depending on their H_u and H_c parameters. Finally, the magnetization is recorded while the field is increased back to positive saturation. Thereby, the magnetization difference between applied and reversal field is directly proportional to the amount of hysterons switching back to the "up" position. The procedure is then repeated with a slightly increased H_r until the interior of the major loop is completely mapped out as indicated in figure 3.9a [109]. By applying a second-order mixed derivative of the magnetization $\vec{M}$ on the set of FORCs beginning at different reversal fields, the so-called FORC distribution ρ_{FORC} can be obtained. This equation contains the information about all hysterons in the system and amplifies subtle changes in the magnetization [111]:

$$\rho_{FORC}(H, H_r) = -\frac{1}{2}\frac{\partial^2 M(H, H_r)}{\partial H \partial H_r} \tag{3.7}$$

a) b)

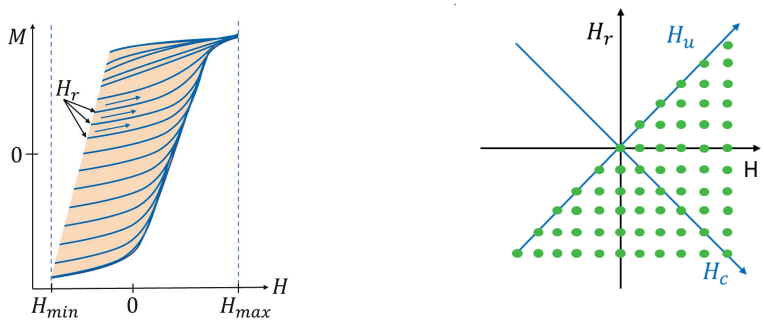


Figure 3.9: a) Example for a family of FORCs probing the interior of the corresponding major loop. b) Illustration of the relation between the $H_r(H)$ and $H_u(H_c)$ coordinate system. Green dots are representing single hysterons.

3.3.3 Data Evaluation

A direct indication for the statistical distribution of mathematical hysterons can be obtained by employing a contour plot of the FORC distribution. Hereby, the coordinates are transformed for convenience to directly read the coercivity and interaction field distributions H_c and H_u, respectively:

$$H_r = -H_c + H_u \tag{3.8}$$

$$H = H_c + H_u \tag{3.9}$$

$$H_c = \frac{H - H_r}{2} \qquad H_u = \frac{H + H_r}{2} \tag{3.10}$$

As shown in figure 3.9b, this leads to a 45°clockwise rotation of the distribution. At first glance, two quantitative parameters, namely the FORC coercivity H_c^{FORC}, which marks the H_c position of the FORC distribution maximum and the global interaction field ΔH_u that corresponds to the FORC density half-width along the H_u axis can directly be deduced. Further analysis is often quite complicated due to the fact, that the FORC distribution corresponds to the statistical distribution of mathematical hysterons, which do not necessarily have a physical meaning. Another problem is the deformation of the FORC distribution if a state-dependent interaction field (e.g. a mean interaction field) is present during the reversal process. Additionally, it is possible that FORC distributions look identical, even though they originate from different physical systems. These obstacles can mostly be overcome by applying the so-called physical analysis model which employs physically meaningful hysterons that represent the supposed magnetic behavior of the system entities. Additionally, the global behavior is simulated by an interaction term which is coupled to the hysterons. For spherical nanoparticles, e.g. the Stoner-Wohlfarth model as discussed in section 2.2.5 can be utilized for the description of the entities. Figure 3.10 exemplarily shows possible hysterons resulting from this assumption where all spins remain parallel to each other during magnetization reversal. If the field is applied along the easy axis, the spins abruptly turn by 180°when a specific threshold value is reached whereas a field applied along the hard axis leads to coherent rotation.

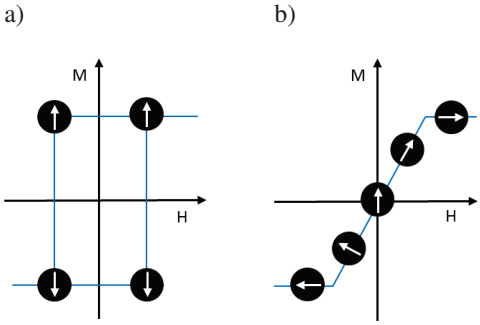


Figure 3.10: Hysterons for the theoretical behavior of an individual nanoparticle for a field applied along the a) easy or b) hard axis.

Depending on the type of hysterons that are utilized, different FORC distributions are obtained: For easy axis hysterons e.g. a normal coercivity distribution spreads ρ_{FORC} along the H_c axis. The effect of interaction fields strongly depends on its direction relative to the magnetization direction: For an antiparallel arrangement ρ_{FORC} is elongated along the H_u axis and parallel alignment translates H_c^{FORC} towards a higher H_c value (figure 3.11) [109].

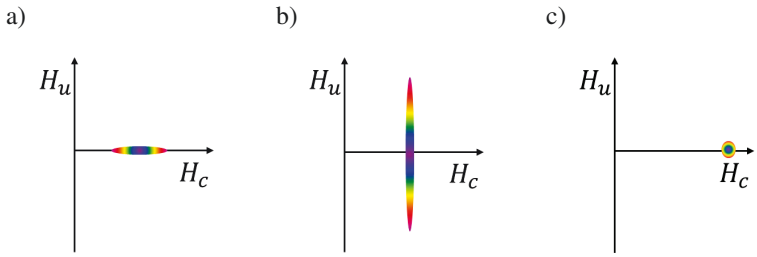


Figure 3.11: Theoretical FORC result obtained using easy axis hysterons for a) a normal coercivity distribution without interaction field and without coercivity distribution. b) Interaction field antiparallel to the magnetization direction c) Interaction field parallel to the magnetization direction.

3.4 Resistivity

For the investigation of the temperature and magnetic field dependency of electrical transport, resistivity measurements were performed. Figure 3.12a shows the schematic layout of the Quantum Design Physical Property Measurement System (PPMS) that was employed for this purpose. The sample chamber is located in the center of a superconducting coil that can generate magnetic fields up to ±9 T. Using liquid helium, temperatures down to 1.9 K can be reached. To avoid ice crystal formation, the sample space is evacuated [113].

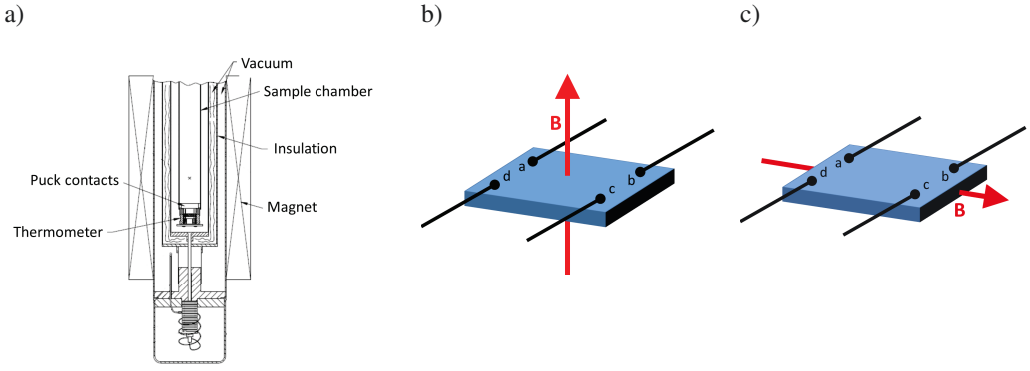


Figure 3.12: a) Schematical setup of the resistivity option of the Quantum Design PPMS system, taken from [113]. b) Sample geometry for resistivity measurements with a magnetic field applied out-of-plane or c) in-plane.

The resistivity measurements shown in this thesis were obtained by the so-called van der Pauw four-point method. Figures 3.12b,c show the corresponding sample geometries for a magnetic field applied either out-of-plane or in-plane. The current hereby either flows between contacts a and b (channel I) or b and c (channel II) whereas the voltage is applied between contacts c and d (channel I) or a and d (channel II), c.f. table 3.1 [114]. The resulting resistance is:

$$R_{ab,cd} = \frac{U_{cd}}{I_{ab}} \qquad R_{bc,da} = \frac{U_{da}}{I_{bc}} \tag{3.11}$$

The corresponding resistivity is then calculated using the layer thickness d and the geometry factor is f_g [86]:

$$\rho = \frac{\pi d f_g (R_{ab,cd} + R_{bc,da})}{2\ln(2)} \tag{3.12}$$

Sample contact	Channel I contact	Channel II contact
a	I+	V+
b	I-	I+
c	V-	I-
d	V+	V-

Table 3.1: Assignment of the sample contacts used.

3.5 X-Ray Powder Diffraction

After its first demonstration by Debye and Scherrer in 1915 X-Ray Powder Diffraction (XRPD) has evolved into a routine technique for the characterization of crystalline samples based on Bragg's law (equation 2.79). A typical diffraction pattern consists of specific reflections and a background. While the former contain information about the lattice parameters (position), crystal structure (intensity) and real structure (shape), the latter is caused by diffuse or Compton scattering from the sample or scattering from air, the sample holder etc. Since every material provides a specific pattern, it can be used as fingerprint for the identification of unknown samples by comparing them to databases like the Inorganic Crystal Structure Database (ICSD) [115].

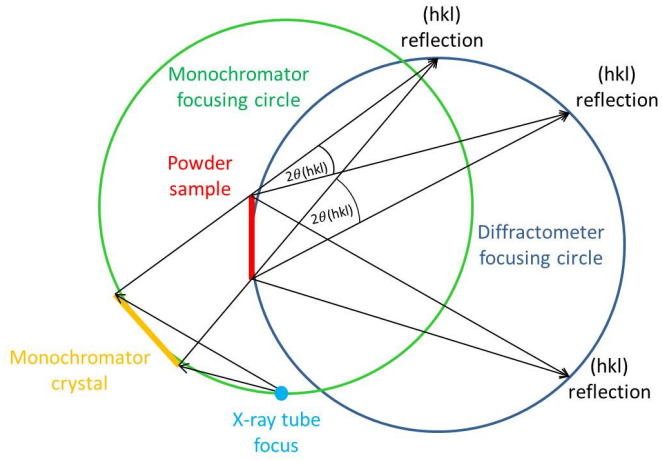


Figure 3.13: Geometrical principle of X-ray powder diffraction using the Guinier method in transmission geometry, according to [116].

For this thesis, powder diffraction was performed in transmission geometry using a copper X-ray source and a curved germanium (111) monochromator crystal combined with a Huber X-ray camera Guinier G670 that utilizes image plate detection.

The arrangement is shown in figure 3.13: first, the incident beam is reflected from the curved monochromator crystal to form a convergent beam. Afterwards it is focused on the inner surface of the cylindrical camera chamber. At the entrance window, the sample is fixed on an X-ray transparent substrate. All beams that are diffracted at Bragg angles $2\theta(hkl)$ here are then focused onto the same surface due to the geometrical fact that from any chord in a circle, the opposing angles on the circumference are equal [116].

3.6 Small Angle X-Ray Scattering

The Small Angle X-ray Scattering (SAXS) technique is widely used in various branches of technology and science to study the structure of matter. It is based on wave diffraction phenomena and thus allows for the determination of the spatial structure of matter averaged over large areas. Using wavelengths in the order of several Ångstrøms (which corresponds to the magnitude of interatomic distances) the diffraction pattern in the small-angle region provides information about the superatomic structure [117].

The basic setup is shown in figure 3.14: After its generation in a synchrotron or laboratory source, the X-ray beam passes through a monochromator and collimation system, to provide a wavelength band with low divergence. It is then scattered by the sample and the corresponding pattern is recorded in a 2D detection system. To avoid that the intense direct beam overshadows the comparably small signal from the sample, it is blocked by a beam stop [118].

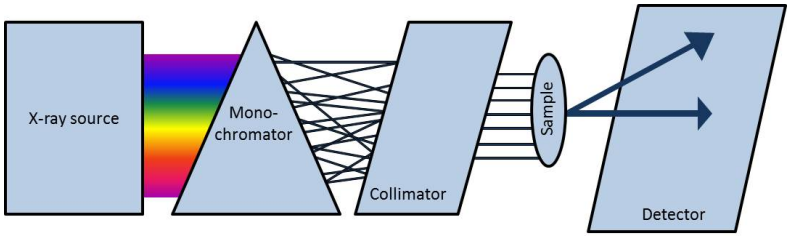


Figure 3.14: Schematic overview on the general measurement setup for (GI)SAXS experiments.

The results shown in this thesis were obtained using the Gallium Anode Low-Angle X-ray Instrument (GALAXI) at the Jülich Center for Neutron Science (JCNS), Research Center Jülich. Its Bruker AXS liquid MetalJet X-ray lab source generates beams that have sufficient brilliance and spot stability to allow for in-house (GI)SAXS measurements without the necessity of employing synchrotron radiation. For X-ray detection a Dectris Pilatus 1M instrument is installed [119].

If a sample is irradiated with X-rays, this can lead to Thomson scattering, where (in a classical picture) strongly bound electrons begin to oscillate at the same frequency as the incident beam. This leads to the emission of radiation at the same frequency and since the motion of neighboring atoms is strictly synchronous, these waves are coherent and can therefore interfere. The

resulting pattern observed at the detector is thus characteristic to distances and orientations of atoms relative to each other. However, all this information is obtained relative to the wavelength λ of the incident radiation. To become independent of λ, it is therefore convenient presenting the results in terms of the absolute value of the scattering vector Q:

$$Q = \frac{4\pi}{\lambda} \cdot \sin(\theta) \tag{3.13}$$

Since its dimension is one over length (e.g. $[1/\mathring{A}]$) SAXS patterns are usually referred to as structure in reciprocal space.

To understand the pattern of particle assemblies, it is helpful starting with a single nanoparticle which consists of a certain amount of atoms. The corresponding interference pattern thus originates from all the waves scattered from every single atom inside the particle. The oscillations observed in such a pattern are characteristic for the particle shape and are therefore referred to as 'form factor' $F(Q)$ with minima strongly depending on the particle size (c.f. figure 3.15a).

If many particles are illuminated simultaneously, every single particle provides its own form factor. The resulting pattern thus corresponds to their incoherent sum, giving averaged information of the whole sample. Hence, for polydisperse samples, less pronounced minima are observed than in the monodisperse case (c.f. figure 3.15a). Additionally, it should be kept in mind that X-rays mainly interact with electrons. Hence, the scattered intensity strongly depends on the amount of electrons in a volume and large particles thus cause a more intense signal than the same number of small ones.

For the considerations presented so far, the particles were assumed to be dilute. But if they are densely packed with separations comparable to interatomic distances, this causes an additional wave originating from the interference of waves scattered from neighboring particles. It multiplies with the form factor and since it contains information about the nanoparticle order, it is referred to as 'structure / lattice factor' $S(Q)$. At small Q-values its intensity decreases (increases) for repulsive (attractive) interaction potentials. If the assembly is highly ordered, the structure factor develops into a pronounced peak at higher Q-values which is referred to as Bragg peak and provides the particle distance d_{Bragg} according to Bragg's law (equation 2.79):

$$d_{Bragg} = \frac{2\pi}{Q_{Bragg}} \tag{3.14}$$

The more pronounced this peak is, the better is the nanoparticle ordering and the overall arrangement can be deduced [118]. Additionally, these peaks can be indexed according to geometrical considerations. Hexagonal order e.g. satisfies the following relation [80]:

$$d(h,k) = \left(\sqrt{\frac{4}{3}\frac{h^2+k^2+hk}{a^2}}\right)^{-1/2} = \frac{2\pi}{Q_y} \tag{3.15}$$

The background that usually superimposes the characteristic pattern has several origins: it can e.g. be caused by Compton scattering or fluorescence due to absorption. Since both effects lead to wavelength changes without a specific phase relationship to the incident radiation, no

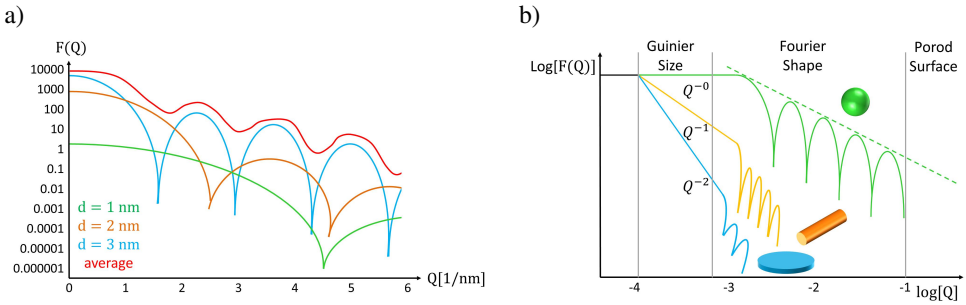


Figure 3.15: a) Form factors of three monodisperse samples (spherical nanoparticles with a diameter of 1 nm (green) / 2 nm (yellow) / 3 nm (blue)) and their sum (red) representing a polydisperse sample. b) Universal Guinier plot of the particle form factor for spherical (green), rod-like (orange) and lamellar shaped nanoparticles illustrating the domains of information, according to [118].

interference phenomena occur and therefore no structural information is carried. Nevertheless, it can provide e.g. information on the atomic composition or electron momentum distribution.

Furthermore, the nanoparticles are usually measured as dispersion. Hence, the empty solvent has to be analyzed as well to remove its signal. Hereby significant difference in electron density is indispensable to establish sufficient contrast. Of course, the dark count of the detector also has to be subtracted.

If absolute values of intensities need to be analyzed as well (for molecular weight determination), further reference measurements, namely on the empty sample holder and the sample holder filled with a reference material like water, have to be performed to subtract their contribution. However, the information contained in the form factor and structure factor is determined by their Q-dependence only. Hence, they can be analyzed using arbitrary units.

In general, the curves obtained can be divided into three regions as shown in figure 3.15b: for small angles, a so called Guinier plot can be utilized for particle size determination. In this region, the form factor $F(Q)$ can be approximated using a Gaussian curve:

$$F(Q) = a_0 e^{-\frac{R_G^2 Q^2}{3}} \tag{3.16}$$

Where the radius of gyration R_G can be used to quantify the particle dimensions. Since it contains no information about the internal structure or shape, these data have to be known to determine the relation to the size. Spherical particles with a homogeneous density for example lead to the following equation:

$$R = \sqrt{\frac{5}{3}} R_G \tag{3.17}$$

R is the average particle radius. The value of R_G can be deduced from the slope if the curve is plotted as follows:

$$\ln[\Delta I(Q)] = \ln[a_0] - \frac{R_G^2}{3} Q^2 s \tag{3.18}$$

Additionally, a rough shape classification is possible by analyzing the power law of the form factor in the mid-q-value (Fourier) region: initial slopes of 0 / -1 / -2 indicate globular, cylindrical or lamellar shapes, respectively. Steeper curves usually appear if the particles are too large to be resolved. For a more detailed analysis, the oscillatory part has to be investigated using Fourier methods to transform it into real space. Finally, the large angle region can be used for surface fraction analysis according to Porod (not discussed here) [118].

3.7 Grazing Incidence Small Angle X-ray Scattering

By combining the surface sensitivity of the grazing incidence geometry with the length scales accessible by small angle scattering, a powerful tool for the analysis of two dimensional nanoparticle arrangements called GISAXS is created. It is non destructive and provides a statistical average of the lateral electron density profile for large sample areas. So far, the use of synchrotron radiation was mandatory since the signal scales with the material quantity [120]. But a new technique for laboratory X-ray generation utilizing a liquid MetalJet provides beams that have sufficient brilliance for GISAXS experiments. This was first implemented at the GALAXI instrument of JCNS, Forschungszentrum Jülich where the results shown in this thesis were obtained.

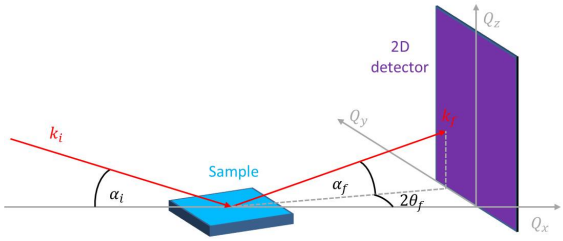


Figure 3.16: Schematical representation of the geometry required for GISAXS experiments, according to [120].

The basic geometry is shown in figure 3.16. By keeping the incident X-ray at a grazing angle (typically close to the angle of total reflection), the background scattering from the bulk is minimized and near-surface scattering is enhanced. Additionally, the fact that all angles are small keeps the wave vector transfer low resulting in large dimensions being probed in real space (i.e. length scale of nanostructures). For data evaluation, the scattering vector $\vec{Q}$ (cf. section 2.4.2) is usually decomposed into a part parallel (Q_y) and perpendicular (Q_z) to the sample surface:

$$Q_y = k_0 \left(\sin(2\theta_f)\cos(\alpha_f)\right) \tag{3.19}$$

$$Q_z = k_0 \left(\sin(\alpha_f) + \sin(\alpha_i)\right) \tag{3.20}$$

$$k_0 = |\vec{k_f}| = |\vec{k_i}| = \frac{2\pi}{\lambda} \tag{3.21}$$

$\vec{k_i}$ and $\vec{k_f}$ represent the wave vectors of incident and scattered beams with angles α_i and α_f, respectively. k_0 denotes the elastically conserved wave vector modulus. Since the curvature of the Ewald's sphere can be neglected for the angle range considered in GISAXS studies, the above equations can be simplified (so-called small angle approximation):

$$Q_y \approx k_0 \sin(2\theta_f) \approx k_0 2\theta_f \tag{3.22}$$

$$Q_z \approx k_0(\alpha_f + \alpha_i) \tag{3.23}$$

For nanoparticle assemblies on solid substrates the scattering pattern usually consists of Crystal Truncation Rods (CTR) caused by the semi-infinite crystal and wide Bragg reflections due to the particle arrangement. The latter can be found at different Q_y / Q_z positions if there is more than one value for the lattice vector parallel / perpendicular to the surface possible. This enables independent analysis of the in-plane and out-of-plane direction. Similar to SAXS studies, poly-supracrystals[3] show all Bragg peaks at once while for mono-supracrystals[4] the sample has to be rotated to identify one peak after another. The origin of the Q-axis is located exactly between the direct beam and the specular reflex (where the scattered angle equals angle of incidence), as shown in figure 3.17. If the surface / interface is rough, refraction and reflection effects can additionally cause off-specular diffuse scattering. Its maximum is found at the critical angle for total external reflection and is referred to as Yoneda peak.

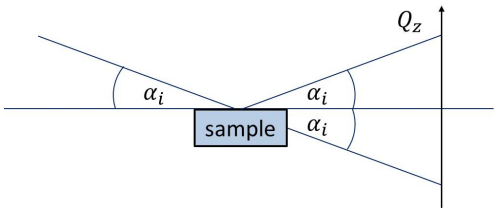


Figure 3.17: Determination of the origin of the Q_z axis using the incident beam and the specular reflection.

The entire pattern contains information about the average inter-nanostructure distance, the nanostructure shape, size and size distribution. Mainly, it originates from coherent scattering, which is the product of the interference function $S(\vec{Q_y})$ (Fourier Transform (FT) of the pair correlation function of nanostructure positions, also referred to as structure factor) and the square modulus of the mean nanostructure form factor $F(Q)$ (FT of the nanostructure shape). If the size distribution is not monodisperse, diffuse scattering is also present but difficult to evaluate. Hence, either the Local Monodisperse Approximation (LMA) is used by assuming that the nanostructure sizes are fully correlated at a scale corresponding to the X-ray beam coherence length, or no correlation at all is assumed in the Decoupling Approximation (DA) [120]. One approach to the quantum mechanical scattering theory is the Lippmann-Schwinger equation, which applies a Greens function method:

[3]Nanoparticle assembly in which the particles are ordered like atoms in a polycrystalline sample
[4]Nanoparticle assembly in which the particles are ordered like atoms in a mono-crystalline sample

$$|\Psi\rangle = |\Phi\rangle + \frac{1}{E - H_0 + i\epsilon} V |\Psi\rangle \tag{3.24}$$

The Hamiltonian H_0 describes the system without interaction with the eigenfunction $|\Phi\rangle$ and the eigenvalue energy E. The interaction on the other hand is given by the potential energy V. The term $i\epsilon$ is mathematically necessary but has not physical origin [121]. However, the usual solution by applying the Born approximation[5] is not valid since multiple scattering effects appear at the low angles required for GISAXS. But an adapted model called Distorted Wave Born Approximation (DWBA) is available which extends the single scattering formalism by incorporating the contribution of scattering processes due to perturbations of the incident, refracted and reflected wavefields by nanostructures on the refraction and reflection of waves at an interface. Hence, the form factor $F(Q)$ is replaced by the coherent sum $\wp(\vec{Q})$ that consists of four terms that represent different scattering events. Nevertheless, if the scattered intensity parallel to the surface is considered only, the Born Approximation (BA) is almost valid and can be applied for simplicity [120].

3.8 X-ray Absorption Spectroscopy

Due to its flexibility and universality X-ray Absorption Spectroscopy (XAS) is broadly used in material science and biochemistry for the investigation of electronic states and the local atomic structure [122]. As shown below, an intense and tunable X-ray source is indispensable. Hence, the experiments have to be performed using synchrotron radiation [123].

Core electrons absorb energy from ionizing radiation and can thus be ejected either into the Lowest Unoccupied Molecular Orbital (LUMO), higher excited ground states or to the continuum. Depending on the shell the electron originates from, particular energies are necessary for excitation leading to several absorption edges that are labeled according to the principal quantum number (figure 3.18a). With increasing atomic number the core-electron binding energy increases (e.g. 284 eV for the carbon K edge compared to 115 keV for the uranium K edge), making it an element specific technique. Since the electron levels within one shell are not degenerate, the edges are further split. In order of decreasing energy, the L edges are e.g. labeled L_1, L_2 and L_3, according to transitions from the 2s, $2p_{1/2}$ and $2p_{3/2}$ states (figure 3.18a, inset). The edge jump of L_3 is twice the height of L_1 and L_2 due to degeneracy [123, 124].

Additionally, closer inspection reveals significant structure at every absorption edge. Hereby, the immediate vicinity of the edge jump is referred to as X-ray Absorption Near Edge Structure (XANES) and the oscillations above the edge are called Extened X-ray Absorption Fine Structure (EXAFS). The former is sensitive to oxidation state and geometry, the latter can be used to determine the radial distribution of electron density around the absorbing atom, the coordination number and bond length.

[5] Power series expansion in the potential V (perturbation theory) and first oder approximation by neglecting $O(V^2)$ [121]

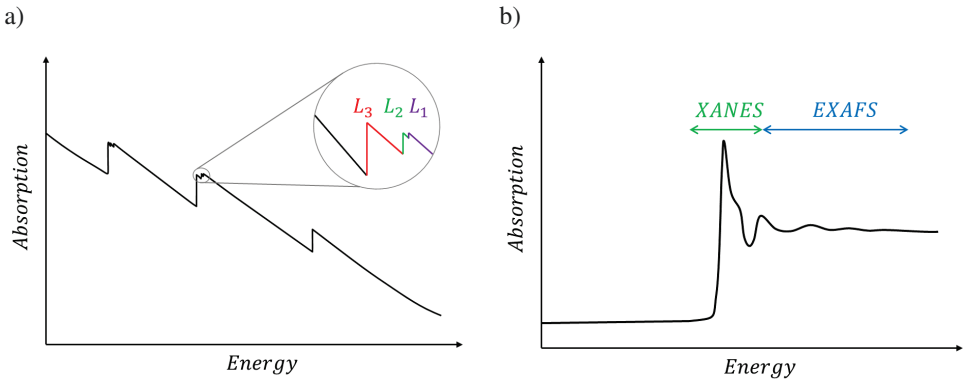


Figure 3.18: X-ray absorption spectrum: a) Complete spectrum showing three major transitions and splitting at higher resolution (inset) b) Schematic view of a single edge, according to [123].

3.8.1 EXAFS

On closer inspection several oscillations can be found in the EXAFS region which originate from interference effects: Photoelectrons[6] in this energy range have a de Broglie wavelength comparable to interatomic distances and are therefore scattered by surrounding atoms. Depending on the energy, out-going and back-scattered waves are in phase, leading to a local maximum in the photoabsorption cross-section due to constructive interference, or out-of-phase, resulting in a local minimum [123].

3.8.2 XANES

In the XANES region the photoelectron has a long mean-free path due to its low kinetic energy. Hence, a huge number of multiple scattering pathways are possible making it very complicated to simulate: Several weak transitions can be found below the edge as well as intense narrow ones on the rising edge ('white lines'). Hence, most simulations remain qualitative, nevertheless allowing for the determination of the electronic structure, oxidation state and three dimensional structure [123].

3.9 X-ray Magnetic Circular Dichroism

One year after its theoretical prediction in 1986 [125], XMCD was demonstrated for the first time [126] and has evolved into a fundamental technique that provides detailed information on the magnetic and electronic structure of organometallic complexes, nanoparticles, thin films, molecular materials, etc.

[6] In fact there are only 'virtual photoelectron waves' which influence transition matrix elements.

XMCD is obtained as difference between two XAS spectra, measured with the polarization vector of circularly polarized light parallel and antiparallel to an external magnetic field. The signal arises from electric dipole transitions of core electrons that are excited into unoccupied conduction states. Due to the large core spin-orbit coupling, this provides a strong effect (except for the K edges).

The p orbit is split into $2p_{3/2}$ (L_3) and $2p_{1/2}$ (L_2) due to parallel and antiparallel spin-orbit coupling, respectively. For an X-ray helicity vector oriented parallel (antiparallel) to the 2p orbital moment, the excitation of spin-up (spin-down) electrons is preferred. If there are less spin-up than spin-down holes available in the 3d valence band, the L_3 edge thus shows a net negative and the L_2 edge a net positive peak [122].

3.9.1 Transition Probabilities

During transition the total spin moment is conserved, because the radiation interacts with the orbital part of the wave function only. For the determination of allowed transitions and their probability, the Wigner-Eckart theorem can be applied. It leads to the following condition which has to be satisfied to enable transitions:

$$m_j = m - q + \sigma. \tag{3.25}$$

Considering dipolar transitions with $\Delta l = 1$, $\Delta m = +1, 0, -1$ only, possible transitions and their probabilities can be determined as summarized in figure 3.19 [122].

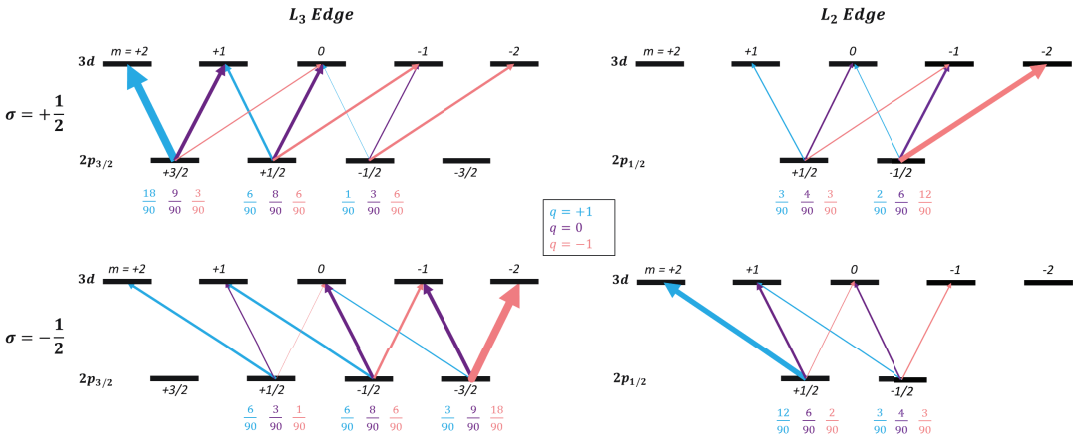


Figure 3.19: Spin-up ($\sigma = +\frac{1}{2}$) and spin-down ($\sigma = -\frac{1}{2}$) transition probabilities at the L_3 and L_2 edges for left-circular (pink, q=-1), linear (purple, q=0) and right circular polarized X-rays (blue, q=+1), according to [122].

3.9.2 Sum Rules

To separately obtain orbital and spin contributions from the integrated XMCD signal, so called sum rules can be applied. For the $L_{2,3}$ edges, which will be analyzed in chapter 4.4, they are given by

$$\langle L_z \rangle = \frac{2}{3} n_h \frac{\int_{L_3+L_2} \mu_c dE}{\int_{L_3+L_2} \mu_0 dE} \tag{3.26}$$

$$2\langle S_z \rangle + 7\langle T_z \rangle = n_h \frac{\int_{L_3} \mu_c dE - 2\int_{L_2} \mu_c dE}{\int_{L_3+L_2} \mu_0 dE} \tag{3.27}$$

$\langle L_z \rangle$, $\langle S_z \rangle$ and $\langle T_z \rangle$ are the expectation values for the orbital, spin and magnetic dipole operators in Bohr magnetons, respectively. The latter is caused either by an anisotropic charge distribution or by spin orbit interaction. For transition metal 3d states it is usually assumed to be negligible. Integration is necessary to include every state of a specific band and to remove effects of the final state core-hole. n_h is the number of final states available for transition [127]. The isotropic absorption signal μ_0 is defined as

$$\mu_0(E) = \frac{\mu^-(E) + \mu^+(E)}{2} \tag{3.28}$$

[128] and the dichroic absorption signal μ_c can be calculated using

$$\mu_c(E) = \mu^-(E) - \mu^+(E). \tag{3.29}$$

Since n_h has to be obtained from theoretical models, the sum rules are often expressed as a ratio to circumvent uncertainties and remove the dependency on shell occupancy, degree of polarization and sample magnetization [127]:

$$\frac{\langle L_z \rangle}{\langle S_z \rangle} = \frac{4}{3} \frac{\int_{L_3+L_2} \mu_c dE}{\int_{L_3} \mu_c dE - 2\int_{L_2} \mu_c dE} \tag{3.30}$$

3.9.3 Experimental Setup

As stated before, XMCD measurements can presently only be performed at synchrotron radiation facilities due to the requirements concerning X-ray flux, energy tunability and polarization variation. The results shown in this thesis were achieved at the 4-ID-D beamline at the Advanced Photon Source (APS) in Oak Ridge, USA. Hence, the components used there will be described in detail only, though there are alternatives. The complete setup is shown in figure 3.20.

To allow for scanning through the energy range considered, the beam has to be monochromatized first. This can be done either by using a dispersive polychromator with a position-sensitive

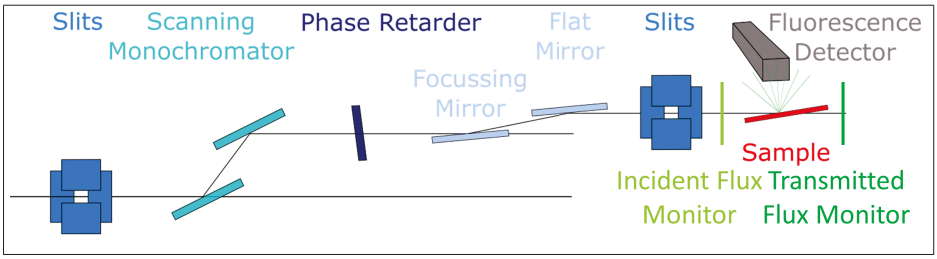


Figure 3.20: Schematic setup of the 4-ID-D Beamline at APS for XMCD measurements, inspired by [39].

detector or by a scanning monochromator arrangement. For the latter a set of silicon single-crystals is used. Bragg's law then determines the energy depending on the angle of incidence. To maintain a fixed X-ray spot on the sample, the crystal positions can be adjusted [127].

For X-ray polarization either phase retarders or off-axis bending magnets can be applied. The former provide the greatest degree of circular polarization using a thin perfect crystal consisting of a low-Z element. The scattering plane of a specific reflection is oriented at a 45 degree angle to linear polarization of the incident beam. By rotating the crystal away from the precise Bragg condition by a small angle, the transmitted X-rays become circularly polarized, with a helicity depending on the direction of rotation [127].

To provide low temperatures the sample can be either mounted in a closed cycle or cold head cryostat. Magnetic fields are supplied by a 6.5 T superconducting magnet or a 0.2 T permanent magnet.

Finally, the signal has to be detected, which can be done directly by two monitors recording the incident and transmitted intensities or indirectly by measuring the X-ray fluorescence. It originates from the filling process of the core hole and is therefore proportional to the number of holes in the initial (2p) state.

3.9.4 Data Treatment

Since there is a large energy gap between the edges considered in this thesis, they had to be measured separately. Hence, the monochromator had to be aligned for every edge individually making a normalization procedure necessary.

The intense peaks in the absorption spectrum (caused by the strong density of states close to the Fermi energy) are superimposed by a step-like function due to transitions to unbound free electron states. Additionally, it was shown that the L edge absorption jumps are scaled in a 2:1 ratio, caused by a different number of initial state electrons [127]. Hence, the curves can be normalized as shown in figure 3.21. This is performed by fitting a linear function to the pre-edge regions, subtracting it from the curves[7] and dividing it by the average value of the post-edge regions. Finally the L_2 curve is multiplied by 0.5 and added to the linear function f(x)=1.

[7] This also removes the background originating from other components in the sample

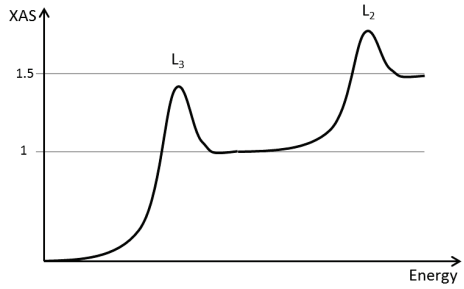


Figure 3.21: Schematical representation of a normalized XAS curve.

As shown in chapter 3.9.1, the spin polarization of a transition is dependent on the X-ray helicity, while spin polarization of the unoccupied 3d-states depends on the magnetization direction of the sample. A high number of transitions and hence large absorption is possible only, if both polarizations are identical. Assuming that full saturation is always achieved, a change in the polarization or magnetization direction should therefore yield the same result. This can be used to remove artifacts by measuring every polarization helicity with both magnetization directions and defining the XMCD curve as the difference of the two dichroic absorption signals (equation 3.29) obtained [129]:

$$XMCD(E) = \frac{\mu_c^{+H}(E) - \mu_c^{-H}(E)}{2} \tag{3.31}$$

Finally, the signal has to be corrected concerning polarization efficiency P and alignment [128]:

$$XMCD^{norm}(E) = \frac{XMCD(E)}{P \cdot \cos\theta} \tag{3.32}$$

θ is the angle of incidence. For the calculation of the expectation values for the orbital and spin operators as shown in section 3.9.2, the isotropic (equation 3.28) and dichroic absorption signal (equation 3.29) is needed. To consider both magnetization directions the average is calculated. Hereby it should be kept in mind that for the dichroic absorption the signal of one magnetic field direction is the mirror image of the other. This leads to the minus sign in the nominator of equation 3.34:

$$\mu_0^{average}(E) = \frac{\mu_0^{+H}(E) + \mu_0^{-H}(E)}{2} \tag{3.33}$$

$$\mu_c^{average}(E) = \frac{\mu_c^{+H}(E) - \mu_c^{-H}(E)}{2} \tag{3.34}$$

Additionally, it should be considered that the step-like function mentioned before (c.f. figure 3.21) needs to be subtracted from $\mu_0^{average}$ before it is inserted in equations 3.26 and 3.27.

3.10 Scanning Electron Microscopy

One of the most frequently applied techniques for sample characterization is Scanning Electron Microscopy (SEM). Using a focused electron beam it generates images with a resolution in the nanometer range. Figure 3.22 shows the schematic setup which consists of an electron gun, electron optics and a detection unit. To avoid charging effects, the samples need to be conductive. In addition, (ultra) high vacuum is required because the beam would otherwise be scattered by gas molecules [130].

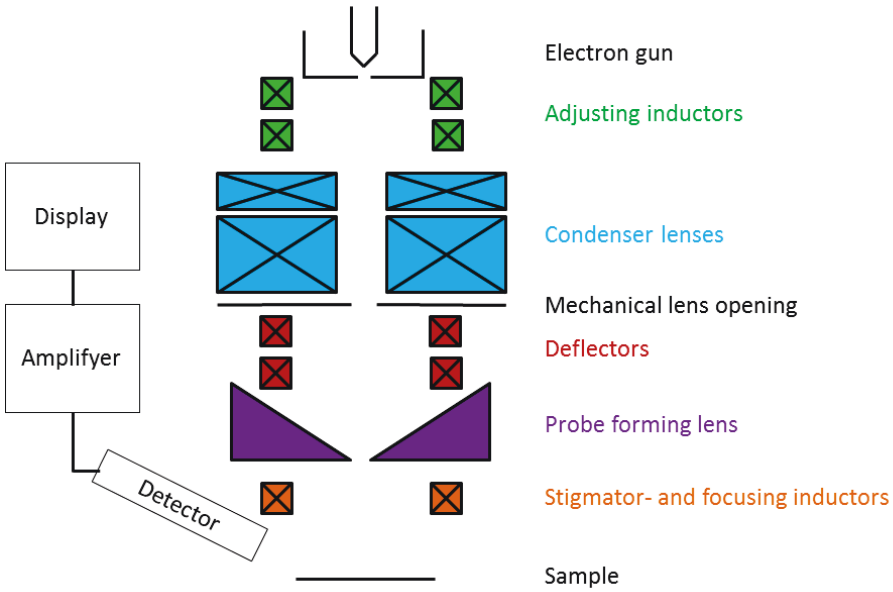


Figure 3.22: Schematical setup for a scanning electron microscope.

The SEM images shown in this thesis were obtained using a Hitachi SU8000 instrument in cooperation with the PGI-7 (Peter Grünberg Institute for Electronic Materials). Its electron gun is designed for Cold Field Emission (CFE), where a tungsten filament is fashioned into a sharp tip and an acceleration voltage of 50-150 kV is applied. This enables the electrons to overcome the work function and escape from the material. An alternative is thermal emission, where an electrical current is used to heat up the filament. Additionally, field emission can be thermally assisted, which is referred to as Schottky emission [131].

The electron optics consists of several magnetic lenses employing the Lorentz force to deflect and focus analogously to light optics. The first pair of inductors centers the beam in the column. Condenser lenses are used to reduce the diameter and set the magnification. A mechanical lens opening (50 μm - 100 μm) is mounted below to suppress marginal rays. Since the sample has to be scanned line by line to produce an image, several deflectors are installed above the probe forming lens to change the beam direction. Finally, a set of stigmator- and focusing-inductors is used to level distortions [130].

When the electron beam hits the sample, this results in several interaction products like X-rays, cathodoluminescence or backscattered electrons. Especially the inelastic collisions are important, because they lead to the emission of Secondary Electrons (SE). Their intensity strongly depends on the inclination angle of the surface, hence they give a good topographical contrast. They are usually detected by an Everhart-Thornley detector which is positioned diagonally above the sample. It employs an electric bias field to accelerate the SE onto a szintillator. A photomultiplier then amplifies the signal which can be displayed e.g. by an image tube [132].

3.11 Coating

Depending on availability, matrix materials and substrate coatings were deposited either by Ion Beam Sputtering (IBS) in cooperation with the Max Planck Institute for Intelligent Systems, department Schütz or by Molecular Beam Epitaxy (MBE) in cooperation with the PGI-6 (Peter Grünberg Institute for Electronic Properties). Both techniques require Ultra High Vacuum (UHV) conditions. Figure 3.23 shows a schematic overview.

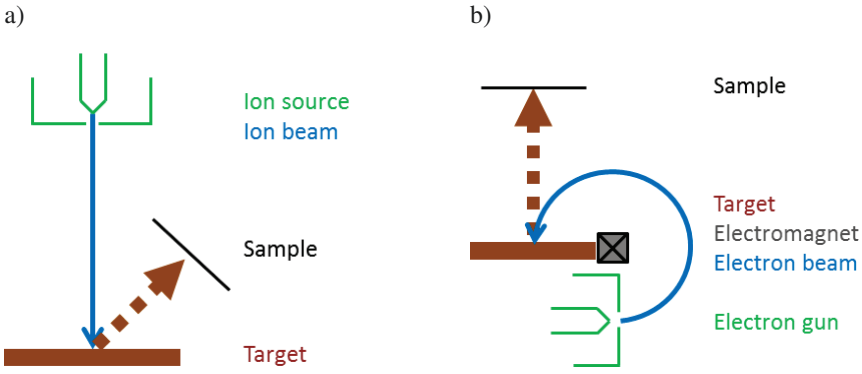


Figure 3.23: Setup illustration for a) Ion Beam Sputtering and b) Molecular Beam Epitaxy.

For IBS a focused ion beam is directed towards a target from which atoms are ejected upon collision and are subsequently deposited on the sample. In the ion source, which consists of an anode and a cathode that share a central axis, a high voltage (2-10 kV) is applied. This leads to an electric field that confines electrons in the source center around a saddle point. By injecting argon gas a plasma emerges. A collimated beam is then produced by accelerating the ions towards the exit aperture. When it impinges upon the target, the material is sputtered onto the sample by momentum transfer [133].

For material deposition by MBE, an electron beam evaporates the target. Therefore, a tungsten cathode is heated to enable electrons to overcome the work function and leave the solid. They are accelerated by a high voltage source and an electromagnet directs them towards the target. The evaporated material is then deposited onto a sample which is mounted above [134].

3.12 Plasma Etching

Plasma processing is versatile tool for surface modification, which can be applied to remove the organic surfactant shell of nanoparticles. This was performed in cooperation with the PGI-7 (Peter Grünberg Institute for Electronic Materials) using the TePla 300 Plasma Processor. After installing the sample, the chamber is evacuated and subsequently flooded with oxygen gas. Injection of microwaves from a magnetron leads to ionization [135]. The emerging vacuum ultraviolet radiation breaks most organic bonds and the oxygen species react with organic contaminants that are subsequently removed with the gas flow [136].

4 Two Dimensional Systems

In this chapter it is discussed how the interactions of iron oxide nanoparticles can be tuned by exchanging the matrix material. Therefore, the samples are first introduced in detail and afterwards the influence of several sample preparation parameters is presented. Finally, the effect of a polarizable matrix material is discussed. In order to retain an overview with sample treatment, every section ends with a table containing detailed preparation descriptions. Additionally, an overview of all samples is provided in appendix B.

4.1 Sample Description

Thanks to substantial progress in chemical synthesis, nanoparticles composed of various materials can nowadays be produced with a high degree of control of parameters like shape and size. For this several methods like electrospray synthesis, microemulsions, sonochemical reactions, precursor thermolysis or hydrolysis (just to name a few examples) have been optimized [137].

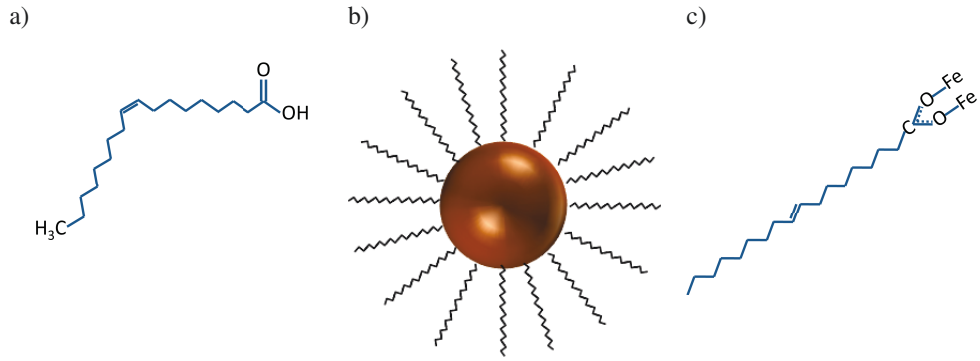


Figure 4.1: a) Chemical structure of oleic acid b) Schematic illustration of an iron oxide nanoparticle, sterically stabilized by oleic acid c) Bidentate interactions of the carboxylic head of oleic acid with iron ions on the surface of the nanoparticle, according to [138].

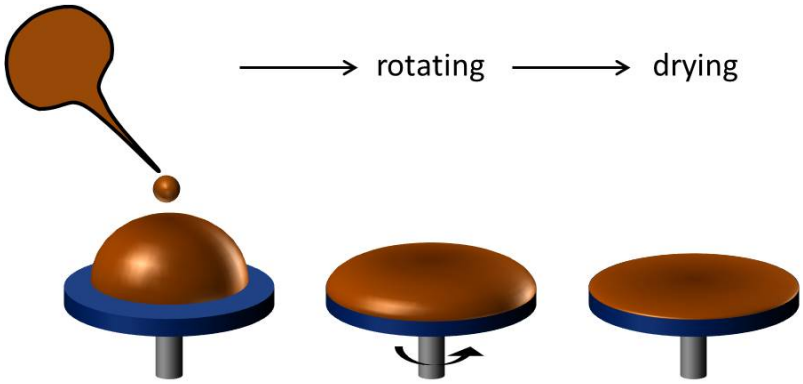


Figure 4.2: Schematic representation of the spin coating process.

The iron oxide nanoparticles used here are commercially available at Ocean Nanotec, LLC (USA). They have a spherical shape with a diameter of 20 nm $\pm$ 2.5 nm (Appendix A). During synthesis via thermolysis of an iron precursor, oleic acid ($CH_3(CH_2)_7CH = CH(CH_2)_7CO_2H$) is added to form a surfactant shell that provides steric stabilization (figure 4.1). For storage, the nanoparticles are dispersed in toluene.

All samples presented in this chapter are prepared by spin coating (figure 4.2): After cleaning 10 x 10 mm^2 silicon substrates successively with ethyl acetate and ethanol in an ultrasonic bath, $9\mu l$ of nanoparticle dispersion are applied. The sample is then fixed by vacuum onto the spin coater and forced into rotation for 60 s at a specific number of Revolutions Per Minute (rpm). A thin layer then covers the whole substrate and after toluene evaporation a mostly homogeneous mono-/multilayer of nanoparticles is formed.

4.1.1 Self-assembly

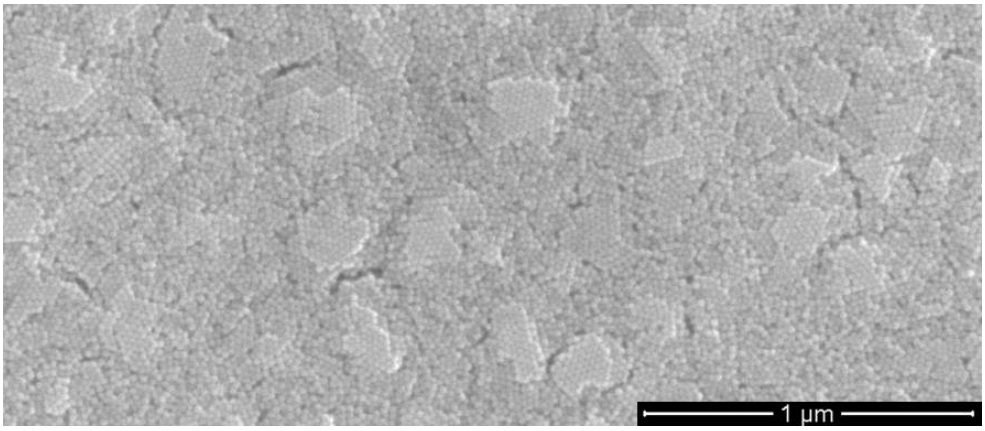


Figure 4.3: Sample 1-01: SEM image in the center of a silicon substrate on which the nanoparticles ($9\mu l$ dispersion with a concentration of 25 mg/ml) are deposited by spincoating (60 s at 3000 rpm).

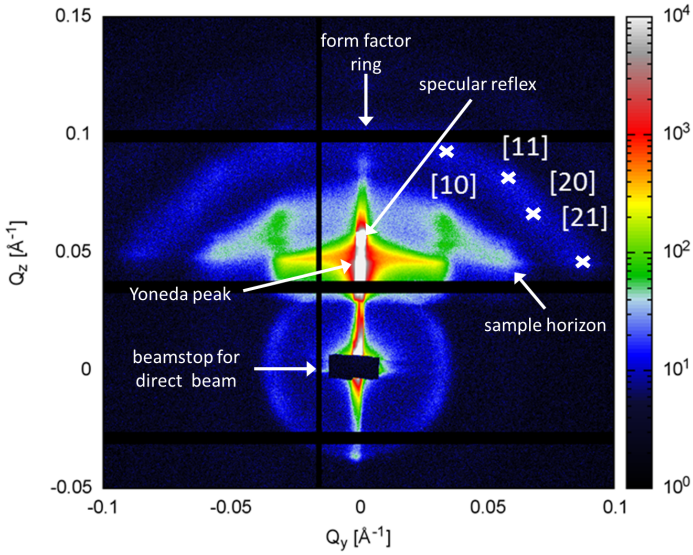


Figure 4.4: Sample 1-01: GISAXS measurement performed at GALAXI revealing that the sample is a two dimensional superpowder with a lattice constant of 217 Å.

Figure 4.3 shows a SEM image taken in the center of sample 1-01. Due to the relatively high nanoparticle concentration of 25 mg/ml a multilayer is formed. Small grains of hexagonally close packed nanoparticles with an average coherence length of 200 nm are formed because of strong van der Waals interactions. To demonstrate, that this order is characteristic for the whole sample, GISAXS measurements were performed at the JCNS GALAXI. Aside from form factor rings caused by the spherical shape of single nanoparticles, several peaks can be clearly identified in figure 4.4. By assuming a hexagonal lattice with $Q_y(h,k) = Q_y(1,0) = 0.0334$ Å^{-1} the lattice constant a can be determined to be 217 Å using formula 3.15. This is in accordance with the nanoparticle size obtained from Transmission Electron Microscopy (TEM) (Appendix A) by assuming a 0.85 nm thick oleic acid shell. Further peak positions calculated for this lattice constant are shown in table 4.1 which match the measured values. Since no sample rotation is necessary to display all peaks, the sample can be regarded as two dimensional powder, consisting of several grains with highly ordered nanoparticles inside (2D superpowder).

(h k)	Q_y calculated [Å^{-}1]	Q_y measured [Å^{-}1]	Difference
(1 0)	0.0334	0.0343	-0.0009
(1 1)	0.0579	0.0587	-0.0008
(2 0)	0.0669	0.0657	0.0012
(2 1)	0.0885	0.0862	0.0023
(3 0)	0.1003	0.1004	-0.0001
(2 2)	0.1158	0.1134	0.0024

Table 4.1: Sample 1-01: Comparison of calculated and measured Q_y values.

4.1.2 Magnetic Properties

As mentioned before, the nanoparticles are deposited on silicon substrates, which cause a diamagnetic background that is routinely removed by fitting a linear function with zero offset to the saturation region of the M(H) curve. Based on the nanoparticle suppliers statement that the product consists of magnetite [139], a monodomain state is expected, since the size is significantly below the critical radius of 49 nm [7] which can be estimated by formula 2.46. Hence, apart from spin-canting effects near the surface [140], all the spins in one nanoparticle can be summed up to one superspin.

Figure 4.5 shows hysteresis curves for sample 1-01 recorded at 300 K (a) and at 5 K (b), revealing the typical behavior of a superparamagnetic system: At room temperature the measurement time scale is larger than the nanoparticle relaxation time, hence the loop is S-shaped and closed as it would be for a paramagnet. By reducing the temperature, the relaxation time increases and when it exceeds the typical time scale of the measurement, the hysteresis loop opens up and becomes similar to a curve that would be expected for a soft ferromagnetic material [7].

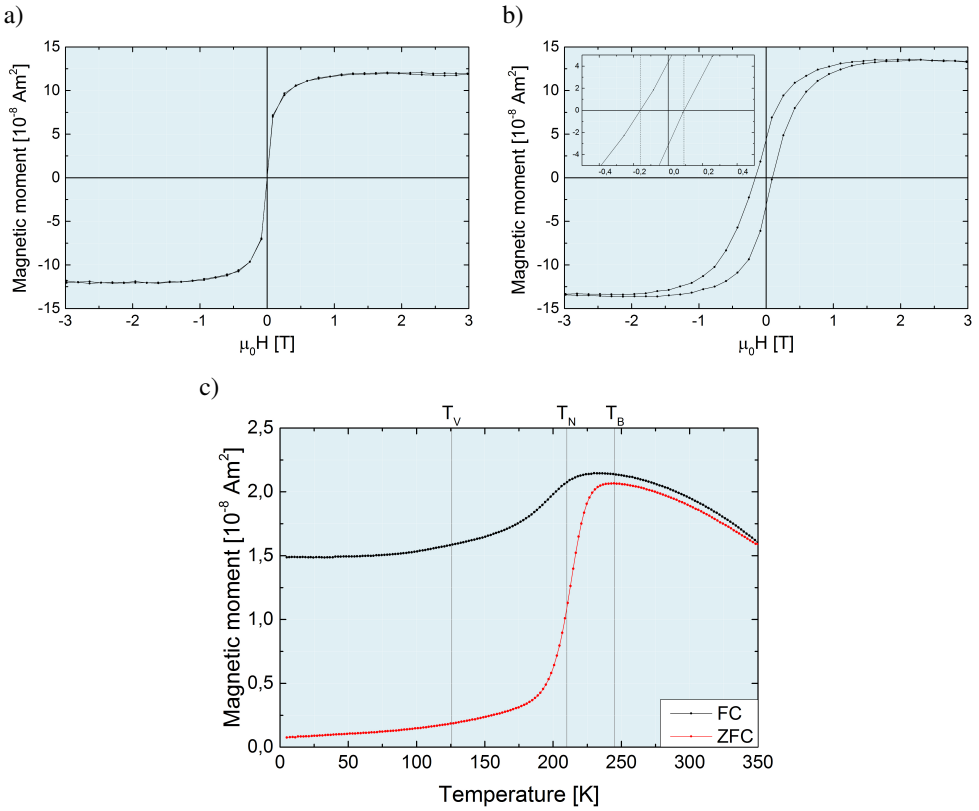


Figure 4.5: Sample 1-01: Hysteresis loops at a) 300 K and b) 5 K showing superparamagnetic behavior and exchange bias. c) ZFC (red) and FC (black) curve measured at $\mu_0 H = 0.005$ T revealing a blocking temperature T_B of 245 ± 2 K and a combined ferri- and antiferromagnetic behavior with a Néel temperature T_N of 210 ± 2 K.

This behavior is further confirmed by ZFC-FC measurements as shown in figure 4.5 c: if the sample is cooled below the blocking temperature T_B in zero field, the superspins are fixed to one of the two possible directions along their easy axis because thermal energy is no longer sufficient to overcome the energy barrier between the equilibrium states. Since the easy axes of the nanoparticles are assumed to be randomly distributed, they should cancel each other out. But in the ZFC curve shown here $M(T \to 0) \neq 0$, hence slight interaction between the superspins giving a favored direction of easy axis orientation during nanoparticle deposition is concluded[1]. By heating up the sample in a small field ($\mu_0 H = 0.005$ T), the superspins begin to orient along the magnetic field direction as the thermal energy is sufficient for movements and the magnetic moment increases. At the blocking temperature $T_B = 245 \pm 2$ K they are aligned parallel and the maximum value is reached. If the temperature is further raised, thermal fluctuations start to counteract and the overall magnetic moment decreases.

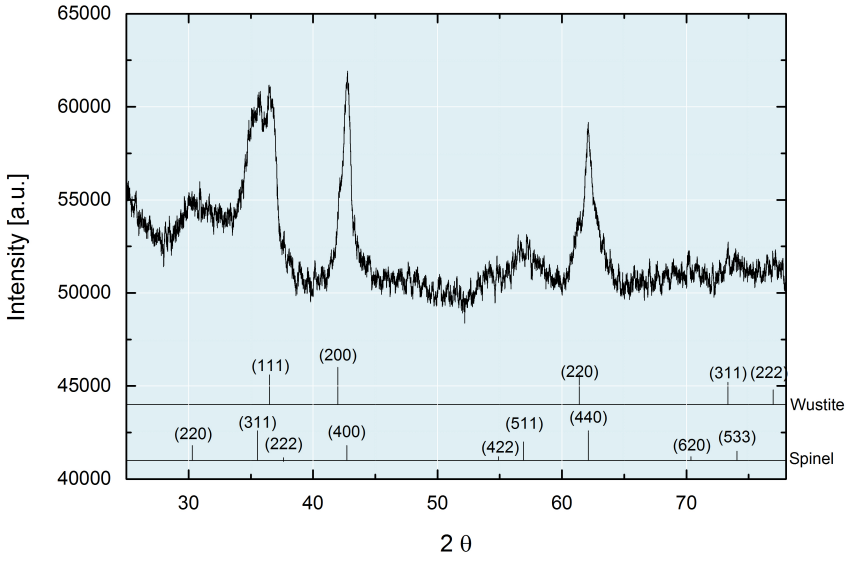


Figure 4.6: X-ray powder diffraction pattern of a nanoparticle multilayer after background subtraction revealing a mixture of wustite with a spinel (maghemite or magnetite). In the lower area of the graph the corresponding XRD patterns are indicated according to the data shown in [141].

Even though the manufacturer claims to deliver magnetite nanoparticles, no Verwey transition is emerging at $T_V = 125$ K [142] and complete suppression due to finite size effects is not expected, since it can still be observed (though shifted to 101 K) for nanoparticles with a diameter of 10 nm [143]. Hence, the sample must consist of another iron oxide phase. Figure 4.6 shows an X-ray powder diffraction pattern obtained from a nanoparticle multilayer after subtracting the background due to the Mylar foil on which it was deposited. The pattern cannot be explained by a spinel structure alone, e.g. due to the double peak at $2\theta = 35°$ and $36°$. If the structure of wustite is added, the pattern fits very well and a two-component system is therefore assumed. Since maghemite is the only iron oxide beside magnetite exhibiting a spinel structure,

[1] The residual fiel was determined as < 0.005 mT.

it must be the second constituent. This composition is further confirmed by the overall shape of the FC curve: for an anitferromagnetic system such as wustite, the FC curve would be similar to the ZFC curve, because of the antiparallel coupling between adjacent spins. Hence, the magnetic moment is reduced below the Néel temperature $T_N = 210 \pm 2$ K [144]. Whereas for the ferrimagnetic material maghemite the magnetic moment is expected to increase upon cooling, until saturation is reached. The FC curve shown in figure 4.5 c can therefore be understood as superimposition of both behaviors[2]. Additionally, the wustite component can be responsible for the slight difference of ZFC and FC curve above the blocking temperature, because it is metastable in that temperature range.

Additional verification for the two-phase system can be found in the low temperature hysteresis curve in figure 4.5 b: Upon closer inspection, a slight shift to negative field values can be observed ($\Delta H = 0.035$ T). This can be caused by an exchange bias effect due to the interaction of an antiferro- and ferrimagnetic system such as wustite and maghemite [145].

Sample No.	NP material / diameter / Batch No.	Substrate	Sample preparation
1-01	Iron oxide / 20 nm / 010411	Silicon	25 mg/ml / 3000 rpm

Table 4.2: Sample overview for section 4.1: The column "sample preparation" provides information about the concentration of the NP dispersion and the rotational speed during spin coating.

4.2 Sub-monolayer Fabrication

Due to the objective of analyzing interface effects, the amount of nanoparticles needs to be reduced to a (sub-) monolayer. Otherwise, interactions between nanoparticles in subjacent layers could superimpose the investigated effects. Hence, the nanoparticle dispersion has to be diluted prior to deposition by spin coating.

Figure 4.7 a shows the center of several samples prepared at a mixing ratio of 1:8 (25 mg/ml NP dispersion:toluene) with varied rotational speed. As the speed increases, multilayers are reduced, but small bilayers are still present even at the maximum value. Therefore, higher degrees of dilution were tested at 3000 rpm (figure 4.7 b) leading to pure sub-monolayers in the center of the sample from a dilution of 1:20. The best compromise between coverage and multilayer supression was found at 1:30, where multilayers are found only if one gets closer than $700\ \mu m$ to the sample edge (reference sample 2-10).

[2] Remark: FC curves declining with temperature are also observed in ferromagnetic SuperSpin Glasses (SSGs) due to dipolar interactions between the nanoparticles. But these systems do not exhibit such a steep decrease below the Néel temperature which must therefore be caused by the antiferromagnetic component.

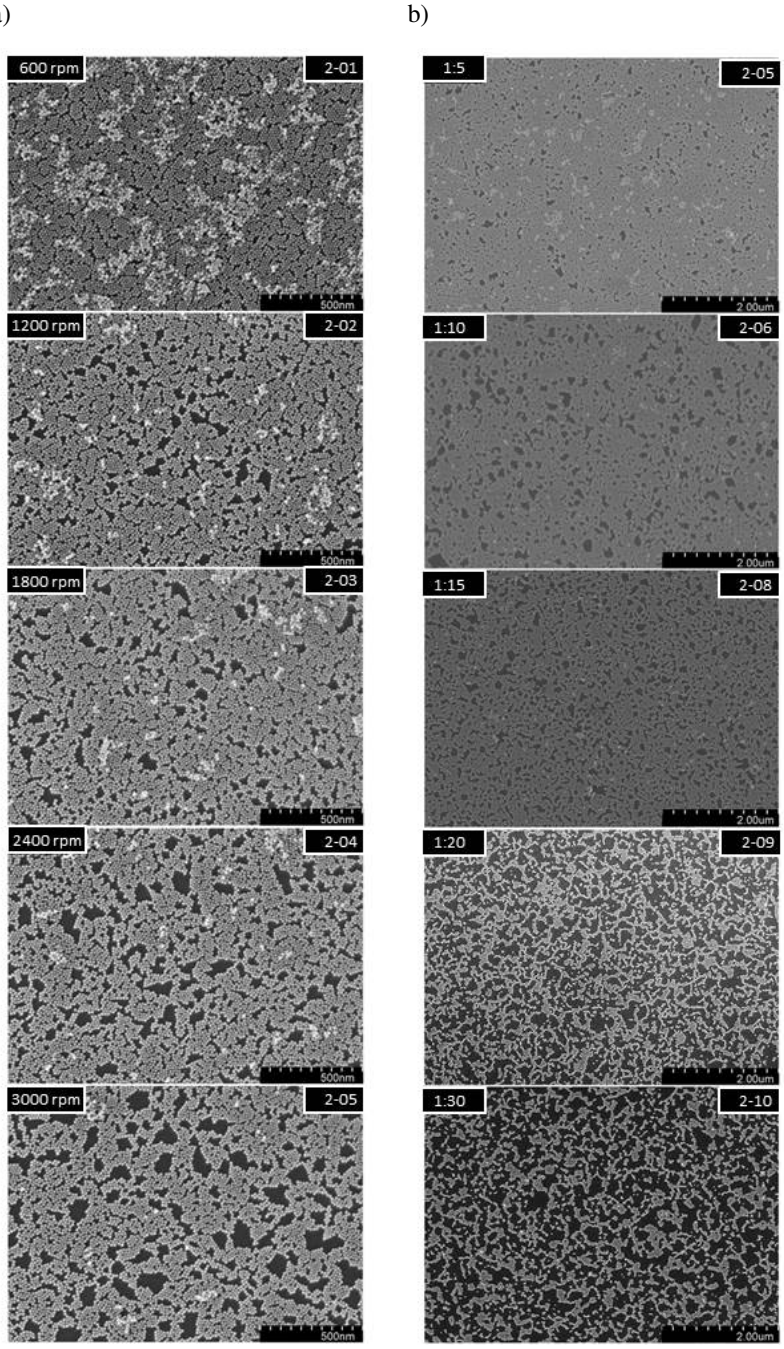


Figure 4.7: SEM images displaying the influence of variations in a) rotational speed (samples 2-01...2-05) and b) dilution with toluene (samples 2-05...2-10) for the fabrication of a (sub-) monolayer of nanoparticles by spin-coating on silicon substrates.

Sample No.	NP material / diameter / Batch No.	Substrate	Sample preparation
2-01	Iron oxide / 20 nm / 010411	Silicon	$\frac{25}{8}$ mg/ml / 600 rpm
2-02	Iron oxide / 20 nm / 010411	Silicon	$\frac{25}{8}$ mg/ml / 1200 rpm
2-03	Iron oxide / 20 nm / 010411	Silicon	$\frac{25}{8}$ mg/ml / 1800 rpm
2-04	Iron oxide / 20 nm / 010411	Silicon	$\frac{25}{8}$ mg/ml / 2400 rpm
2-05	Iron oxide / 20 nm / 010411	Silicon	$\frac{25}{8}$ mg/ml / 3000 rpm
2-06	Iron oxide / 20 nm / 010411	Silicon	$\frac{25}{5}$ mg/ml / 3000 rpm
2-07	Iron oxide / 20 nm / 010411	Silicon	$\frac{25}{10}$ mg/ml / 3000 rpm
2-08	Iron oxide / 20 nm / 010411	Silicon	$\frac{25}{15}$ mg/ml / 3000 rpm
2-09	Iron oxide / 20 nm / 010411	Silicon	$\frac{25}{20}$ mg/ml / 3000 rpm
2-10	Iron oxide / 20 nm / 010411	Silicon	$\frac{25}{30}$ mg/ml / 3000 rpm

Table 4.3: Sample overview for section 4.2: The column "sample preparation" provides information about the concentration of the NP dispersion and the rotational speed during spin coating.

4.3 Plasma Treatment

In order to investigate magnetic proximity effects emerging at the nanoparticle surface, the organic surfactant shell has to be removed. This can be achieved by an oxygen plasma process[3]. The influence on the magnetic properties will be discussed in this section. The sample preparation prior to the plasma treatment is identical to sample 2-10 for all samples presented.

4.3.1 Reference Sample

Figures 4.8 a-b show hysteresis curves obtained for sample 2-10 at 300 K and 5 K that reveal superparamagnetic behavior and a small, negative exchange bias of $\Delta H = -0.04$ T. In comparison to the multilayer sample 1-01 the only difference is a reduced saturation magnetization that is caused by a smaller amount of nanoparticles.

For the ZFC-FC curves displayed in figure 4.8 c, the overall behavior is also similar, revealing a blocking temperature of 237 ± 2 K and mixed maghemite / wustite composition with a Néel temperature of 210 ± 2 K. But the saturation magnetization in the FC curve and the minimum magnetization in the ZFC curve measured at 5 K are reduced. While saturation magnetizations in FC curve and hysteresis loop are both equivalent to 40 % of the value obtained for sample 1-01, the minimum value after zero field cooling accounts only for 9 % what cannot be explained by fewer nanoparticles only: For the multilayer sample 1-01 the interaction is stronger because the NPs interact in three dimensions, whereas for the (sub-) monolayer sample 2-10 the interaction is two- (and partially only one-) dimensional and thus weaker. This leads to a reduced preference in easy axis orientation during deposition what causes a lower minimum magnetization in the ZFC curve and a slightly decreased blocking temperature (-8$\pm$2 K).

[3]Remark: Since the nanoparticles are fixed on the silicon substrate due to strong van der Waals interactions, no particle movement or agglomeration is expected after deposition. Hence, steric stabilization is no longer necessary.

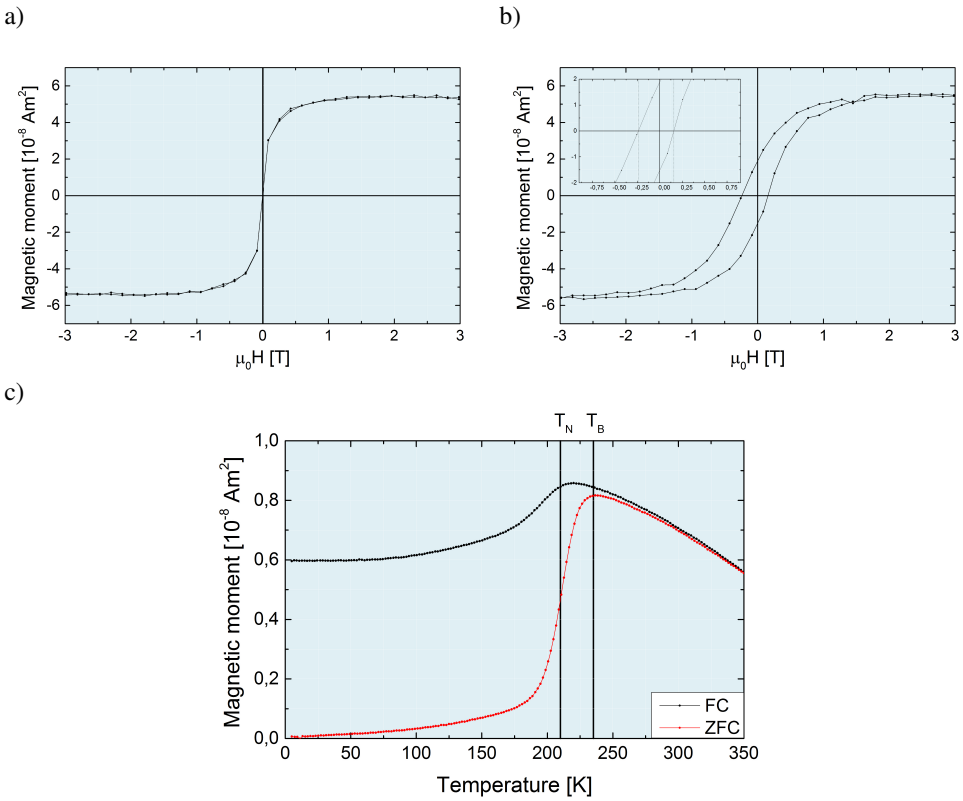


Figure 4.8: Sample 2-10: Hysteresis loops at a) 300 K and b) 5 K showing superparamagnetic behavior and exchange bias. c) ZFC (red) and FC (black) curve measured at $\mu_0 H = 0.005$ T revealing a blocking temperature T_B of 237 ± 2 K and a combined ferri- and anitferromagnetic behavior with a Néel temperature T_N of 210 ± 2 K.

In addition, the magnetic volume V_{mag} can be calculated by fitting the room temperature hysteresis curve with the Langevin equation

$$M = M_s \left[\coth\left(\frac{M_s V_{mag} \mu_0 H}{k_B T} \right) - \frac{k_B T}{M_s V_{mag} \mu_0 H} \right] + \chi \mu_0 H \tag{4.1}$$

M_s is the saturation magnetization and the phenomenological term $\chi \mu_0 H$ accounts for the diamagnetic background originating from the silicon substrate [80]. For sample 2-10 the fit shown in figure 4.9 provides a total magnetic volume of $2.87 \cdot 10^{-12}$ m^{-3} and a saturation magnetization of $(4.6 \pm 0.1) \cdot 10^{-8}$Am^2. The nanoparticle coverage derived from SEM images using the Gwyddion software is 20 ± 1 % leading to a total particle number of approximately $4 \cdot 10^{10}$. Hence, the magnetic volume per particle is $7.18 \cdot 10^{-23}$ m^{-3} which corresponds to a radius of 25 ± 1 nm. This is twice as much as the physical particle radius. A possible explanation are strong magnetic interparticle interactions which will be discussed in section 4.4.

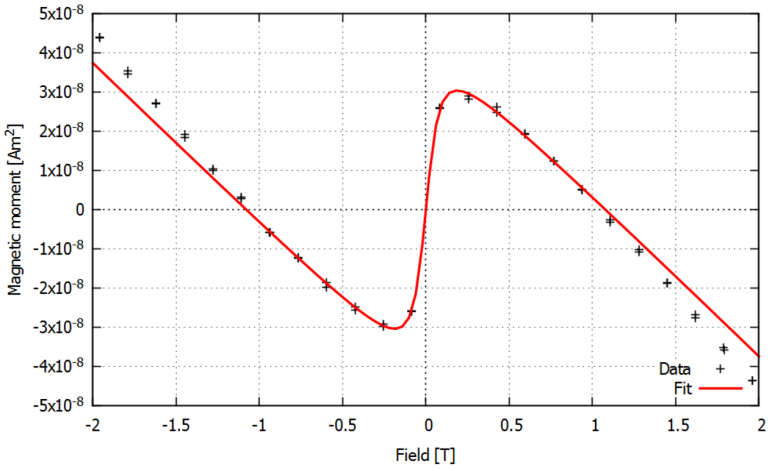


Figure 4.9: Sample 2-10: Raw data of the hysteresis loop measured at 300 K (black) and corresponding Langevin fit (red).

4.3.2 Oleic Acid Removal

Sample 3-01 is prepared analogously to 2-10 and subsequently treated with a 300 W oxygen plasma for 30 min at an oxygen flow of 200 ml/min. This leads to a slight shape modification as shown in figure 4.10 a and also affects the magnetic properties (figure 4.10 b): the peak in the ZFC curve becomes extremely flat. Nevertheless, a blocking temperature can roughly be estimated from the point where the slope significantly decreases. The value of $T_B \approx 175$ K identified like this is 60 K lower than for the reference sample. In the FC curve the magnetic moment reduction during cool down is less prominent and not as steep. It can therefore be concluded that the amount of anitferromagnetic material (wustite) is significantly reduced due to a transformation towards the ferrimagnetic phase (maghemite). This is also consistent with the fact that Fe_2O_3 has the highest oxidation state of the three iron oxides considered. As it will be shown in section 4.4 the system is a superspin glass, which causes the remaining decrease. Additionally, the minimum magnetization in the ZFC curve is higher than for the reference sample 2-10. This indicates a preferred easy axis orientation during the phase transformation.

The hysteresis curves shown in figure 4.10 c-d further confirm this hypothesis: The coercive field strength at 5 K is significantly reduced due to the lowered blocking temperature and almost no exchange bias effect is observable ($\mu_0 \Delta H = -0.003$ T). Therefore, it is assumed that the remaining amount of wustite is negligible.

4.3.3 Phase Transformation

For a better understanding of the phase transition process shown in section 4.3.2, further experiments were performed and will be described below:

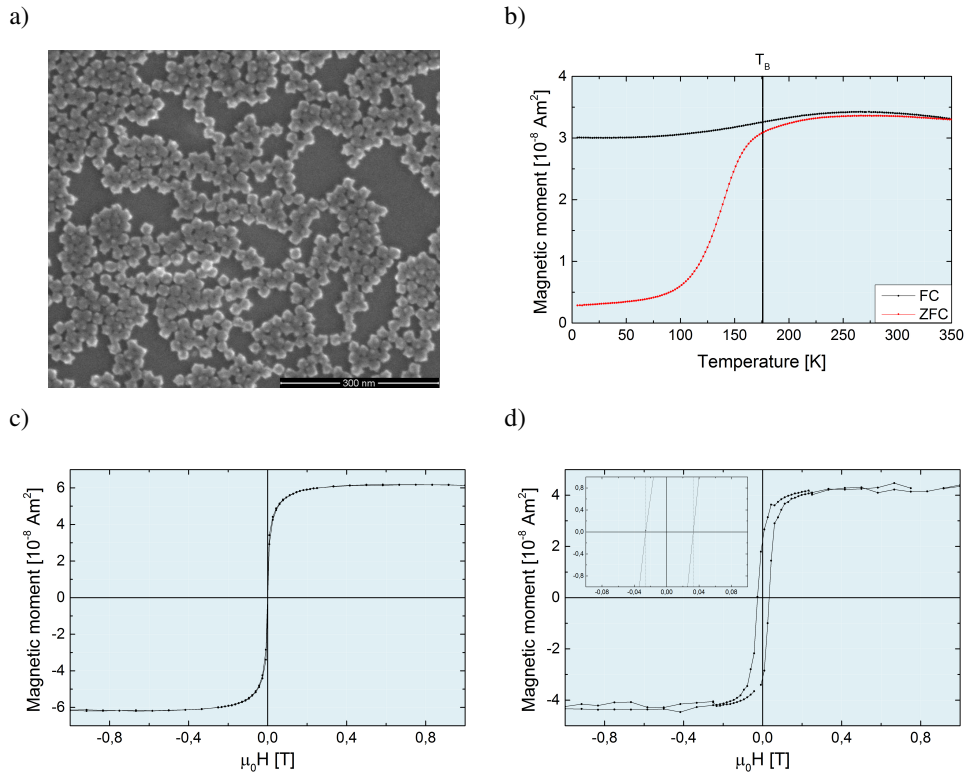


Figure 4.10: Sample 3-01: a) SEM image and b) ZFC (red) and FC (black) curve measured at $\mu_0 H = 0.005$ T indicating a phase transformation towards maghemite. The hysteresis loops obtained at a) 300 K and b) 5 K reveal superparamagnetic behavior.

Metastable State and Onset

In order to find the onset for phase transformation sample 3-02 was prepared with a reduced plasma treatment duration of 2 min while keeping the parameters power and oxygen flow constant. As the SEM image in figure 4.11 a shows, this procedure does not influence the spherical shape, but the magnetic properties are affected: the ZFC-FC curves in figure 4.11 b exhibit a superposition of the behavior found for reference sample 2-10 and 30 min plasma sample 3-01. Some parts of the sample are still in the as-prepared state with a blocking temperature of 235 K, some are already transformed, hence their blocking temperature is 175 K. Additionally, the FC curve is less decreasing at low temperatures and the minimum magnetic moment of the ZFC curve is higher compared to the reference sample, but the values are changed to a smaller extent than it was found after 30 min of plasma treatment.

The exchange bias of $\mu_0 \Delta H = -0.034$ T found at 5 K (figure 4.11 d) is only slightly lower than for the reference sample 2-10 and therefore supports the assumption that only a small amount of wustite has been transformed.

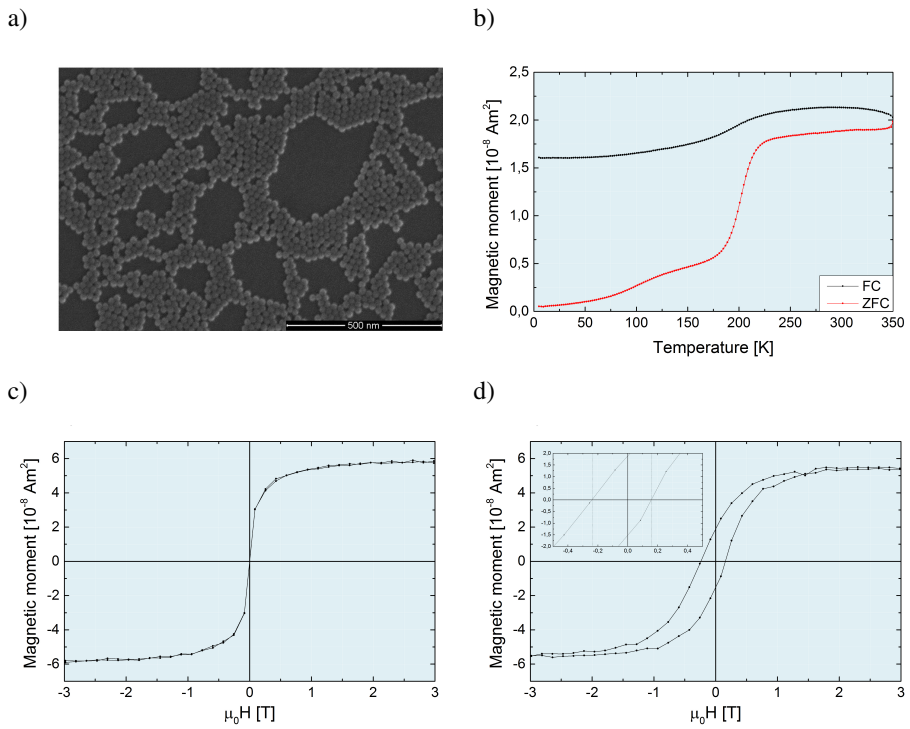


Figure 4.11: Sample 3-02: a) SEM image b) ZFC (red) and FC (black) curve measured at $\mu_0 H = 0.005$ T exhibiting a metastable state during the phase transformation of wustite to maghemite c) Hysteresis loop at 300 K and d) 5 K showing superparamagnetic behavior and exchange bias.

Besides, the sample seems to be in a metastable state: for the ZFC the NPs are aligned as much as possible for the applied magnetic field if the blocking temperature is reached. By further increasing the temperature, thermal fluctuations begin to dominate leading to the reduction of the magnetic moment. The FC curve begins at high temperatures with an applied field. By cooling the sample, thermal fluctuations are reduced and the magnetic moment increases until the blocking temperature is reached. Hence, the ZFC and FC curve are expected to be equal in the high temperature region (i.e. at $T > T_B$). Since this is not observed here, the sample must transform during the measurement and is therefore assumed to be metastable.

For further analysis, another sample was fabricated analogously to sample 3-02 and subsequently placed onto a hotplate at 85° C for 3 h (3-03). This has no effect on the spherical shape of the nanoparticles (figure 4.12 a). But figure 4.12 b shows that the phase transformation process is slightly continued but not completed and the sample is in a stable condition. The low exchange bias of $\mu_0 \Delta H = -0.01$ T found at 5 K (figure 4.12 d) also supports this assumption: it is higher than after 30 min of plasma processing (sample 3-01) but significantly reduced compared to the reference sample (2-10) or the sample without hotplate treatment (sample 3-02). In addition, the minimum value in the ZFC-curve is higher than for sample 2-10 and 3-02, which confirms the assumption of a preferred easy axis orientation during phase transformation mentioned above.

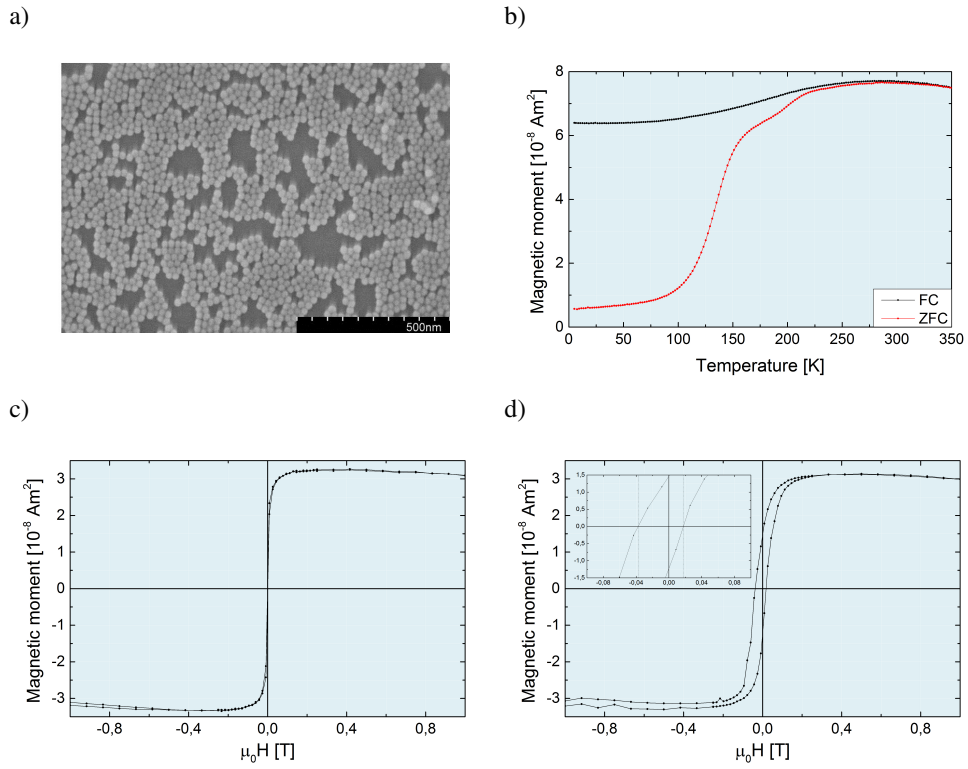


Figure 4.12: Sample 3-03: a) SEM image b) ZFC (red) and FC (black) curve measured at $\mu_0 H = 0.005$ T displaying a stable, partial phase transition c) Hysteresis loop at 300 K and d) 5 K exhibiting superparamagnetism and a slight exchange bias.

To avoid the metastable state, all short-time plasma samples were hotplate treated as described before. The onset for phase transition was then found after 30 s (figure 4.13 a, sample 3-04). Figure 4.13 b additionally shows the ZFC-FC curves for the logest plasma duration without transformation (10 s, sample 3-05). Besides, hotplate treatment without subsequent plasma does not start the transition process (figure 4.13 c, sample 3-06).

Completion

For a plasma duration longer than 2 min, no hotplate treatment is necessary because there is enough energy provided for a stable condition. Figure 4.14 shows ZFC curves obtained after 11 min (sample 3-07) and 12 min (sample 3-08), respectively. The broad dip close to the blocking temperature observed after 11 min vanishes for the 12 min sample thus indicating, that the transition is completed after 12 min.

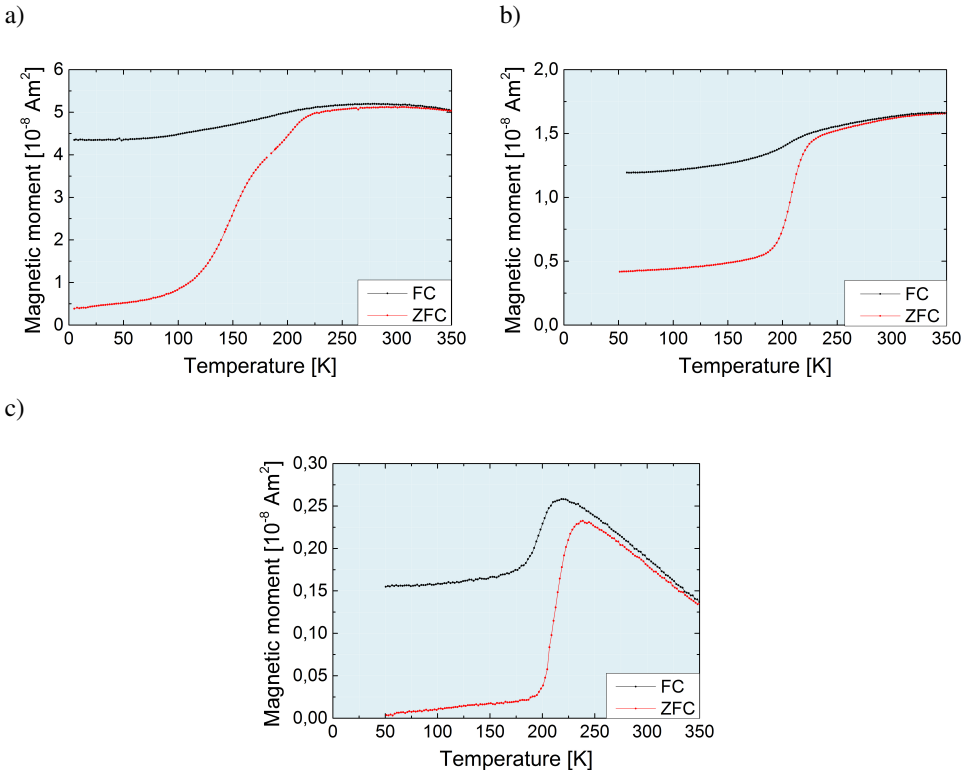


Figure 4.13: ZFC-FC curves measured at $\mu_0 H = 0.005$ T showing a) the onset (sample 3-04) of phase transition after 30 s of plasma treatment and b) the longest plasma duration possible without phase transition (10 s, sample 3-05). c) Sample 3-06 reveals that hotplate treatment only has almost no influence on the magnetic behavior.

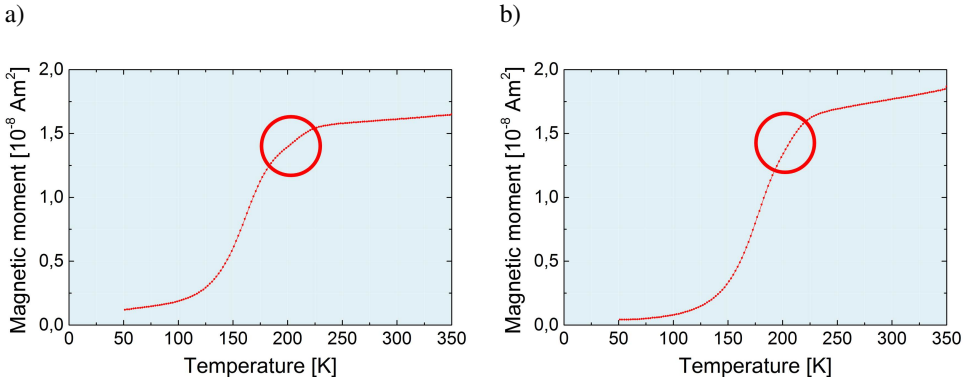


Figure 4.14: Comparison of ZFC curves (measured at $\mu_0 H = 0.005$ T) for a) a sample treated with oxygen plasma for 11 min (3-07) and b) 12 min (3-08), displaying the necessary duration for phase transition completion.

Sample No.	NP material / diameter / Batch No.	Substrate	Sample preparation
3-01	Iron oxide / 20 nm / 010411	Silicon	$\frac{25}{30}$ mg/ml / 3000 rpm Plasma 30min 300W 200ml/min
3-02	Iron oxide / 20 nm / 010411	Silicon	$\frac{25}{30}$ mg/ml / 3000 rpm Plasma 2min 300W 200ml/min
3-03	Iron oxide / 20 nm / 010411	Silicon	$\frac{25}{30}$ mg/ml / 3000 rpm Plasma 2min 300W 200ml/min Hotplate 85° C 3h
3-04	Iron oxide / 20 nm / 010411	Silicon	$\frac{25}{30}$ mg/ml / 3000 rpm Plasma 30s 300W 200ml/min Hotplate 85° C 3h
3-05	Iron oxide / 20 nm / 010411	Silicon	$\frac{25}{30}$ mg/ml / 3000 rpm Plasma 10s 300W 200ml/min Hotplate 85° C 3h
3-06	Iron oxide / 20 nm / 010411	Silicon	$\frac{25}{30}$ mg/ml / 3000 rpm Hotplate 85° C 3h
3-07	Iron oxide / 20 nm / 010411	Silicon	$\frac{25}{30}$ mg/ml / 3000 rpm Plasma 11min 300W 200ml/min
3-08	Iron oxide / 20 nm / 010411	Silicon	$\frac{25}{30}$ mg/ml / 3000 rpm Plasma 12min 300W 200ml/min

Table 4.4: Sample overview for section 4.3: The column "sample preparation" provides information about the concentration of the NP dispersion, the rotational speed during spin coating and the plasma process parameters.

4.4 Polarization Effects

After depositing the nanoparticles on a solid substrate and removing the organic surfactant shell, a matrix material can be applied. To make sure that the oleic acid is removed completely and that no significant amount of wustite is left, the sample preparation prior to applying the matrix is identical to sample 3-01 for all samples that are analyzed in this section. The matrix deposition was performed by IBS in cooperation with the Max-Planck-Institute for Intelligent Systems, department Schütz.

Figure 4.15 shows the ZFC-FC measurements of samples 4-01 and 4-02. While the former is covered with 2 nm of platinum, on the latter 5 nm of palladium are applied. These materials were chosen, because they are very close to the fulfillment of the Stoner criterion: the corresponding Stoner parameters are 0.5 [146] and 0.78 [147], respectively. At first sight, the results seem disappointing, because no change in the magnetic behavior compared to the uncovered sample 3-01 can be observed. However, closer inspection reveals surprising effects, which will be discussed in detail below.

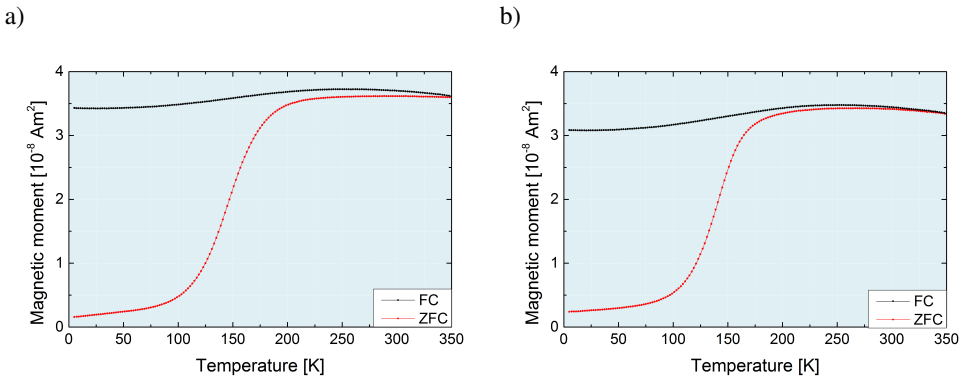


Figure 4.15: ZFC (red) and FC (black) curves (measured at 0.005 T) for a) sample 4-01 which is covered with 2 nm platinum and b) sample 4-02 where 5 nm of palladium are applied. Both curves exhibit characteristics similar to the uncovered sample 3-01 (cf. figure 4.10).

The result of a memory effect measurement performed with an aging stop at 140 K for 10000 s on the uncovered sample 3-01 is presented in figure 4.16 a. It clearly shows a peak close to the aging temperature indicating that the system is in a superspin glass state[4] [5]. If the matrix material is then applied, the peak height is significantly reduced by 40 % for Pt and 20 % for Pd (figure 4.16 b-c) what hints at a partial suppression of the superspin glass behavior. Hence, the inter-particle interactions can obviously be tuned by the deposition of a polarizable material.

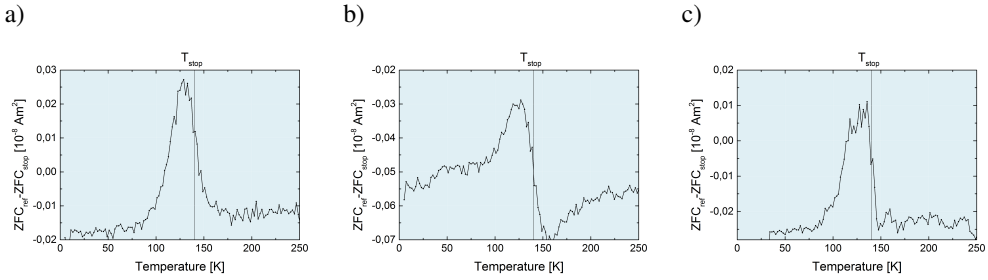


Figure 4.16: Memory effect measurements performed with an aging stop at 140 K for 10000 s on a) the uncovered sample 3-01, b) sample 4-01 which is covered with 2 nm of platinum and c) sample 4-02 on which 5 nm of palladium are applied.

To gain insight into the details of individual and overall magnetization reversal, FORC measurements were performed in cooperation with the Max-Planck-Institute for Intelligent Systems,

[4] In general, the peak is expected on a zero-baseline. However, if the system freezes differently during the two ZFC measurements due to the residual field (-0.005...+0.005 mT), it has different m(T) start values which can cause a background.

[5] Even though the peak is expected to be located at 140 K, finite cooling / heating rates can lead to deviations: from a theoretical perspective, the memory effect is a relaxation process at constant temperatures. However, the presented results were measured in sweep mode which causes additional effects that can lead to a peak shift and broadening.

department Schütz. Figure 4.17 shows the FORC densities for the platinum and palladium covered samples obtained at 300 K and 10 K, respectively. Since the Coercive Field Distributions (CFDs) correspond to the measurement resolution of $\mu_0 H = 0.05$ T for all samples, it is assumed to be negligible. Hence, the real coercivity distribution of the particles from the entire system is also insignificant, revealing that the nanoparticles exhibit an identical magnetic behavior. This confirms the above mentioned assumption that the size distribution is very low and that the particles are in a monodomain state with almost no wustite impurities after oxygen plasma processing (cf. section 4.3.2). Therefore, the samples are a very good model system for the study of the influence of the polarization of matrix materials where the nanoparticles can be regarded as the switching entities according to the physical analysis model (cf. section 3.3).

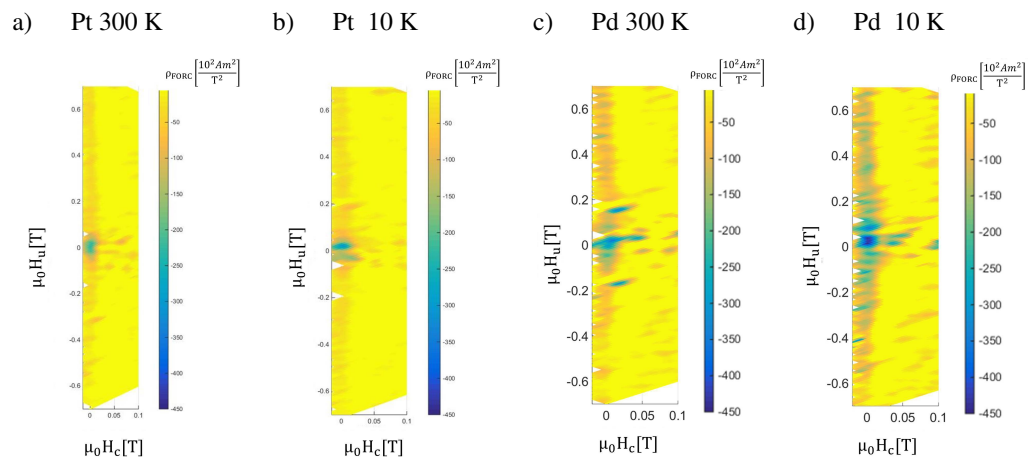


Figure 4.17: FORC distributions for a,b) sample 4-01 (Pt covered) and sample 4-02 (Pd covered) obtained at a,c) 300 K and b,d) 10 K showing significant changes in the interaction field distribution upon temperature reduction and a negligible coercivity field distribution.

For the interpretation of the Interaction Field Distribution (IFD), figure 4.18 shows the FORC densities ρ_{FORC} in dependency of the interaction field H_u at zero coercive field H_c. Upon temperature reduction, the absolute value of the peak around H_u = 0 and the integrated FORC density significantly increase for both samples. This corresponds to an increase in irreversible processes that can be assigned to the mechanism of superspins being fixed in a particular direction below the blocking temperature. The minor maxima are measurement artifacts: when the applied magnetic field is varied, the measurement range sometimes has to be shifted. This leads to characteristic signal spikes in the raw data that cause (due to the second derivative) such sharp peaks in the FORC density.

As it is expected due to its higher Stoner parameter, Pd seems to mediate the coupling better than Pt: while the interaction field quickly approaches zero (already at $\mu_0 H = \pm 0.15$ T) for the latter, the former still shows an interaction field at $\mu_0 H = \pm 0.6$ T. Additionally, the increase in irreversible processes upon temperature reduction is with +9% for the Pt sample relatively low compared to Pd where +54% can be observed.

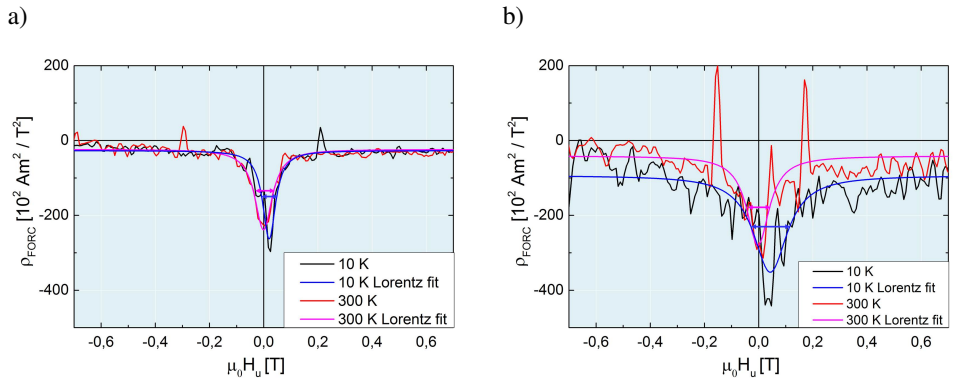


Figure 4.18: FORC density in dependency of the interaction field at zero coercive field and corresponding Lorentz fit for a) the platinum covered sample 4-01 and b) the palladium covered sample 4-02 at 300 K and 10 K, respectively. The arrows indicate the calculated FWHM.

Interestingly, the full width half maximum of Lorentz fits to the curves (indicated by arrows in figure 4.18), which correspond to the maximum interaction fields in the array, shows an unexpected behavior for the Pt covered sample: it decreases from $\mu_0 H = 0.078$ T to $\mu_0 H = 0.058$ T upon cooling, where an increase is expected due to blocking, as it is found for the Pd sample ($\mu_0 H = 0.1$ T at 300 K and $\mu_0 H = 0.15$ T at 10 K). This could be caused by the measurement artifact at $\mu_0 H = 0.05$ T. Removing this area would significantly broaden the fit and thus lead to a larger FWHM value than for the low temperature measurement, as it would be expected.

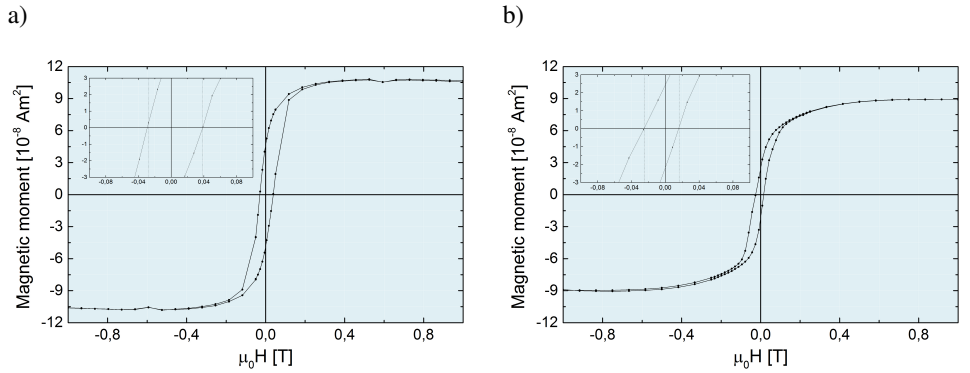


Figure 4.19: Hysteresis curves obtained at 5 K for a) the platinum covered sample 4-01 and b) the palladium covered sample 4-02 demonstrating that -1 T are sufficient for negative saturation.

Since a clear change in nanoparticle interaction after matrix deposition could be shown, the question remains as to what is the physical origin. Hence, delta-M measurements are utilized for further investigation. According to the hysteresis loops shown in figures 4.10 and 4.19, -1 T are sufficient for all samples to reach negative saturation at the beginning of the measurement procedure.

Figure 4.20 shows the measured IRM and DCD curves together with the calculated delta-M for the covered and uncovered samples. The area enclosed by the x-axis and delta-M curve has a negative sign for all samples, indicating a demagnetizing type of interaction that can be attributed to the dipolar interaction between the nanoparticles independent of the matrix.

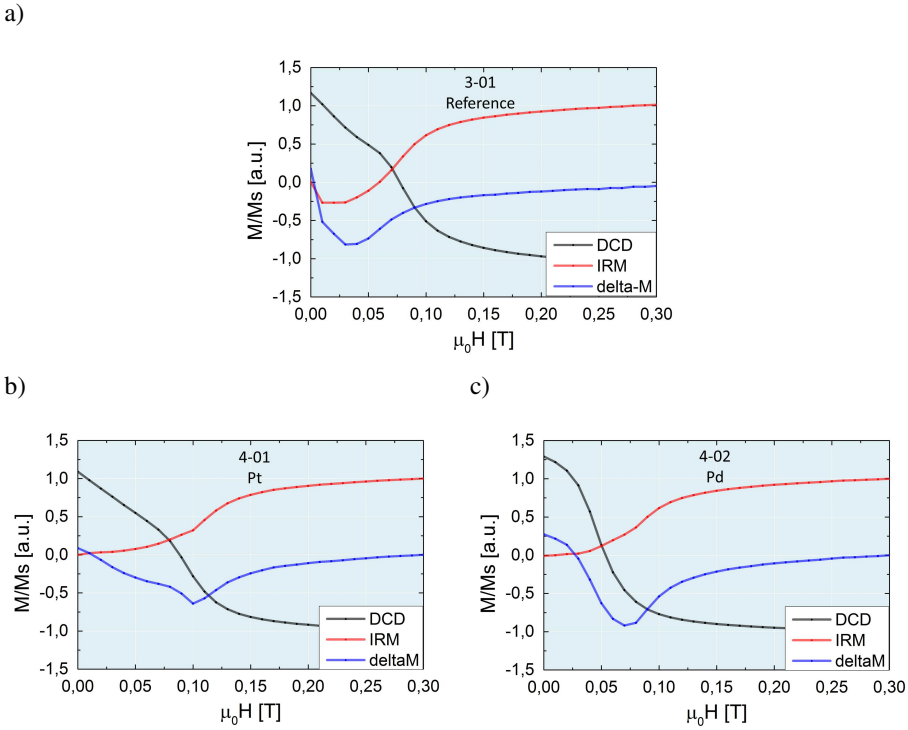


Figure 4.20: DCD (black), IRM (red) and Delta-M (blue) curves for a) the uncovered sample 3-01, b) sample 4-01 which is covered with 2 nm of platinum and c) sample 4-02 on which 5 nm of palladium showing different strengths of demagnetizing interaction.

However, closer inspection reveals that the absolute value of the area, which is a measure for the strength of the interaction, decreases upon matrix deposition: While the uncovered sample 3-01 exhibits a value of -817, for the platinum covered sample 4-01 a value of -587 and for the palladium sample 4-02 a value of -707 can be obtained. This complies with the results derived from the memory effect measurements shown in figure 4.16 where the effect is also more prominent in the Pt sample.

These results imply that the nanoparticles could have polarized the matrix material. This would be an interesting effect, because maghemite seems rather unsuitable for polarizing Pt or Pd due to its small asymmetry and low density of states (DOS) near the Fermi energy (c.f. figure 4.21). Hence, an unambiguous proof by an element specific characterization method such as XMCD is necessary. Figures 4.22 a,c and b,d respectively show the XAS measurements on sample 4-01 and 4-02 performed at the Advanced Photon Source (APS) of the Argonne National Laboratory (USA) using the 4ID-D beamline. The platinum covered sample 4-01 was field-cooled with a liquid helium cryostat from 300 K to 5 K at ± 3 T using an electromagnet. The results were

obtained by a 4-element-vortex detector at an angle of incidence α =1° with a polarization efficiency of P = 0.85. Figure 4.22 c shows the resulting XMCD curve normalized to α and P revealing a clear signal that **evidences the platinum polarization** at the interface to the iron oxide nanoparticles. The spin magnetic moment $\mu_S = g_e \langle S_z \rangle = (-3 \pm 0.01) \cdot 10^{-3} \mu_B$ (where $g_e \approx 2$) and orbital magnetic moment $\mu_L = \langle L_z \rangle = (-1.2 \pm 0.01) \cdot 10^{-3} \mu_B$ can be obtained as described in section 3.9.2. These values are 1...2 orders of magnitude smaller than the values found e.g. for Pd/Fe multilayers [39, 148].

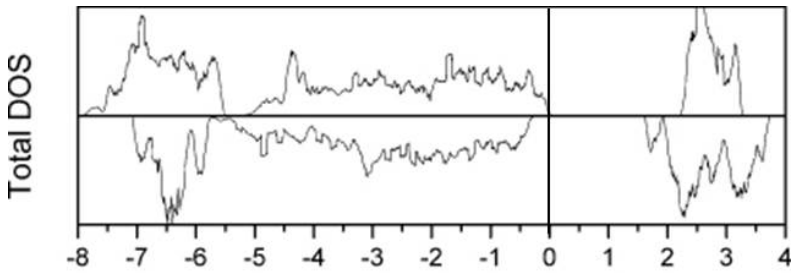


Figure 4.21: Electronic density of states for maghemite. Reprinted with permission from [149].

For the field cooling of the palladium covered sample 4-02 a cold head cryostat was combined with a permanent magnet that exhibits a field of approximately 0.2 T. Unfortunately, the better 4-element-vortex detector had to be replaced by a 1-element-vortex detector due to mounting problems. This leads to a worse signal to noise ratio as the XMCD curve in figure 4.22 d clearly shows. The results were obtained at an angle of incidence α =2.2° and a polarization efficiency of 69%. Even though a clear signal is expected since the Stoner parameter is even higher than the value of Pt and due to the results obtained from the FORC measurements, it is hard to make a statement for the L2 edge. Nevertheless, the L3 edge shows a clear peak and hence it is at least safe to say that Pd is **most probably** also polarized by the oxidic nanoparticles, but it has not been proven unambiguously yet.

Sample No.	NP material / diameter / Batch No.	Substrate	Sample preparation
4-01	Iron oxide / 20 nm / 010411	Silicon	$\frac{25}{30}$ mg/ml / 3000 rpm Plasma 30min 300W 200ml/min Pt 2 nm IBS
4-02	Iron oxide / 20 nm / 010411	Silicon	$\frac{25}{30}$ mg/ml / 3000 rpm Plasma 30min 300W 200ml/min Pd 5 nm IBS

Table 4.5: Sample overview for section 4.4: The column "sample preparation" provides information about the concentration of the NP dispersion, the rotational speed during spin coating, the plasma process parameters and the matrix material, thickness and deposition method.

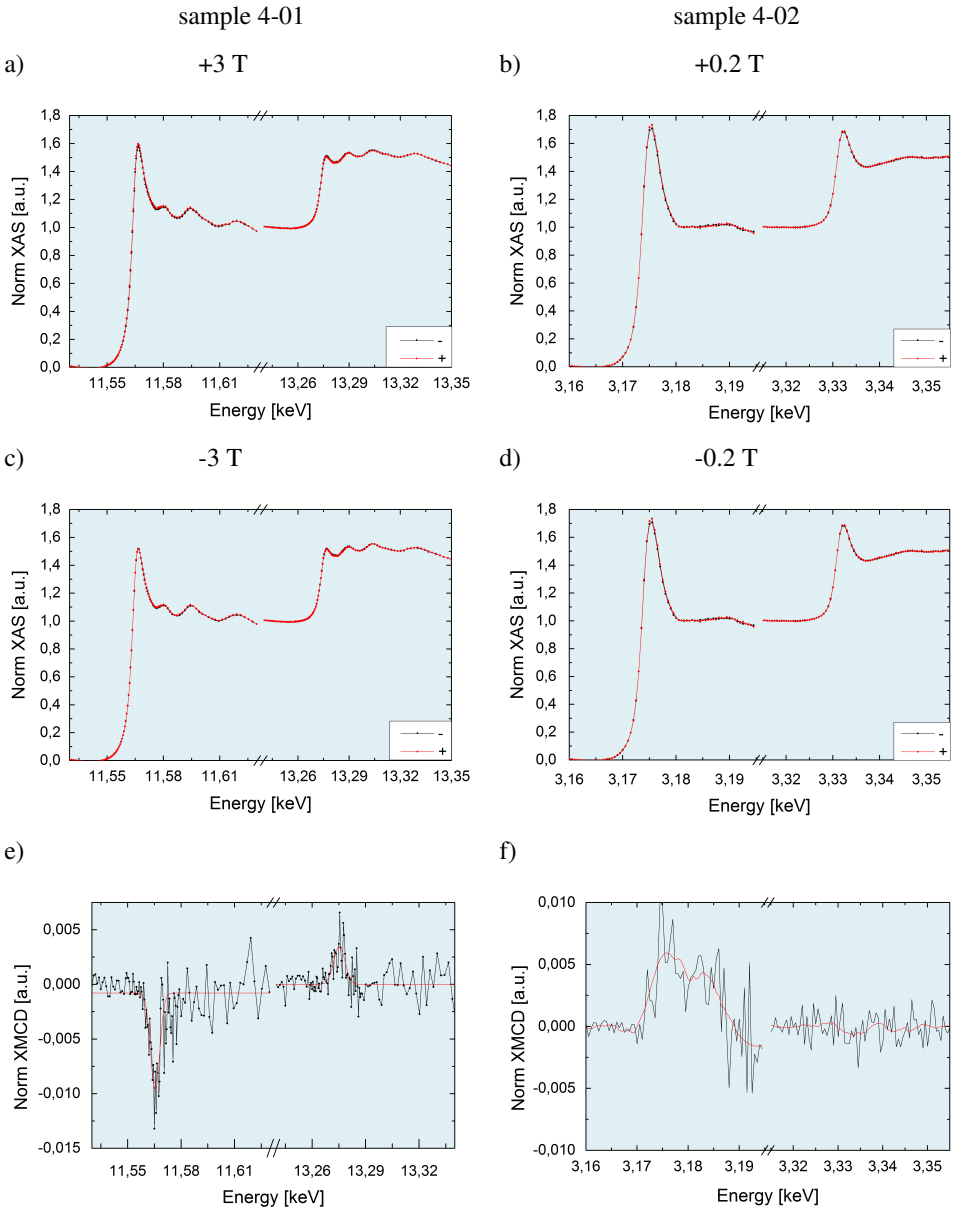


Figure 4.22: XAS measurements for a left and right circularly polarized beam after field-cooling from 300 K to 5 K for a) sample 4-01 with an angle of incidence of 1°and a polarization efficiency of 85% at +3 T and c) -3 T and for b) sample 4-02 with an angle of incidence of 2.2°and a polarization efficiency of 69% at +0.2 T and d) -0.2 T. The corresponding XMCD signals (black) and smoothed curves as guide to the eye (red) are respectively shown in e) for sample 4-01 and f) for sample 4-02.

4.5 Magnetoresistance Effects

In the previous section it was shown that iron oxide nanoparticles can cause a polarization of the matrix material they are embedded in. But they can also influence the electrical transport properties. For the investigation of such magnetoresistance effects, the field and temperature dependency of the sample resistivity is measured using a Quantum Design PPMS device.

4.5.1 Measurements in van der Pauw Geometry

The reference sample (5-01) is a 1x1 cm^2 silicon substrate covered with 5 nm palladium deposited by MBE. Figure 4.23 shows the resistivity in dependency of the applied magnetic field measured according to the van der Pauw method (c.f. section 3.4) at 10 K. All relevant geometries exhibit the same characteristics. Without an external field (0 T), the resistivity has a minimum. By applying a magnetic field, the resistivity increases with increasing field strength. This is typical for the Lorentz magnetoresistance effect. The external field causes a Lorentz force that deflects the conduction electrons on a circular path. By increasing the magnetic field strength, the original trajectories are more and more altered leading to higher resistivity values. Hence, the same behavior is observed, no matter if the magnetic field is applied parallel or perpendicular (in-plane and out-of-plane) to the current flow direction. These characteristics are also found in literature where a resistivity increase in the order of magnitude of $\propto 10^{-3}\Omega$m is demonstrated for palladium layers of 2.5 nm thickness if a magnetic field of 0.8 T is applied [150]. The effect observed here is one order of magnitude smaller which can be caused by the different deposition methods which results in different layer qualities.

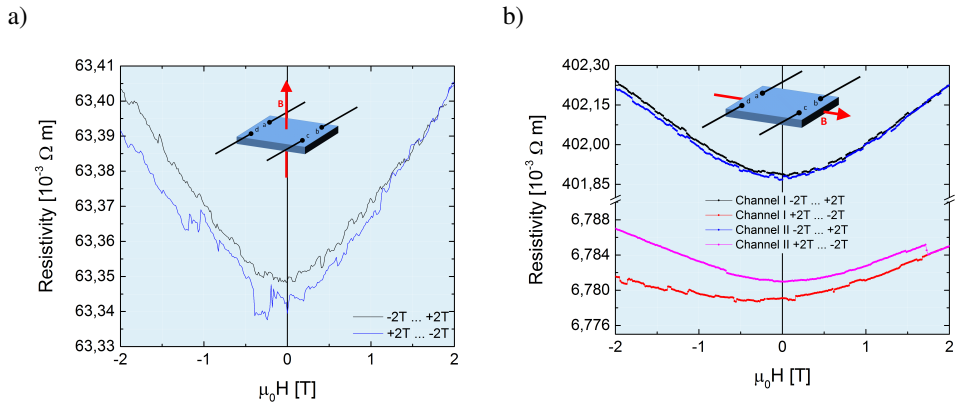


Figure 4.23: Sample 5-01 (reference sample, 5 nm palladium only): Resistivity measurements performed at 10 K according to the van der Pauw method with the magnetic field applied a) out-of-plane and b) in plane. For channel I the current flows between a and b and for channel II it flows between b and c.

To investigate the influence of iron oxide nanoparticles, sample 5-02 is prepared identically to sample 3-01 and subsequently covered with 5 nm palladium by MBE. The corresponding resistivity measurements depicted in figure 4.24 show a Lorentz magnetoresistance effect in the same order of magnitude as it was observed in the reference sample without nanoparticles.

However, in the out-of-plane geometry (a) an additional peak is observed which could be caused by anisotropic magnetoresistance. By applying a magnetic field, the electron clouds about the nuclei are slightly deformed perpendicular to the magnetic field direction. The current flowing in the sample plane is thus less scattered and the resistivity decreases. Upon closer inspection, slight differences in the curve characteristics of channel I and II are visible. This is most probably caused by a preferred superspin orientation that emerges during the plasma treatment (c.f. section 4.3.2). For the in-plane geometry (b), a peak around 0 T is expected for channel II where the current flows perpendicular to the magnetic field, but it is not present. In addition, the LMR effect is less pronounced. This can either be caused by the sample anisotropy mentioned before, or the measurement simply failed. Concerning channel I, an additional dip close to 0 T would be expected for the AMR effect due to the parallel alignment of current and field. However, the measurement is very noisy and the effect is very small. It could thus be present but not visible.

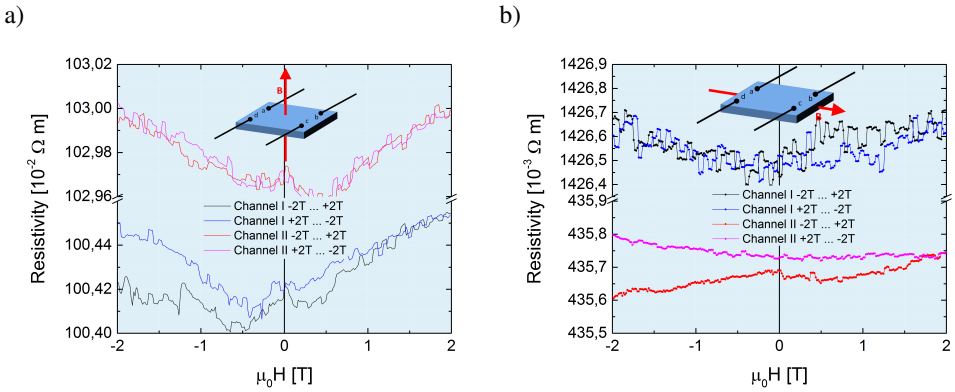


Figure 4.24: Sample 5-02 (NPs + 5 nm palladium): Resistivity measurements performed at 10 K according to the van der Pauw method with the magnetic field applied a) out-of-plane and b) in plane. For channel I the current flows between a and b and for channel II it flows between b and c.

Figure 4.25 shows the temperature dependencies of the resistivity for the sample without (a) and with nanoparticles (b). For the former, a typical metallic behavior can be observed, where the resistivity decreases with decreasing temperatures ($\frac{\Delta R}{\Delta T} = 4 \cdot 10^{-4}$) due to reduced thermal fluctuations. The saturation in the curve at low temperatures is caused by impurities. The small features at 50 K and 200 K are most likely measurement artifacts because they are originate from single outliers.

For the sample that contains nanoparticles this behavior is found as well, but the slope is one order of magnitude smaller ($\frac{\Delta R}{\Delta T} = 1 \cdot 10^{-5}$) and the resistivity at elevated temperatures is also significantly i.e. two orders of magnitude smaller. Furthermore, a huge resistivity increase upon cooling from 180 K to 100 K is observed. This is exactly the temperature region where the nanoparticle blocking is observed (c.f. figure 4.15b). It is therefore assumed, that the Pd polarization cloud around the nanoparticles increases while thermal fluctuations of the nanoparticles are reduced. This leads to increased scattering of the conduction electrons in the palladium close to the NP interface which increases the observed resistivity value. However, this would be an extraordinary effect, because it would originate from extended particles instead of atomic defects.

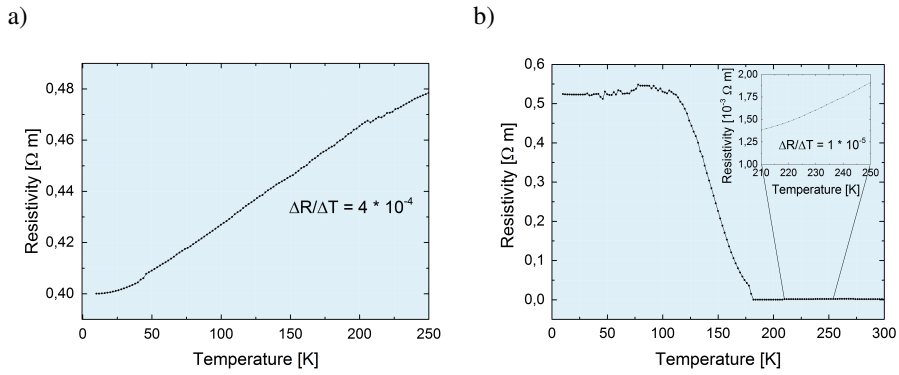


Figure 4.25: Temperature dependency of the resistivity for a) reference sample 5-01 (5 nm palladium only) and b) sample 5-02 (NPs + 5 nm palladium).

To further investigate this effect, another field dependent resistivity measurement is performed. Since one would expect a large magnetoresistance effect in the temperature region where the resistivity value changes significantly, 150 K is chosen as measurement temperature because it corresponds to the inflection point of the curve shown in figure 4.25b. However, the resulting curve shown in figure 4.26 exhibits none of the characteristics found at 10 K, i.e. neither LRM nor AMR is observed. Instead, its shape can be explained by a pure spin disorder magnetoresistance effect (SD-MR). At 150 K the spins of localized Pd d electrons perform thermal fluctuations that cause an inhomogeneous exchange potential from which the itinerant, conducting Pd s electrons are scattered. If a large magnetic field is applied, the d electrons align and the effect is reduced leading to smaller resistivity values. If the temperature is lowered to 10 K, thermal fluctuations and thus the spin disorder magnetoresistance effect decrease to such an extent, that LMR and AMR become visible[6].

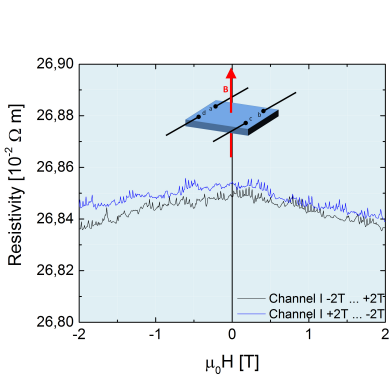


Figure 4.26: Sample 5-02 (NPs + 5 nm palladium): Resistivity measurements performed at 150 K according to the van der Pauw method with the magnetic field applied out-of-plane. The current flows between a and b (channel I).

[6]The measurements shown in figures 4.23a, 4.24a and 4.25 were performed together with T. Moerstedt, c.f. [86].

4.5.2 Measurements on Hall Bar Structures

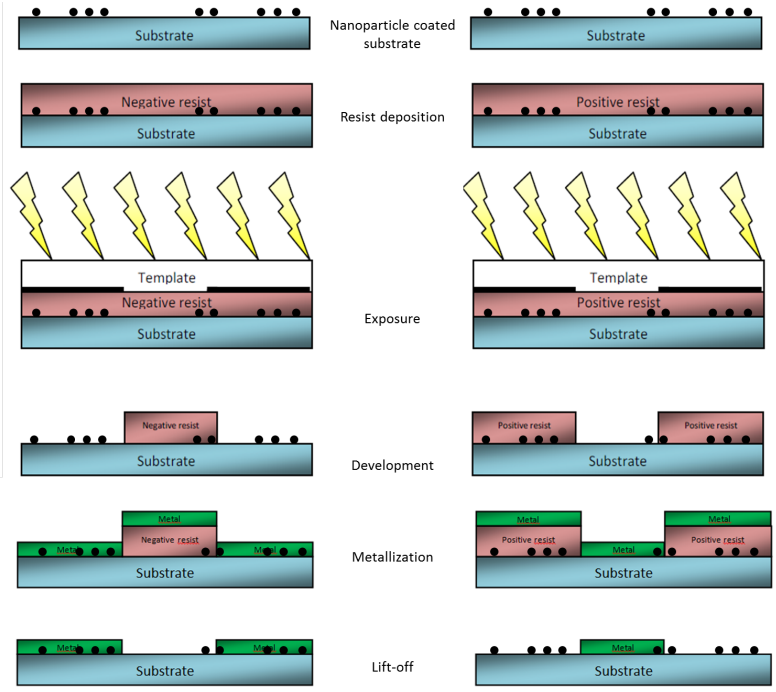


Figure 4.27: Overview on the main steps of lithography using either a positive or negative resist, modified [151].

For a better understanding of the ambiguous field dependencies observed for sample 5-02, another sample (5-03) is prepared where a one dimensional current flow is created. This is realized with a Hall bar structure that is prepared by lithography in cooperation with the Helmholtz Nanoelectronic Facility (HNF). After depositing the nanoparticles and removing their oleic acid shell in the same way as for sample 3-01, a thin palladium structure is defined in a first lithography step. For dehydration, the sample is placed for 90 s on a hotplate at 140°C and subsequently cooled down at room temperature for 60 s. The negative tone resist AZ n-lof 2020 is then applied by spincoating at 4000 rpm for 30 s. Afterwards, the sample is left for 60 s to relax and a soft bake is performed for 60 s on a hotplate at 110°C. Using a 4 SUSS MABA8Gen3 mask aligner, the resist is exposed with 40 mJ/cm^2 in vacuum contact mode. For the post exposure bake, the sample is placed on a hotplate at 110°C for 60 s. Afterwards, the resist is developed in AZ 326 MIF for 45 s and subsequently rinsed in deionized (DI) water (1 min pre-rinse and 3 min clean-rinse). To remove residual resist from the structure, the sample is then oxygen plasma treated for 30 s at 200 W and 200 cm^2 O_2/min. Next, the sample is cut to 1x1 cm^2 and 10 nm palladium are deposited by physical vapor deposition (PVD) using a Pfeiffer PLS 500 system that evaporates the target by an electron beam and exhibits a deposition rate of 0...2 nm/s. The palladium layer thickness had to be increased, because a layer of 5 nm thickness as it is deposited on samples 5-01 / 5-02 / 5-03 would lead to resistivity values in the MΩ region due to

the one dimensional current flow thus disabling measurements using the PPMS system. For the lift-off, the sample is immersed in acetone for 10 min and the metal is removed with a pipette. Rinsing with isopropyl alcohol clears the sample from acetone remains. Finally the sample is rinsed in DI water and blow dried with nitrogen. An overview on the main steps of lithography is provided in figure 4.27.

Figure 4.28 shows the resulting palladium structure. The gold contacts at the sample edge are manufactured in a second lithography step. It begins with dehydration for 90 s on a hotplate at 135°C. After cool down for 60 s at room temperature, the positive tone resist AZ 5214 is deposited by spincoating at 4000 rpm for 30 s. The resist is allowed to relax for 60 s and subsequently soft baked at 90°C for 300 s. Using the 4 SUSS MABA8Gen3 mask aligner again, the sample is exposed by 75 mJ/cm^2 in hard contact mode. Subsequently, it is immersed in AZ 326 MIF for 60 s to develop the resist and afterwards rinsed in DI water (1 min pre-rinse and 3 min clean-rinse). To remove residual resist, the sample is then oxygen plasma treated. First, the reactor is conditioned for 5 min at 200 W and 200 cm^2 O_2/min and afterwards the sample is processed for 15 s at 200 W and 200 cm^2 O_2/min. Due to the poor adherence of gold on the sample, a thin 10 nm titanium sticking layer is deposited before applying the 100 nm gold layer (both using the Pfeiffer PLS 500 system). Subsequently, the sample is immersed in acetone for 10 min to perform the lift-off by carefully removing the metal with a pipette. To remove acetone remains, the sample is then rinsed with isopropyl alcohol, cleaned with DI water and blow dried with nitrogen. Finally, the sample is cut to a size of 2x4 mm^2 to fit into a chip carrier. The sample is then connected to the chip carrier by wire bonding in cooperation with the Peter Grünberg Institute for Semiconductor Nanoelectronics (PGI-9) and mounted in the PPMS system.

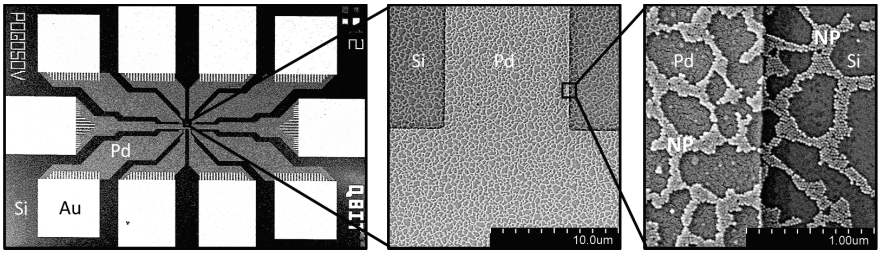


Figure 4.28: Sample 5-03: SEM image of the Hall bar structure manufactured by a two step lithography process. The enlarged section on the right shows that the nanoparticles still remain on the surface, covered by a thin, homogeneous Pd film.

Figure 4.29a shows the field dependency of the resistivity for this sample measured in the out-of-plane geometry. It is expected that the AMR effect observed on sample 5-02 is present and more pronounced. However, only the Lorentz magnetoresistance that was also found for the sample without nanoparticles (c.f. figure 4.23) is visible. The effect is two orders of magnitude smaller than in samples 5-01 and 5-02 which can be caused by the confined sample geometry. Furthermore, the temperature dependency shown in figure 4.29b exhibits no nanoparticle effect as well. Only the typical metallic behavior as it was observed for the reference sample 5-01 is present. A possible explanation for these unexpected characteristics could be remains of the resist that isolate the nanoparticles from the palladium which avoids the polarization and thus suppresses the nanoparticle induced AMR effect.

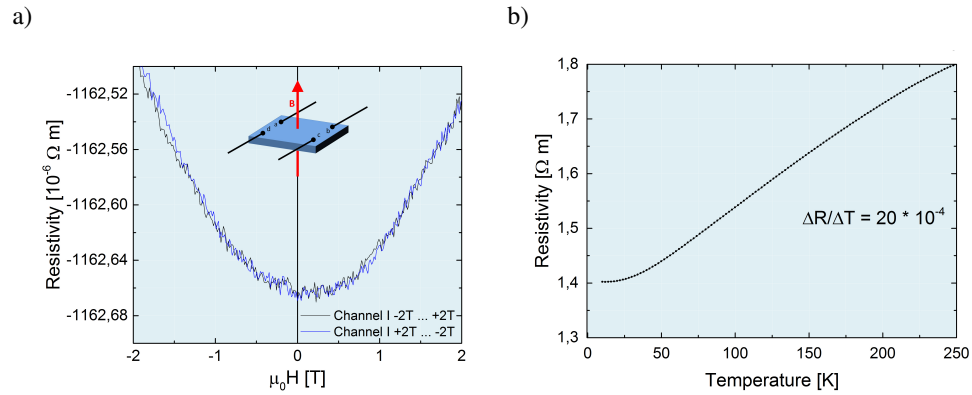


Figure 4.29: Sample 5-03: Magnetic field and temperature dependency of the resistivity for the out-of-plane geometry.

4.5.3 Influence of Nanoparticle Size

For the investigation of the influence of the nanoparticle size, a sample (5-04) is prepared the same way as sample 5-02, but using nanoparticles with a smaller diameter (12.5 nm) that exhibit a blocking temperature of 50 K[7]. Figure 4.30 shows the magnetic field dependency of the resistivity measured at 10 K according to the van der Pauw method in out-of-plane geometry revealing interesting curve characteristics. In addition to the Lorentz magnetoresistance (orange) observed for the other samples as well, a decrease in the resistivity values with increasing field strength (green) can be observed. These characteristics are typical for spin-disorder magnetoresistance, but it is surprising that it is present at 10 K. For sample 5-02 is found only if the measurement temperature was set to 150 K (c.f. figure 4.26). However, sample 5-04 contains smaller nanoparticles that exhibit a lower blocking temperature. Hence, the amount of NP superspin fluctuations at 10 K is larger for sample 5.4. Assuming that these fluctuations influence the fluctuations of localized Pd d electrons in the surrounding matrix, the resistivity would decrease with increasing field strength due to spin alignment as it is observed here. Similar to the effects shown in section 4.5.1 this would be an extraordinary phenomenon since it would originate from extended particles instead of atomic defects though the effect being in the order of magnitude of $\propto 10^{-6}\Omega m$ is comparably small.

Furthermore, a significant dip emerges close to 0 T that exhibits different minima for field changes + $\rightarrow$ - and - $\rightarrow$ +. These characteristics cannot be explained by the magnetoresistance effects summarized in section 2.5.3, because all additional phenomena that could emerge in this system (i.e. AMR, GMR, TMR) would cause a peak and no dip for this geometry. It is possible that the effect is caused by the interaction of the nanoparticles with the matrix material, but for modeling a hypothesis concerning the physical origin, further experiments are necessary.

[7] Batch C2, detailed particle characteristics are provided in section 5.1

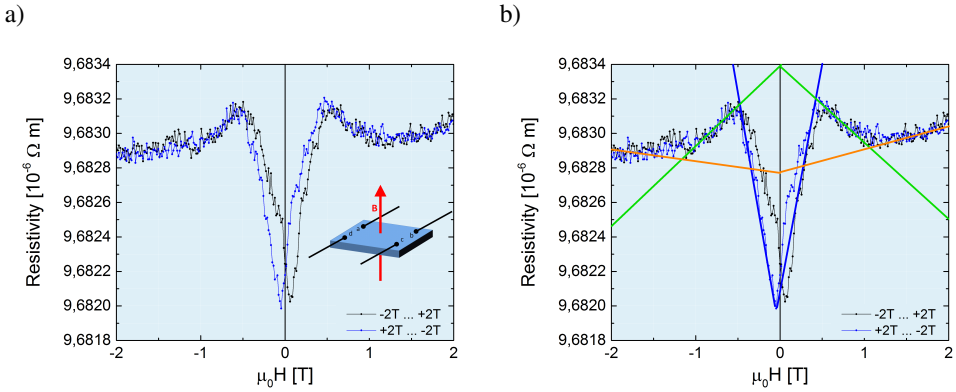


Figure 4.30: Sample 5-04: a) Magnetic field dependency of the resistivity for the out-of-plane geometry. The lines shown in b) are a guide to the eye to highlight the Lorentz (orange), spin disorder (green) and nanoparticle magnetoresistance effect (blue).

Sample No.	NP material / diameter / Batch No.	Substrate	Sample preparation
5-01	No NPs	Silicon	Pd 5 nm MBE
5-02	Iron oxide / 20 nm / 010411	Silicon	$\frac{25}{30}$ mg/ml / 3000 rpm Plasma 30min 300W 200ml/min Pd 5 nm MBE
5-03	Iron oxide / 20 nm / 010411	Silicon	$\frac{25}{30}$ mg/ml / 3000 rpm Plasma 30min 300W 200ml/min Pd 10 nm Lithography
5-04	Iron oxide / 12.5 nm / C2	Silicon	$\frac{25}{30}$ mg/ml / 3000 rpm Plasma 30min 300W 200ml/min Pd 5 nm MBE

Table 4.6: Sample overview for section 4.5: The column "sample preparation" provides information about the concentration of the NP dispersion, the rotational speed during spin coating, the plasma process parameters and the matrix material, thickness and deposition method.

4.6 Conclusion

Within this chapter the magnetic proximity effect via a polarizable matrix has been demonstrated for the first time using oxide nanoparticles. This results in an additional inter-particle interaction besides the regular dipole-dipole interaction, which might enable developments of novel spintronic or functional nanomaterials (e.g. for magnetically controllable optical coatings).

It was demonstrated how to prepare a (sub-)monolayer of iron oxide nanoparticles via spin-coating and how to remove their organic surfactant shell by oxygen plasma treatment. By carefully monitoring the influence of every step when manufacturing the samples, well defined systems have been prepared.

NP/Pt and NP/Pd composite systems were investigated by magnetometry and FORC revealing strong indications for a magnetic proximity effect in both systems. XMCD measurements provided an unambiguous proof for the polarization of the platinum matrix by iron oxide nanoparticles. For the field of spintronics this is an interesting effect and has (to our knowledge) never been demonstrated before. Of all nonmagnetic materials platinum is the one most often used as pure spin current detector. But if it is polarized by maghemite nanoparticles it is no longer suitable.

However, the systems investigated in this chapter contain both, oxides and metals. While the former are often described by the Hubbard model being partly itinerant and partly localized, the latter are usually characterized by the delocalized band structure model. To describe the effects observed in these samples a crossover of both approaches is therefore necessary, though being very speculative.

Considering the electronic density of states (DOS) of bulk maghemite the Pt polarization is a surprising effect. Moreover, it is remarkable that this effect is not observed in the palladium system as well because its electronic (bulk) density of states near the Fermi energy is even higher than for platinum (c.f. figure 4.31). A possible explanation can be found by investigating exchange interactions which are also relevant according to the Stoner criterion $U \cdot D(E_F) > 1$.

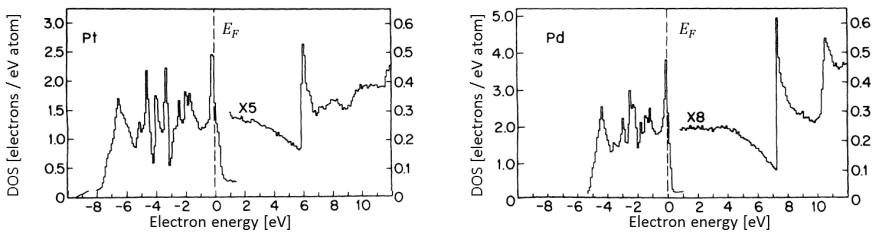


Figure 4.31: Density of states histograms for platinum and palladium, reprinted with permission from [152].

The electron configuration of palladium is [Kr]$4d^{10}$ and its favored oxidation state is +2. The resulting orbital diagrams depicted in figure 4.32a demonstrate that donated electrons originate from the 4d orbital and are oriented antiparallel to the moment of the remaining ion. Oxygen ions usually have the oxidation number -2. Hence, -Pd-O-Pd- bonds can be formed with

O^{2-} ions originating from the maghemite nanoparticles at the interface to the matrix material. According to the superexchange interaction rules (c.f. section 2.2.2) this leads to an antiferromagnetic arrangement of adjacent Pd ions as shown in figure 4.34a.

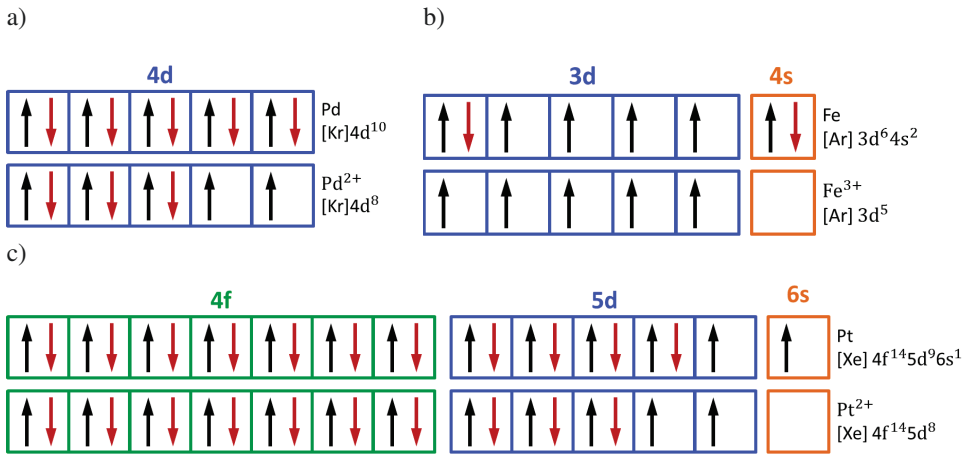


Figure 4.32: Orbital diagrams of a) palladium, b) iron, c) platinum and corresponding ions.

Since maghemite also contains trivalent iron ions, =Fe-O-Pd- bonds can be formed at the nanoparticle surface as well. Iron has the electron configuration $[Ar]3d^64s^2$ which leads to the orbital diagrams shown in figure 4.32b for Fe and Fe^{3+}. It demonstrates that half of the electrons donated from the 4s orbital are oriented parallel to the moment of the remaining ion and half are aligned antiparallel. Hence, in total no contribution to induced ferromagnetism in the Pd matrix is expected. However, electrons originating from the Fe 3d orbital are oriented antiparallel to the moment of the remaining ion. Since electrons originating from the Pd 4d orbital are also antiparallel to the moment of the remaining ion, Fe and Pd are antiparallel to each other in =Fe-O-Pd- bonds as shown in figure 4.34b. Even though this predefines the same mutual alignment between all Fe^{3+} and Pd^{2+} ions in such bonds, most of the induced magnetic moments in the palladium matrix cancel each other out due to the iron ion arrangement inside the maghemite unit cell: eight Fe^{3+} ions occupy tetrahedrally coordinated sites and 13 $\frac{1}{3}$ ions are coordinated octahedrally. Since tetrahedral and octahedral sites are oriented antiparallel to each other, only 5 $\frac{1}{3}$ iron ions per maghemite unit cell contribute to a ferromagnetic alignment of adjacent palladium ions leading to a very small signal. In addition, the matrix material is several nanometers thick to ensure the deposition of a homogeneous layer. The polarization effect on the other hand occurs only within a few atomic layers. Since the XMCD signal intensity decreases with increasing layer thickness [148], it is assumed that the signal (which is very small anyway) is reduced by the overlaying matrix material to such an extent that it is below the detection limit.

Platinum has the favored oxidation states +2 and +4. By calculating the ratio of the XAS intensity measured at the Pt L_3 edge and the intensity in the corresponding XANES region, the amount of Pt^{4+} ions can be estimated [153]. The values obtained from figure 4.33 showing the Pt L_3 XAS data of sample 4-01 without normalization result in a ratio of $\frac{820832}{631019} = 1.3$.

According to M.D. Hall et al. this corresponds to zero Pt^{4+} content [153]. Hence, the oxidation state +2 will be considered only.

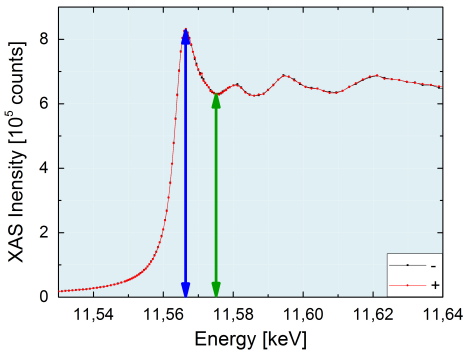


Figure 4.33: Sample 4-01: X-ray absorption spectroscopy measurement without normalization performed at the Pt L_3 edge. The edge intensity is indicated by a blue arrow. The green arrow shows the signal intensity in the XANES region.

Platinum has the electron configuration $[Xe]4f^{14}5d^{9}6s^{1}$ resulting in the orbital diagrams shown in figure 4.32c. While the 6s electrons are extremely mobile and form nearly free electron bands, 5d electrons can be donated and form -Pt-O-Pt- bonds at the nanoparticle interface with oxygen ions originating from the maghemite particles. This results in an antiparallel orientation of adjacent Pt ions (figure 4.34c).

As mentioned before, electrons originating from the Fe 3d orbital are oriented antiparallel to the moment of the remaining ion. Hence, =Fe-O-Pt- bonds with Pt 5d orbitals cause antiferromagnetic alignment (figure 4.34d). Considering the iron ion arrangement in the maghemite unit cell as described above, this can lead to a net magnetic moment in the platinum matrix.

Hence, Pd and Pt seem to be very similar concerning the bonds forming at the NP/matrix interface and the resulting spin arrangement. But Pt also contains a nearly free s electron band with a spin polarization parallel to the semi-localized d band. This could lead to stronger ferromagnetism. On the other hand, the Pt layer is 3 nm thinner than the Pd layer. As mentioned before, the XMCD signal intensity decreases with increasing layer thickness. Hence, it is also possible that the effect is (due to the interface bonds described above) present in both systems to the same extent, but it is not visible in Pd due to the higher matrix thickness.

As complimentary approach for a better understanding of nanoparticle composite systems magnetoresistance was investigated as well. First implications for several interesting effects were found but more measurements are necessary for in depth understanding of the physical origin: a systematic study of the influence of the matrix layer thickness could e.g. demonstrate to what extent the observations originate from an interface effect. In addition, ab initio simulations would be beneficial to find out how much the model assumption deviates from real samples (e.g. because the nanoparticles are not exactly in a monodomain state).

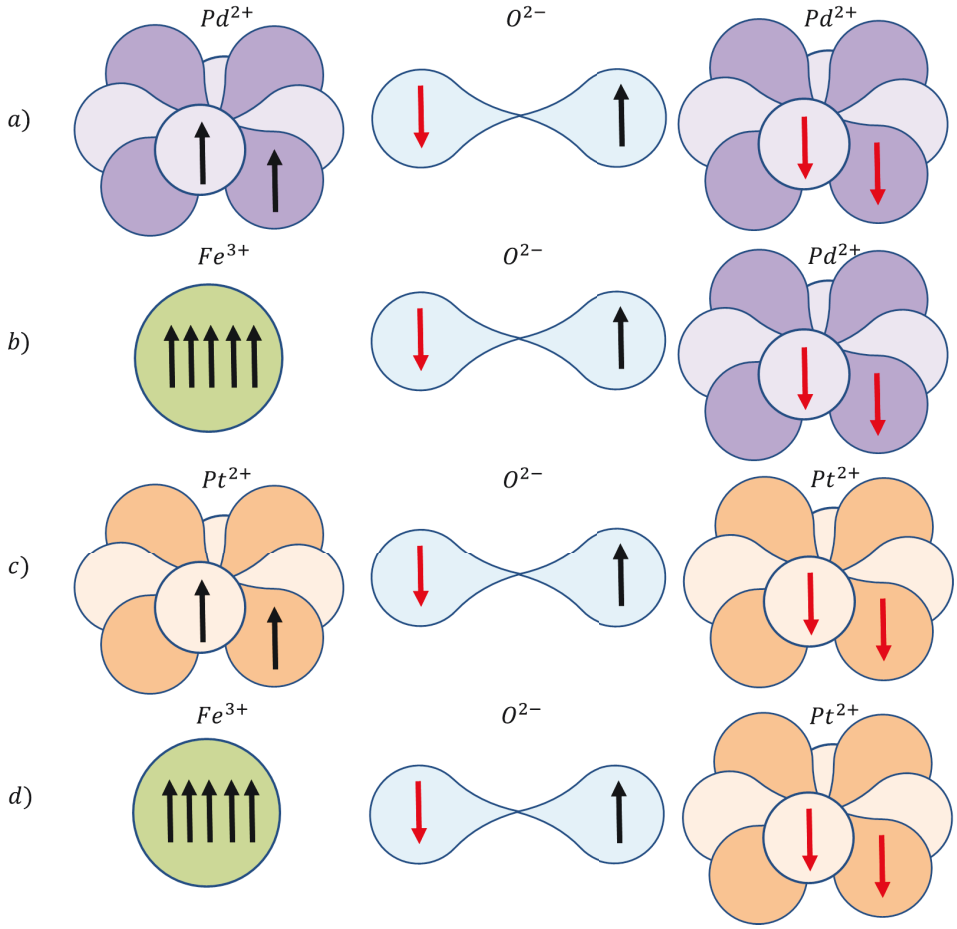


Figure 4.34: Spin arrangement for the a) -Pd-O-Pd- b) =Fe-O-Pd- c) -Pt-O-Pt- and d) =Fe-O-Pt- bond. For Pd and Pt ions only the two relevant d orbitals (one d orbital in a lighter, one in a darker shade) are shown. For the oxygen ions in the middle the relevant p orbital is depicted. Fe^{3+} is spherical symmetric as $3d^5$ ion and therefore depicted as sphere. In a crystal field environment the degeneracy of the od-states is lifted but here the nanoparticle surface is considered where the crystal field has no defined symmetry so that the splitting is not well defined.

5 Three Dimensional Systems

In this chapter it is shown, how the self-assembly of magnetic nanoparticles can be exploited to obtain regular arrangements on length scales of 300...1000 μm. These so-called macrocrystals are analyzed in detail concerning their nanoparticle arrangement, macrocrystal morphology and magnetic properties.

5.1 Nanoparticle Description

For the fabrication of macrocrystals five batches of spherical iron oxide nanoparticles dispersed in toluene were used. Batches C1, C2 and C3 were synthesized according to the process described in [154] by our cooperation partner at the Magnetism and Nano-Bio Technology Center at the University of Hong Kong, department of Electrical and Electronic Engineering in China. To stabilize the dispersions by steric repulsion, C1 and C2 NPs are covered with oleic acid (c.f. section 4.1) and C2 NPs are coated with decanoic acid (figure 5.1). Table 5.1 gives an overview of batch characteristics.



Figure 5.1: Chemical structure of decanoic acid, according to [155].

No.	Manufacturer	Coating	Diameter	Size distribution	Iron oxide phase
C1	Hong Kong University	Oleic acid	10 nm	Polydisperse	Maghemite
C2	Hong Kong University	Oleic acid	12.5 nm	12.0 %	Maghemite
C3	Hong Kong University	Decanoic acid	10 nm	Polydisperse	Maghemite
O1	Ocean NanoTech	Oleic acid	15.6 nm	28.3 %	Maghemite
O2	Ocean NanoTech	Oleic acid	15.6 nm	13.5 %	Maghemite

Table 5.1: Overview of nanoparticle batches used to manufacture macrocrystals.

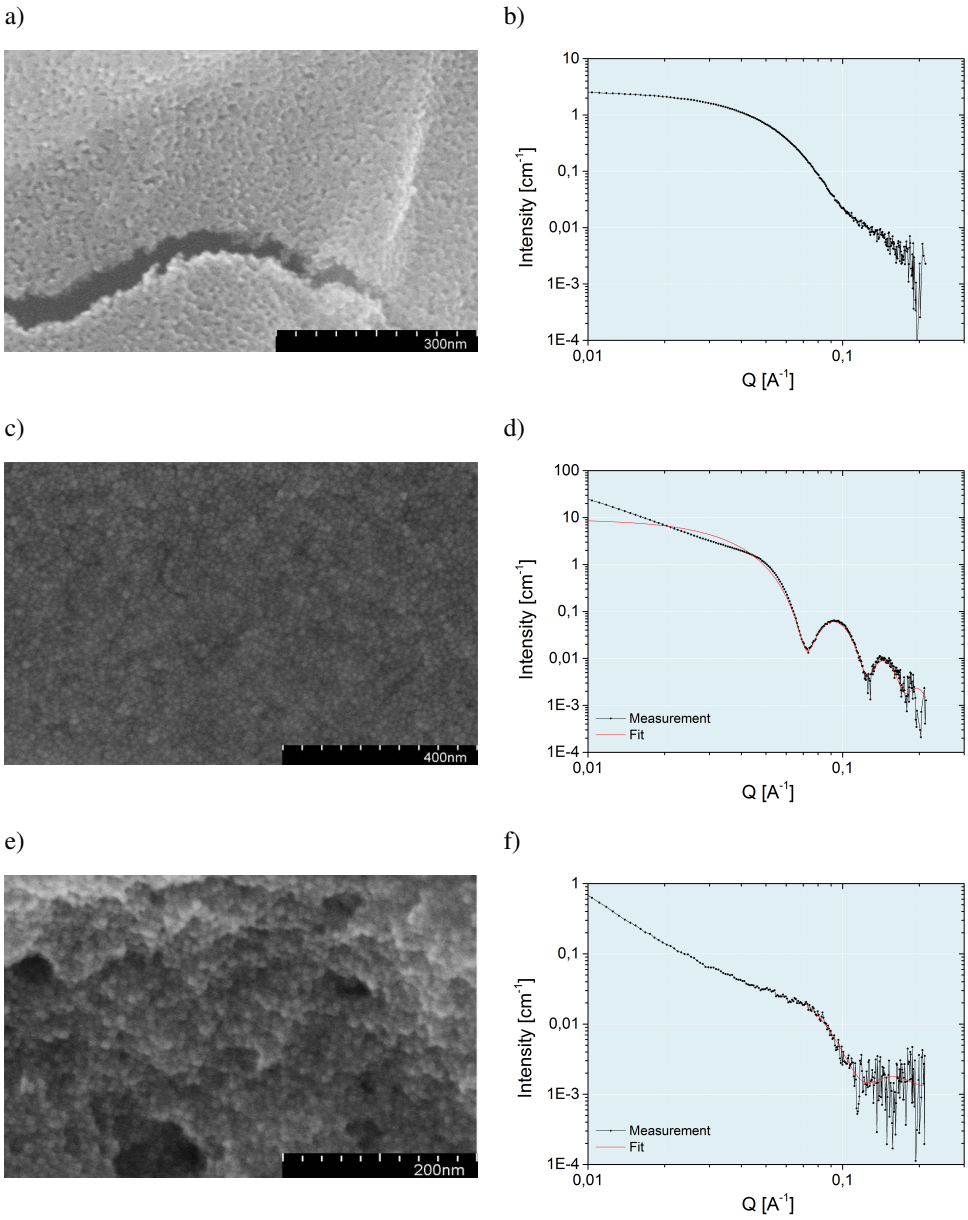


Figure 5.2: SEM images of iron oxide nanoparticles after deposition on a silicon substrate by drop casting, solvent evaporation and oxygen plasma cleaning for a) batch C1, c) batch C2, e) batch C3 and Small Angle X-ray Scattering patterns of 25/30 mg/ml dispersions obtained with GALAXI for b) batch C1, d) batch C2, f) batch C3.

Figures 5.2 a,c,e) show SEM images obtained after depositing 10 μl of 25 mg NP / ml toluene dispersions of batches C1, C2 and C3 on a silicon substrate by drop-casting. At 17 °C the solvent evaporates completely within 30 min and the nanoparticles assemble randomly. To avoid charging effects during imaging, the organic capping agents are previously removed by 5 min oxygen plasma treatment at 300 W with a gas flow of 200 ml/min. The SAXS patterns of dispersions with a nanoparticle concentration of 25/30 mg NP / ml toluene shown in figures 5.2 b,d,f) were measured at the JCNS GALAXI. They reveal that the nanoparticles in C1 and C3 are polydisperse. The average diameter of 10 nm (both batches) is therefore estimated using SEM images. For C2 the average nanoparticle diameter of 12.5 nm with a size distribution of 12 % is determined by SAXS data fitting.

Furthermore, two commercially available batches were used. These oleic acid coated nanoparticles purchased at Ocean Nanotech, LLC (USA) were synthesized by thermolysis, similar to the nanoparticles presented in section 4.1. Figures 5.3 a,c) show SEM images obtained at the surface of macrocrystals manufactured with batch O1 (a) and batch O2 (c) nanoparticles after oxygen plasma cleaning (5 min, 300 W, 200 ml O_2/min). The SAXS patterns of 25/30 mg NP / ml toluene dispersions shown in figures 5.3 b,d) give an average nanoparticle diameter of 15.6 nm for both batches with a size distribution of 28.3 % for O1 and 13.5 % for O2.

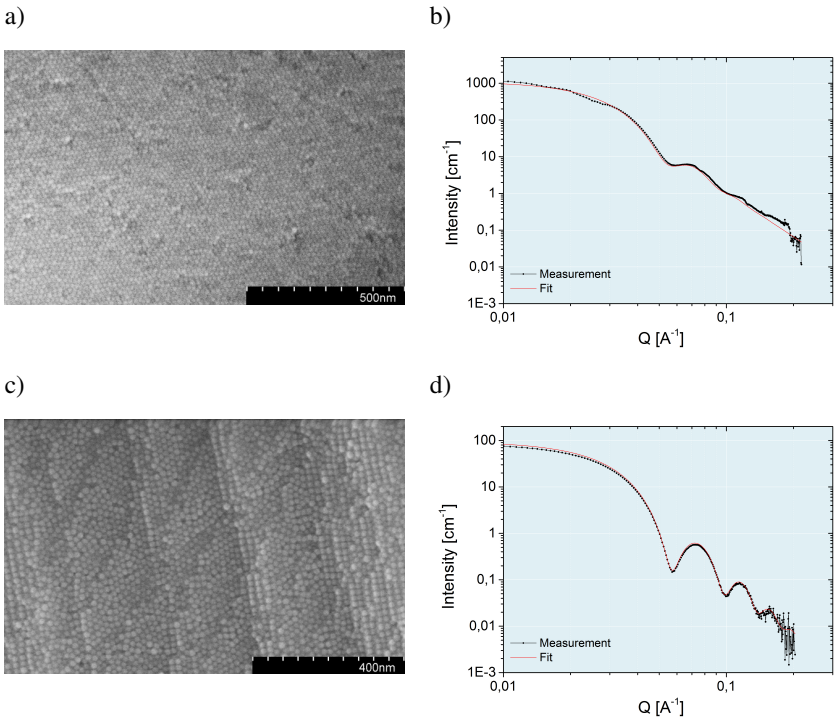


Figure 5.3: SEM images of iron oxide nanoparticles at the surface of macrocrystals for a) batch O1, c) batch O2 and Small Angle X-ray Scattering patterns of 25/30 mg NP / ml toluene dispersions obtained with GALAXI for b) batch O1, d) batch O2.

Figure 5.4 shows the result of X-ray diffraction measurements of the batches C1, C2, and C3, all revealing a spinel structure. To define whether the nanoparticles consist of maghemite, magnetite or both, 10 μl of diluted dispersions (25/30 mg NP / ml toluene) were deposited on 10x10 mm^2 silicon substrates by spincoating (60 s at 3000 rpm) as described in section 4.1. Since the ZFC-FC measurements performed on these samples (figure 5.4) exhibit no Verwey transition, batches C1, C2 and C3 contain pure maghemite nanoparticles. Additionally, the high bifurcation temperatures for batches C1 (325 K) and C3 (225 K) confirm the polydispersity indicated by the corresponding SAXS patterns.

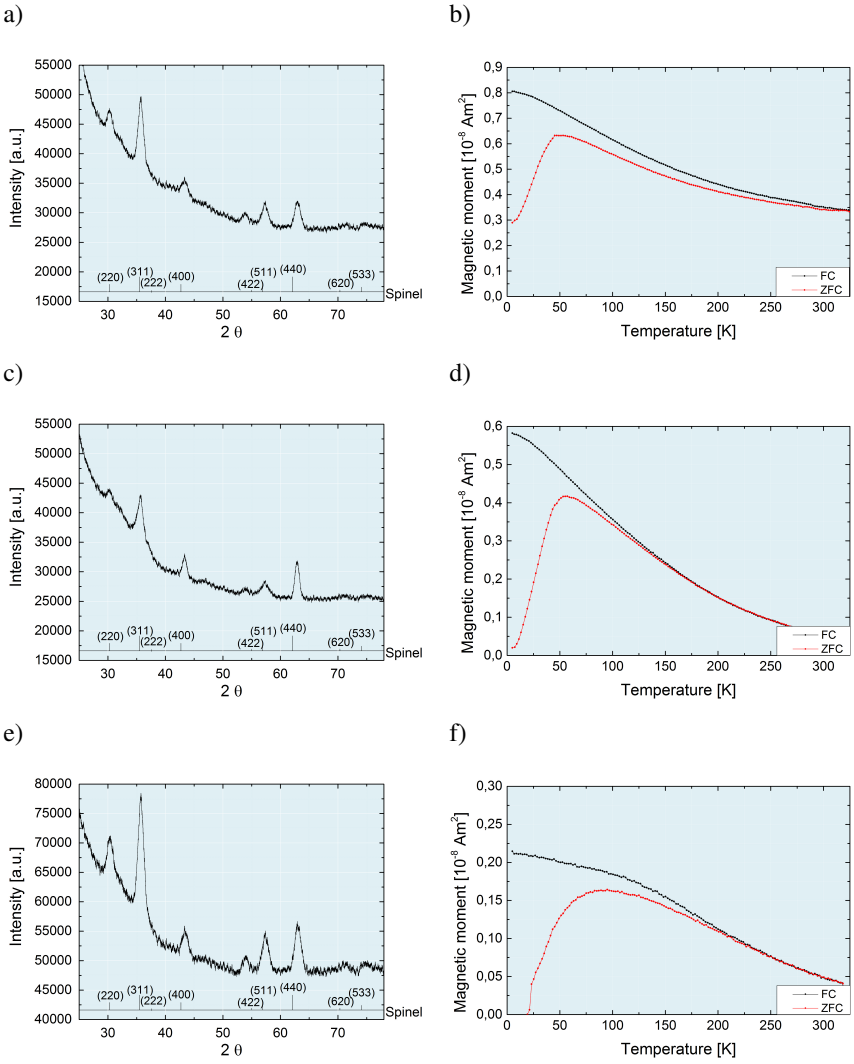


Figure 5.4: X-ray diffraction patterns together with simulated pattern for a spinel structure of a) batch C1, c) batch C2, e) batch C3 and ZFC-FC curves obtained on a nanoparticle (sub-)monolayer deposited on a silicon substrate using b) batch C1, d) batch C2, f) batch C3.

For the commercially available batches O1 and O2, the result of ZFC-FC measurements performed on single macrocrystals is shown in figures 5.5 b,d). Both samples exhibit no Verwey transition, hence the spinel observed in the XRD patterns shown in figures 5.5 a,c) correspond to the maghemite structure. In contrast to the nanoparticles investigated in chapter 4 which were also obtained from Ocean NanoTech, no (antiferromagnetic) wustite component is observed. Hence, the decrease in the FC-curves below the blocking temperature is assigned to dipole-dipole interactions between the nanoparticles. Since this decrease is not present for batches C1, C2 and C3, the inter-particle interactions seem to be stronger in batches O1 and O2. This can e.g. be caused by a smaller oleic acid proportion.

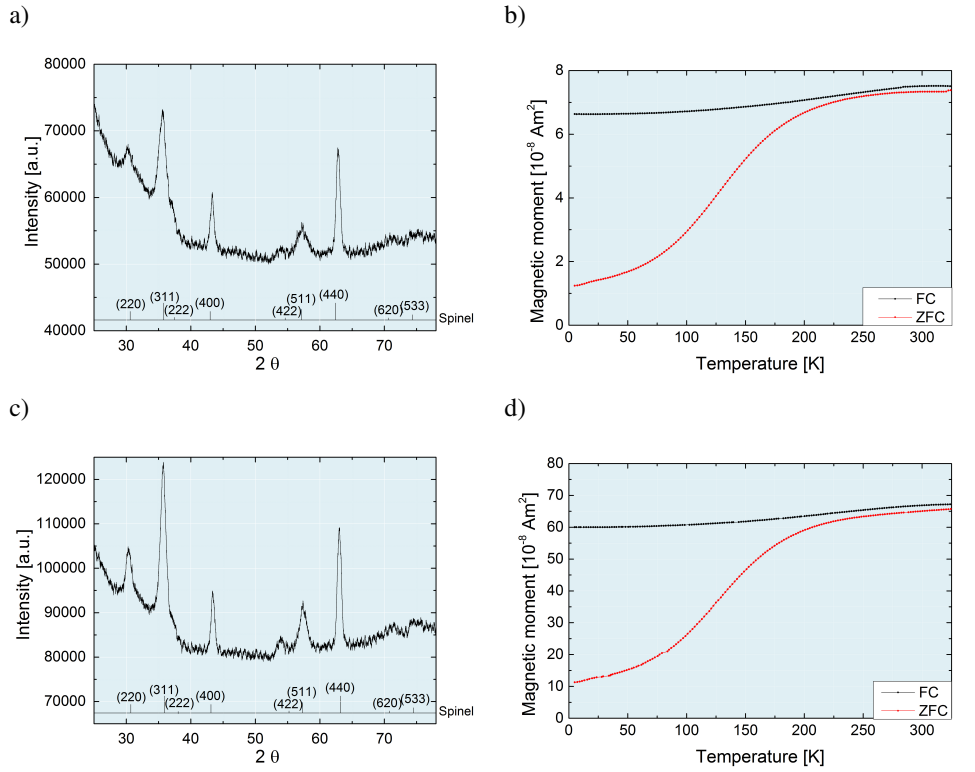


Figure 5.5: X-ray diffraction patterns together with simulated pattern for a spinel structure of a) batch O1, c) batch O2 and ZFC-FC curves obtained on a single macrocrystal consisting of nanoparticles from b) batch O1, d) batch O2.

Figure 5.6 shows hysteresis curves measured at 300 K and 5 K, respectively. For batches C1, C2 and C2 the nanoparticles were deposited on silicon substrates causing a diamagnetic background which had to be removed. The features at ± 4 T in figures 5.6 a,b) are caused by measurement inaccuracies (these were the positions of zero-crossing prior to diamagnetic correction). Similar to the nanoparticles analyzed in chapter 4, all five batches presented in this chapter are superparamagnetic (c.f. section 4.1.2).

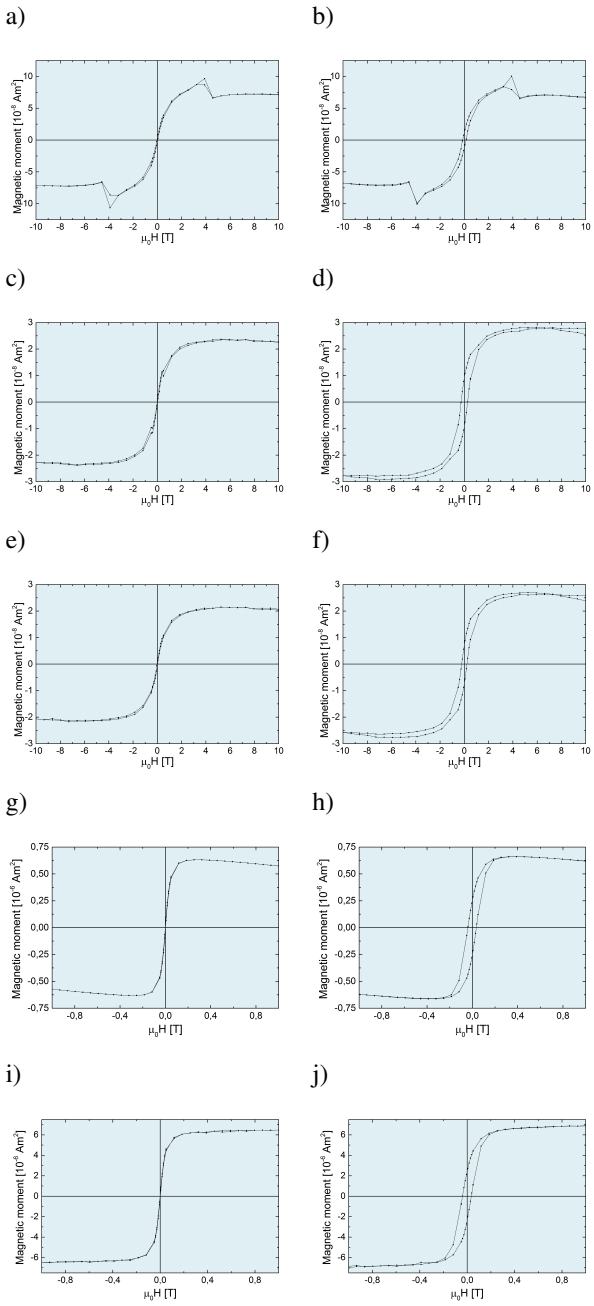


Figure 5.6: Hysteresis curves measured at 300 K (a,c,e,g,i) and 5 K (b,d,f,h,j) for batches C1 (a,b), C2 (c,d), C3 (e,f), O1 (g,h) and O2 (i,j) revealing superparamagnetic behavior.

5.2 Macrocrystal Preparation

For the fabrication of macroscopic nanoparticle assemblies several approaches like drop-casting, spin-coating, centrifugation or making use of the Rosensweig instability are possible. One of the most promising techniques for obtaining regular arrangements with a large coherence length is a centrifuge assisted sedimentation technique. For the investigation of the influence of centrifugation temperature and acceleration, a Thermo Scientific Heraeus Fresco 21 Refrigerated Microcentrifuge is employed.

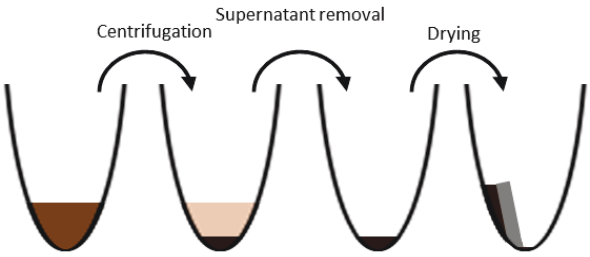


Figure 5.7: Schematic overview of the macrocrystal preparation steps.

First, the nanoparticle concentration is adjusted to 25 mg/ml. 50 μl of the dispersion are then filled into a sample tube and centrifuged for 2 h at 0 °C, 10 °C, 20 °C or 30 °C at an acceleration of 21 000 x g, 20 000 x g, ..., 2 000 x g or 1 000 x g. Due to mass inertia the solvent is separated from the nanoparticles and can be removed using a micro pipette. A 2x10 mm^2 silicon substrate, successively cleaned with ethyl acetate and ethanol in an ultrasonic bath, is then added facing the sample tube wall with the polished side. If it is placed properly, the small gap between the substrate and the sample tube wall is filled with the nanoparticle sediment due to capillary forces. The remaining solvent evaporates mainly at the sample edge, leading to a nanoparticle transport towards the sample edge and macrocrystal formation. After 24 h at 17 °C the sample is sufficiently dry and can be removed. A schematic overview of the preparation steps is depicted in figure 5.7.

For batches O1 and O2, figure 5.8 shows the phase separation after centrifugation at 10 °C for 21 different accelerations. In general, the phase separation for batch O1 (a) is not as good as for batch O2 (b): Since the solvent (toluene) is a clear liquid, the color of the supernatant indicates the amount of remaining (brown) nanoparticles. For O1 samples the supernatant color is just a few shades lighter than the sediment even for the highest acceleration of 21 000 x g. Samples produced with batch O2 on the other hand exhibit an almost clear supernatant down to the lowest acceleration of 1 000 x g. The cause for this effect is the different size dispersion of the batches described in the previous section: The larger (and thus heavier) the nanoparticles are, the faster are they forced to the sample tube bottom. If all the nanoparticles have almost the same size, they sediment more or less simultaneously (batch O2). If the sample also contains a large amount of smaller (thus lighter) nanoparticles, these remain (for the given centrifugation duration and acceleration) in the supernatant resulting in a darker color (batch O1). The samples prepared at a centrifugation temperature of 0 °C, 20 °C or 30 °C show the same behavior, namely sufficient phase separation for batch O1 down to 2 000 x g and good phase separation for batch

O2 for all 21 accelerations tested, even at 1 000 x g. Batches C1, C2 and C3 could not be tested in a similar fashion because of the small amount of material that was available.

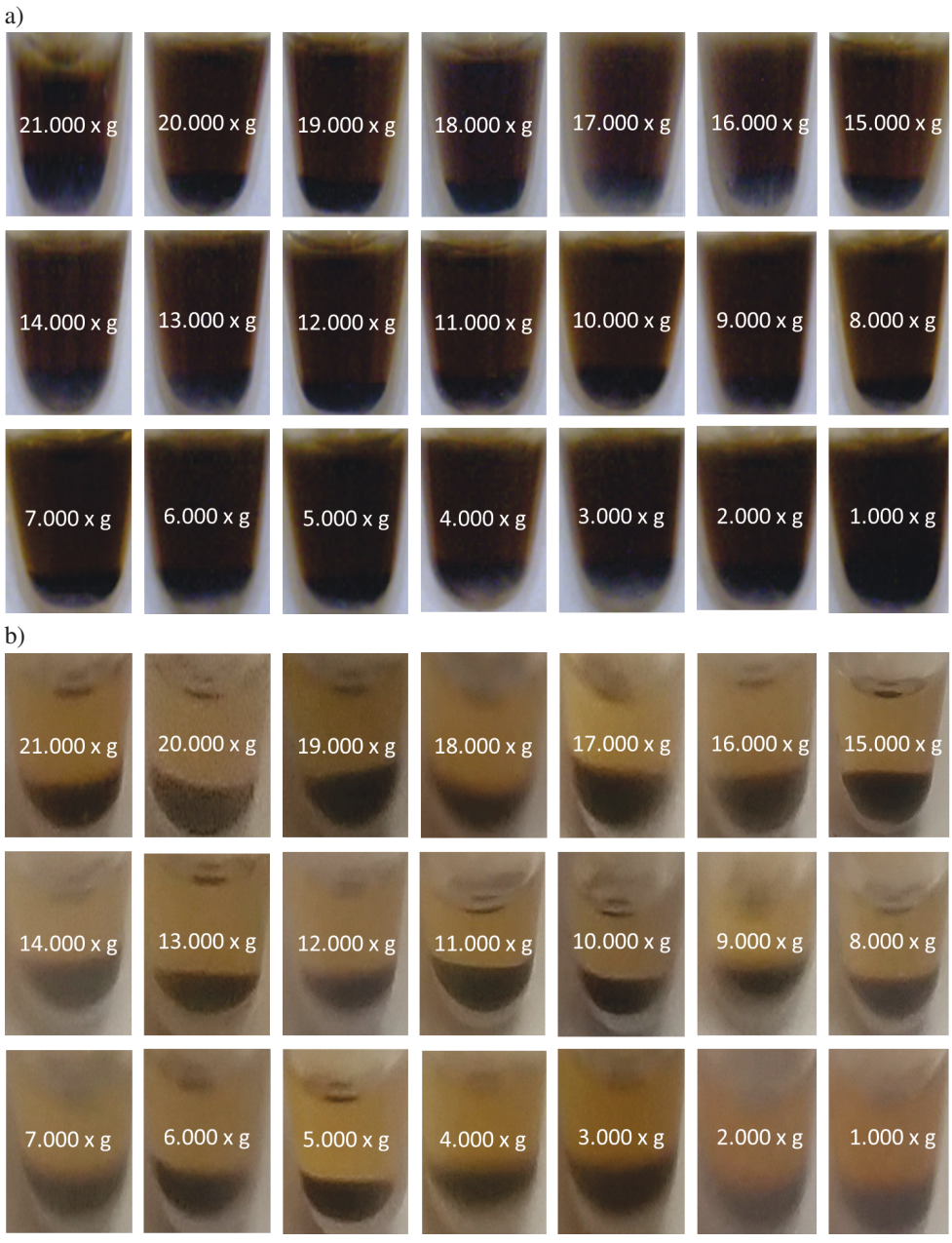


Figure 5.8: Nanoparticle sedimentation after 2 h of centrifugation at 10 °C for different accelerations, a) batch O1, b) batch O2.

5.3 Macrocrystal Morphology

5.3.1 Batch O1

To investigate the influence of the centrifugation acceleration at a temperature of 0 °C, 21 samples were manufactured, starting at 1 000 x g in increments of 1 000 x g up to 21 000 x g using batch O1. Figure 5.9 exemplarily shows an image of the sample prepared at 16 000 x g obtained with an Hitachi SU8000 ultra-high resolution scanning electron microscope (SEM images of all samples are provided in appendix D). The area that was at the bottom of the sample tube while drying is labeled in the picture. It clearly differs from the top, where the largest macrocrystals are found for the majority of the samples. Additionally, many macrocrystals are often formed at the left and right margin of the substrate. This is caused by the drying procedure. As mentioned in the previous section, there is a small gap between the substrate and the sample tube wall due to its curvature. Capillary forces cause the sediment to fill this gap and when the sample is left to dry, the remaining solvent mainly evaporates at the sample edge. It is then replenished by solvent from the interior resulting in an edgeward flow which carries dispersed nanoparticles (c.f coffee ring effect [156]). Hence, only thin nanoparticle layers are found in the center of the sample and macrocrystals form at the edge.

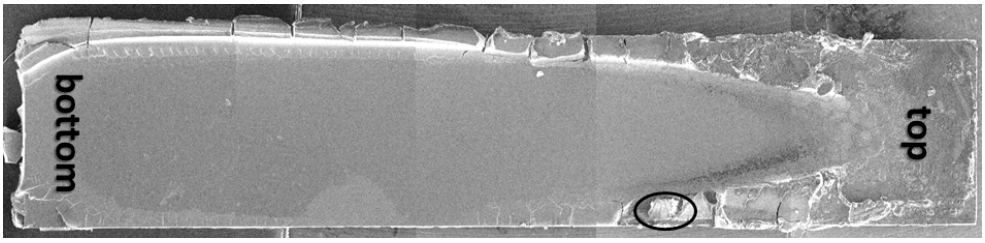


Figure 5.9: SEM image of the macrocrystals on top of a 10x2 mm^2 silicon substrate. The left-hand side of the image shows the sample area that was placed in the sample tube bottom for drying. The encircled area shows a thin macrocrystal (height < 100 μm, see below).

On every sample the amount of macrocrystals is counted according to the following rules: since most of the macrocrystals exhibit a more or less rectangular shape, the shorter side is referred to as width and has to be larger than 100 μm. The other side is defined as length and is used to assign the macrocrystals to one of the following size categories:

- 300 ... 399 μm
- 400 ... 699 μm
- 700 ... 999 μm
- > 1000 μm

Figure 5.10 shows the number of macrocrystals counted per size category for all the samples prepared at 0 °C. The most frequent size category is 400 ... 699 μm (comprising 52 % of the macrocrystals) and macrocrystals with a length in the order of mm are found from 11 000 x g upwards.

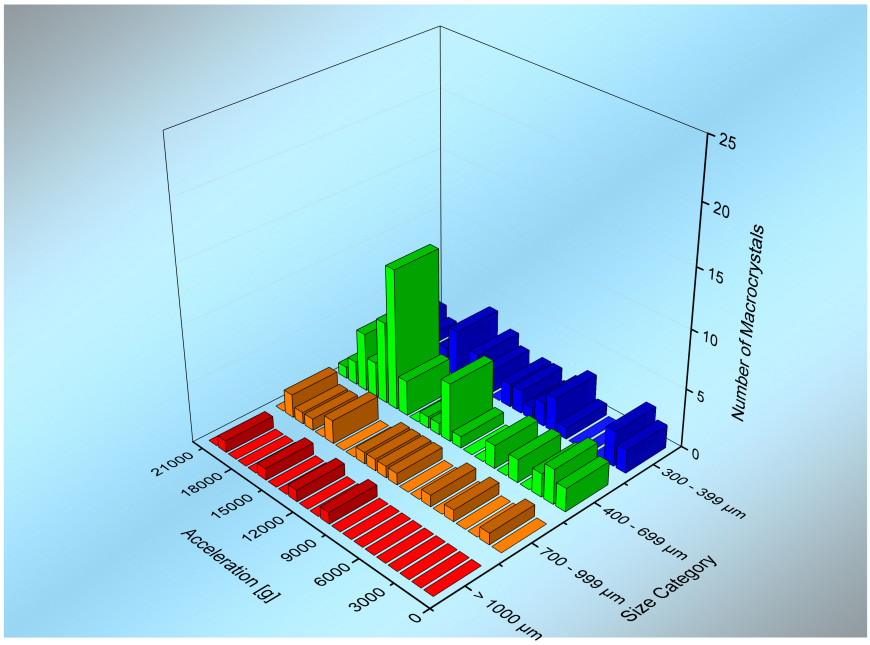


Figure 5.10: Number of macrocrystals per size category for all 21 samples prepared at a centrifugation temperature of 0 °C.

For handling, the macrocrystal shape is also a very important aspect. If it exhibits a small width, it can easily break when transferring it to a measurement device. If it is too thin, removing it from the substrate is also very difficult. Hence, every single macrocrystal is assigned to one of the following shape categories:

- A : height > 100 μm, width > 200 μm
- B : height > 100 μm, width < 200 μm
- C : height < 100 μm

In line with the definition of a weighed average a score value S is then defined for data reduction. Since shape category A is the best and C is the worst for handling the macrocrystals, S is calculated according to the following equation for every size category on each sample:

$$S = \frac{N_A \cdot 3 + N_B \cdot 2 + N_C \cdot 1}{6}. \tag{5.1}$$

N gives the number of macrocrystals that are assigned to the respective shape category. Figure 5.11 shows the result for the 21 samples prepared at 0°C. The dot color gives the size category and its diameter is proportional to the score value S. This type of graph has been chosen to provide a better overview on the number and size as well as the morphology of macrocrystals found on every sample.

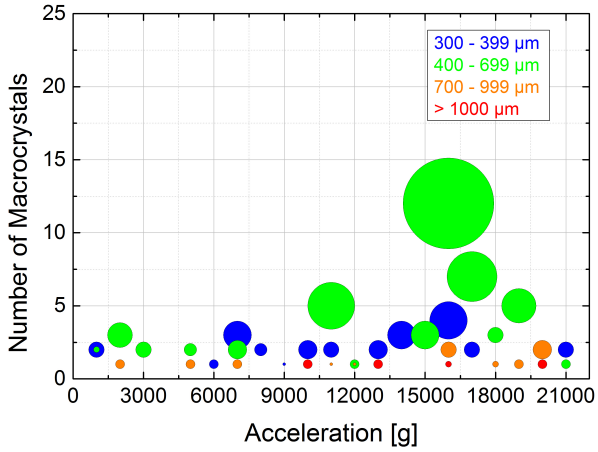


Figure 5.11: Number of macrocrystals per size category for all samples centrifuged at 0°C, where the dot diameter is proportional to the score value S.

Furthermore, an average quality factor Q is defined to assign a single value to every sample and thus facilitate the analysis of the influence of the parameter variation. This is again in line with the definition of the weighed average:

$$Q = \frac{S_{300...399} \cdot 3 + S_{400...699} \cdot 4 + S_{700...999} \cdot 7 + S_{>1000} \cdot 10}{24} \tag{5.2}$$

S is the score value of the respective size category. The chosen weights are related to the smallest macrocrystal length of the size category described by the corresponding score value. Figure 5.12 shows the result, indicating that the overall quality is more or less independent of the centrifugation acceleration. Except for the outlier at 16 000 x g, all values are relatively close to the linear fit that increases only very slightly.

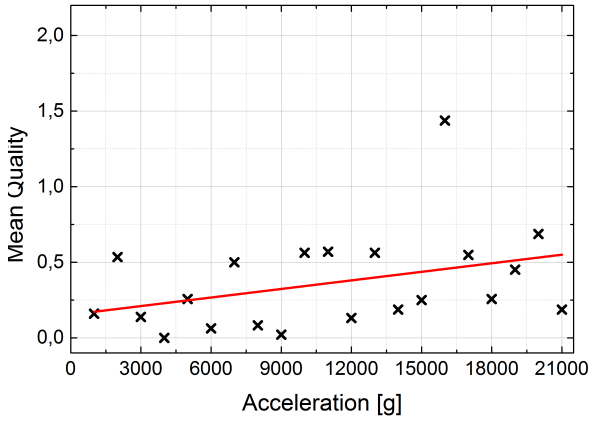


Figure 5.12: Quality factor for all samples centrifuged at 0°C (black) including a linear fit (red).

To validate these results, all 21 samples were reproduced. Figure 5.13a demonstrates, that the size category 400...699 μm is again the most frequent one (52 %). Macrocrystals with a length larger than 700 μm are also preferably found at elevated accelerations though their total amount is smaller. If the score values are included as shown in figure 5.13b, the pattern is very similar to the one found for the first samples (c.f. figure 5.11). The linear fit to the quality factor values and their dispersion around this line is also comparable to the first run as shown in figure 5.13c. The best sample was again centrifuged at an acceleration of 16 000 x g and exhibits the largest deviation from the fit as well. The arithmetic averages of the mean quality factors are 0.36 and 0.32. Hence, the presented results are considered to be reproducible.

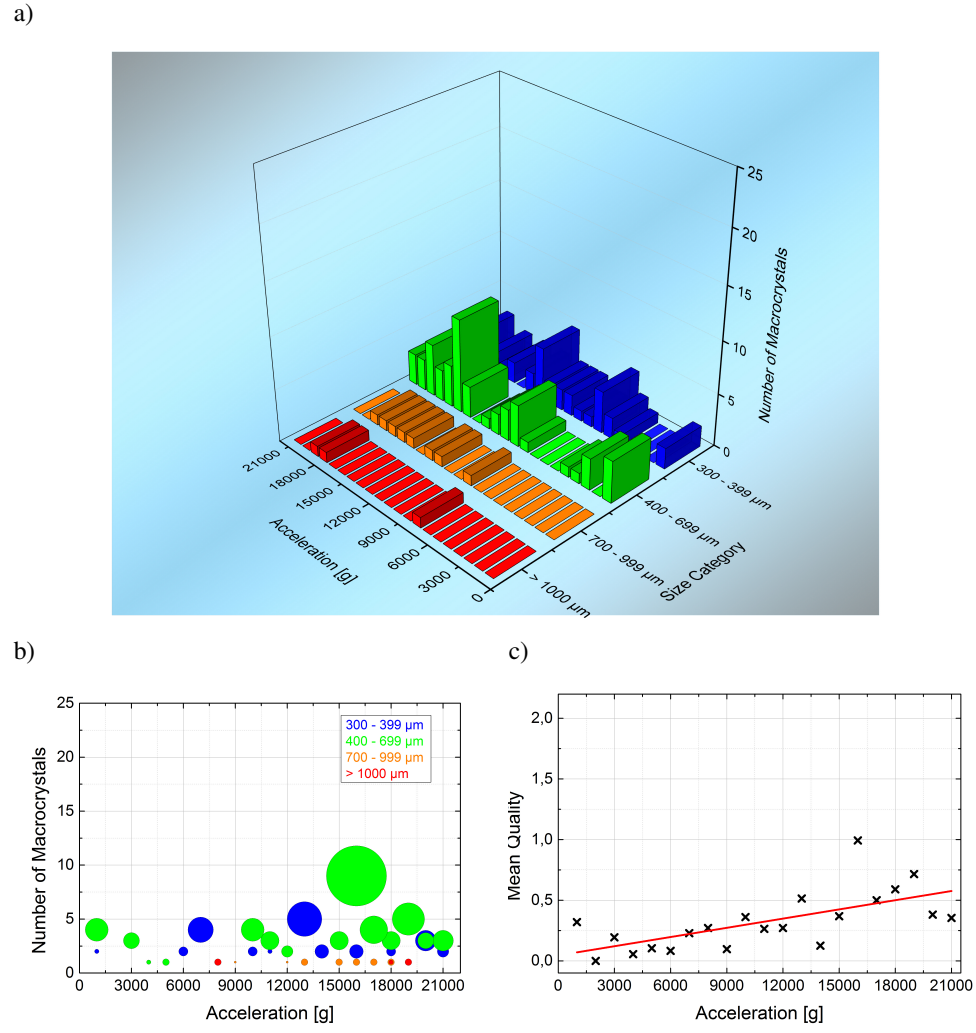


Figure 5.13: Number of macrocrystals per size category for the reproduced samples at a centrifugation temperature of 0°C a) without and b) with illustration of the score value S which corresponds to the dot size. c) Quality factor (black) and linear fit (red).

For the investigation of the influence of the centrifugation temperature, 21 samples were manufactured with the same acceleration values but at 10°C. This was also done twice to check for reproducibility. Figures 5.14a,c,e show the results for the first and figures 5.14b,d,f for the second run. In both cases the most frequent size category is 300...399 μm (59 % and 46 %, respectively) which is smaller than for the samples centrifuged at 0°C.

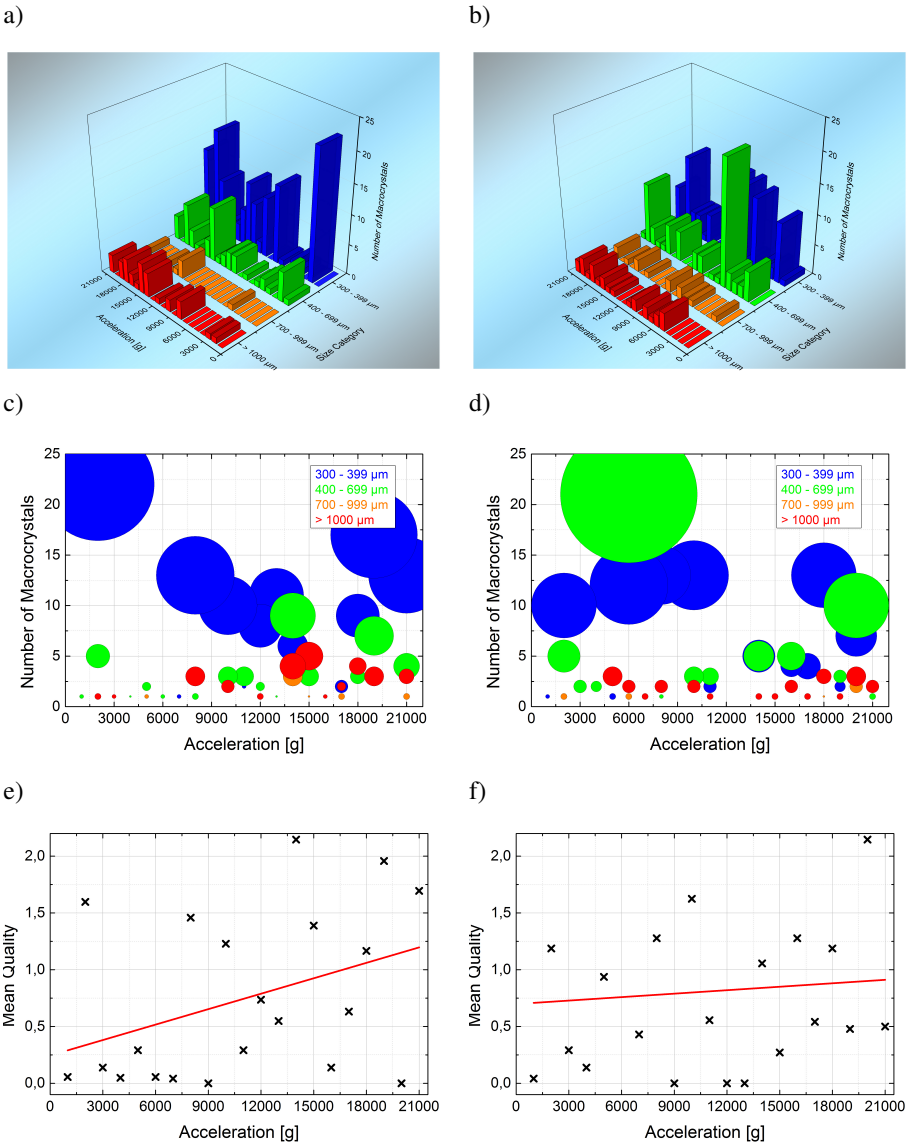


Figure 5.14: Number of macrocrystals per size category for all 21 samples centrifuged at 10°C a) without and c) with illustration of the score value S which corresponds to the dot size. e) Quality factor (black) and linear fit (red). b), d) and f) correspond to the reproduced samples.

However, huge macrocrystals longer than 1000 μm can be found at 2 000 x g and 5 000 x g already, which is a significantly slower acceleration than for the 0°C samples. Additionally, the total amount of macrocrystals longer than 1000 μm counted on all 21 samples of a run (21 different accelerations) is much larger: 30 and 25, respectively, counted for the samples centrifuged at 0°C, 4 and 3 at 10°C (figures 5.14a,b). When taking the score value into account (figure 5.14c,d)) which is assigned to the size categories, a significantly better macrocrystal morphology compared to the 0°C samples can be observed for all size categories. The quality factors for whole samples depicted in figures 5.14e,f exhibit a greater spread around the fit but the arithmetic average of 0.74 and 0.81 for the two runs at 10°C is significantly higher than for the 0°C samples.

If the samples are centrifuged at 20°C, 48% or 46% of the macrocrystals are 400...699 μm long (figures 5.15a,b). This size category also is the most frequent one at 0°C. The amount of macrocrystals > 1000 μm is very low (2 and 1, respectively, counted on 21 samples) and they are found at 6 000 x g, 11 000 x g and 18 000 x g. The score values of the size categories at different accelerations are comparable to those found at 0°C though they are a little bit higher (figures 5.15c,d). Concerning the quality factors shown in figures 5.15e,f the values scatter less than the 10°C samples and more than the 0°C samples around the linear fit. In contrast to all the sample runs presented so far, the fit slightly decreases with increasing acceleration. However, since the slope is very small, it is assumed to be negligible thus demonstrating that the macrocrystal quality is independent of the centrifugation acceleration at 20°C.

For the samples centrifuged at 30°C, most macrocrystals can be assigned to the size category 300...399 μm (71% and 61%, respectively) which is the same as for the 10°C samples (figures 5.16a,b). However, only one macrocrystal > 1000 μm can be found per run (at 18 000 x g and 11 000 x g, respectively). The score values are comparable to those found at 20°C (figures 5.16c,d) and the quality factors exhibit small deviations from the fit curve with an arithmetic average value of 0.23 and 0.33, respectively. An overview of the most important data is given in table 5.2 for all 8 runs prepared using batch O1 (respectively comprising 21 samples centrifuged at the same temperature but at different accelerations).

In summary, it can be ascertained that among the tested values - concerning the macrocrystal morphology - the best centrifugation temperature is 10°C. Even though many macrocrystals in the smallest size category are found, samples centrifuged at this temperature also contain the largest amount of macrocrystals belonging to the largest size category. In addition, the score values are by far the best for all size categories. The quality factors are widely scattered around the linear fit, but the arithmetic average is at least twice the values found for the runs at all other temperatures. The cause for these observations could be the oleic acid coating of the nanoparticles. This chemical has a melting temperature of 16.3°C [157] thus being frozen after centrifugation at 10°C. If the samples are then stored at 17°C during the drying process, the oleic acid partly melts thus allowing the nanoparticles only to arrange very slowly thus forming many huge macrocrystals with a rectangular shape. However, the drying temperature is very close to the melting point. So, if the samples are centrifuged at 0°C, heating up and melting is not sufficient to allow for the right amount of nanoparticle movement before all the solvent is evaporated. Hereby it should be kept in mind, that the oleic acid forms a thin, two dimensional shell around the nanoparticles. The freezing and melting can therefore not be compared to the bulk process. Nevertheless, the temperature influences the flexibility of the oleic acid molecules and thus the steric stabilization to a sufficient extent to either favor or disfavor the formation of

macrocrystals. For samples centrifuged at 20°C and 30°C the freezing and melting procedure is not initiated thus leading to worse samples concerning the macrocrystal morphology.

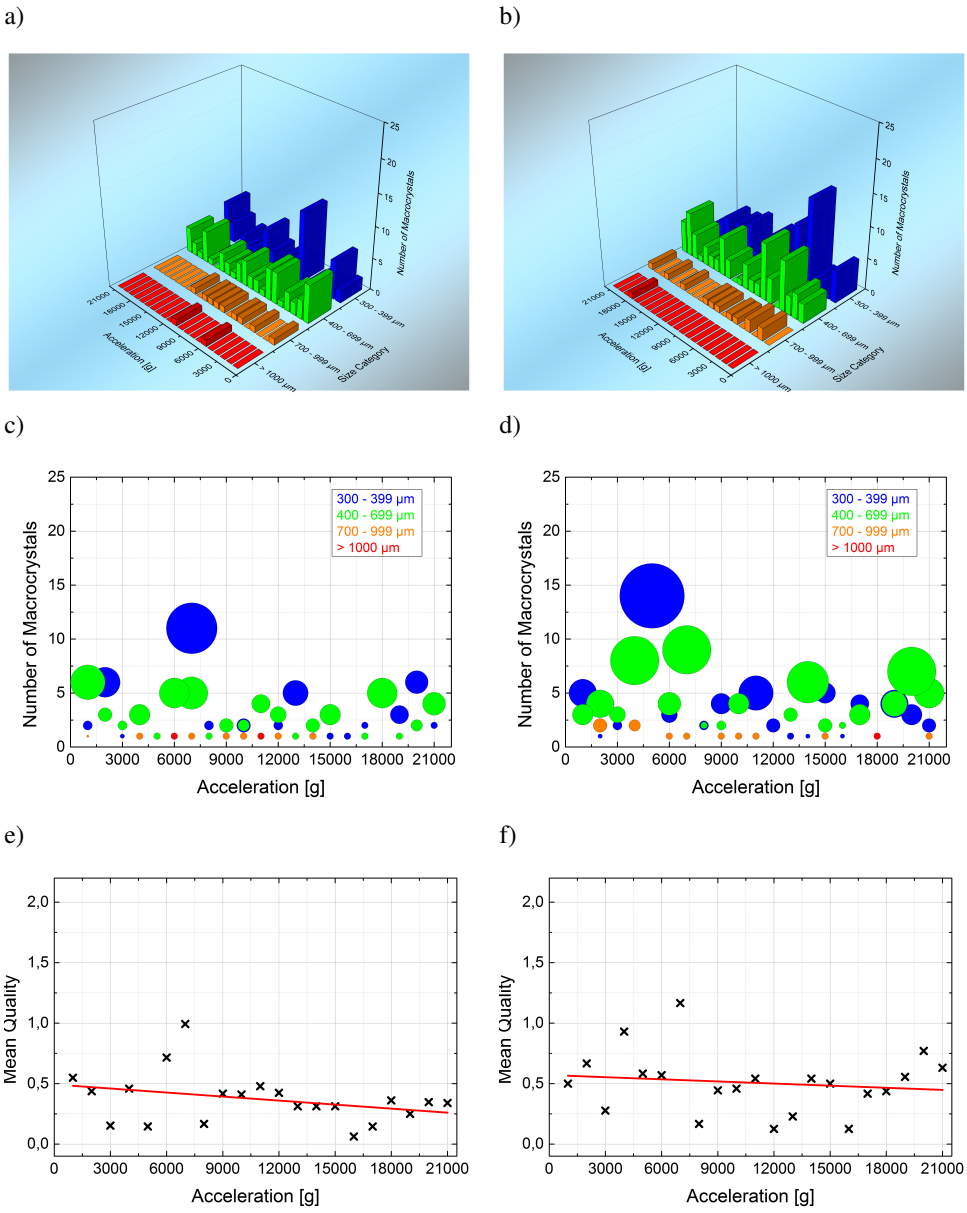


Figure 5.15: Number of macrocrystals per size category for all 21 samples centrifuged at 20°C a) without and c) with illustration of the score value S which corresponds to the dot size. e) Quality factor (black) and linear fit (red). b), d) and f) correspond to the reproduced samples.

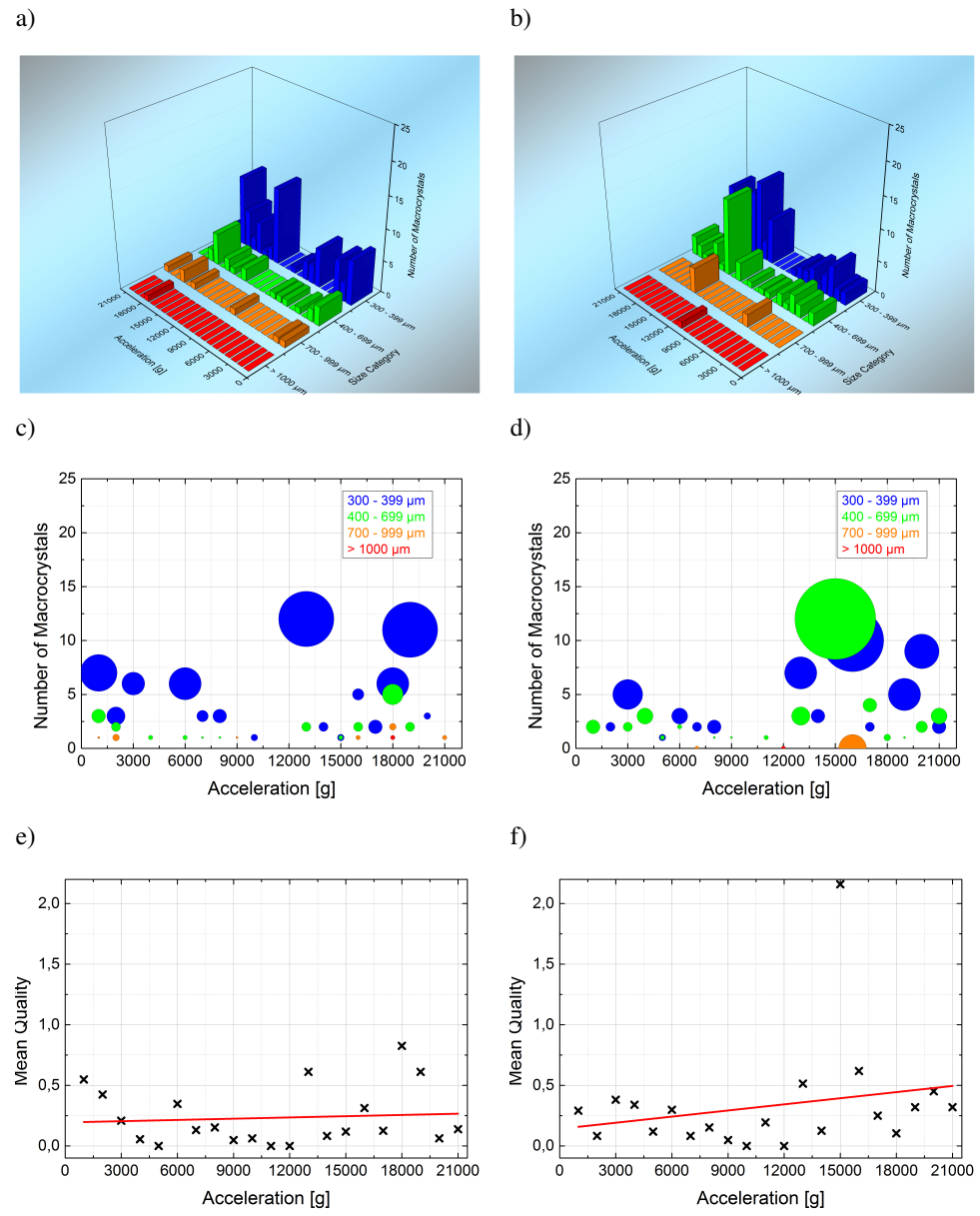


Figure 5.16: Number of macrocrystals per size category for all 21 samples centrifuged at 30°C a) without and c) with illustration of the score value S which corresponds to the dot size. e) Quality factor (black) and linear fit (red). b), d) and f) correspond to the reproduced samples.

T	Most frequent size category	a_{min}	a_{best}	M
0°C	400...699 μm	11 000 x g	16 000 x g	0.36
0°C	400...699 μm	8 000 x g	16 000 x g	0.32
10°C	300...399 μm	2 000 x g	14 000 x g	0.74
10°C	300...399 μm	5 000 x g	20 000 x g	0.81
20°C	400...699 μm	6 000 x g	7 000 x g	0.37
20°C	400...699 μm	18 000 x g	7 000 x g	0.50
30°C	300...399 μm	18 000 x g	8 000 x g	0.23
30°C	300...399 μm	11 000 x g	15 000 x g	0.33

Table 5.2: Overview of sample characteristics at different centrifugation temperatures T, where a_{min} is the minimum acceleration to find macrocrystals longer than 1000 μm, a_{best} is the acceleration of the best sample according to the mean quality factor and M is the arithmetic average of the mean quality values for all samples centrifuged at a specific temperature.

5.3.2 Batch O2

Using batch O2, further samples were manufactured to analyze the influence of the nanoparticle size dispersion on the macrocrystal morphology. Again, all samples were prepared twice to check for reproducibility. The results for the samples centrifuged at 10°C are shown in figure 5.18: The most frequent size category is 300...399 μm (62 % or 64 %) as it was found for batch O1. Considering the first 21 samples, huge macrocrystals > 1000 μm can be found at very low accelerations (4 000 x g) already, what is similar to batch O1. But for the reproduced samples, macrocrystals that can be assigned to the largest size category are found at elevated accelerations (15 000 x g and 16 000 x g) only. However, at low accelerations significantly more small macrocrystals are found. It is thus assumed, that huge macrocrystals form on these samples, too, but that they break into smaller pieces due to mechanical stress when the substrate is removed from the sample tube after drying. This is exemplarily shown in figure 5.17 for the sample centrifuged at 10 000 x g.

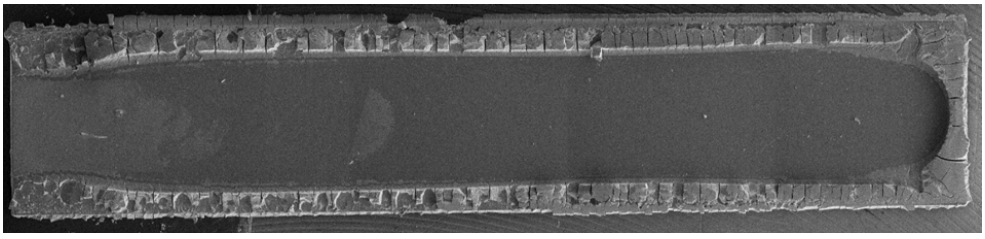


Figure 5.17: SEM image of the macrocrystals on top of a 10x2 mm^2 silicon substrate demonstrating how huge macrocrystals at the sample edge break into many small pieces. The left-hand side of the image shows the sample area that was placed in the sample tube bottom for drying. The nanoparticle dispersion used to prepare this sample was centrifuged at 10 000 x g.

The score values assigned to the size categories demonstrated by the dot size in figures 5.18c,d are comparable to those found for batch O1 at 10°C. Concerning the mean quality also a slight increase with increasing acceleration can be observed for the first samples. For the reproduced samples the quality factor is more or less constant which is caused by the missing macrocrystals > 1000 μm at low accelerations due to fracturing. Except for three outliers, the values scatter

very little around the linear fit and the best sample is observed at 16 000 x and 11 000 x g, respectively. The arithmetic average of the quality factor values is 0.62 or 0.64, which is slightly lower than for the 10°C samples prepared using batch O1.

Next, 2 x 21 samples were prepared at a centrifugation temperature of 20°C to analyze whether they are as similar to those manufactured using batch O1 as it was found at 10°C. Figures 5.19a,b show that the most frequent size category is 300...399 μm, which is smaller than for batch O1. Simultaneously, significantly more (small) macrocrystals are counted for batch O2. Huge macrocrystals > 1000μm are preferably found at low accelerations (up to 5 000 x g or 8 000 x g for the first and reproduced samples, respectively) which is not observed for batch O1. Concerning the score values shown in figures 5.19c,d the results - especially for small macrocrystals - are comparable to those obtained at 10°C which means significantly larger values than those found for the 20°C samples manufactured using batch O1. That is also reflected in figures 5.19e,f where the mean qualities for all samples centrifuged at 20°C are shown. The values scatter a little more than it was found using batch O1. However, the linear fit slightly decreases with increasing acceleration, which is the first and only aspect that the samples prepared using batch O2 have in common with the samples prepared using batch O1 at 20°C.

In summary, it can be ascertained, that all results are reproducible, independent of nanoparticle size dispersion and centrifugation temperature. The macrocrystal number, size and morphology in dependency of the centrifugation acceleration obtained at 10°C is similar for batches with different size dispersions. However, at 20°C, which is above the melting temperature of oleic acid, completely different results are obtained if the size dispersion is varied. Table 5.3 gives an overview on the most important features of the samples prepared using batch O2.

T	Most frequent size category	a_{min}	a_{best}	M
10°C	300...399 μm	4 000 x g	16 000 x g	0.62
10°C	300...399 μm	15 000 x g	11 000 x g	0.64
20°C	300...399 μm	2 000 x g	10 000 x g	0.72
20°C	300...399 μm	2 000 x g	10 000 x g	0.56

Table 5.3: Overview of sample characteristics at different centrifugation temperatures T, where a_{min} is the minimum acceleration to find macrocrystals longer than 1000 μm, a_{best} is the acceleration of the best sample according to the mean quality factor and M is the arithmetic average of the mean quality values for all samples centrifuged at a specific temperature.

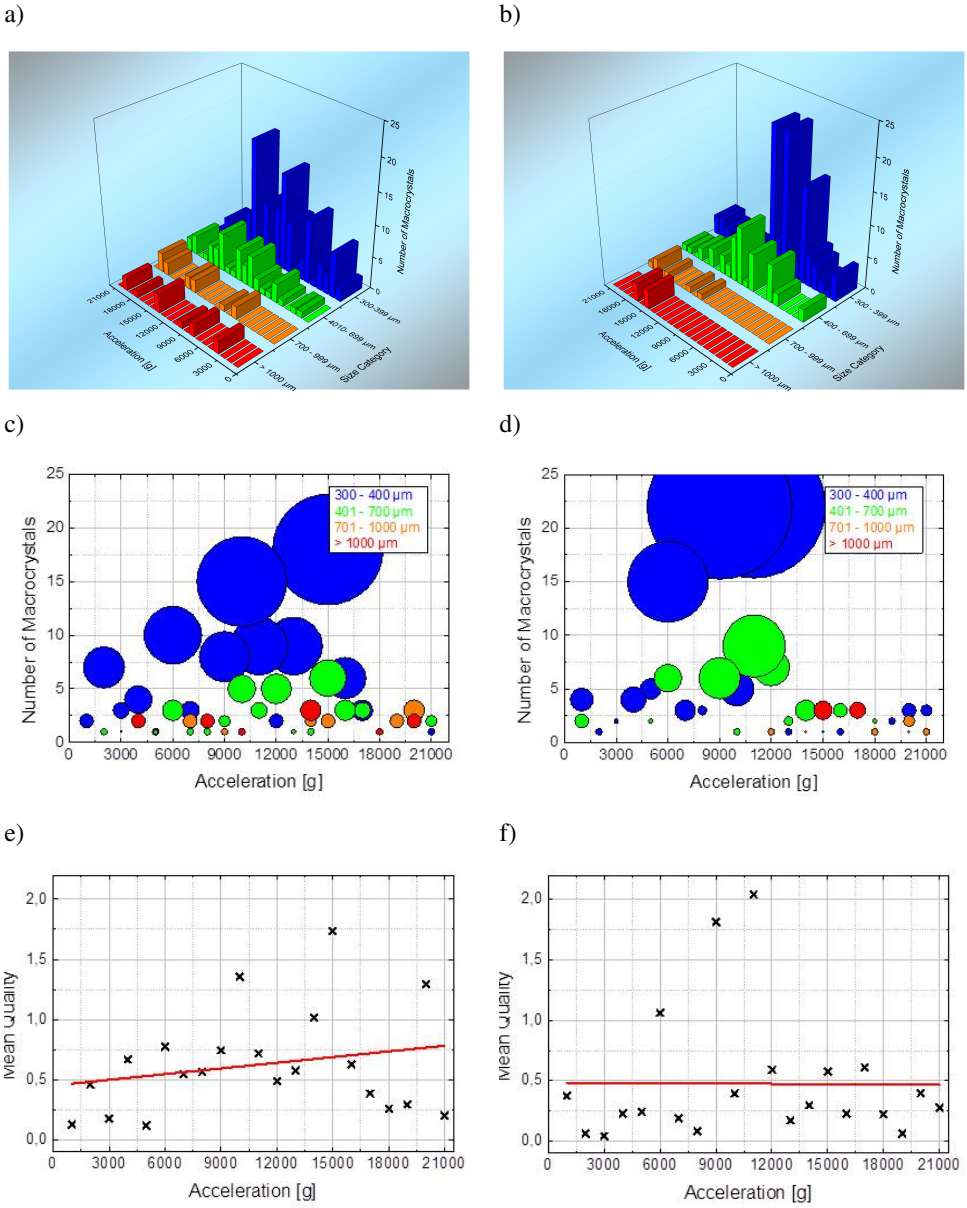


Figure 5.18: Number of macrocrystals per size category for all 21 samples centrifuged at 10°C a) without and c) with illustration of the score value S which corresponds to the dot size. e) Quality factor (black) and linear fit (red). b), d) and f) correspond to the reproduced samples.

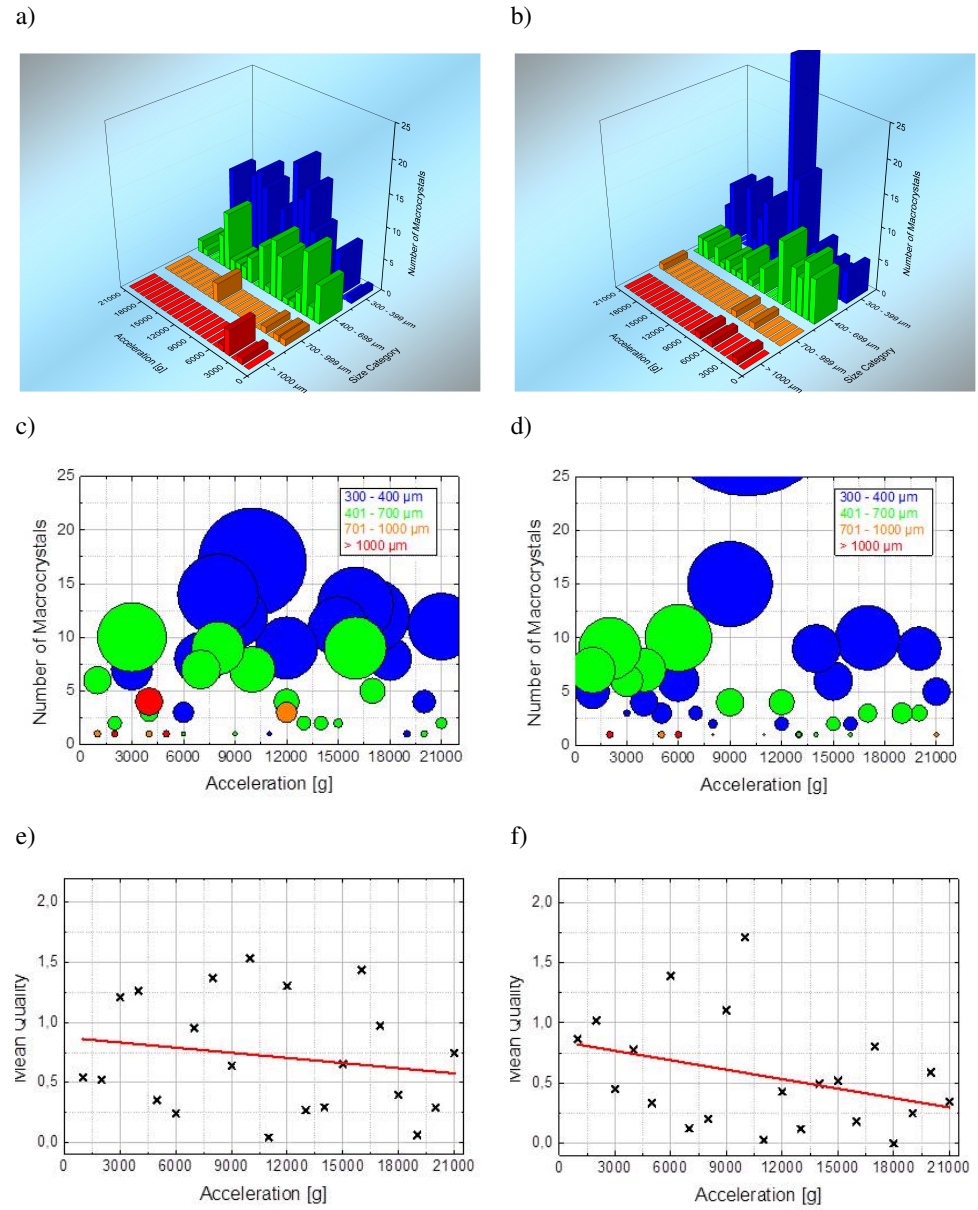


Figure 5.19: Number of macrocrystals per size category for all 21 samples centrifuged at 20°C a) without and c) with illustration of the score value S which corresponds to the dot size. e) Quality factor (black) and linear fit (red). b), d) and f) correspond to the reproduced samples.

5.4 Nanoparticle Arrangement

When investigating macrocrystals using imaging techniques like e.g. scanning electron microscopy, this gives information of the nanoparticle order at the surface only. To reveal the arrangement inside, small angle X-ray scattering measurements were performed at the JCNS GALAXI. For this, single macrocrystals (thickness ≈0.5 mm) were carefully removed from selected samples and measured in transmission geometry.

5.4.1 Influence of Size Distribution

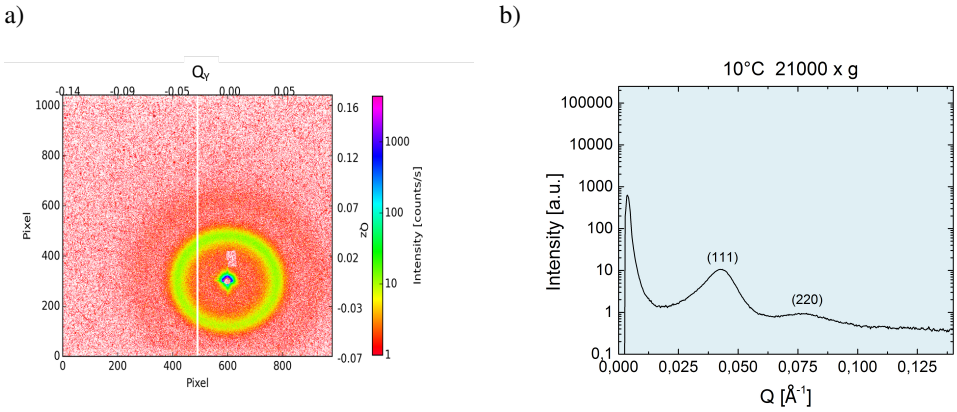


Figure 5.20: a) SAXS pattern of a single macrocrystal removed from the sample centrifuged at 10°C at 21 000 x g using batch O1 and b) radial integrated intensity.

In the previous section it was demonstrated that for batches O1 and O2 a great number of huge macrocrystals (i.e. ≈ mm) with a morphology that allows for handling without micromanipulators can be obtained at 10°C. Figures 5.20a and 5.21a show SAXS patterns of macrocrystals removed from samples centrifuged at 21 000 x g. As expected, batch O1 exhibits no long ranged order due to its broad nanoparticle size distribution (c.f. section 5.1). For batch O2 on the other hand, powder rings can be observed. The SEM images shown in figure 5.21c were obtained at the macrocrystal surface and indicate cubic order. Hence, powder rings should be found at positions according to the following equation [158]:

$$Q_{hkl} = 2\pi\sqrt{\frac{h^2+k^2+l^2}{a^2}} \tag{5.3}$$

$$a = \frac{2\pi}{Q_{hkl}}\sqrt{h^2+k^2+l^2} \tag{5.4}$$

$h,\ k,\ l$ are the Miller indices and a is the lattice constant. The first peak in cubic systems is caused by diffraction from planes with the lowest Miller indices. Assuming a face centered

cubic (FCC) system, this is (111) [158]. For the measurement shown in figure 5.21a, the corresponding Q_y = 0.047 Å^{-1} is identified using radial integrated intensities as shown in figure 5.21b (red). The lattice constant $a = 23.2$ nm is then calculated by employing equation 5.4. For the FCC lattice the relationship between lattice constant a and particle diameter d is

$$d = \frac{a}{\sqrt{2}} \tag{5.5}$$

This leads to a diameter of $d = 16.4$ nm which is slightly larger than the value determined by the SAXS measurement of the NP dispersion (c.f. section 5.1) because of the oleic acid coating that increases the particle distance and thus the lattice constant. Further peak positions are then calculated using equation 5.3. The allowed peaks for face centered cubic systems in terms of the quadratic form of the Miller indices are as follows:

$$h^2 + k^2 + l^2 = 3, 4, 8, 11, 12, 16, 19, 20, 24, 27, 32... \tag{5.6}$$

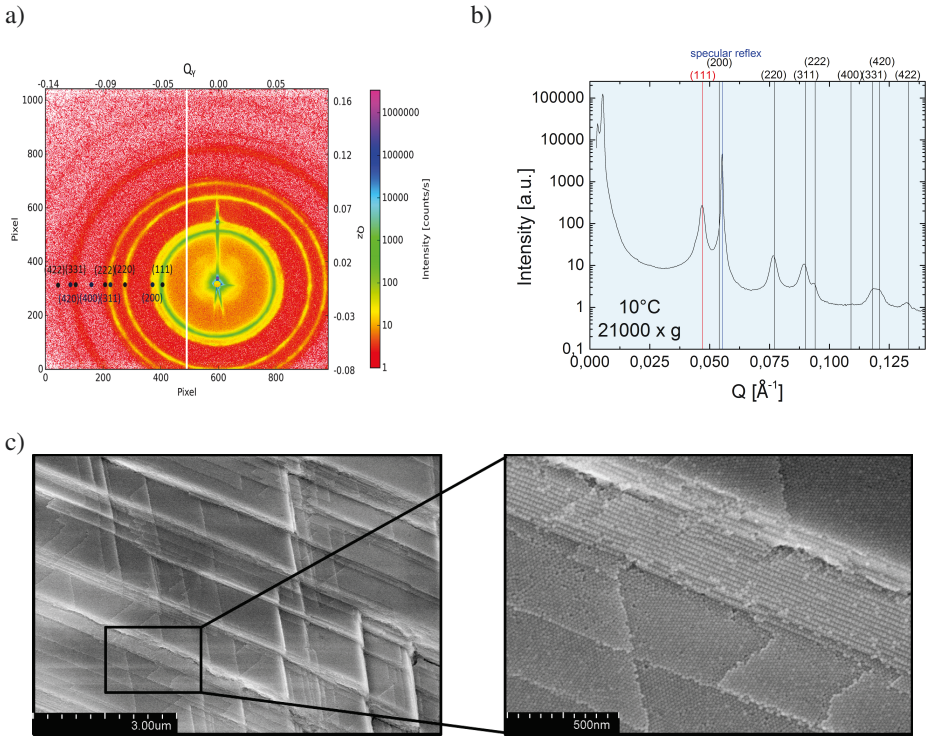


Figure 5.21: a) SAXS measurements performed on a single macrocrystal removed from the sample centrifuged at 10°C at 21 000 x g using batch O2 and b) radial integrated intensity. The measured (111) peak is labeled in red and further, calculated peak positions for a FCC lattice are shown in black. The specular reflex is highlighted in blue. c) SEM image of an FCC ordered grain at the macrocrystal surface.

The calculated values are shown in table 5.4 and marked in figures 5.21a,b (black). They are in accordance with the powder ring positions (maximum deviation $\pm 0.001 Å^{-1}$) thus verifying the assumption of a face centered cubic nanoparticle arrangement. Additionally, several peaks can be identified on the powder rings. This texture indicates that the FCC grains inside the macrocrystal exhibit a preferred orientation. Hence, the sample can be understood as nanoparticle-macro-polycrystal.

(hkl)	$h^2 + k^2 + l^2$	Q_{peak} [$Å^{-1}$]
(111)	3	0.047
(200) (020) (002)	4	0.054
(220) (202) (022)	8	0.077
(311) (131) (113)	11	0.090
(222)	12	0.094
(400) (040) (004)	16	0.109
(331) (313) (331)	19	0.118
(420) (042) (402)	20	0.121
(422) (242) (224)	24	0.133

Table 5.4: Measured Q_y value for the (111) reflex together with calculated positions of further peaks (equation 5.3) for face centered cubic symmetry (cf. equation 5.6) and a lattice constant of 23.2 nm.

5.4.2 Influence of Centrifugation Parameters

In section 5.3 it was demonstrated that the centrifugation parameters have a significant influence on the macrocrystal morphology. Using batch O1 it was tested if adjustments in the centrifugation temperature and acceleration can result in ordered macrocrystals despite the broad nanoparticle size distribution. SAXS measurements were thus performed on macrocrystals removed from samples centrifuged at 0°C, 10°C, 20°C and 30°C, respectively. For each temperature a sample centrifuged at intermediate (12 000 x g, figure 5.22) and high acceleration (21 000 x g, figure 5.24) was checked. For all samples two broad powder rings that are assumed to be the (111) and (220) reflex can be identified. Except for a single, sharp peak that originates from the specular reflex found in some measurements (position depending on the angle of incidence), no further peaks are visible because they are damped due to disorder. Hence, none of these samples exhibits long ranged order independent of the centrifugation parameters. This is further confirmed by the intensity distribution on the (111) ring as function of the azimuthal angle integrated over a ring width of 0.03 $Å^{-1}$ shown in figures 5.23 and 5.25. For all samples an almost constant value is found that is interrupted only by features caused by detection gaps.

A narrow nanoparticle size distribution as observed for batch O2 can therefore be assumed to be indispensable for the preparation of ordered macrocrystals. Figures 5.26 and 5.28 show SAXS measurements together with radial integrated intensities for macrocrystals that were removed from samples centrifuged at the same parameters as tested for batch O1. For all samples, powder rings are observed revealing that the macrocrystals contain ordered nanoparticle grains with a FCC lattice and a lattice constant of 23.7±0.5 nm independent of temperature and acceleration. The calculated peak positions are summarized in table 5.5 and marked in the corresponding images in figures 5.26 and 5.28.

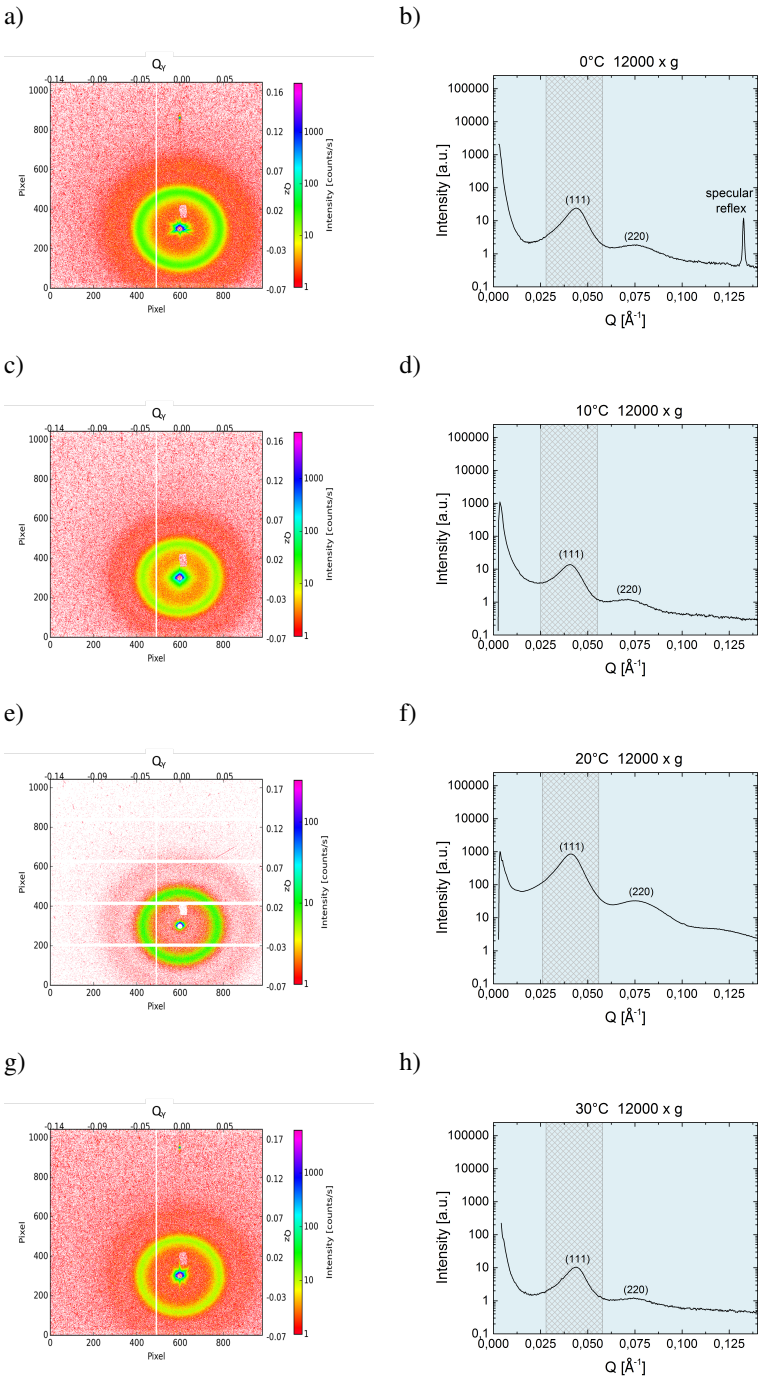


Figure 5.22: Batch O1: SAXS measurements performed on single macrocrystals removed from samples that were centrifuged at 12 000 x g (a,c,e,g) and radial integrated intensities (b,d,f,h). The gray area marks the region over which the intensity is integrated for the plots shown in figure 5.23. The centrifugation temperature was a,b) 0°C, c,d) 10°C, e,f) 20°C, g,h) 30°C.

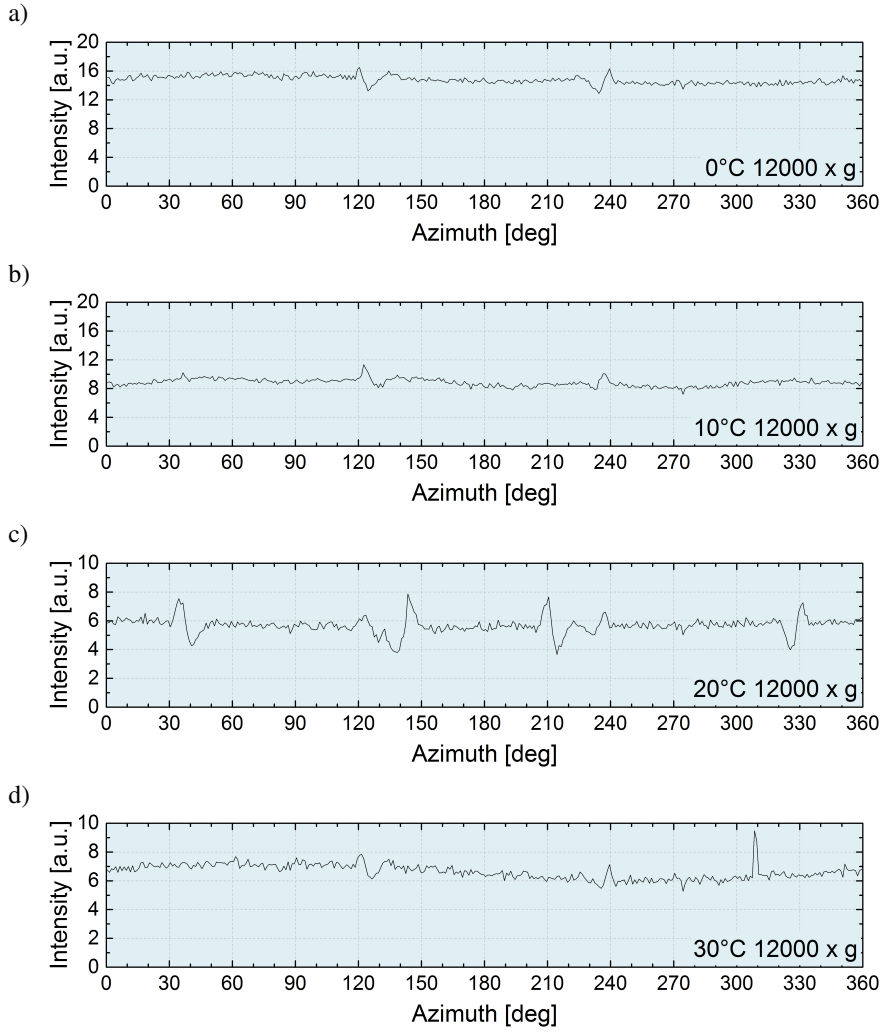


Figure 5.23: Intensities on the (111) powder ring as function of the azimuthal angle integrated over a ring width of 0.03 $Å^{-1}$ for the SAXS patterns shown in figure 5.22 (batch O1).

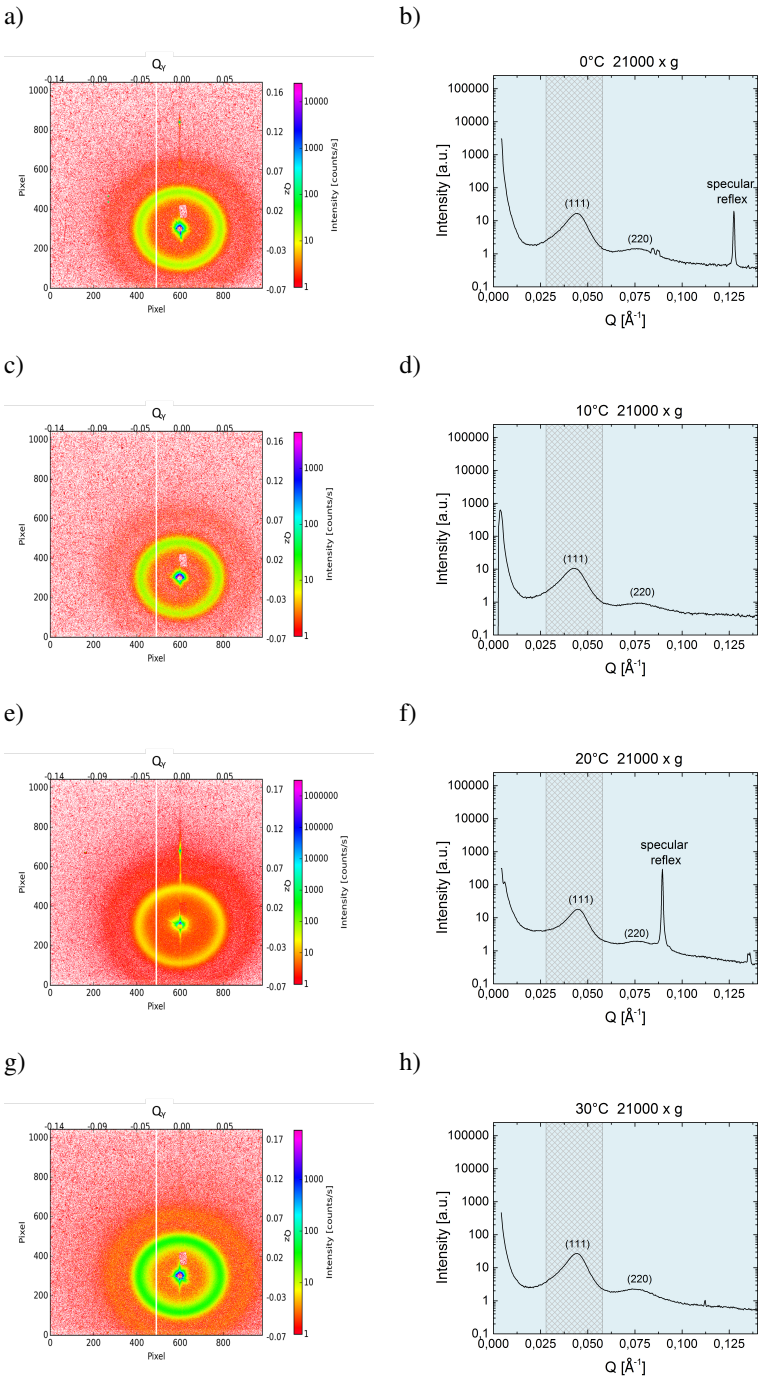


Figure 5.24: Batch O1: SAXS measurements performed on single macrocrystals removed from samples that were centrifuged at 21 000 x g (a,c,e,g) and radial integrated intensities (b,d,f,h). The gray area marks the region over which the intensity is integrated for the plots shown in figure 5.25. The centrifugation temperature was a,b) 0°C, c,d) 10°C, e,f) 20°C, g,h) 30°C.

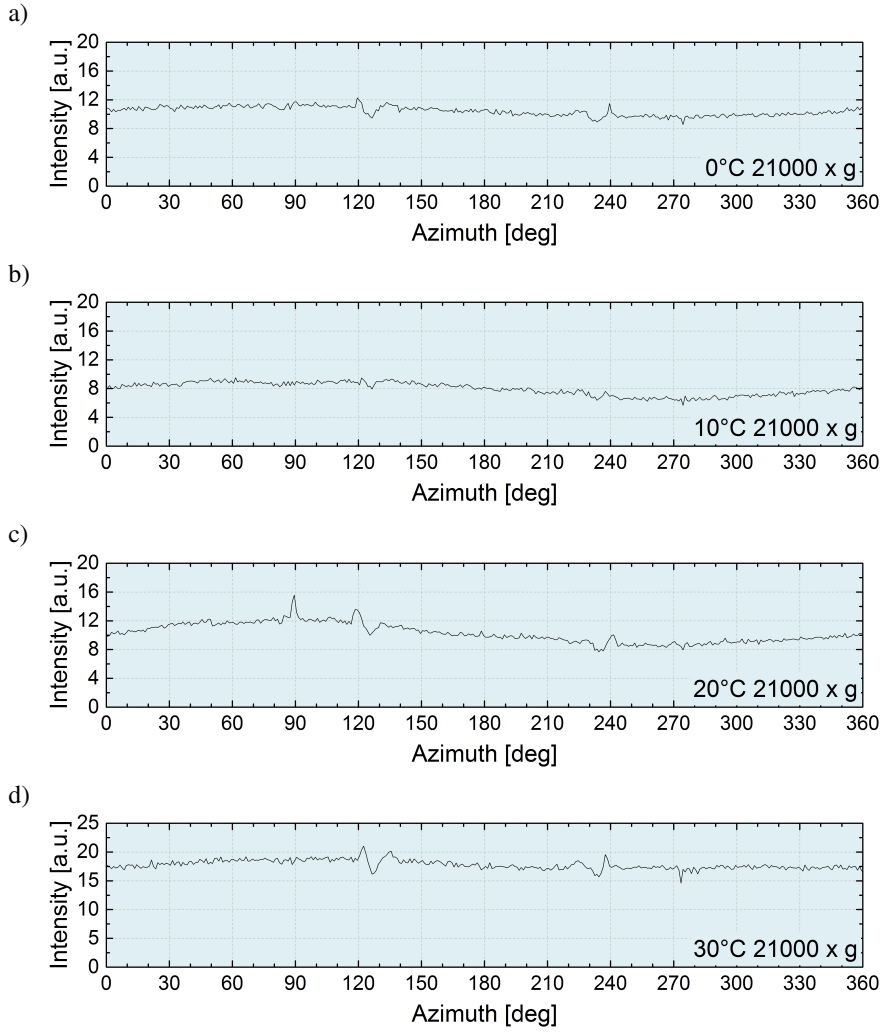


Figure 5.25: Intensities on the (111) powder ring as function of the azimuthal angle integrated over a ring width of 0.03 $Å^{-1}$ for the SAXS patterns shown in figure 5.24 (batch O1).

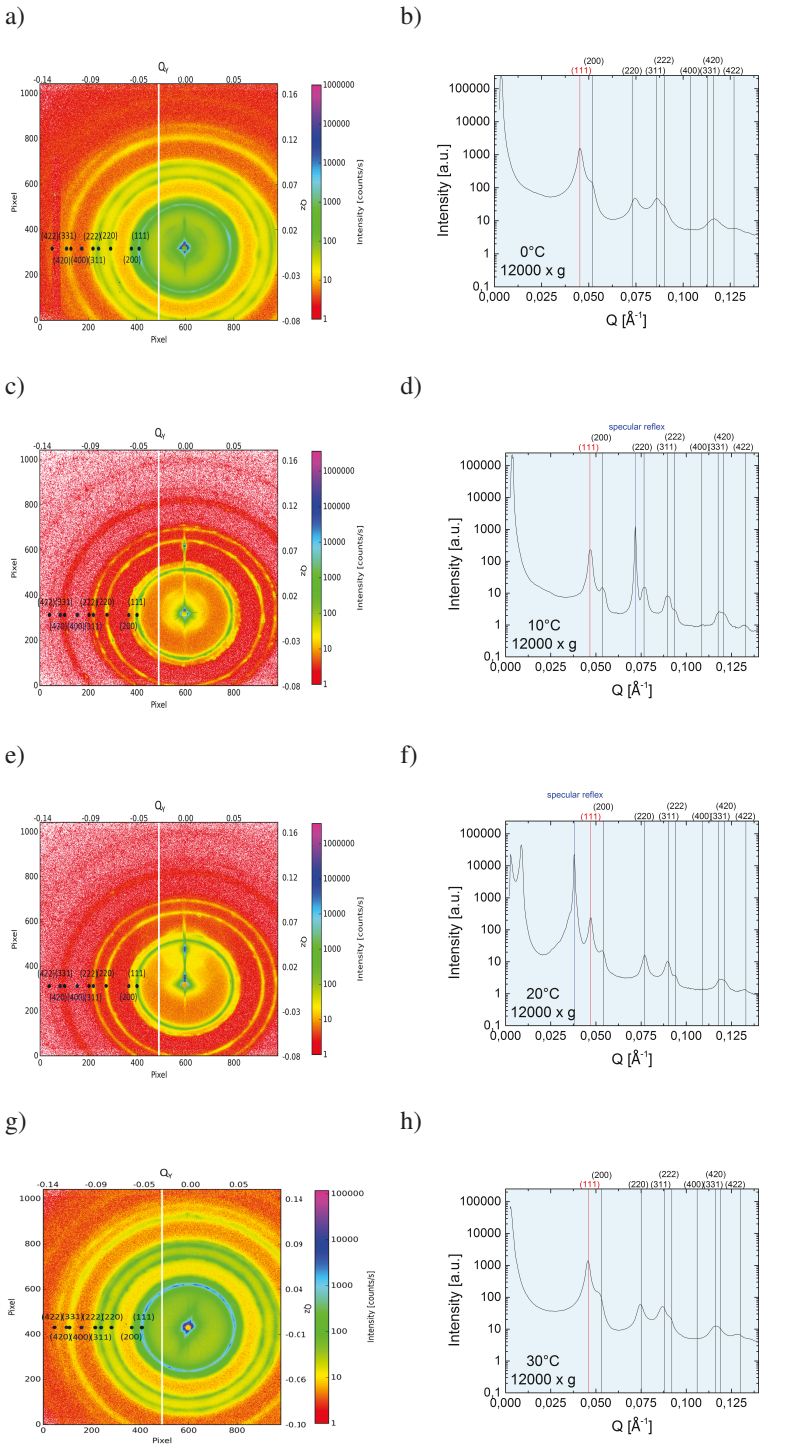


Figure 5.26: Batch O2: SAXS measurements performed on single macrocrystals removed from samples that were centrifuged at 12 000 x g (a,c,e,g) and radial integrated intensities (b,d,f,h). The measured (111) peak is labeled in red and further, calculated peak positions for a FCC lattice are shown in black. The specular reflex is highlighted in blue. The centrifugation temperature was a,b) 0°C, c,d) 10°C, e,f) 20°C, g,h) 30°C.

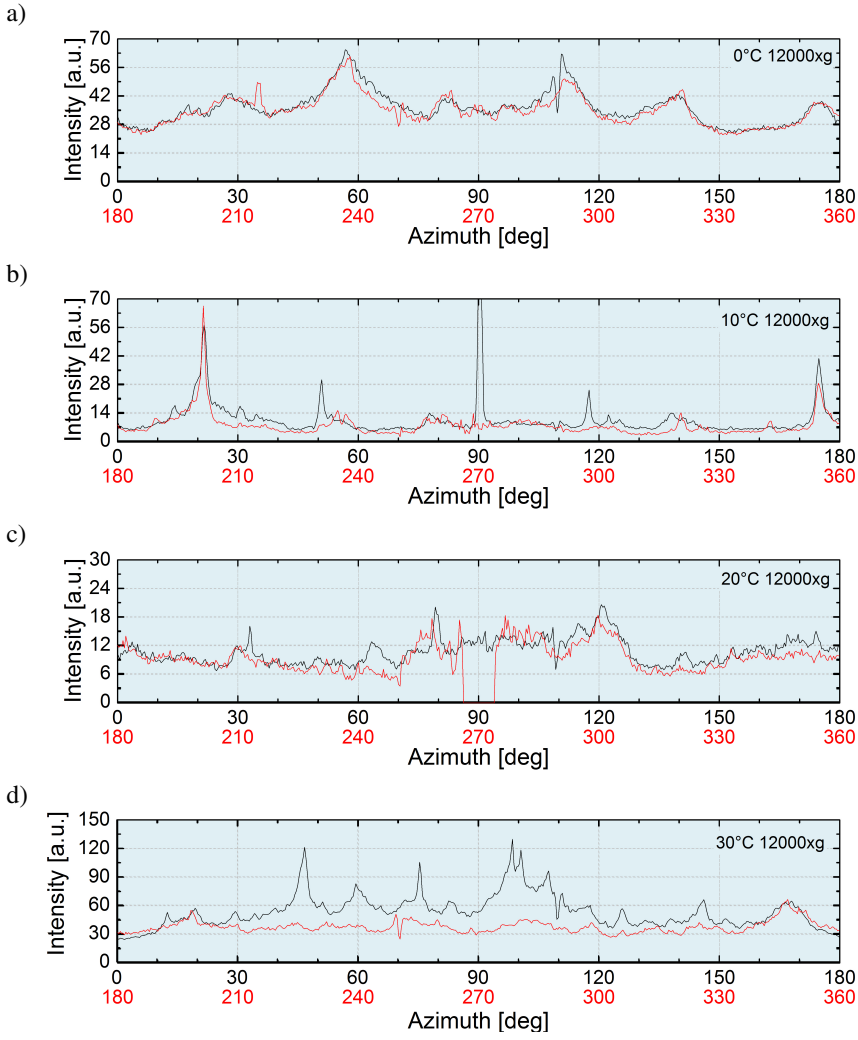


Figure 5.27: Intensities on the (220) powder ring as function of the azimuthal angle integrated over a ring width of 0.01 $Å^{-1}$ for the SAXS patterns shown in figure 5.26 (batch O2).

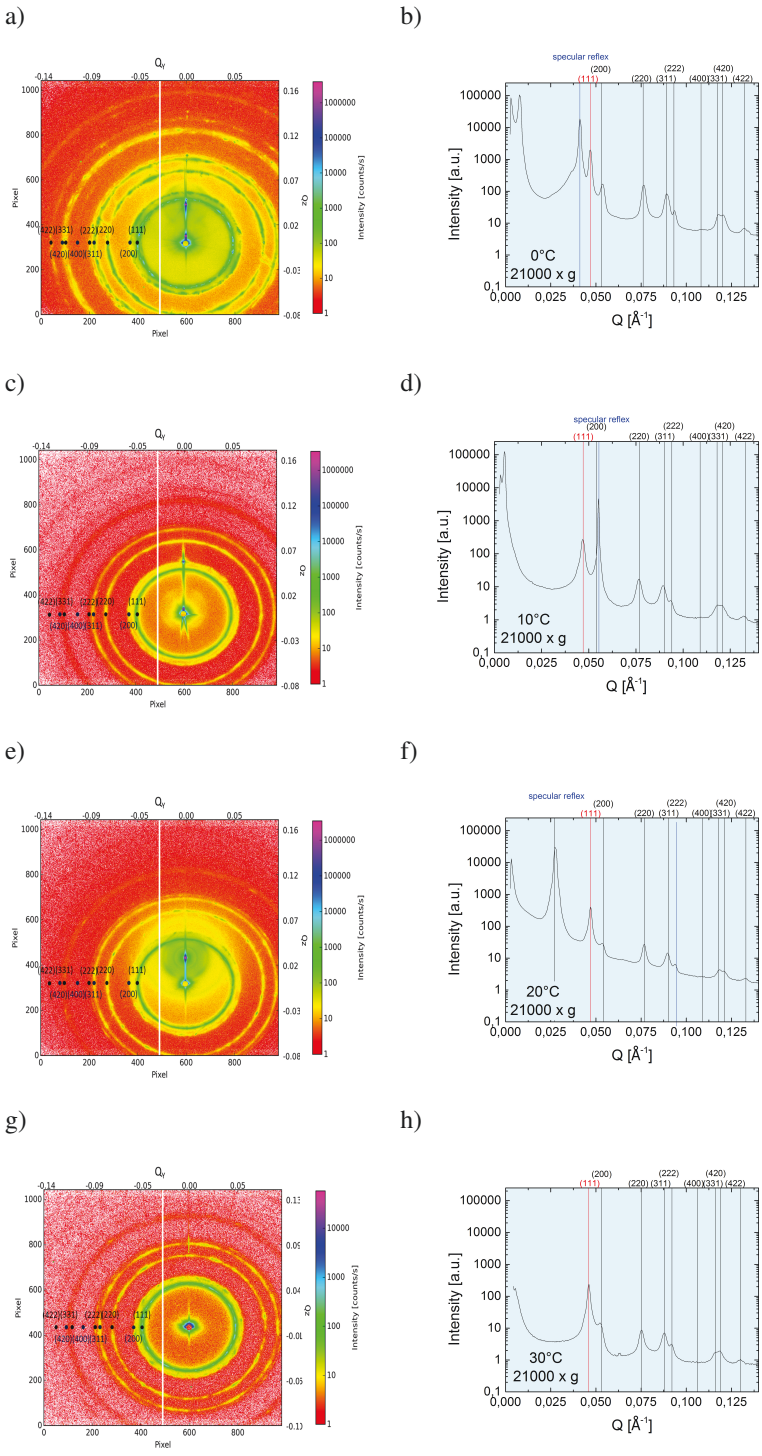


Figure 5.28: Batch O2: SAXS measurements performed on single macrocrystals removed from samples that were centrifuged at 21 000 x g (a,c,e,g) and radial integrated intensities (b,d,f,h). The measured (111) peak is labeled in red and further, calculated peak positions for a FCC lattice are shown in black. The specular reflex is highlighted in blue. The centrifugation temperature was a,b) 0°C, c,d) 10°C, e,f) 20°C, g,h) 30°C.

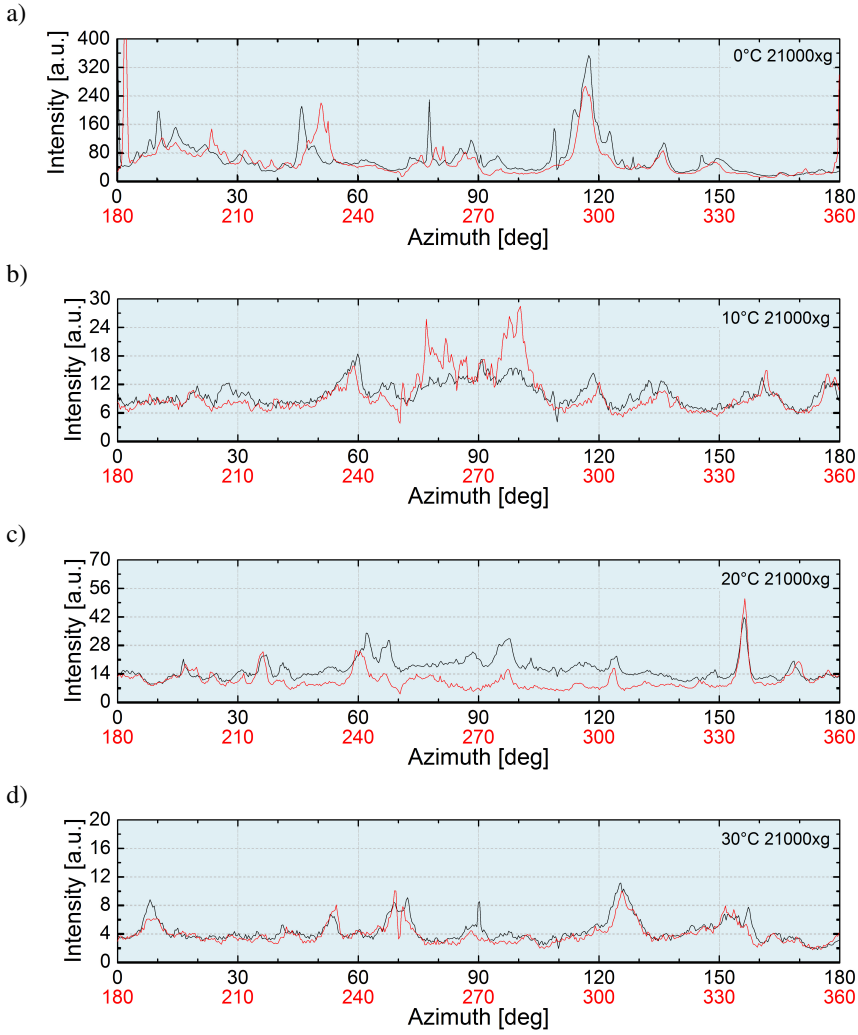


Figure 5.29: Intensities on the (220) powder ring as function of the azimuthal angle integrated over a ring width of 0.01 $Å^{-1}$ for the SAXS patterns shown in figure 5.28 (batch O2).

(hkl)	$h^2+k^2+l^2$	Q_{peak} [Å^{-1}]							
		0°C		10°C		20°C		30°C	
		12 000 x g	21 000 x g	12 000 x g	21 000 x g	12 000 x g	21 000 x g	12 000 x g	21 000 x g
		a = 24.2 nm	a = 23.2 nm	a = 23.2 nm	a = 23.2 nm	a = 23.2 nm	a = 23.2 nm	a = 23.7 nm	a = 23.7 nm
(111)	3	0.045	0.047	0.047	0.047	0.047	0.047	0.046	0.046
(200)	4	0.052	0.054	0.054	0.054	0.054	0.054	0.053	0.053
(220)	8	0.073	0.077	0.077	0.077	0.077	0.077	0.075	0.075
(311)	11	0.086	0.090	0.090	0.090	0.090	0.090	0.088	0.088
(222)	12	0.090	0.094	0.094	0.094	0.094	0.094	0.092	0.092
(400)	16	0.104	0.109	0.109	0.109	0.109	0.109	0.106	0.106
(331)	19	0.113	0.118	0.118	0.118	0.118	0.118	0.116	0.116
(420)	20	0.116	0.121	0.121	0.121	0.121	0.121	0.119	0.119
(422)	24	0.127	0.133	0.133	0.133	0.133	0.133	0.130	0.130

Table 5.5: Measured Q_y values for the (111) reflex together with the calculated lattice constants (according to equation 5.4) and the calculated positions of further peaks (according to equation 5.3) for face centered cubic symmetry (cf. equation 5.6).

The Scherrer grain size analysis can be employed to make quantitative statements regarding the presence and degree of preferred grain orientations.

$$D_{hkl} = \frac{2\pi K}{\Delta Q_{hkl}} \tag{5.7}$$

D_{hkl} is the average grain size related to a specific diffraction spot (hkl) and ΔQ_{hkl} is the corresponding peak width determined using its Full Width Half Maximum (FWHM). The dimensionless factor K is the Scherrer constant which is 0.93 for spherical crystals in cubic symmetry [159].

In general, it has to be considered that peak broadening is not only caused by a finite grain size. Temperature factors, nanoparticle size distribution, the instrumental resolution (wavelength spread in the incident radiation, beam divergence, detector pixel size etc.) and microstrain can influence the peak width [159]. However, since all results shown in figures 5.26 and 5.28 were performed on the same instrument and the samples were prepared using the same nanoparticle batch, this background is assumed to be identical for all eight measurements. The presented values are therefore rather thought of as correlation distance which does not directly give the absolute grain size. Nevertheless it can be used to compare the degree of order inside the macrocrystals.

For the determination of the average size of coherently scattering areas the FWHM of the (220) ring integrated in radial direction is employed. The resulting values summarized in table 5.6 demonstrate that larger grains form at 21 000 x g than at 12 000 x g which is attributed to denser packing after centrifugation at higher accelerations. Furthermore, the grain size is largest at 20°C and decreases at higher and lower temperatures for both accelerations. This is most likely caused by the organic coating which shows different 'stiffness' and hence different steric repulsion properties if the temperature is varied. In contrast to the macrocrystal morphology evaluated in the previous section where the optimum temperature was found below the bulk melting temperature of oleic acid (16.3°C), the nanoparticles order best slightly above that temperature.

T	a	ΔQ_{220} [nm^{-1}]	D_{220} [nm]
0°C	12 000 x g	0.045	130
10°C	12 000 x g	0.031	188
20°C	12 000 x g	0.029	201
30°C	12 000 x g	0.042	139
0°C	21 000 x g	0.025	234
10°C	21 000 x g	0.024	243
20°C	21 000 x g	0.021	278
30°C	21 000 x g	0.026	225

Table 5.6: Average sizes of coherently scattering areas D_{220} calculated using the FWHM of the (220) ring integrated in radial direction ΔQ_{220}. T and a are the centrifugation temperature and acceleration, respectively.

Furthermore, the intensity distribution on the (220) ring as function of the azimuthal angle integrated over a ring width of 0.01 $Å^{-1}$ shown in figures 5.27 and 5.29 demonstrates that all patterns obtained from samples fabricated using batch O2 are textured to varying degrees depending on the centrifugation parameters. Hence, equation 5.7 can be employed to estimate the 'mosaic width' by determining D_{hkl} using the FWHM of these peaks. Appendix E provides a complete list of all peaks identified in figures 5.27 and 5.29 together with their FWHM, intensities and calculated D_{220}. These data are summarized in the boxplots shown in figure 5.30 where the black dot shows the average value and the whiskers mark the maximum and minimum. Bottom and top of the box are the first and third quartiles, respectively and the band inside marks the median. At 12 000 x g the largest mosaic width is found at 10°C which fits the results concerning the macrocrystal morphology, where the largest total macrocrystal size was also found at 10°C (c.f. section 5.3). However, at 21 000 x g this temperature results in the smallest mosaic width. For this acceleration larger mosaic widths are found both, at higher and lower centrifugation temperatures. This is most likely caused by the complex interplay of dense nanoparticle packing by the centrifugation process and subsequent rearrangement that is significantly influenced by the 'stiffness' of the oleic acid coating which depends on the centrifugation and drying temperature. However, for in-depth understanding of the detailed process further experiments are necessary.

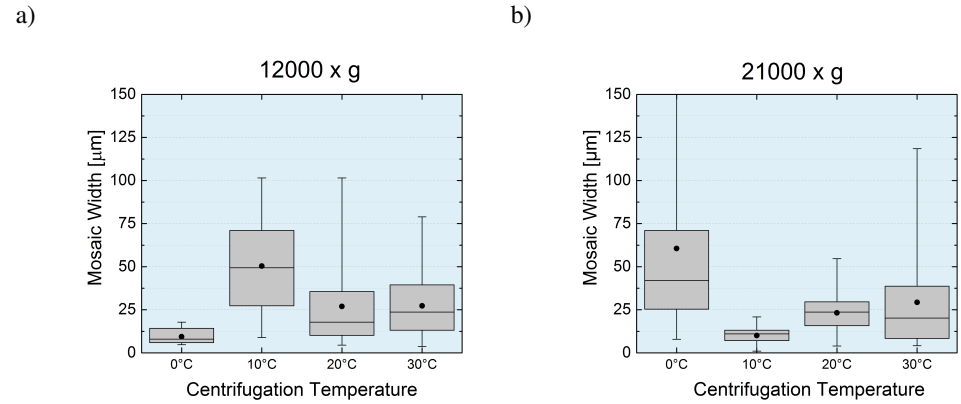


Figure 5.30: Boxplots summarizing the 'mosaic widths' determined from the FWHM of the peaks identified in azimuthal direction on the (220) powder ring for the measurements shown in figures 5.27 and 5.29. The black dots mark the average values and the whiskers indicate minimum and maximum. Bottom and top of the boxes are the first and third quartiles, respectively. The bands inside the boxes show the median values.

5.4.3 Influence of Surfactants

Aside from the commercially available nanoparticle batches O1 and O2, three nanoparticle batches from our cooperation partner at the Magnetism and Nano-Bio Technology Center at the University of Hong Kong, department of Electrical and Electronic Engineering in China were presented in section 5.1. These nanoparticles are smaller (c.f. table 5.1) thus requiring

larger amounts of surfactant inside the nanoparticle dispersion to avoid agglomeration. After centrifuging the samples at 10°C and 21 000 x g most of the additional surfactant (either oleic acid or decanoic acid) is found in the sediment. In contrast to the remaining toluene, it does not (or rather extremely slow) evaporate, leading to very small (300...399 μm) and greasy macrocrystals, which are complicated to handle.

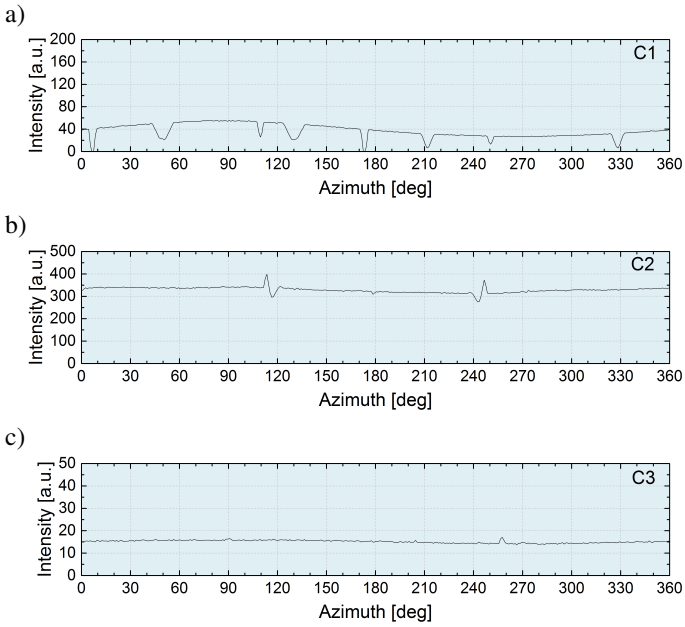


Figure 5.31: Intensities as function of the azimuthal angle integrated over a ring width of 0.04 Å^{-1} for the SAXS patterns shown in figure 5.32. a) Batch C1, b) batch C2, c) batch C3.

However, for every batch (C1, C2 and C3) one macrocrystal was successfully prepared to perform SAXS measuremets. The resulting patterns are shown in figure 5.32a,c,e together with integrated intensities in radial direction (b,d,f). They demonstrate that batches C1 and C2 exhibit no long ranged order as it was expected due to their broad nanoparticle size distribution. This is further confirmed by the intensity distribution in azimuthal direction integrated over a ring width of 0.04 Å^{-1} shown in figure 5.31a,c. The chosen inner radius is 0.025 Å^{-1} for batch C1 and 0.065 Å^{-1} for batch C2. Both curves are mostly constant except for several features caused by detection gaps.

For batch C2 the result is similar to the data obtained from batch O1, i.e. two very broad peaks that are assumed to be the (111) and (220) reflex. The intensity distribution in azimuthal direction, integrated over a ring width of 0.04 Å^{-1} on the (111) ring shown in figure 5.31b is also mostly constant (except for two features caused by detection gaps). This is rather surprising, because the size distribution is even narrower than for batch O2, where well ordered grains were obtained. It can therefore be ascertained that for the preparation of huge, ordered macrocrystals not only the centrifugation parameters and nanoparticle size distribution, but also the amount of surfactant is a significant aspect that has to be considered.

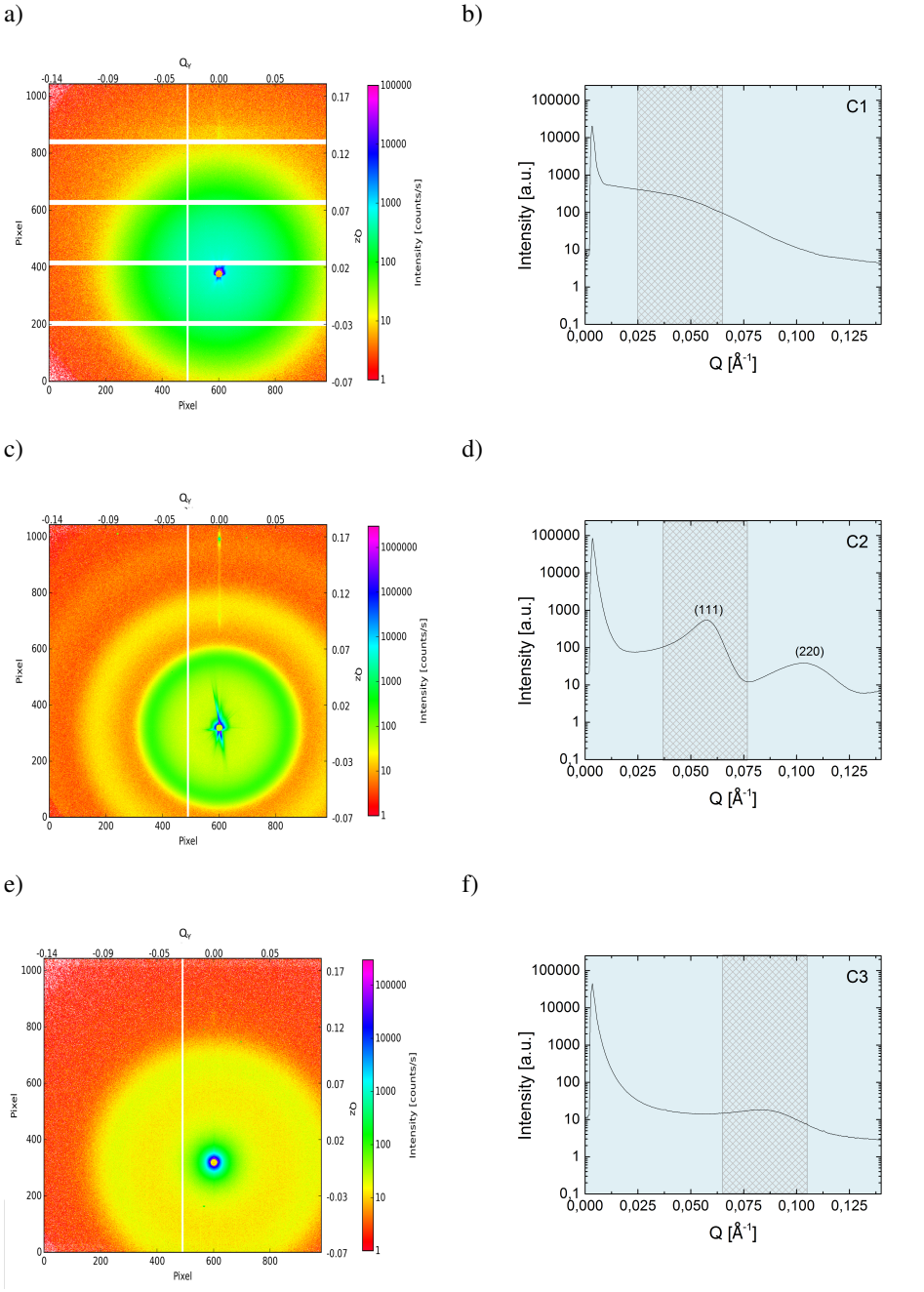


Figure 5.32: a,c,e) SAXS pattern of a single macrocrystal removed from samples centrifuged at 10°C and 21 000 x g using a) batch C1, b) batch C2, c) batch C3 and b,d,f) radial integrated intensities. The gray area marks the region over which the intensity is integrated for the plots shown in figure 5.31.

5.5 Magnetic Properties

In chapter 4 the two dimensional nanoparticle arrangements are found to be in a superspin glass state. To analyze whether this holds for three dimensional assemblies as well, memory effect measurements were performed. Batches C1, C2 and C3 contain smaller nanoparticles with a lower blocking temperature than the nanoparticles in batches O1 and O2. Since the memory effect is more prominent at a temperature close to the rising edge of the ZFC curve, the aging stop is performed at 25 K for the former and at 140 K for the latter (c.f. figures 5.4b,d,f and 5.4b,d). In all cases the waiting time was 10 000 s. Figure 5.33 shows that a memory effect can be clearly identified by dips close to the aging temperature thus indicating superspin glass systems independent of nanoparticle size, size distribution, surfactant, macrocrystal morphology and nanoparticle order[1].

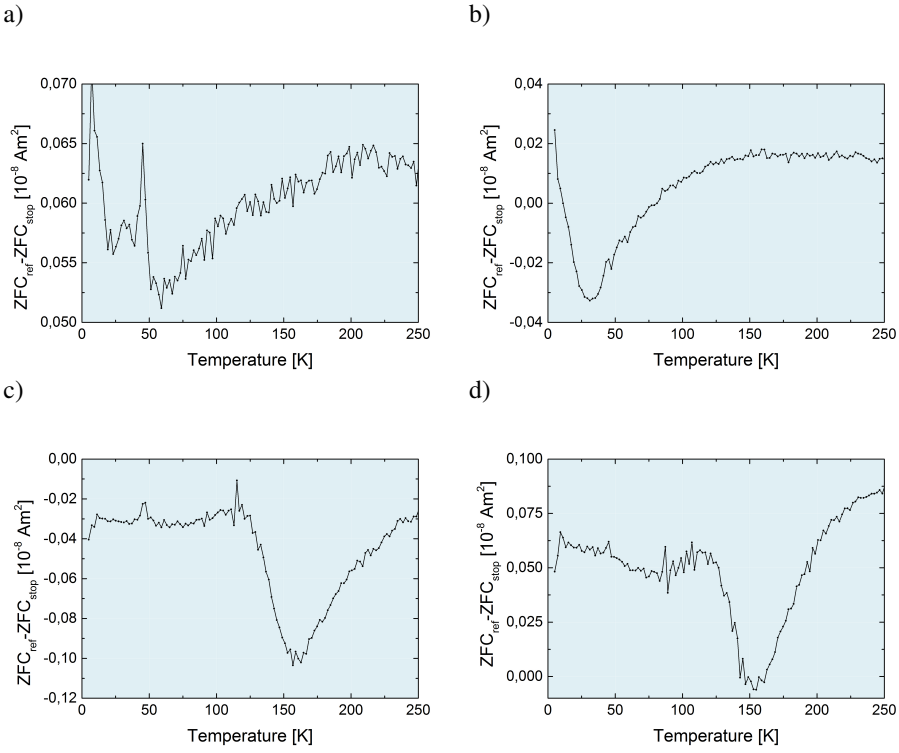


Figure 5.33: Memory effect measurements with an aging time of 10 000 s performed on single macrocrystals that were obtained after centrifugation at 10°C at 21 000 x g using a) batch C1, b) batch C2, c) batch O1 and d) batch O2. Hereby the aging stop was performed at 25 K for a) and b) or at 140 K for c) and d).

[1]The peak at 50 K in figure 5.33a is a measurement artifact.

As shown in the previous sections, the best macrocrystals concerning morphology and order could be manufactured using batch O2. However, significant differences were observed depending on the centrifugation temperature. Hence, ZFC-FC measurements were performed on macrocrystals removed from samples prepared at 21 000 x g at 0°C, 20°C and 30°C, respectively. Figures 5.34a,b,c show that the curve characteristics are similar to those obtained for the sample centrifuged at 10°C (c.f. figure 5.5d). The sample centrifuged at 12 000 x g at 10°(figure 5.34d) also exhibits the same curve characteristics. Hence, the overall blocking process and magnetic properties of the macrocrystals can be assumed to be independent of the centrifugation parameters.

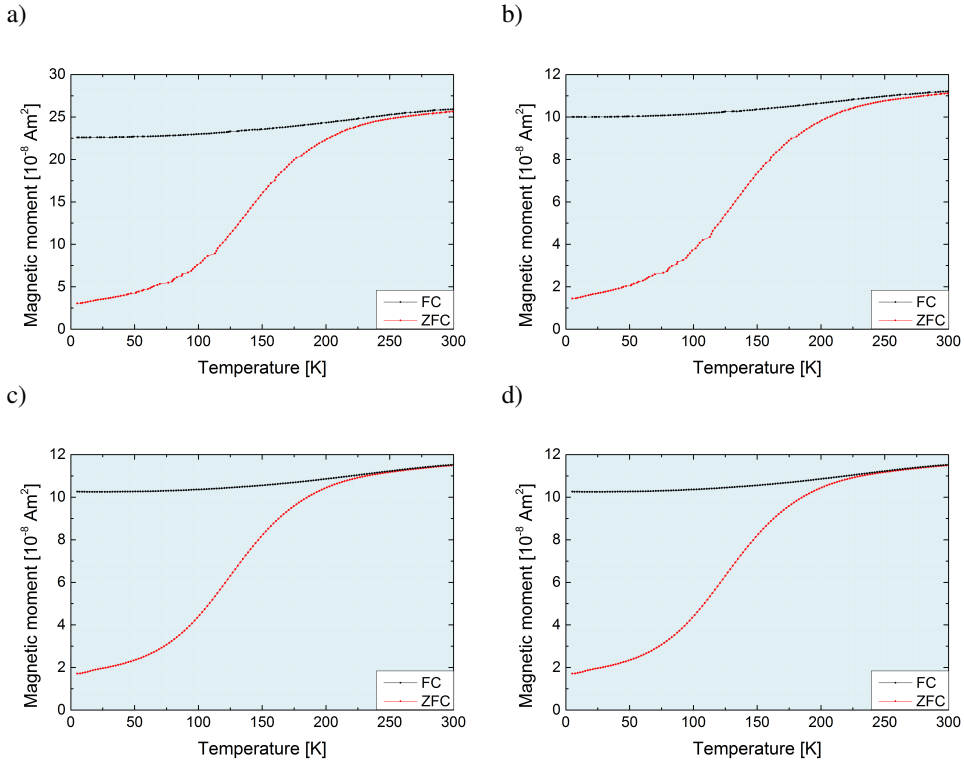


Figure 5.34: ZFC-FC measurements performed on single macrocrystals removed from samples prepared using batch O2 by centrifugation at a) 0°C at 21 000 x g, b) 20°C at 21 000 x g, c) 30°C at 21 000 x g and d) 10°C at 12 000 x g.

5.6 Polarization and Magnetoresistance Effects

In chapter 4 it was demonstrated how two-dimensional iron oxide nanoparticle assemblies can influence a polarizable matrix material. To transfer these considerations to three-dimensional systems, the matrix material must not only cover the macrocrystal surface, but has to be deposited in between the nanoparticle layers as well. For this, a sample is manufactured in the same way as sample 4-01: First, a (sub-)monolayer of nanoparticles is deposited by spin coating, then the organic surfactant shell is removed by oxygen plasma treatment and finally, 5 nm of palladium are deposited by IBS. This process is then repeated seven times resulting in a densely packed, three-dimensional assembly, where all the nanoparticles are separated by a thin palladium layer. Figure 5.36 shows, how the nanoparticle/palladium multilayer evolves step by step: In the first layer, small areas in which the nanoparticles are well ordered and densely packed can be observed. In between, nanoparticle chains are formed, that connect these areas. One cause for this arrangement is the strong van der Waals interaction acting between the nanoparticles. Another aspect is the evaporation process: When the solvent thickness reaches a critical value, holes in the solvent film open up and expand, hereby pushing the nanoparticles together. When further nanoparticle layers are deposited, the structure of the first sub-monolayer is still visible in the SEM images, even after manufacturing the eighth layer.

Using a scanning electron microscope, large areas of the sample surface were investigated revealing that most of the nanoparticles at the surface exhibit no long range order. To study the nanoparticle arrangement inside this system, GISAXS measurements were performed on the JCNS GALAXI. However, as figure 5.35 shows, this attempt failed due to the large scattering length density of palladium.

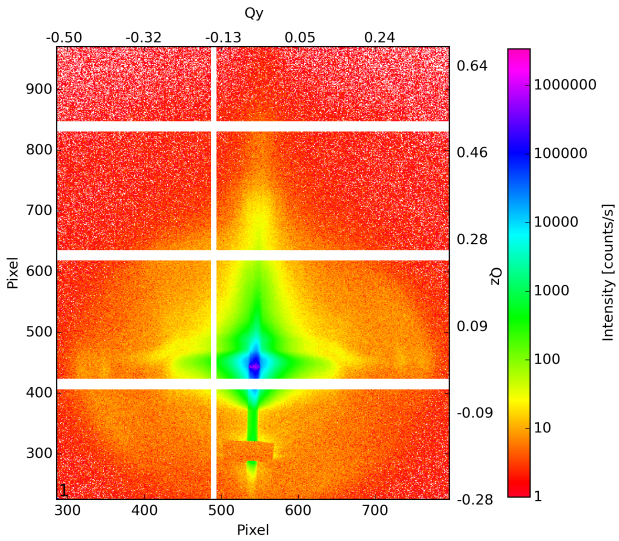


Figure 5.35: GISAXS measurement performed at the JCNS GALAXI on the nanoparticle/palladium multilayer showing only diffuse scattering due to the large scattering length density of palladium.

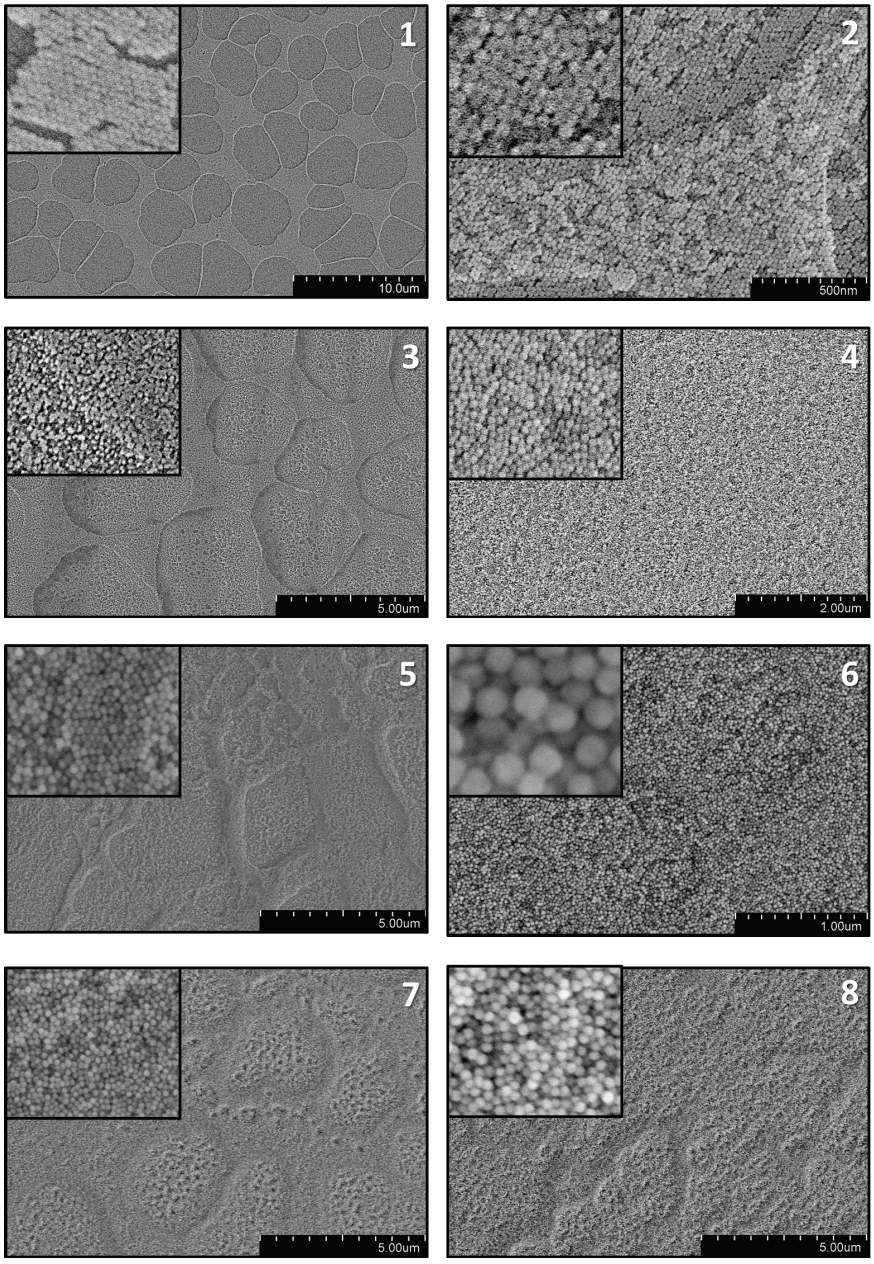


Figure 5.36: SEM images of the sample center after each preparation step consisting of nanoparticle deposition, surfactant removal and palladium deposition.

Figure 5.37 shows the ZFC-FC curves obtained with a Quantum Design MPMS device. Even though every nanoparticle layer was oxygen plasma treated for 30 min, the curve characteristics indicate a mixed maghemite/wustite iron oxide phase. This is surprising, because in section 4.3 it was shown that for a single (sub-)monolayer 12 min are sufficient to completely transform the wustite components towards maghemite. Hence, it seems to be not only the nanoparticles that influence the matrix, but also the matrix that influences the nanoparticles. Except for the first layer, the nanoparticles always lay on top of a thin palladium film. This seems to partially suppress the transformation resulting in wustite remains even after 30 min of oxygen plasma treatment.

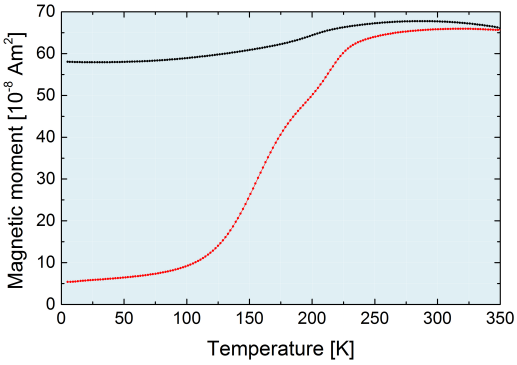


Figure 5.37: ZFC-FC curves measured on the nanoparticle/palladium multilayer revealing that the nanoparticles still contain wustite remains despite the extensive oxygen plasma treatment.

The hysteresis curves measured at 5 K and 300 K, respectively, are shown in figure 5.38. They demonstrate the superparamagnetic behavior of the nanoparticles. In addition, the exchange bias of 0.0174 T confirms the assumed nanoparticle composition, because this effect is found only, if a specific combination of magnetic materials is in close contact (e.g AF wustite and FiM maghemite).

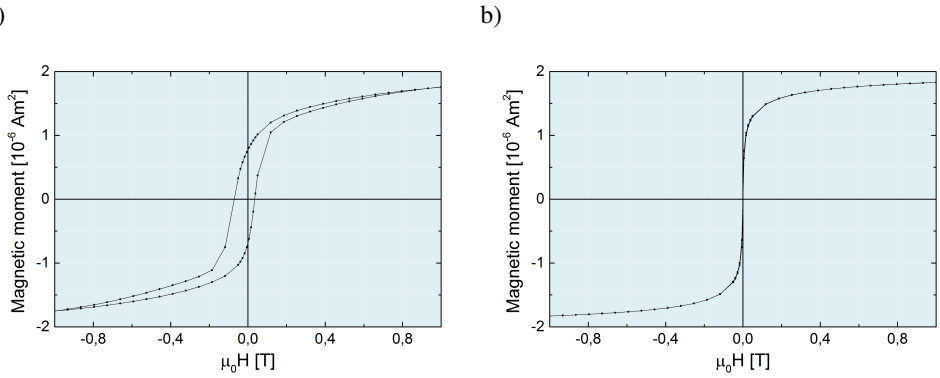


Figure 5.38: Hysteresis curves of the nanoparticle/palladium multilayer measured at a) 5 K and b) 300 K, revealing superparamagnetism and exchange bias.

For the investigation of the nanoparticle interaction, memory effect measurements were performed with an aging stop at 140 K for 10 000 s. Figure 5.39 shows a significant dip revealing that the system is in a superspin glass state. However, this dip is remarkably broadened. It is assumed that this characteristic emerges because the nanoparticles contain two different iron oxide phases and are therefore not in a monodomain state.

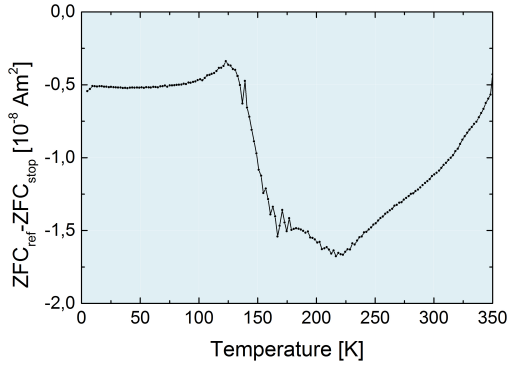


Figure 5.39: Nanoparticle/palladium multilayer: Memory effect measurement performed with an aging stop at 140 K for 10 000 s demonstrating the superspin glass state of the system. The peak broadening is assigned to the mixed wustite/maghemite iron oxide phase inside the nanoparticles.

Figure 5.40 shows the measured IRM and DCD curves together with the calculated delta-M. The area enclosed by the x-axis and delta-M curve is -230 T. Its a negative sign indicates a demagnetizing type of interaction that can be attributed to the dipolar interaction between the nanoparticles. The delta-M measurements presented in section 4.4 exhibit values of -817 T for pure nanoparticles and -707 T for a palladium covered (sub-)monolayer. Hence, the effect found in the two-dimensional system is not only present in the three-dimensional assembly, but also even more pronounced.

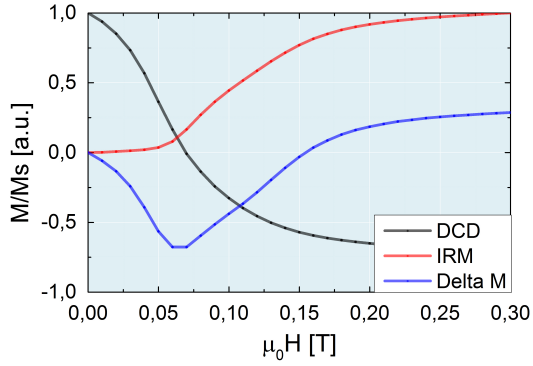


Figure 5.40: Nanoparticle/palladium multilayer: IRM (red), DCD (black) and Delta-M (blue) curves indicating a polarization effect.

Finally, resistivity measurements were performed on the nanoparticle/palladium multilayer. Figure 5.41 shows that the Lorentz magnetoresistance effect observed in all two-dimensional systems investigated in section 4.5 is present in this system as well. However, the effect is several orders of magnitude smaller than in the two-dimensional samples and none of the nanoparticle effects observed in chapter 4 can be found in this system even though the nanoparticle / palladium ratio is the same.

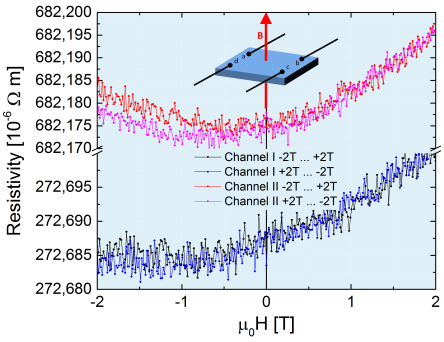


Figure 5.41: Nanoparticle/palladium multilayer: Resistivity in dependency of a magnetic field applied perpendicular to the sample plane, measured at 10 K.

5.7 Conclusion

Within this chapter a new approach for manufacturing three-dimensional nanoparticle assemblies on length scales of up to 300...1000 μm was introduced. This new kind of artificial material is a promising approach for the development of functional materials. The dependency of e.g. optical or mechanical properties on an applied magnetic field is interesting e.g. for the development of ferrofluidic shock-absorbers. Furthermore, magnetic excitations in dipolar systems become measurable with 3D NP assemblies containing enough material.

To provide well defined raw materials, several nanoparticle batches were investigated in detail concerning their composition, particle size, size distribution and magnetic properties. Afterwards they were assembled into $\propto$0.1 mm arrangements by a novel centrifuge assisted sedimentation method. The final macrocrystals were studied concerning their morphology, nanoparticle arrangement and magnetism. Hereby, it could be demonstrated how slight differences in the particle characteristics significantly influence the crystal formation process.

Furthermore, a three-dimensional NP/Pd composite system was manufactured by repeating the nanoparticle deposition, plasma treatment and coating process used for the two-dimensional systems several times on a single sample. While the polarization effect observed in the two-dimensional system was found to be even more pronounced, the magnetoresistance effect was not found in the 3D system. However, for a detailed understanding further studies are necessary.

6 Summary and Outlook

In this thesis, iron oxide nanoparticles are used to investigate magnetic proximity effects. For this, several batches, both, commercially available samples from Ocean NanoTech and non-commercial samples from our cooperation partner at the Magnetism and Nano-Bio Technology Center at the University of Hong Kong, department of Electrical and Electronic Engineering in China are investigated in detail. The average nanoparticle diameters and size distributions are determined by SEM and SAX studies in cooperation with the Peter Grünberg Institute for Electronic Materials. This reveals major differences in the nanoparticle quality, which influences the overall sample properties. By combining XRD measurements with SQUID magnetometry it is shown that the Ocean NanoTech particles contain maghemite and wustite as they are delivered. Using oxygen plasma it is demonstrated, how the wustite component is transformed towards maghemite to form single domain nanoparticles. These are then used to study how magnetic proximity effects can be employed to tune the properties of matrix materials. For this, the nanoparticles are first self-assembled to form a (sub-)monolayer and then oxygen plasma treated. This removes the organic surfactant shell that avoids agglomeration during storage and results in pure maghemite nanoparticles. Finally, a thin layer of either palladium or platinum is deposited in cooperation with the Max-Planck-Institute for Intelligent Systems, department Schütz, to form the matrix material. Both metals are close to the fulfillment of the Stoner criterion. In several studies, a polarization by other metals - no matter if thin films, nanoparticles or single atoms - could be shown. However, as far as we know, it has never been demonstrated using an oxide. But in this thesis, using XMCD measurements performed at the Advanced Photon Source of the Argonne National Laboratory, USA, it is unambiguously evidenced that platinum can be polarized by iron oxide nanoparticles. For palladium this is tested as well, but these results are not as clear as for the platinum samples. Furthermore, FORC measurements performed in cooperation with the Max-Planck-Institute for Intelligent Systems, department Schütz, give insight to the details of the individual and overall magnetization reversal of these samples and demonstrate that Pd mediates the coupling better than Pt as it is expected due to its higher Stoner parameter.

Additionally, it is investigated how iron oxide nanoparticles influence the electrical transport properties of palladium. Several very interesting effects could hereby be observed. It is demonstrated that the palladium thin film exhibits a Lorentz magnetoresistance effect which is superimposed by a small anisotropic magnetoresistance effect if nanoparticles are added. They

also cause a significant resistivity increase upon cooling below 180 K. Furthermore, a (most likely) novel NP induced MR effect at 10 K is observed, where the resistivity increases if a magnetic field is applied (out of plane) perpendicular to the current flow direction. However, the investigation of the physical origin of these effects is beyond the scope of this thesis.

In a second project, the iron oxide nanoparticles are used to manufacture nanoparticle macro-polycrystals that exhibit lengths in the order of magnitude of several 0.1 mm. These are obtained by employing a novel centrifuge assisted sedimentation process and carefully adjusting the preparation parameters. It is investigated by extensive SEM studies, how the centrifugation temperature and acceleration influence the number of macrocrystals and how their morphology is affected revealing that the largest total macrocrystal size is found at 10°C (more or less) independent of the acceleration. GISAXS measurements are performed on single macrocrystals, demonstrating that it is indispensable that the nanoparticles exhibit a narrow size distribution to form ordered assemblies. Concerning the nanoparticle order, the largest grains are found at 20°C and 21 000 x g. Furthermore, it is shown that the amount of organic surfactants also has to be considered. If it is too high, this can completely inhibit the formation of macrocrystals.

Finally, a nanoparticle/palladium multilayer is manufactured to investigate polarization and magnetoresistance effects in three dimensional assemblies as well. The attempt to perform a GISAXS measurement on this sample failed due the large scattering length density of palladium. Nevertheless, insight to the nanoparticle arrangement could be gained by SEM images obtained after the deposition of every nanoparticle layer. According to ZFC-FC curves, the palladium matrix seems to influence the transformation of wustite towards maghemite during the oxygen plasma treatment. This results in mixed phase nanoparticles, what also affects the properties of the superspin glass state (according to memory effect measurements). The influence of the nanoparticles on the matrix material observed in the delta-M curves of the two dimensional systems is found in this three dimensional sample as well and it is even more pronounced. However, concerning the resistivity no explicit nanoparticle effect could be observed.

Even though this thesis answers a few questions, it causes several new ones. It should definitely be investigated, how the new polarization effect found in platinum influences electrical components that contain this configuration of materials (e.g. for spintronics). Of course, the polarization of palladium by iron oxide nanoparticles must be verified and lots of measurements are necessary to understand how the electrical transport in a thin palladium layer is influenced by iron oxide nanoparticles. The macrocrystal study gives a good starting point for manufacturing huge, ordered systems out of nanometer sized particles which forms a new kind of artificial material. This is a promising approach for the development of functional materials which employ the dependency of e.g. mechanical or optical properties on an external field. However, the fine tuning of the assembling process still remains to be done.

A Nanoparticle Data Sheet Ocean NanoTech

Ocean NanoTech, LLC
2143 Worth Lane, Springdale, AR 72764
Phone : (479) 751-5500; Fax: (479) 751-5502
E-mail: orders@oceannanotech.com

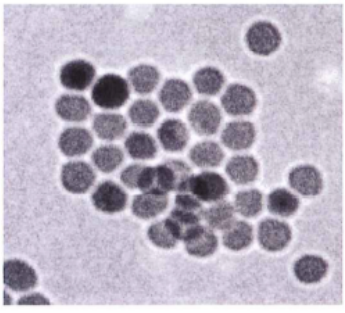
Cetificate of Analysis-Product ID

Catalog number:	SOR-20-0050
Product name:	Iron Oxide Nanocrystals with Oleic Acid Coating
Lot number:	010411
Solvent:	Toluene
Size tolerance:	±2.5 nm
Surface group:	Oleic Acid
Storage:	4-25°C
Shelf life:	6 months
Volume:	2 mL
Concentration:	25 mg/mL

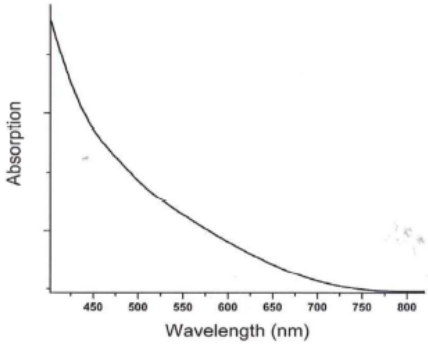
Analysis

PROPERTY	SPECIFICATIONS	METHOD
IO Size	20 nm	TEM
Absorbance	N/A	Spectrophotometry

TEM Image



Absorption Spectra



Signature: John DiXon

Date: 5-1-13

Disclaimer: For R&D only. Not intended for food, drug, household, agricultural, or cosmetic use. Ocean NanoTech, LLC shall not be held liable for any damage resulting from handling or contact with the above product.

B Sample List 2D

Sample number	Nanoparticles	Substrate	Sample preparation
1-01	Iron oxide / 20 nm / 010411	Silicon	25 mg/ml / 3000 rpm
2-01	Iron oxide / 20 nm / 010411	Silicon	$\frac{25}{8}$ mg/ml / 600 rpm
2-02	Iron oxide / 20 nm / 010411	Silicon	$\frac{25}{8}$ mg/ml / 1200 rpm
2-03	Iron oxide / 20 nm / 010411	Silicon	$\frac{25}{8}$ mg/ml / 1800 rpm
2-04	Iron oxide / 20 nm / 010411	Silicon	$\frac{25}{8}$ mg/ml / 2400 rpm
2-05	Iron oxide / 20 nm / 010411	Silicon	$\frac{25}{8}$ mg/ml / 3000 rpm
2-06	Iron oxide / 20 nm / 010411	Silicon	$\frac{25}{5}$ mg/ml / 3000 rpm
2-07	Iron oxide / 20 nm / 010411	Silicon	$\frac{25}{10}$ mg/ml / 3000 rpm
2-08	Iron oxide / 20 nm / 010411	Silicon	$\frac{25}{15}$ mg/ml / 3000 rpm
2-09	Iron oxide / 20 nm / 010411	Silicon	$\frac{25}{20}$ mg/ml / 3000 rpm
2-10	Iron oxide / 20 nm / 010411	Silicon	$\frac{25}{30}$ mg/ml / 3000 rpm
3-01	Iron oxide / 20 nm / 010411	Silicon	$\frac{25}{30}$ mg/ml / 3000 rpm Plasma 30min 300W 200ml/min
3-02	Iron oxide / 20 nm / 010411	Silicon	$\frac{25}{30}$ mg/ml / 3000 rpm Plasma 2min 300W 200ml/min
3-03	Iron oxide / 20 nm / 010411	Silicon	$\frac{25}{30}$ mg/ml / 3000 rpm Plasma 2min 300W 200ml/min Hotplate 85° C 3h
3-04	Iron oxide / 20 nm / 010411	Silicon	$\frac{25}{30}$ mg/ml / 3000 rpm Plasma 30s 300W 200ml/min Hotplate 85° C 3h
3-05	Iron oxide / 20 nm / 010411	Silicon	$\frac{25}{30}$ mg/ml / 3000 rpm Plasma 10s 300W 200ml/min Hotplate 85° C 3h
3-06	Iron oxide / 20 nm / 010411	Silicon	$\frac{25}{30}$ mg/ml / 3000 rpm Hotplate 85° C 3h
3-07	Iron oxide / 20 nm / 010411	Silicon	$\frac{25}{30}$ mg/ml / 3000 rpm Plasma 11min 300W 200ml/min
3-08	Iron oxide / 20 nm / 010411	Silicon	$\frac{25}{30}$ mg/ml / 3000 rpm Plasma 12min 300W 200ml/min
4-01	Iron oxide / 20 nm / 010411	Silicon	$\frac{25}{30}$ mg/ml / 3000 rpm Plasma 30min 300W 200ml/min Pt 2 nm IBS
4-02	Iron oxide / 20 nm / 010411	Silicon	$\frac{25}{30}$ mg/ml / 3000 rpm Plasma 30min 300W 200ml/min Pd 5 nm IBS

C Magnetometry

Hysteresis loops

Sample number	Temperature	Slope for diamagn. corr.	H_c [T]	Exchange bias [T]
1-01	300 K	$-1.250 \cdot 10^{-9}$	-	
1-01	5 K	$-1.154 \cdot 10^{-9}$	-0.16 / +0.09	0.035
2-10	300 K	$-5.007 \cdot 10^{-9}$	-	
2-10	5 K	$-5.258 \cdot 10^{-9}$	-0.24 / +0.16	0.04
3-01	300 K	$-2.667 \cdot 10^{-9}$	-	
3-01	5 K	$-2.718 \cdot 10^{-9}$	-0.027 / +0.033	0.003
3-02	300 K	$-5.165 \cdot 10^{-9}$	-	
3-02	5 K	$-5.260 \cdot 10^{-9}$	-0.23 / +0.162	0.034
3-03	300 K	$-2.996 \cdot 10^{-9}$	-	
3-03	5 K	$-2.292 \cdot 10^{-9}$	-0.04 / +0.02	0.01
4-01	300 K	$-2.121 \cdot 10^{-8}$	-	
4-01	5 K	$-1.895 \cdot 10^{-8}$	-0.03 / +0.04	0.005
4-02	300 K	$-1.690 \cdot 10^{-8}$	-	
4-02	5 K	$-3.703 \cdot 10^{-9}$	-0.023 / +0.017	0.003

ZFC-FC curves

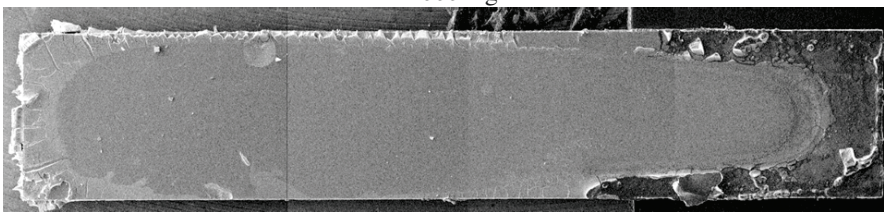
Sample number	T_B	T_N
1-01	245 K	210 K
2-10	237 K	210 K
3-01	175 K	-
3-02	175 K / 237 K	210 K
3-03	175 K / 237 K	210 K
3-04	175 K / 237 K	210 K
3-05	237 K	210 K
3-06	237 K	210 K
3-07	175 K / 237 K	210 K
3-08	200 K	-
4-01	200 K	-
4-02	200 K	-

D SEM Images of Macrocrystals

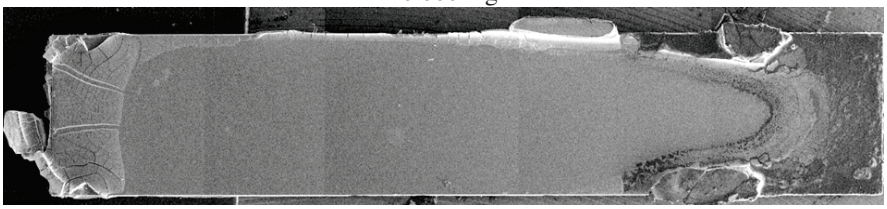
SEM images of the macrocrystals formed on top of 10x2 mm^2 silicon substrates. The left-hand side of the images shows the sample area that was placed in the sample tube bottom while drying.

Batch O1 - Centrifugation Temperature 0°C

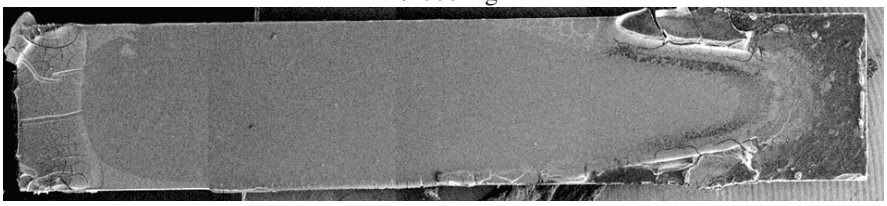
21 000 x g



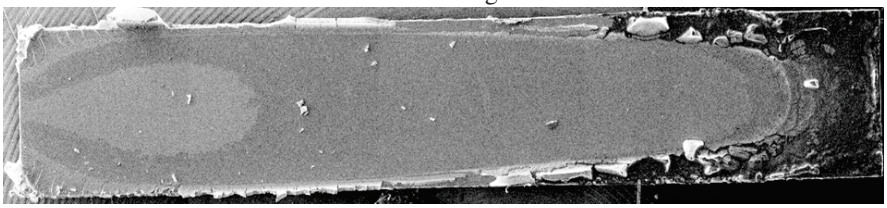
20 000 x g



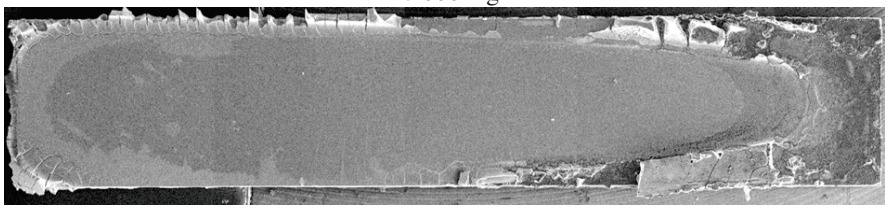
19 000 x g



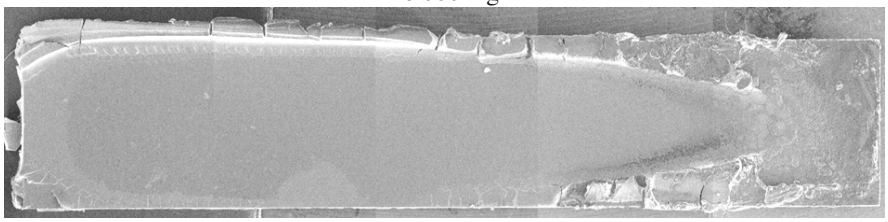
18 000 x g



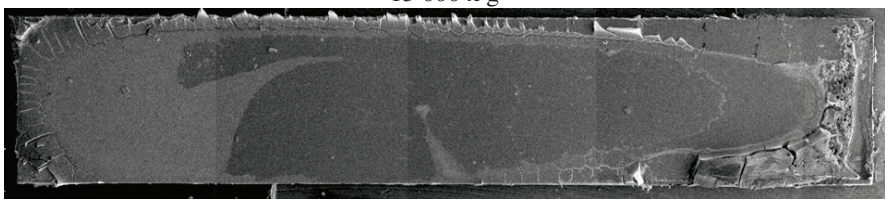
17 000 x g



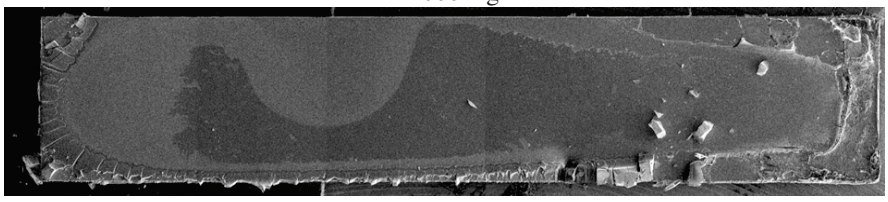
16 000 x g



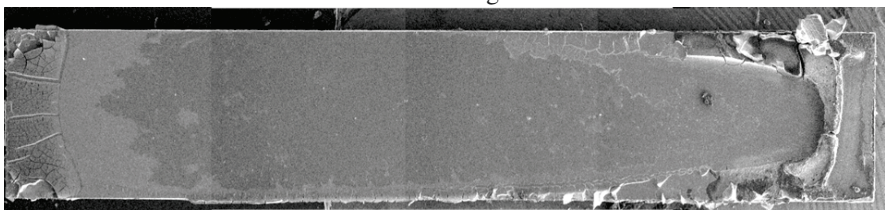
15 000 x g



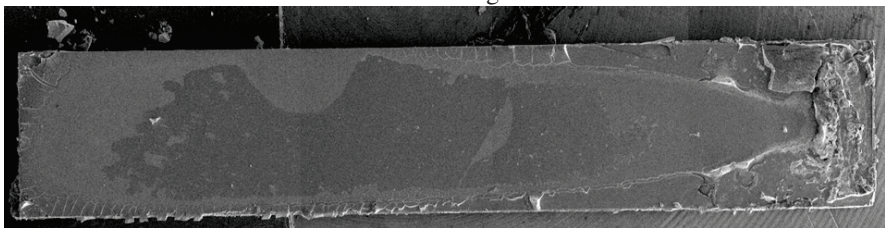
14 000 x g



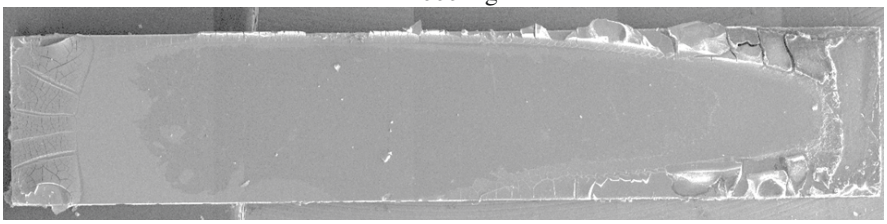
13 000 x g



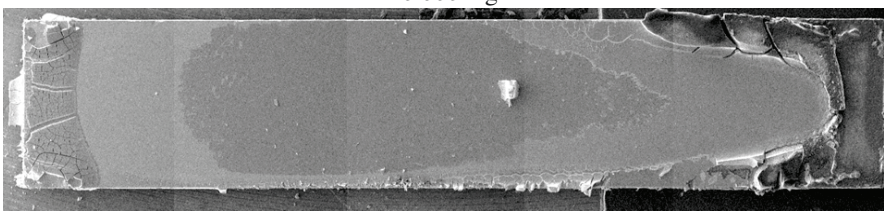
12 000 x g



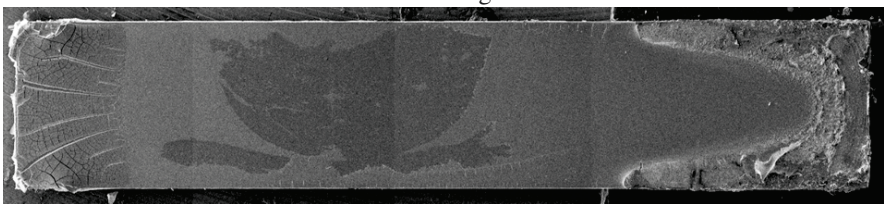
11 000 x g



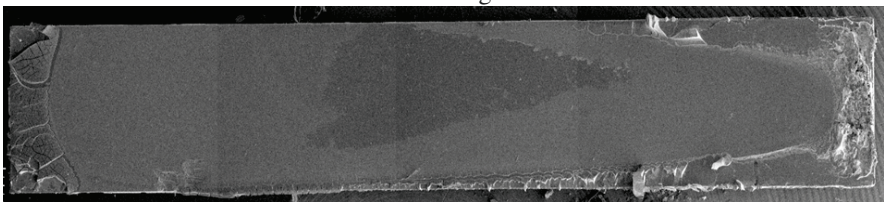
10 000 x g



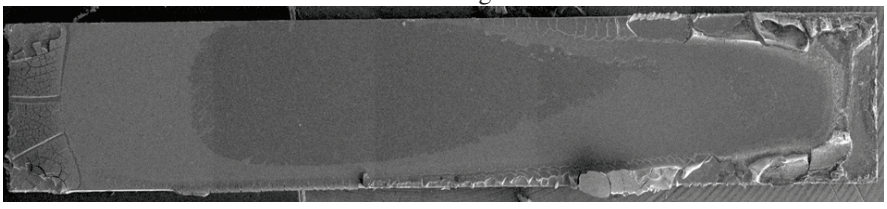
9 000 x g



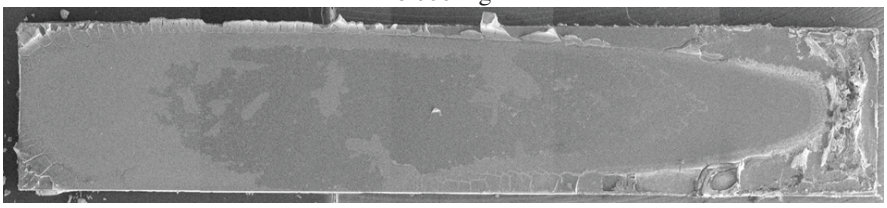
8 000 x g



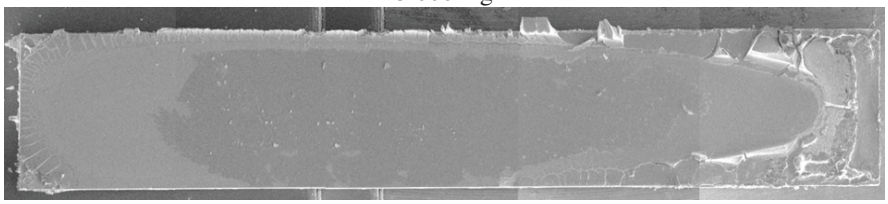
7 000 x g



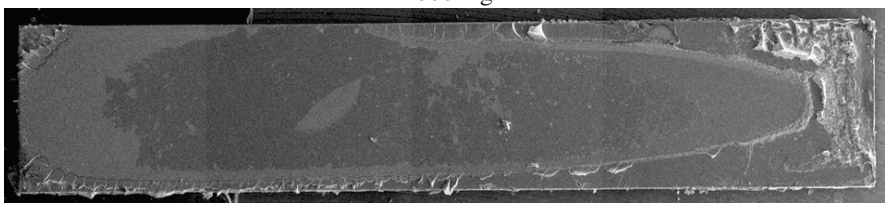
6 000 x g



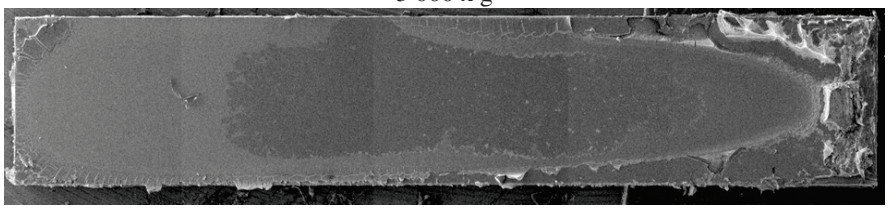
5 000 x g



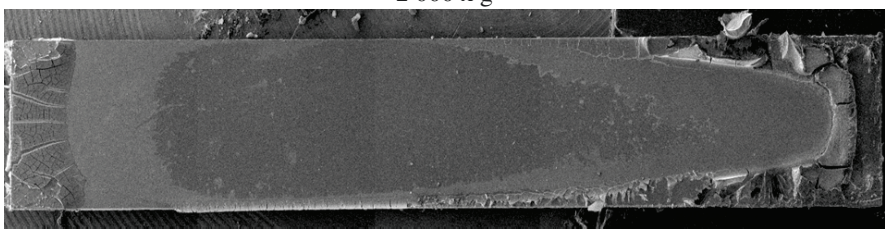
4 000 x g



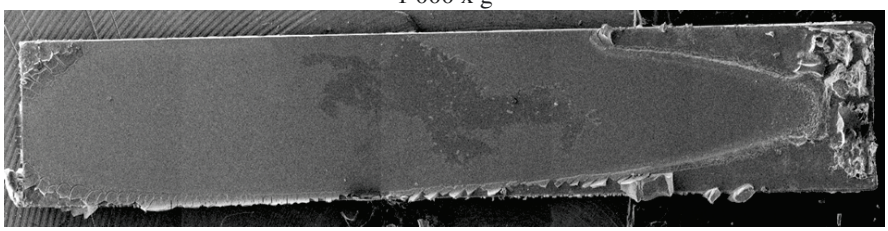
3 000 x g



2 000 x g

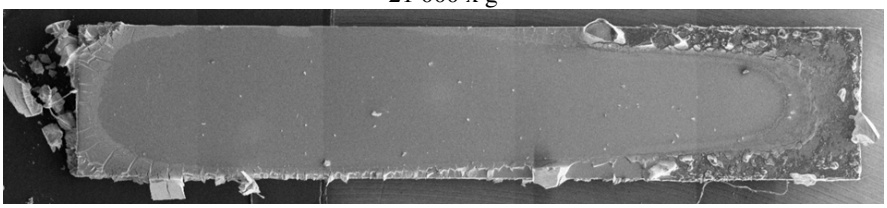


1 000 x g

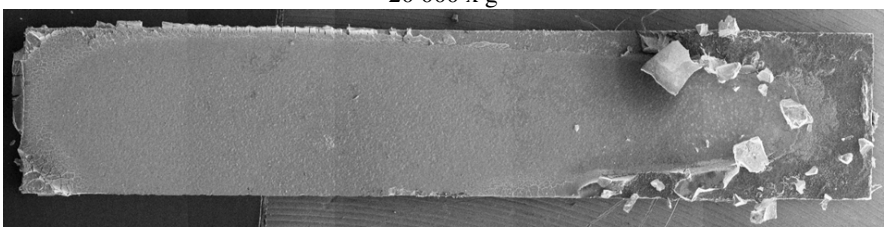


Batch O1 - Centrifugation Temperature 0°C - Reproduced

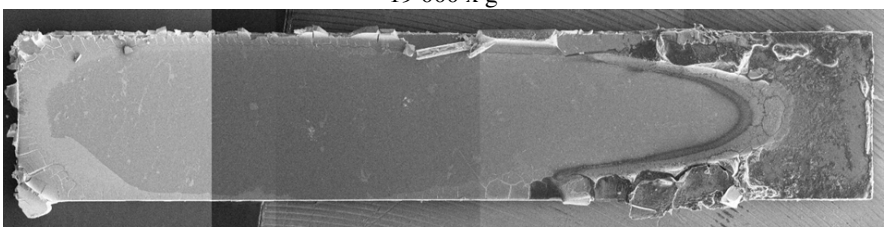
21 000 x g



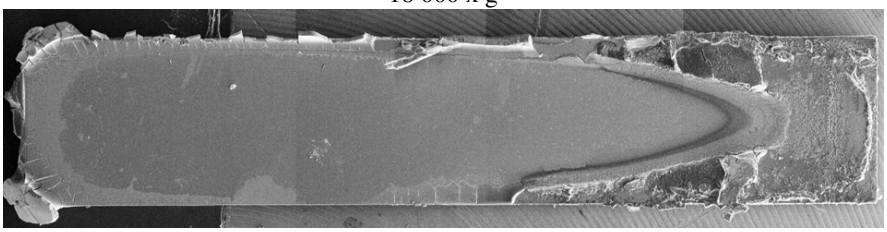
20 000 x g



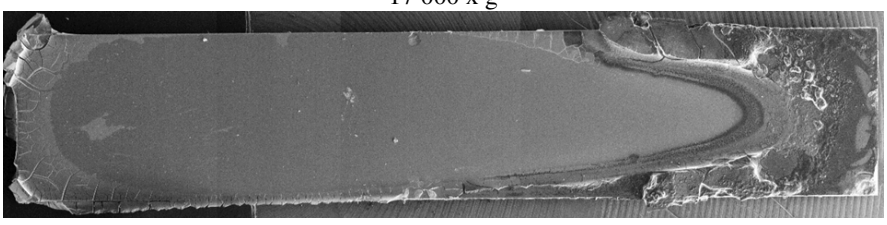
19 000 x g



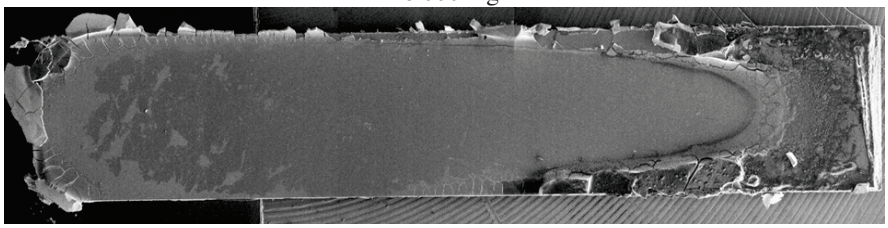
18 000 x g



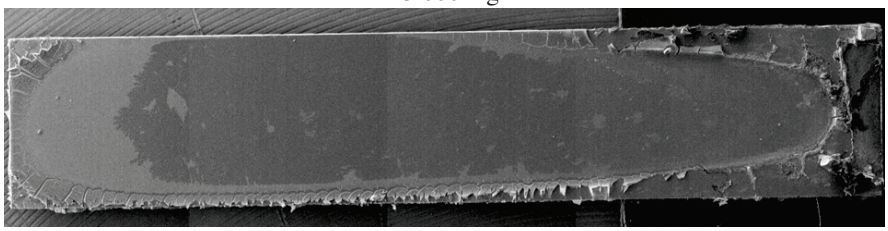
17 000 x g



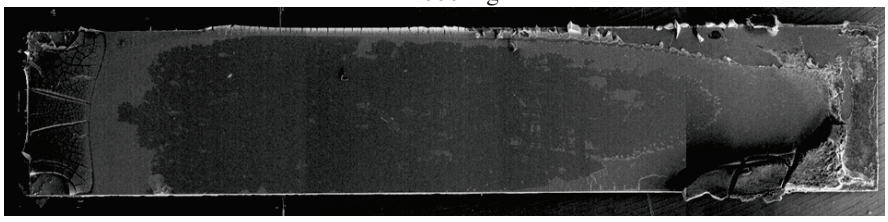
16 000 x g



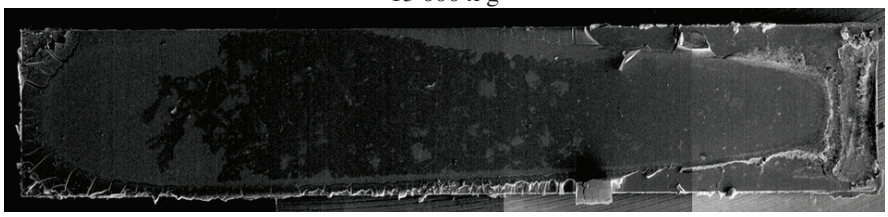
15 000 x g



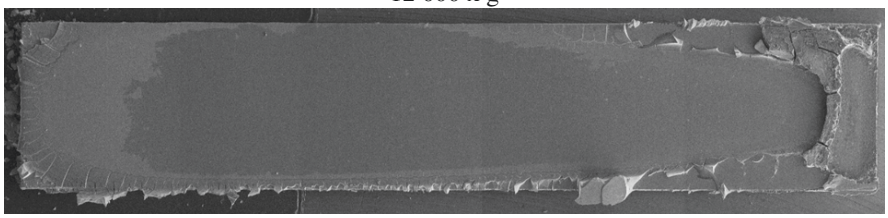
14 000 x g



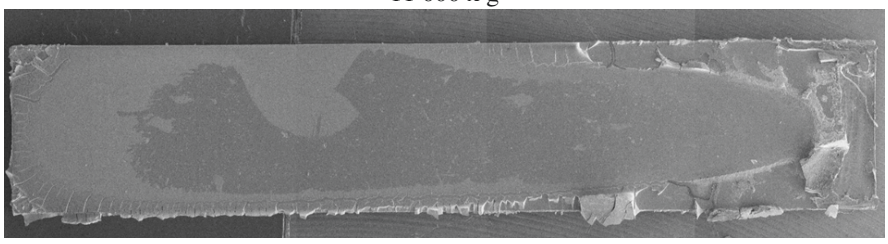
13 000 x g



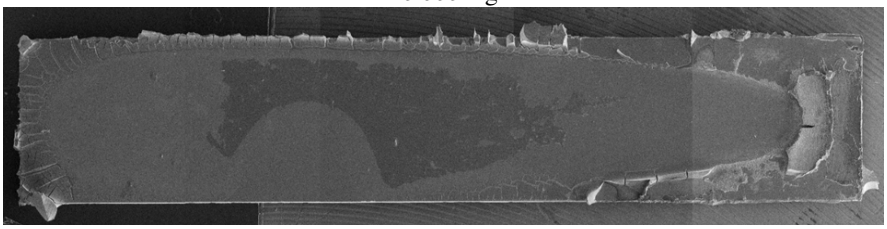
12 000 x g



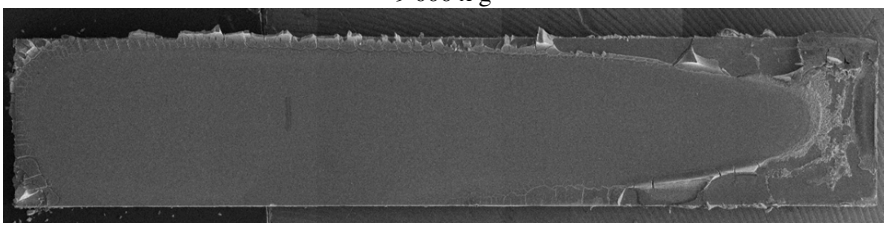
11 000 x g



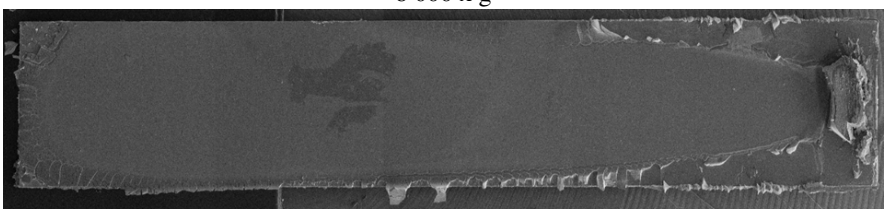
10 000 x g



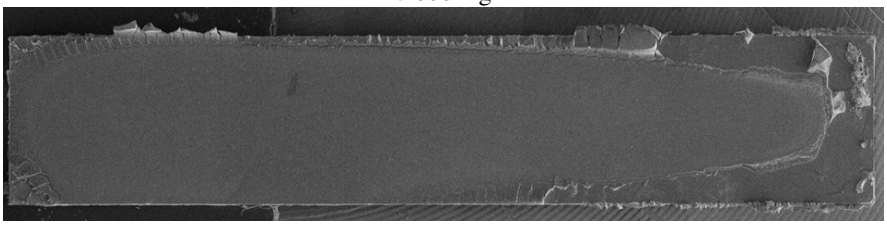
9 000 x g



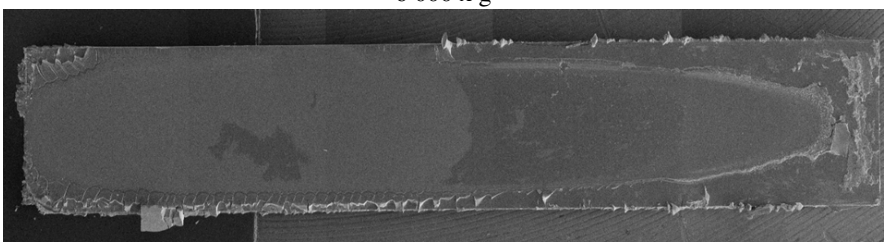
8 000 x g



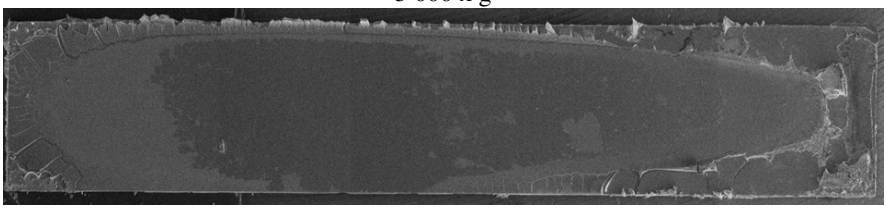
7 000 x g



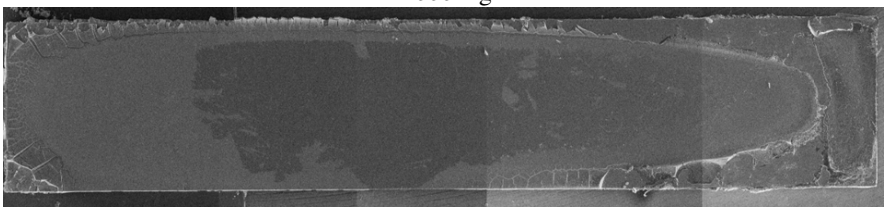
6 000 x g



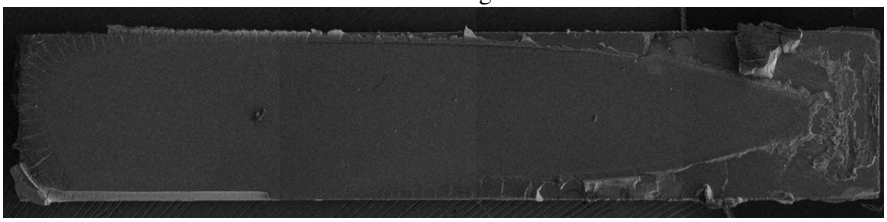
5 000 x g



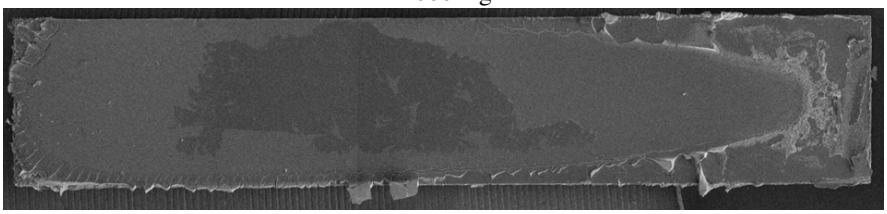
4 000 x g



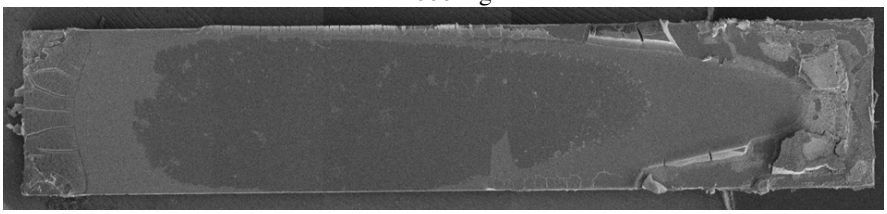
3 000 x g



2 000 x g

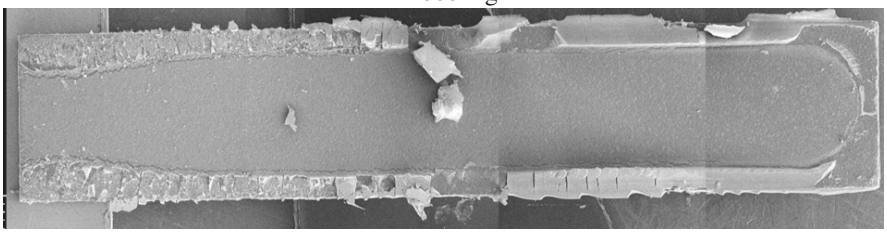


1 000 x g

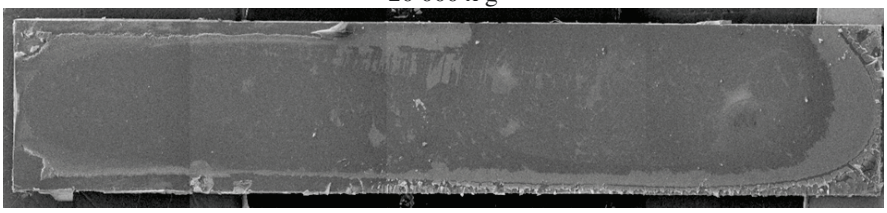


Batch O1 - Centrifugation Temperature 10°C

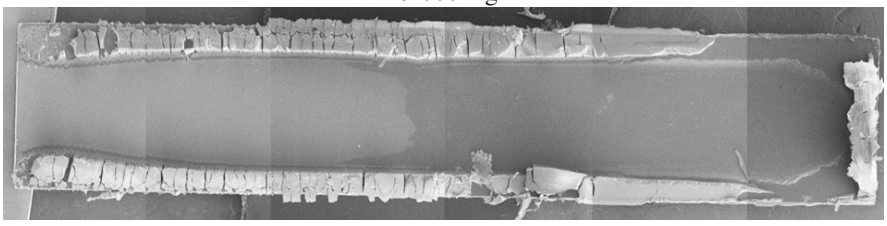
21 000 x g



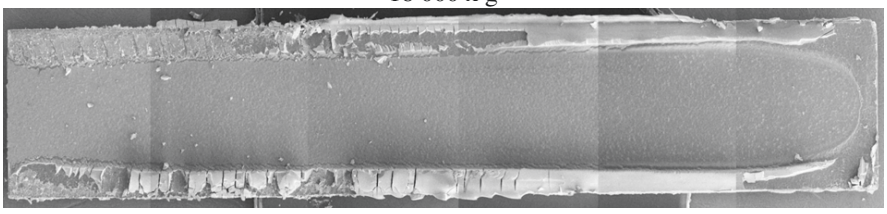
20 000 x g



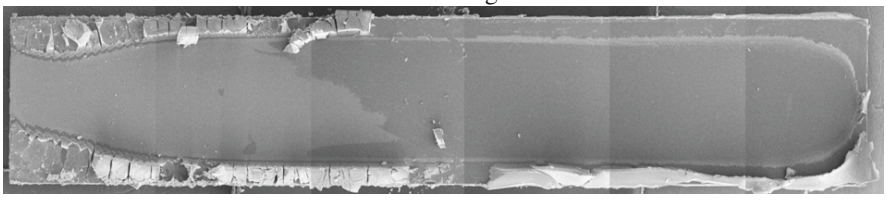
19 000 x g



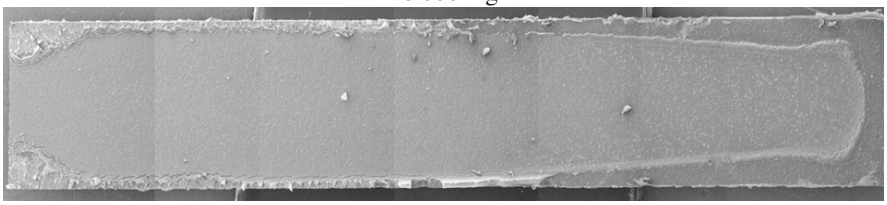
18 000 x g



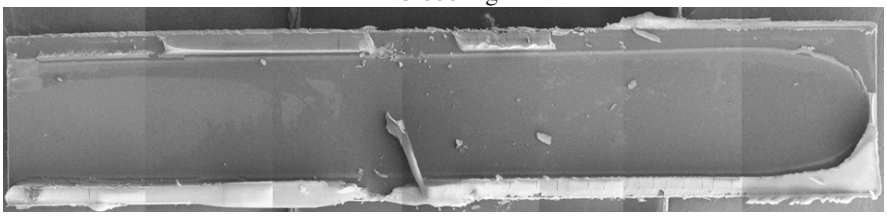
17 000 x g



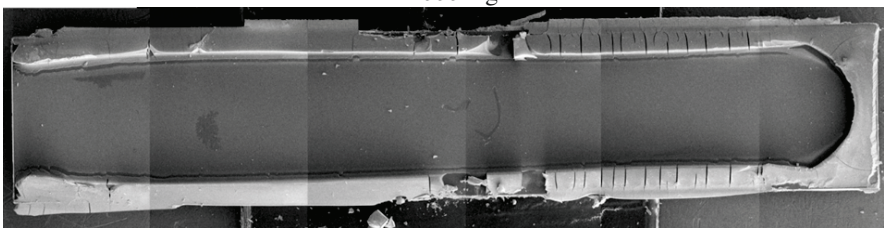
16 000 x g



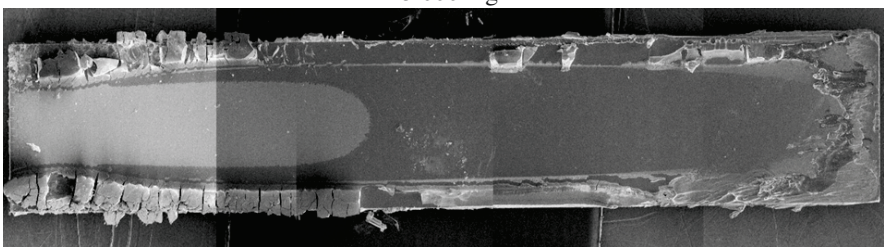
15 000 x g



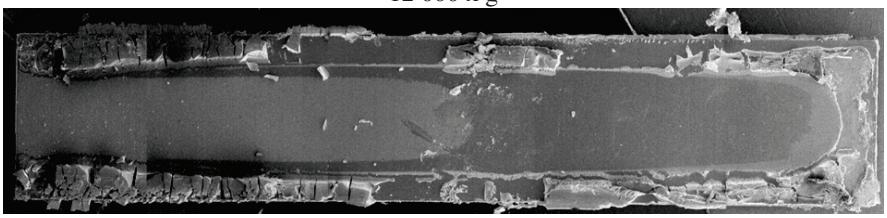
14 000 x g



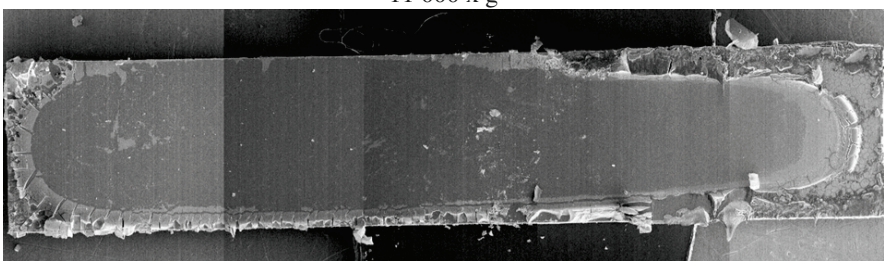
13 000 x g



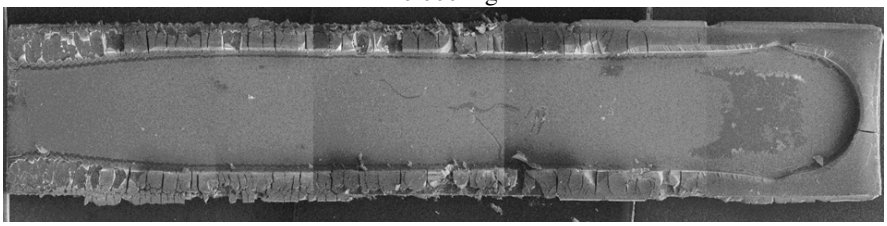
12 000 x g



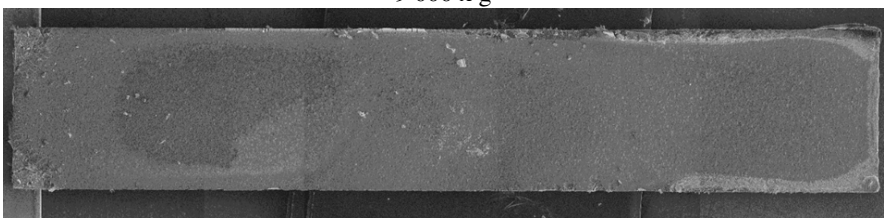
11 000 x g



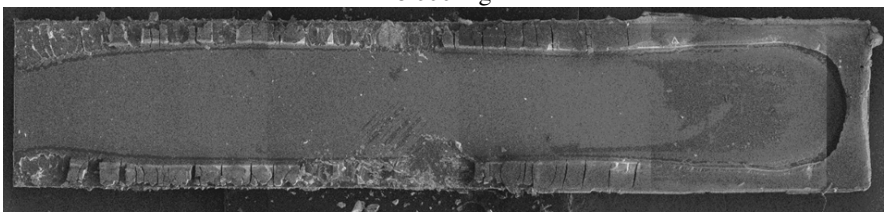
10 000 x g



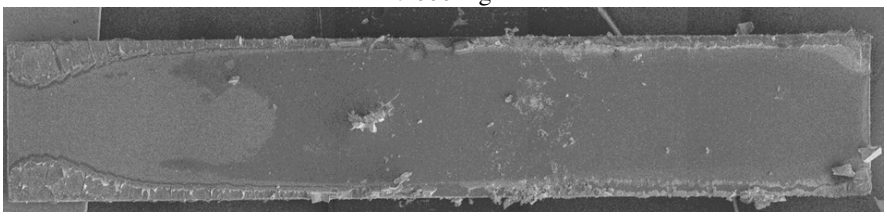
9 000 x g



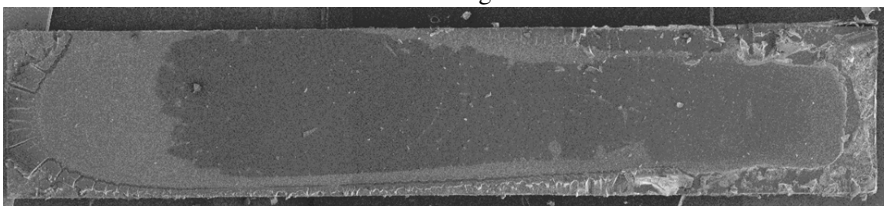
8 000 x g



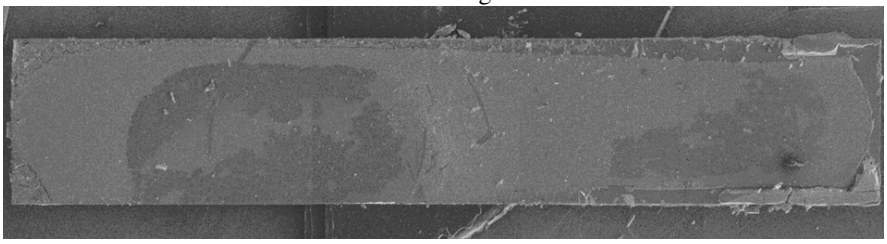
7 000 x g



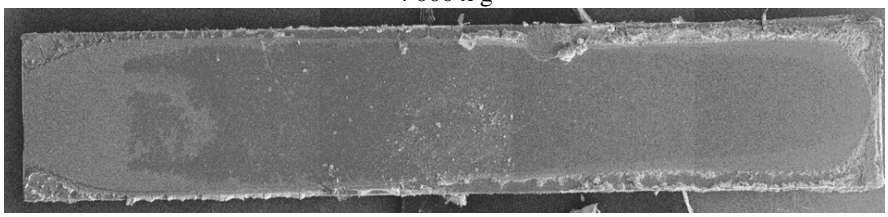
6 000 x g



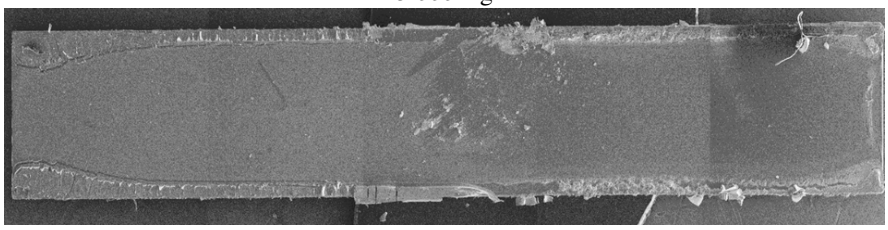
5 000 x g



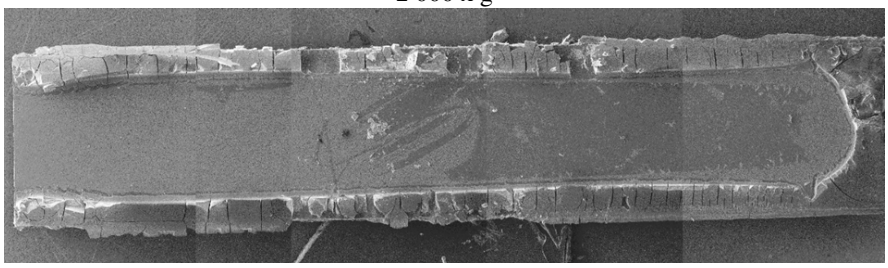
4 000 x g



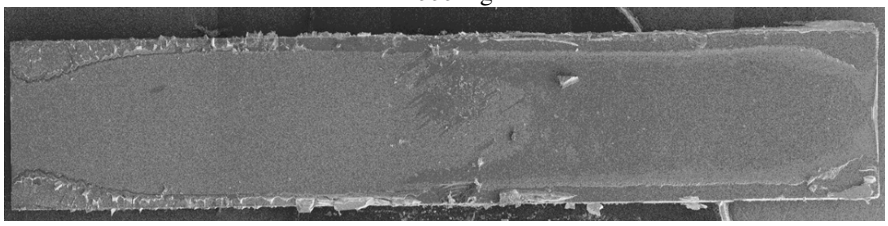
3 000 x g



2 000 x g

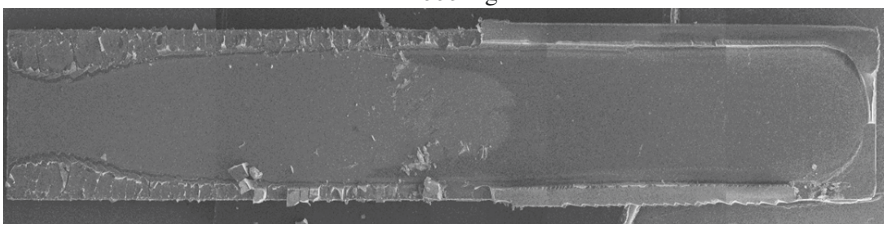


1 000 x g

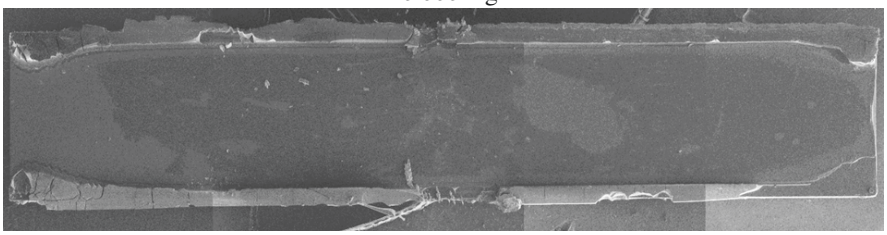


Batch O1 - Centrifugation Temperature 10°C - Reproduced

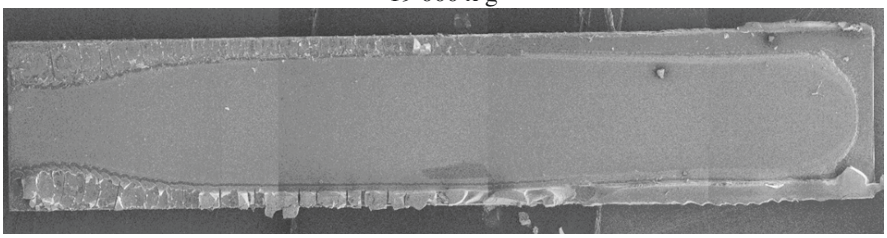
21 000 x g



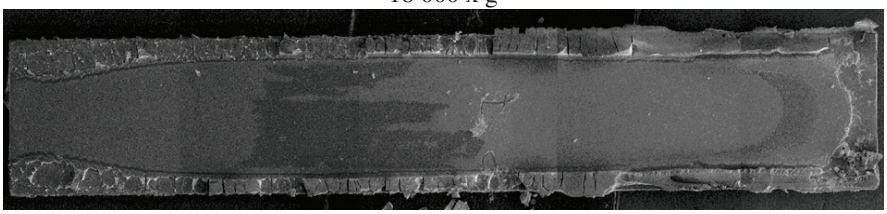
20 000 x g



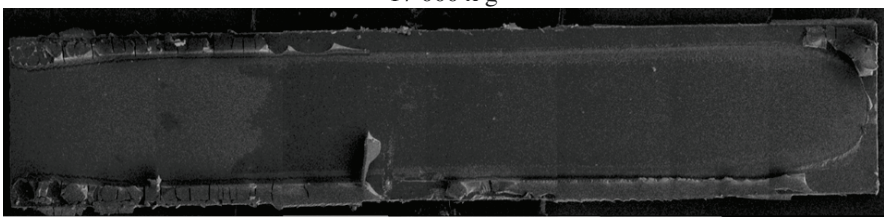
19 000 x g



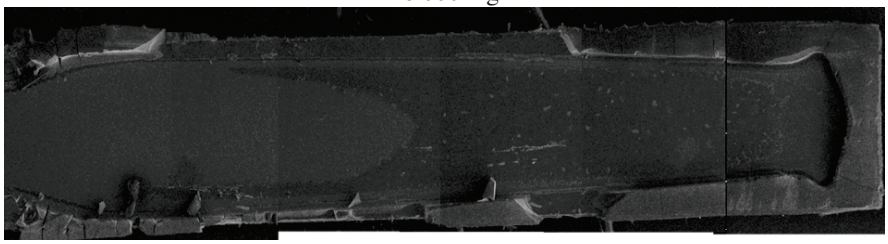
18 000 x g



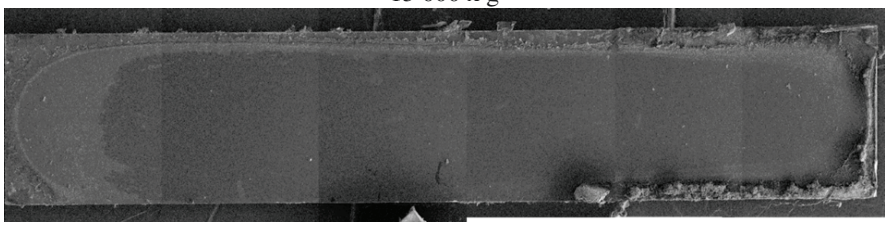
17 000 x g



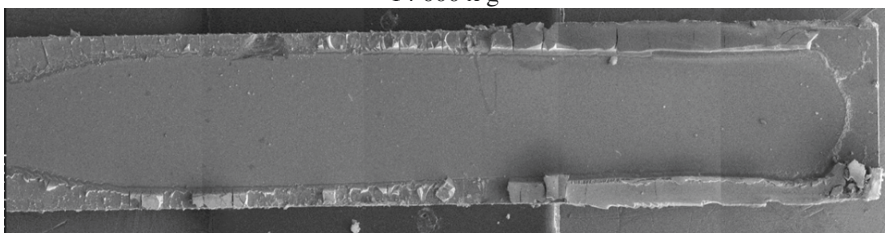
16 000 x g



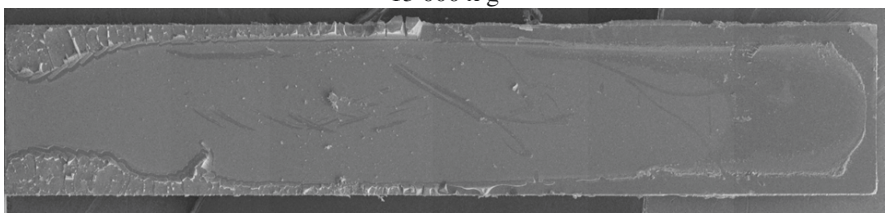
15 000 x g



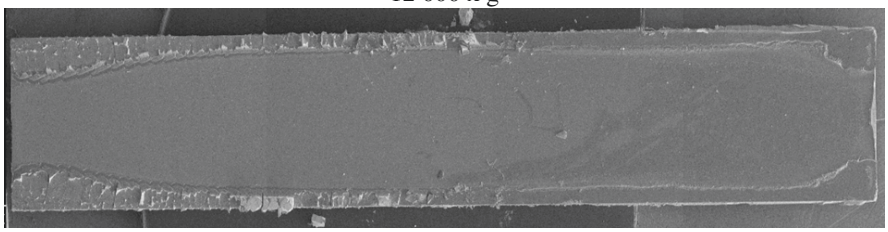
14 000 x g



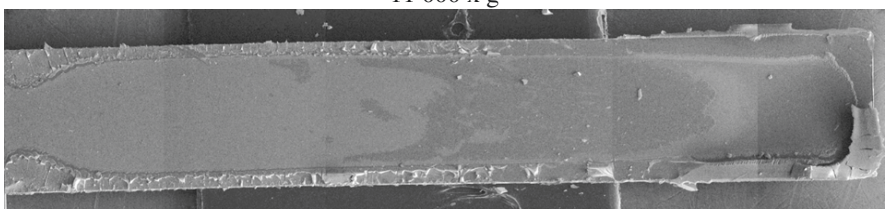
13 000 x g



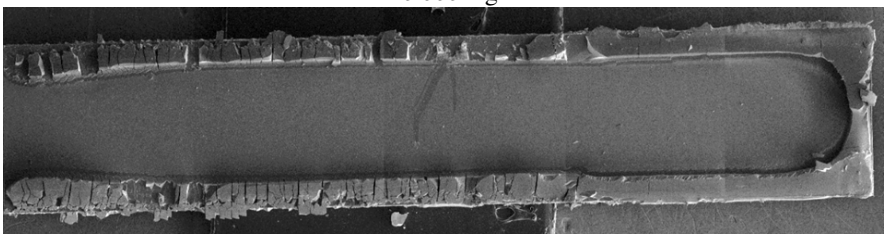
12 000 x g



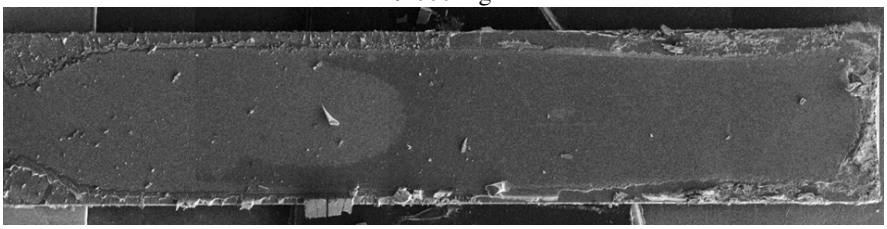
11 000 x g



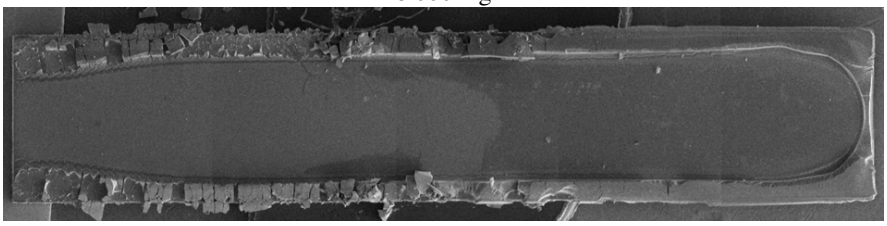
10 000 x g



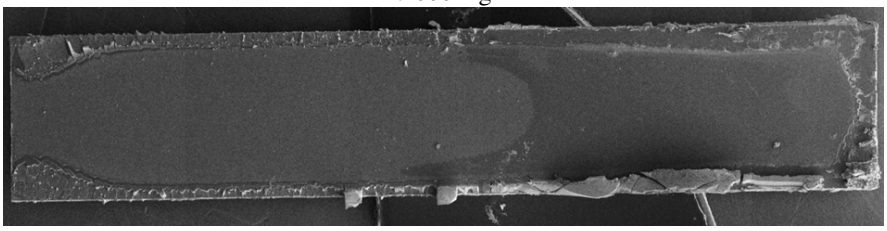
9 000 x g



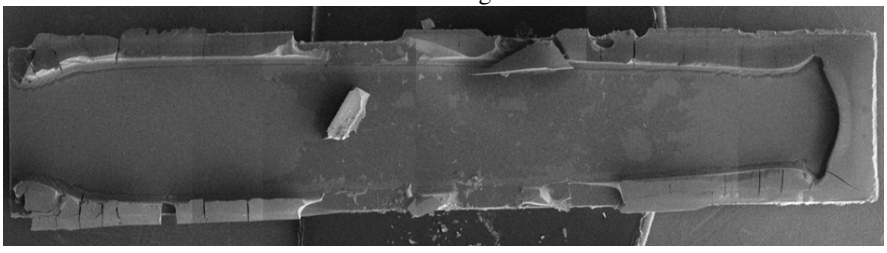
8 000 x g



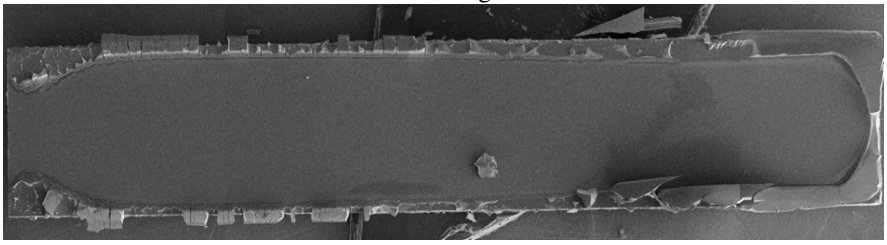
7 000 x g



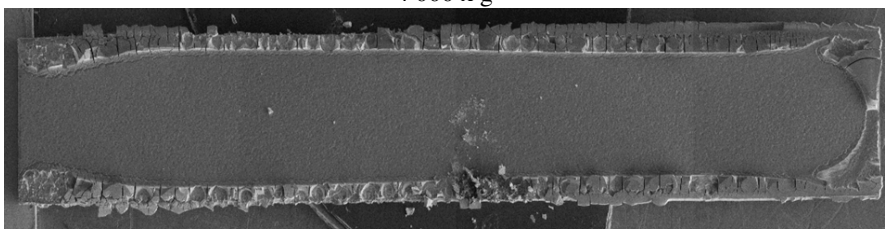
6 000 x g



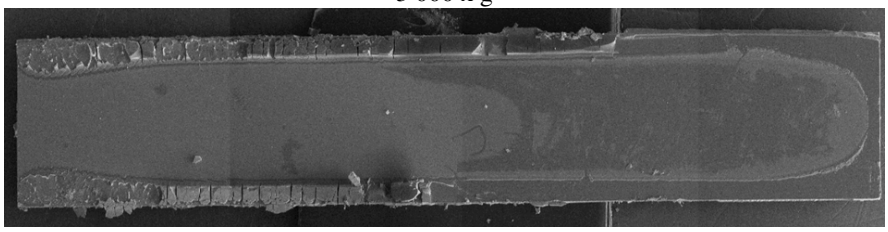
5 000 x g



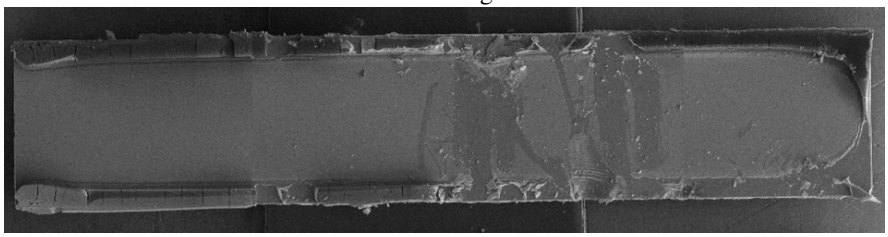
4 000 x g



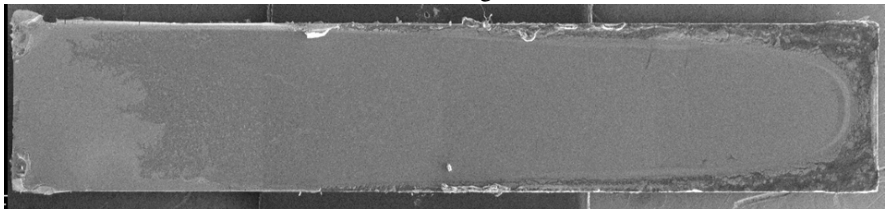
3 000 x g



2 000 x g

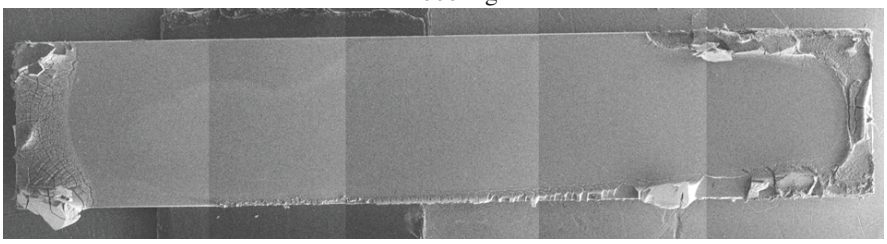


1 000 x g

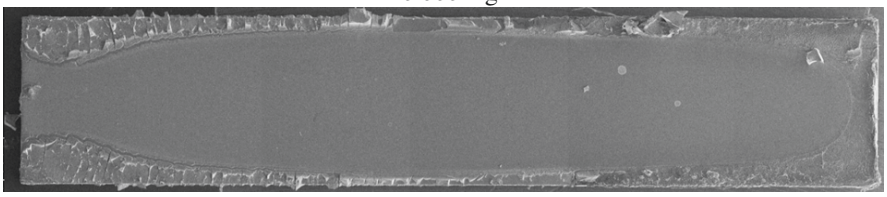


Batch O1 - Centrifugation Temperature 20°C

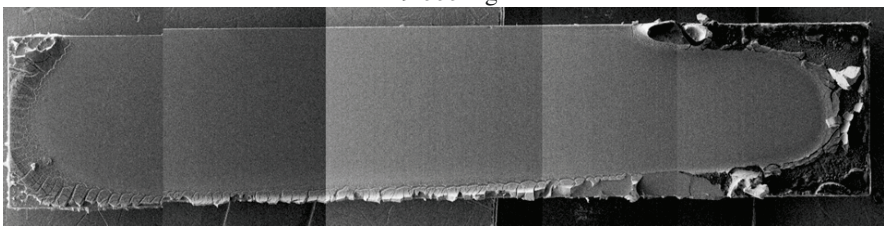
21 000 x g



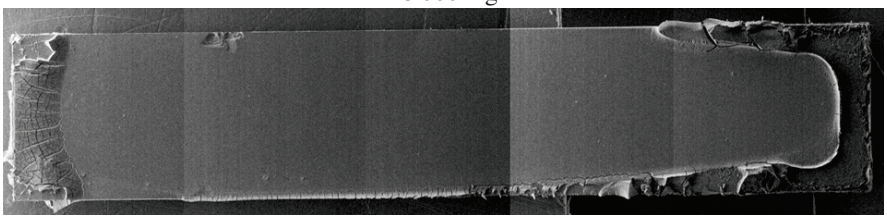
20 000 x g



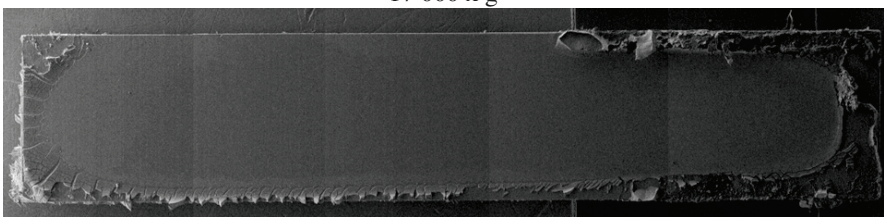
19 000 x g



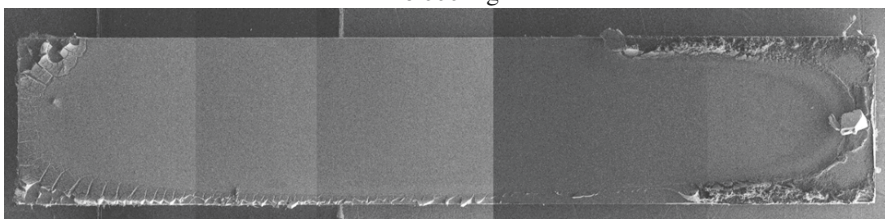
18 000 x g



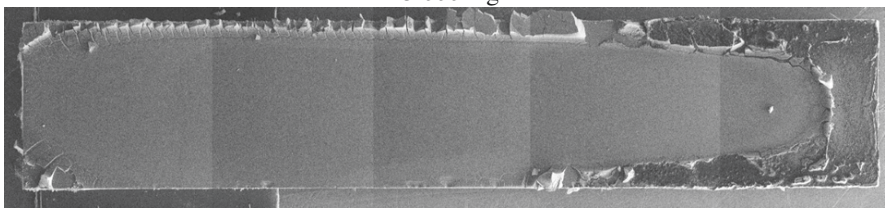
17 000 x g



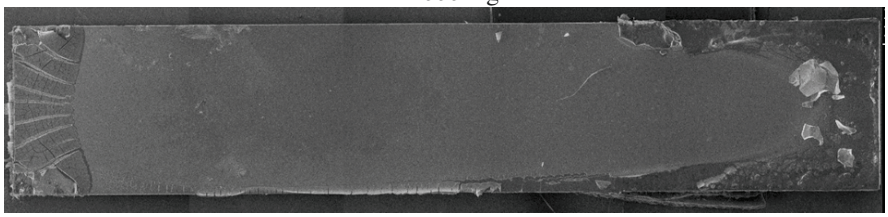
16 000 x g



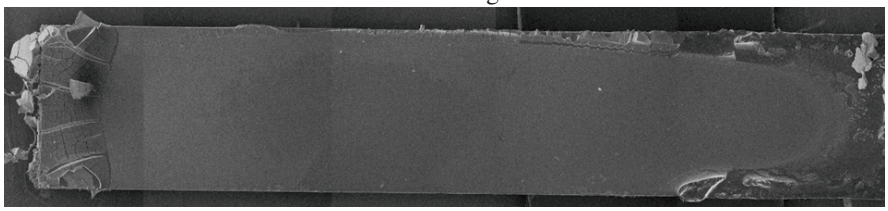
15 000 x g



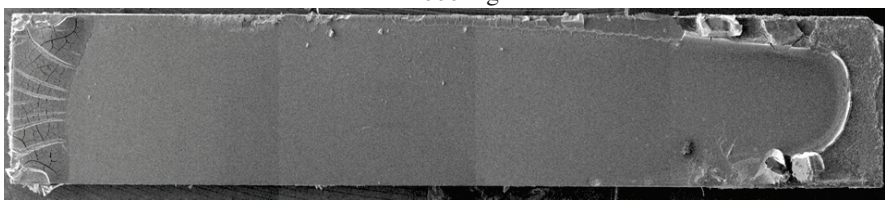
14 000 x g



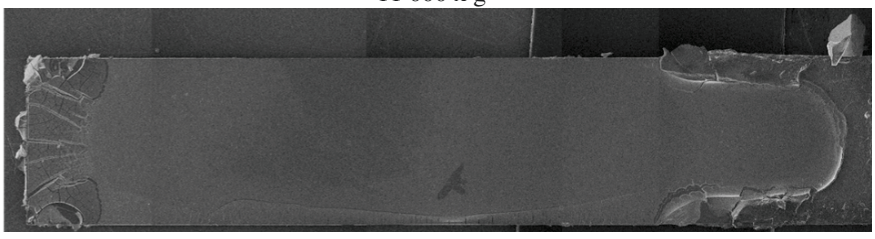
13 000 x g



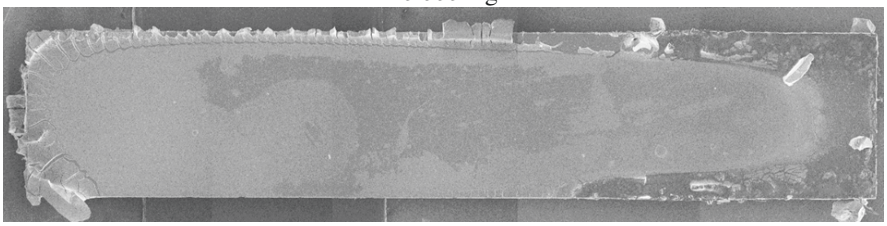
12 000 x g



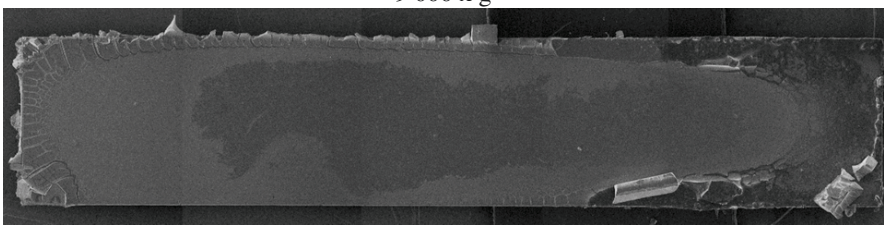
11 000 x g



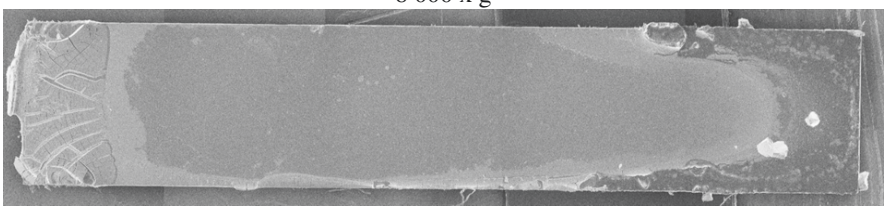
10 000 x g



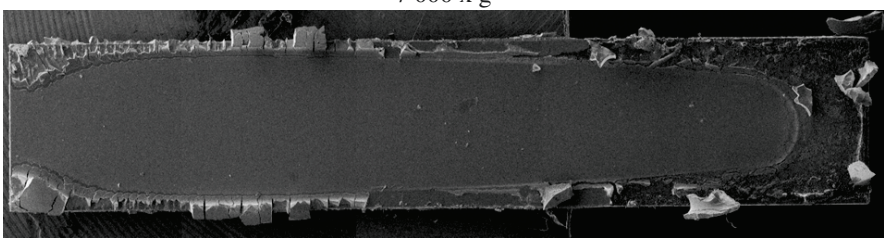
9 000 x g



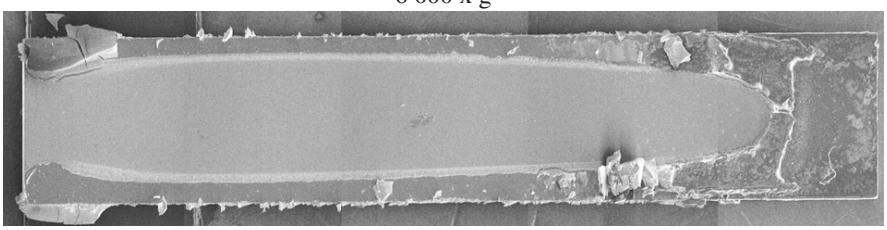
8 000 x g



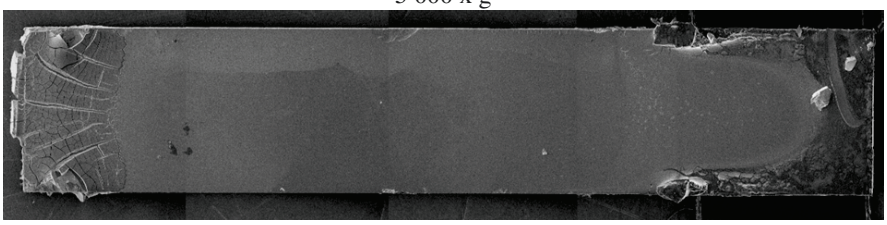
7 000 x g



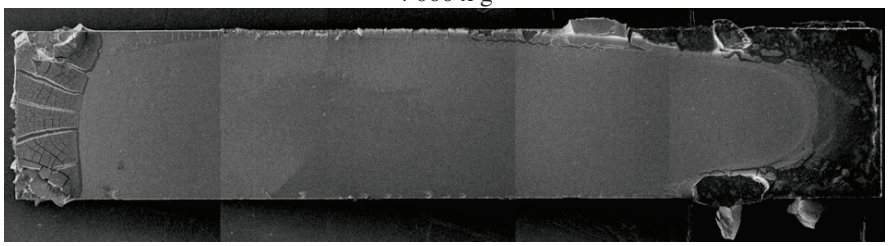
6 000 x g



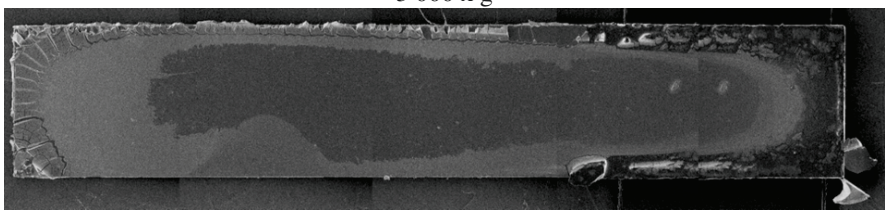
5 000 x g



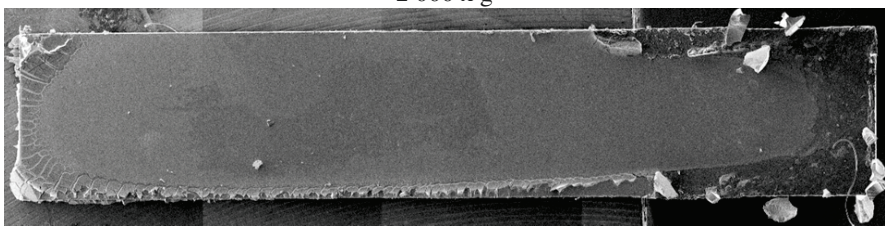
4 000 x g



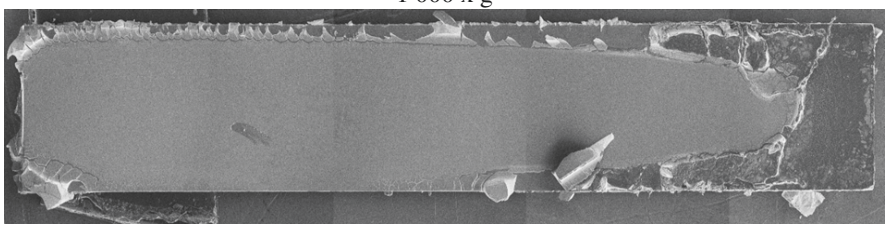
3 000 x g



2 000 x g

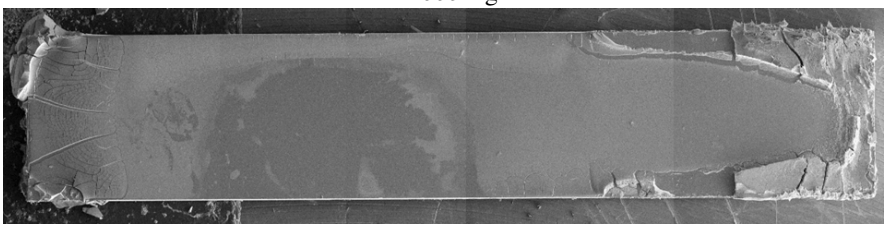


1 000 x g

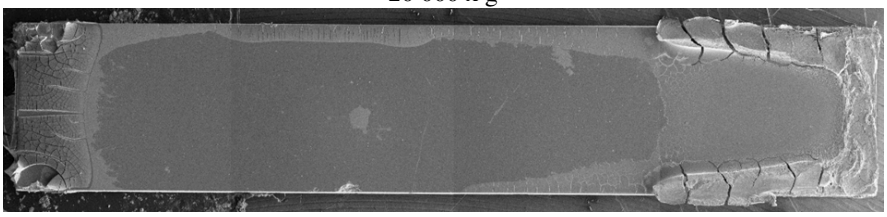


Batch O1 - Centrifugation Temperature 20°C - Reproduced

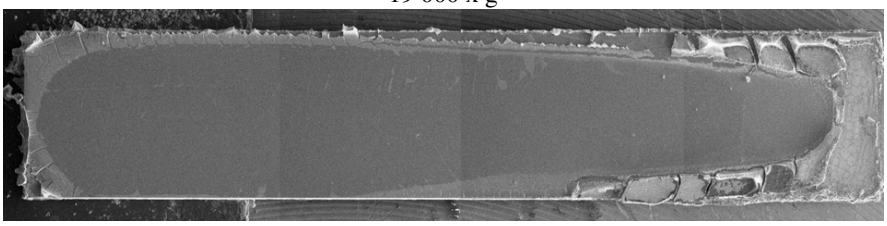
21 000 x g



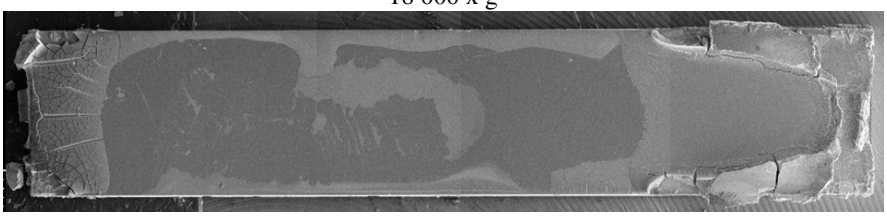
20 000 x g



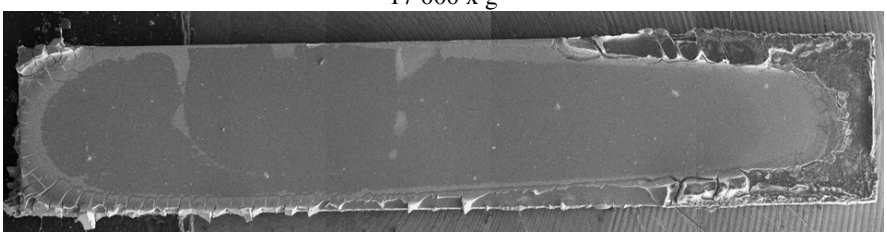
19 000 x g



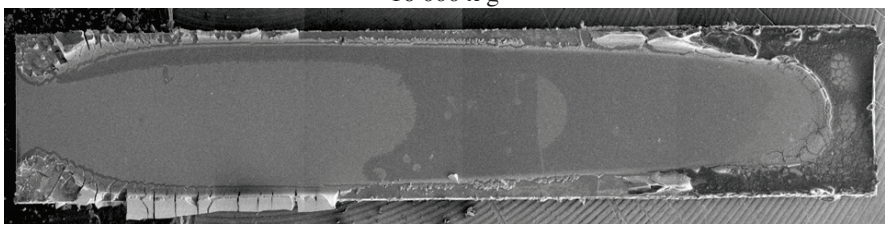
18 000 x g



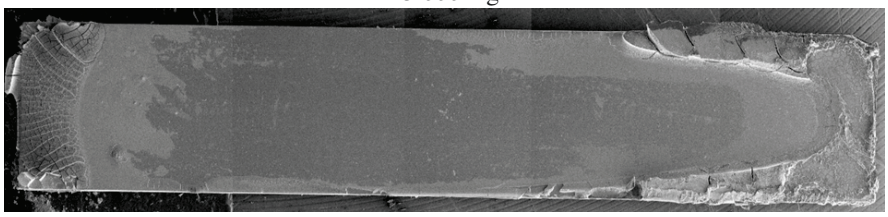
17 000 x g



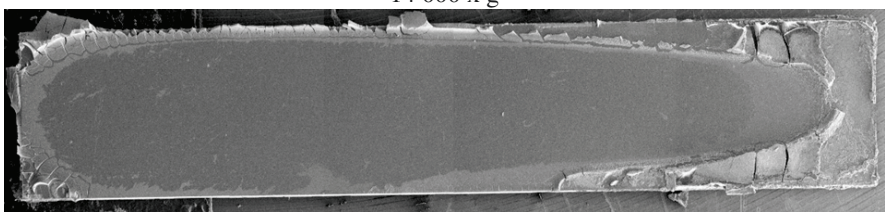
16 000 x g



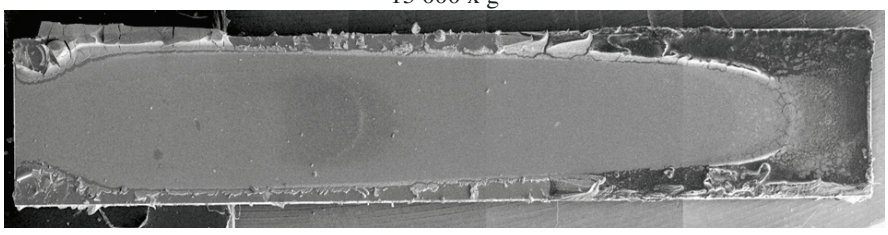
15 000 x g



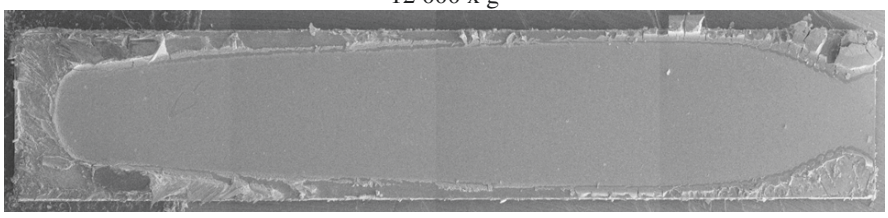
14 000 x g



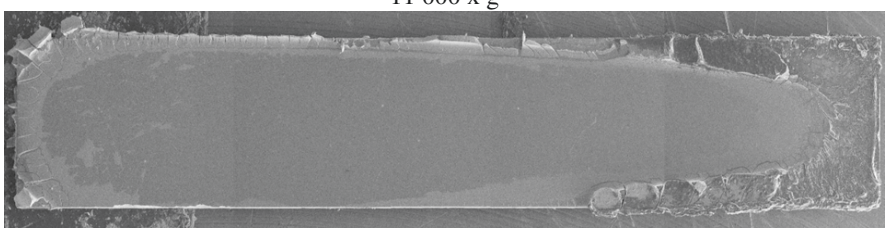
13 000 x g



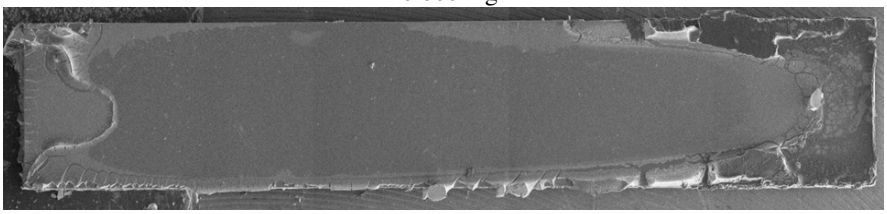
12 000 x g



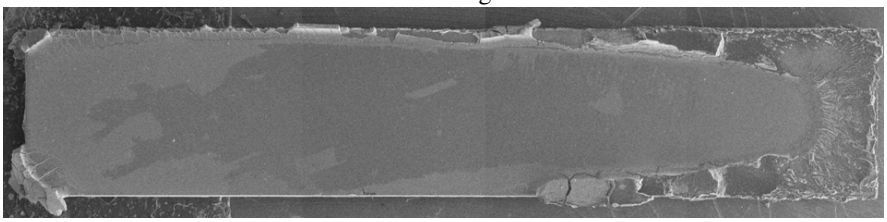
11 000 x g



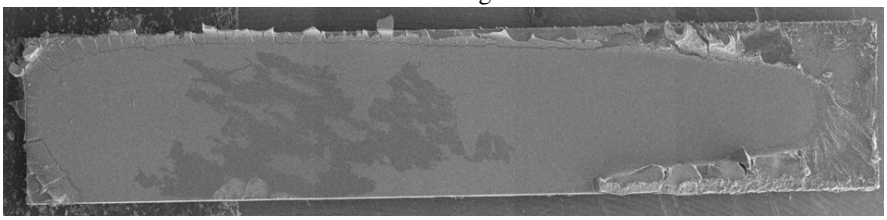
10 000 x g



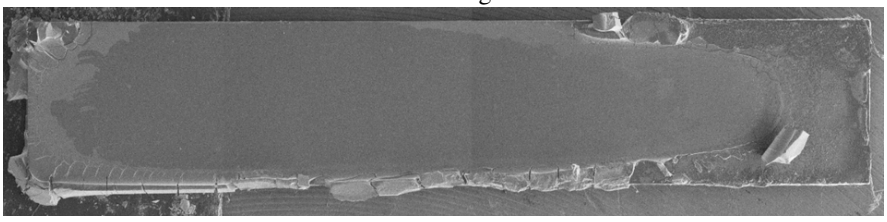
9 000 x g



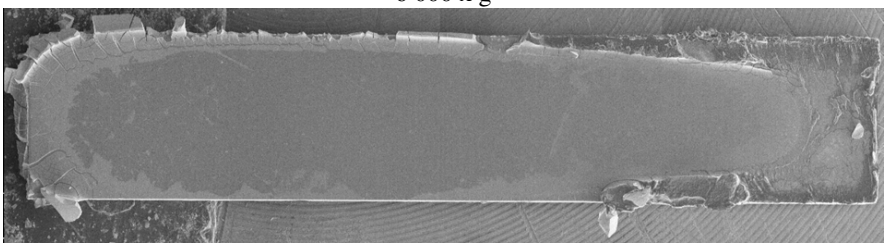
8 000 x g



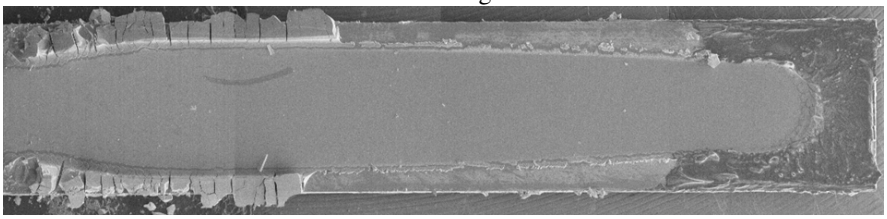
7 000 x g



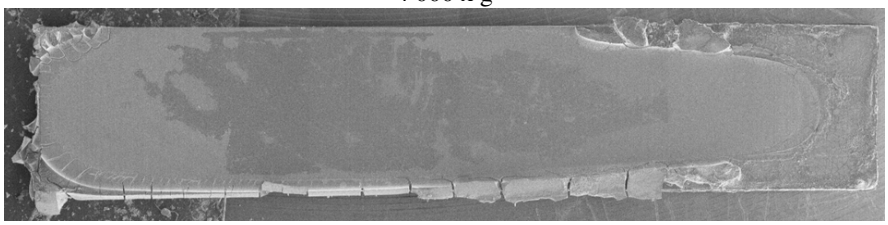
6 000 x g



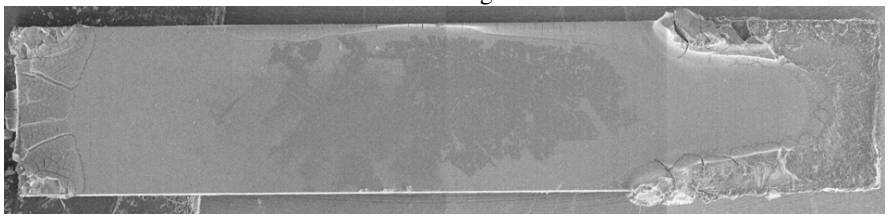
5 000 x g



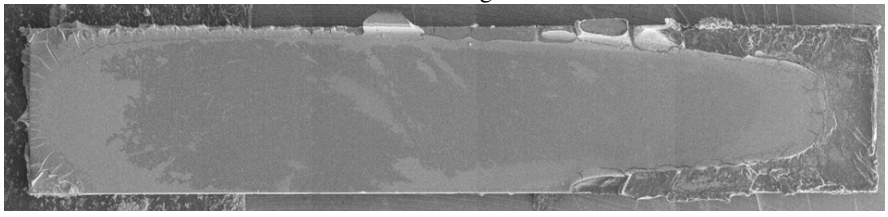
4 000 x g



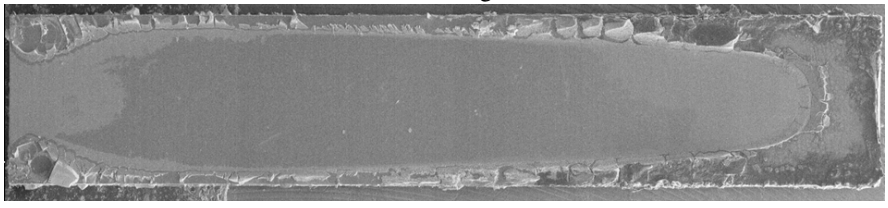
3 000 x g



2 000 x g

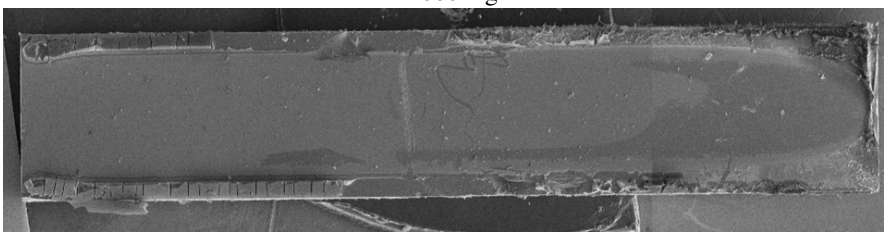


1 000 x g

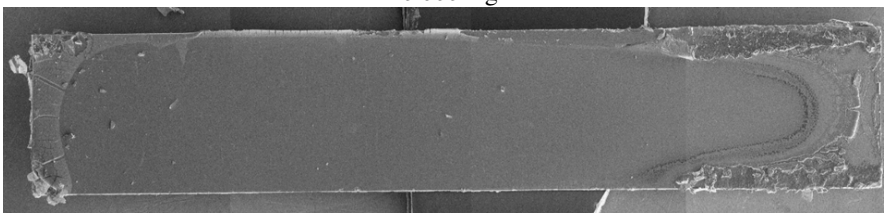


Batch O1 - Centrifugation Temperature 30°C

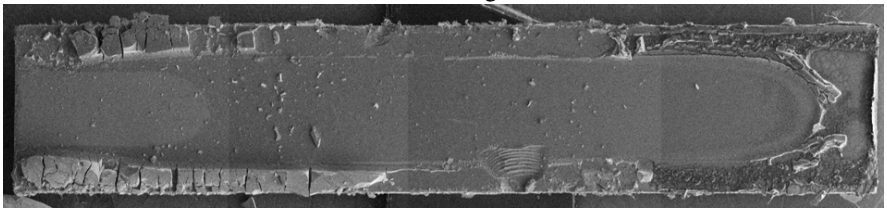
21 000 x g



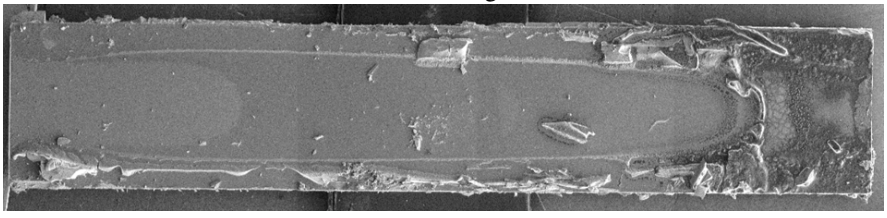
20 000 x g



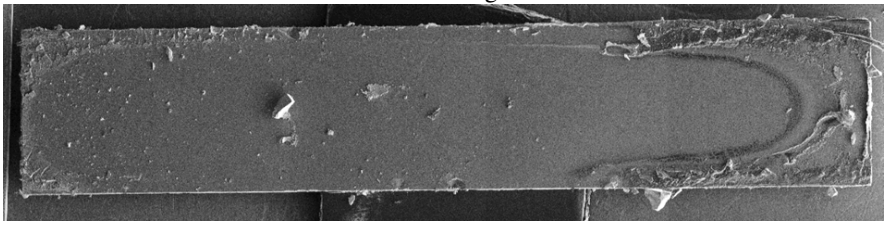
19 000 x g



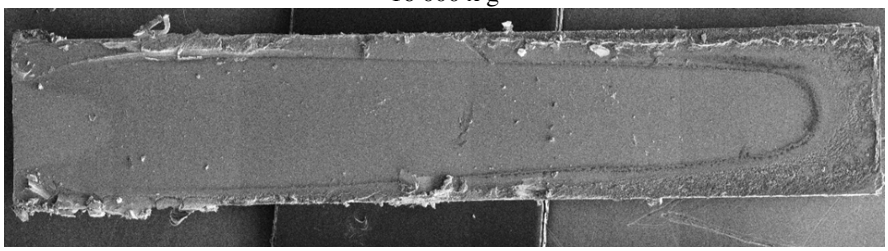
18 000 x g



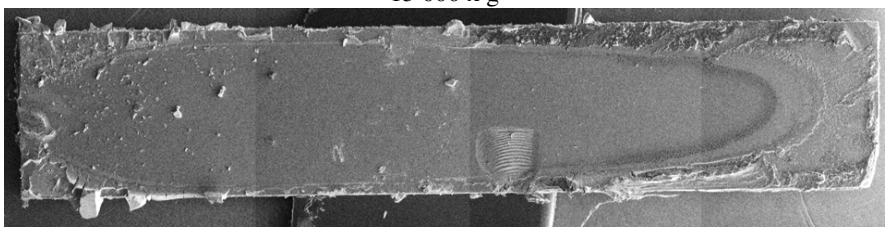
17 000 x g



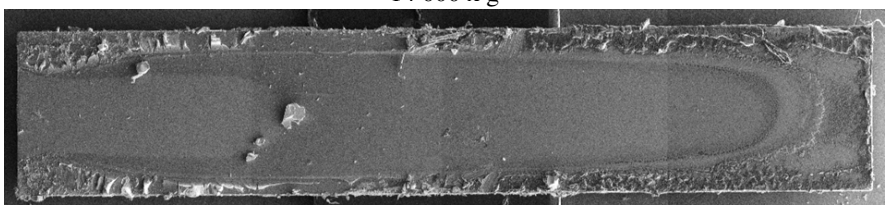
16 000 x g



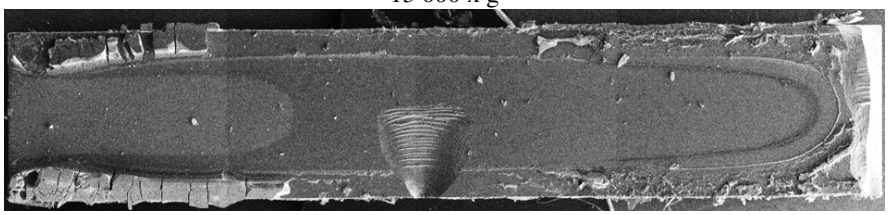
15 000 x g



14 000 x g



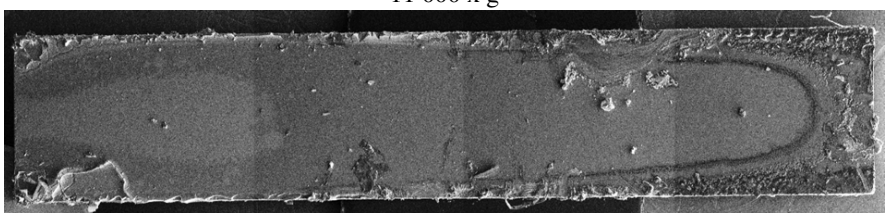
13 000 x g



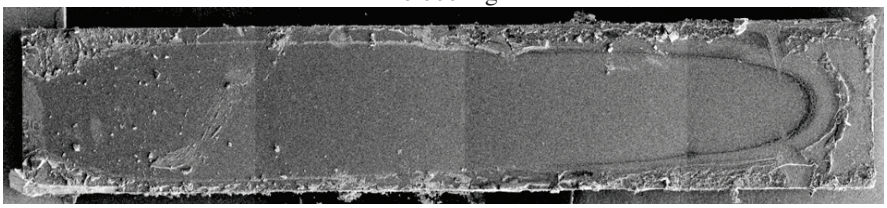
12 000 x g



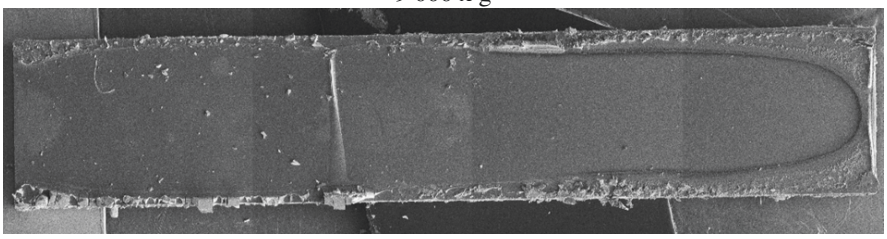
11 000 x g



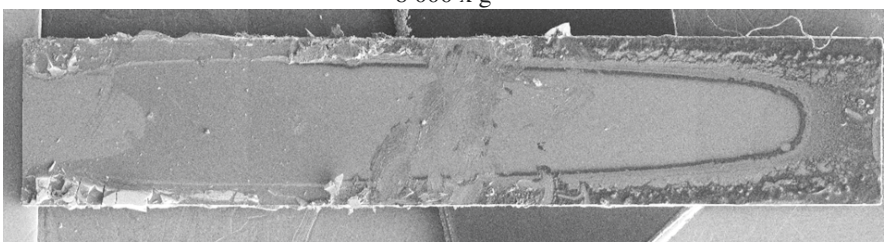
10 000 x g



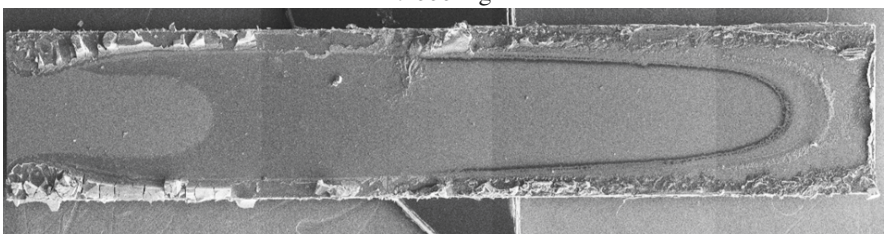
9 000 x g



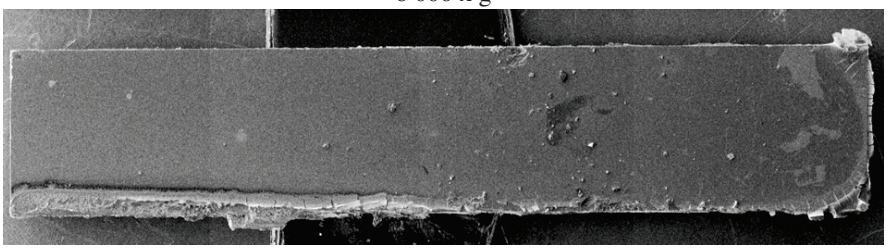
8 000 x g



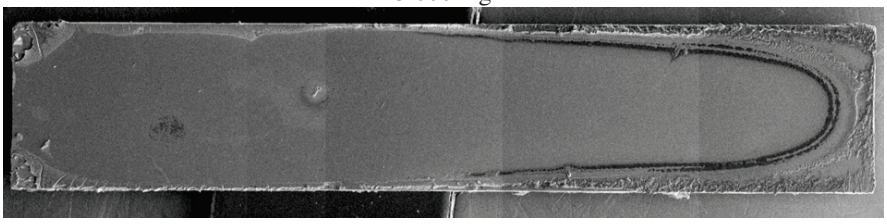
7 000 x g



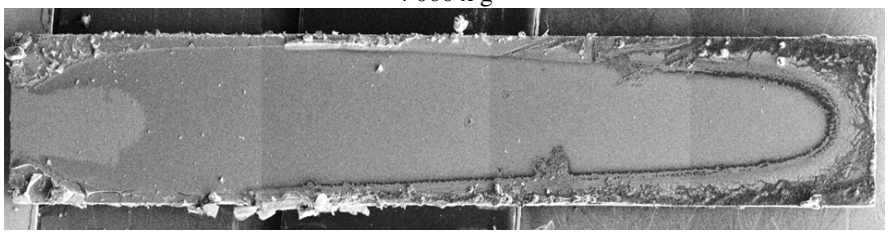
6 000 x g



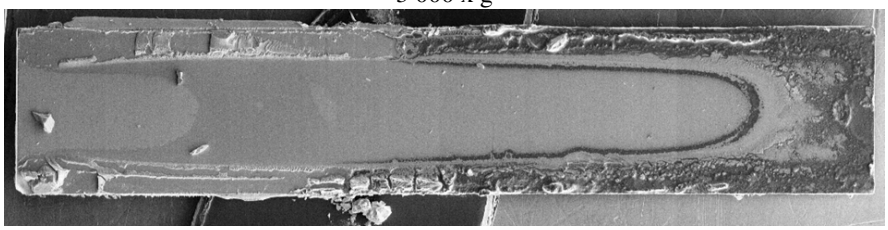
5 000 x g



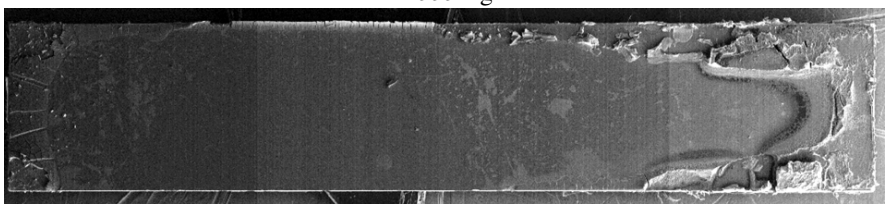
4 000 x g



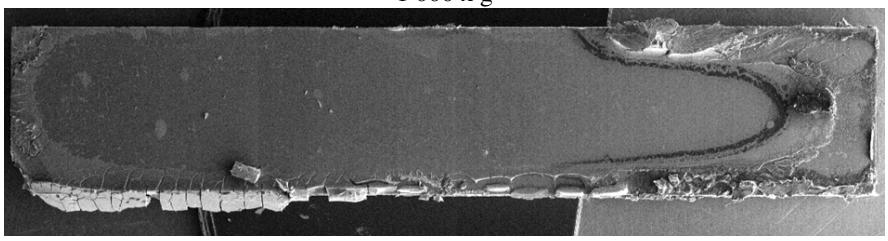
3 000 x g



2 000 x g

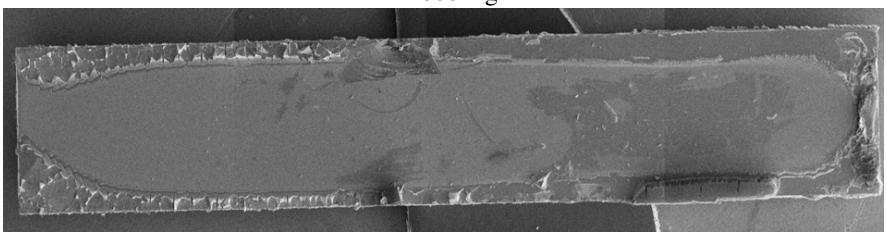


1 000 x g

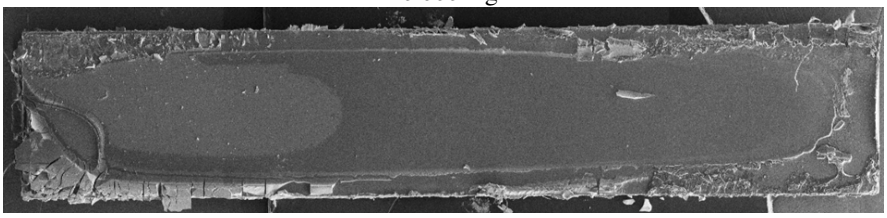


Batch O1 - Centrifugation Temperature 30°C - Reproduced

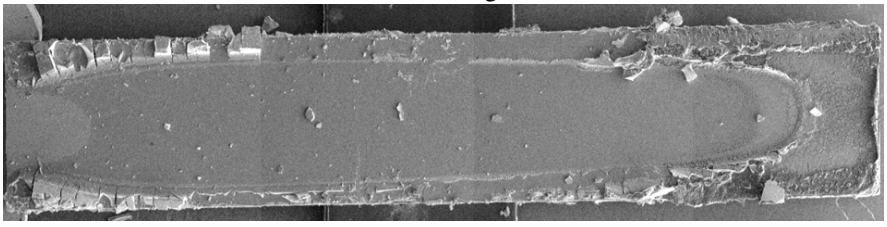
21 000 x g



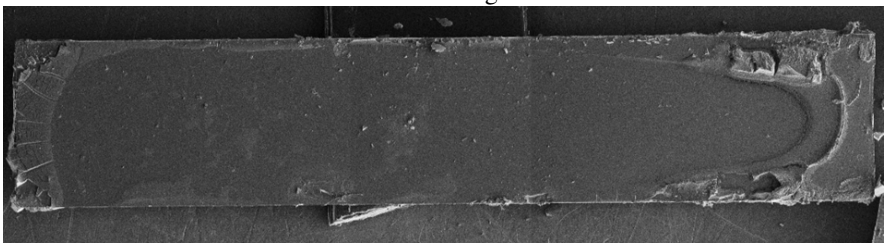
20 000 x g



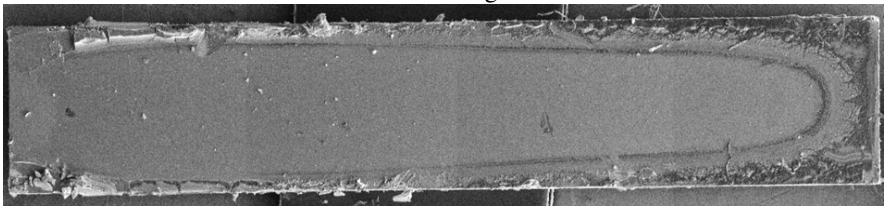
19 000 x g



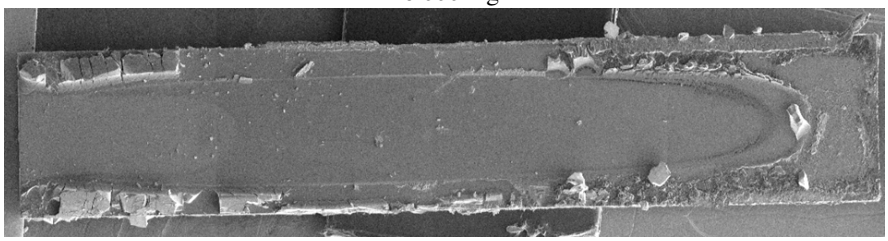
18 000 x g



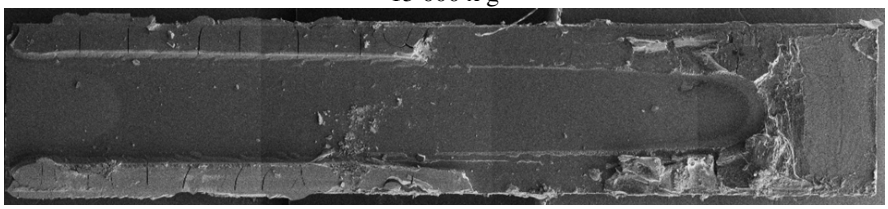
17 000 x g



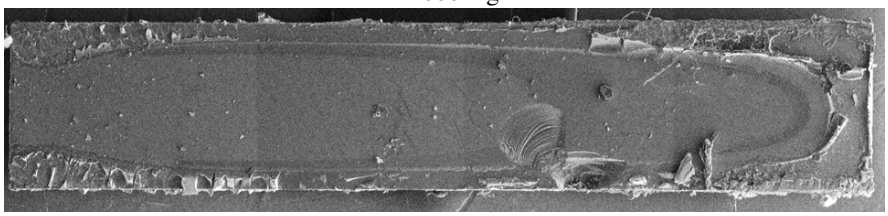
16 000 x g



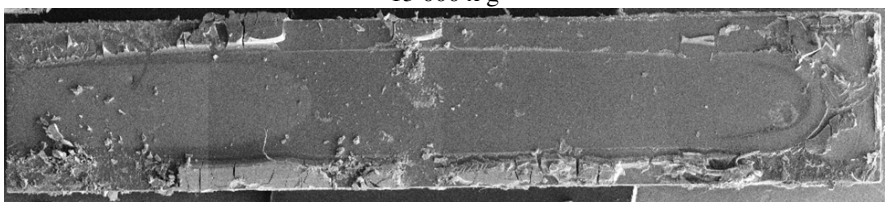
15 000 x g



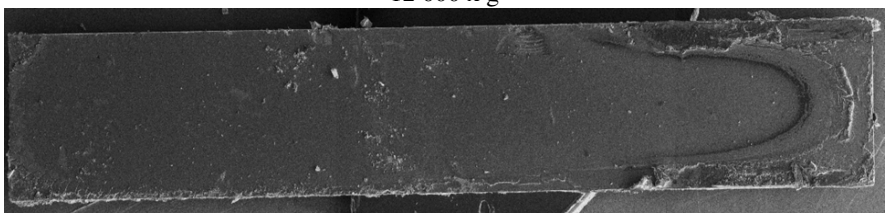
14 000 x g



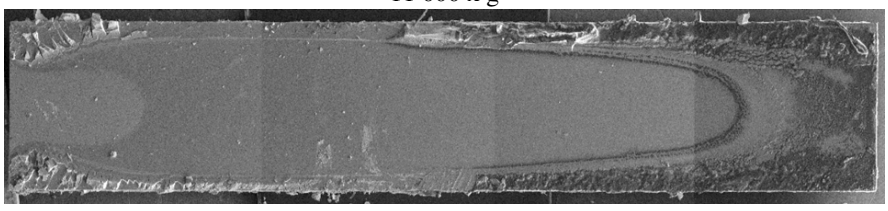
13 000 x g



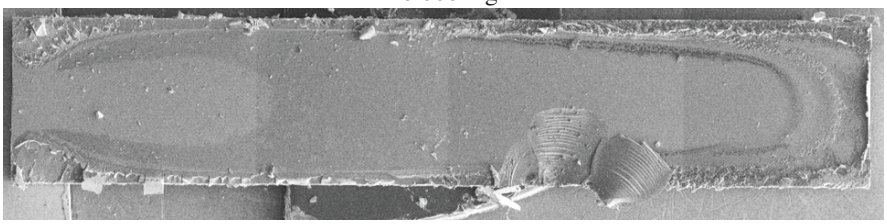
12 000 x g



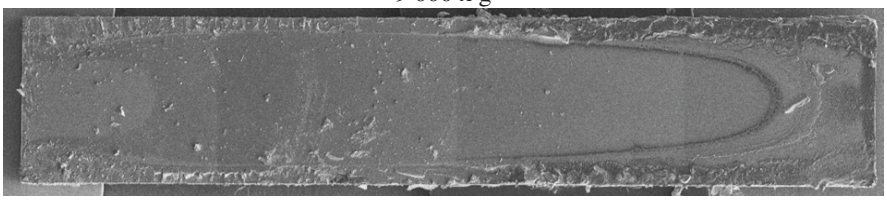
11 000 x g



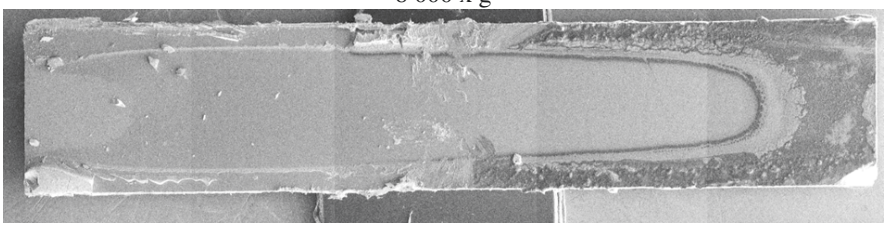
10 000 x g



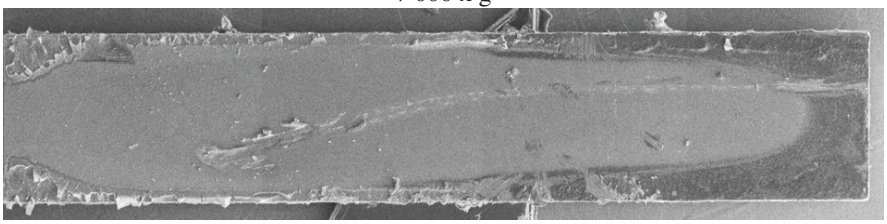
9 000 x g



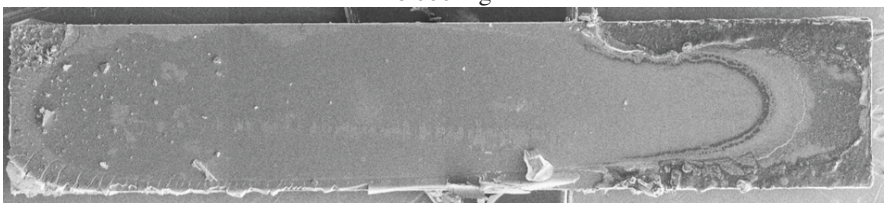
8 000 x g



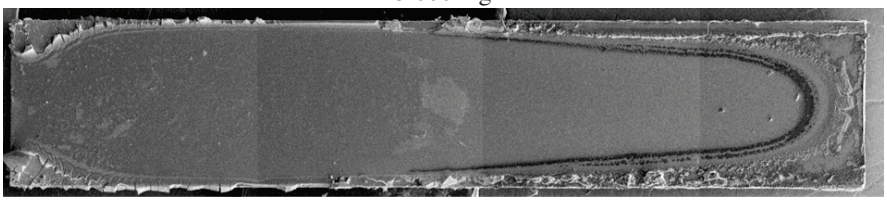
7 000 x g



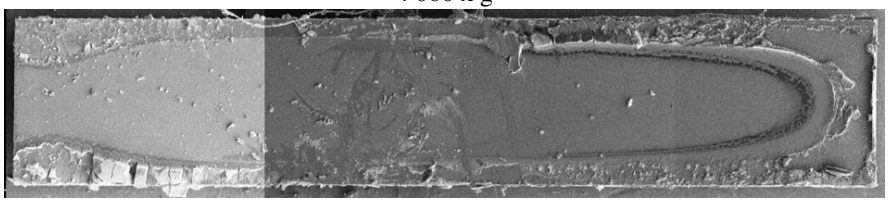
6 000 x g



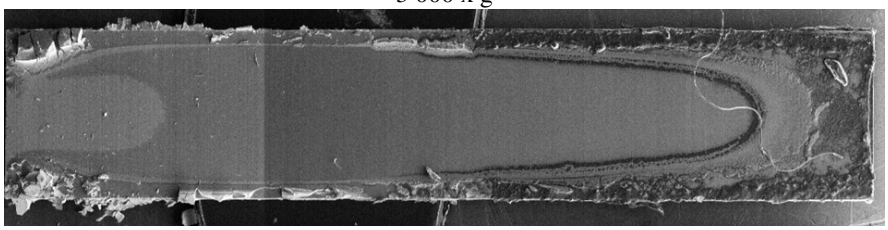
5 000 x g



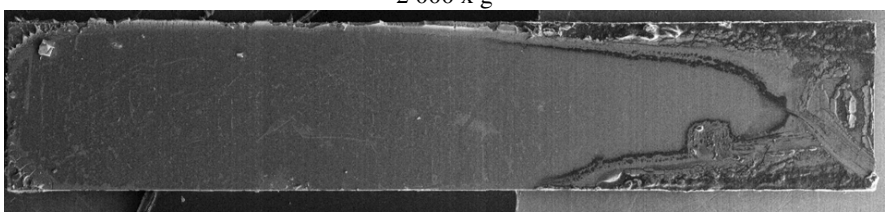
4 000 x g



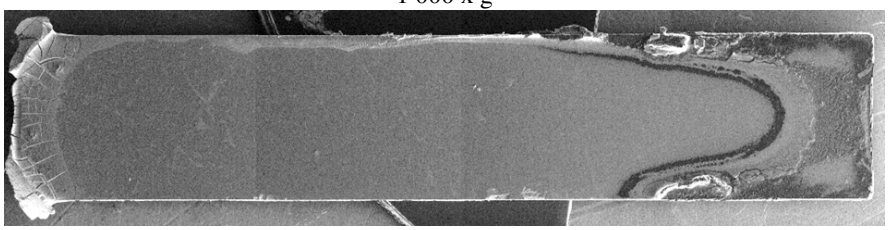
3 000 x g



2 000 x g

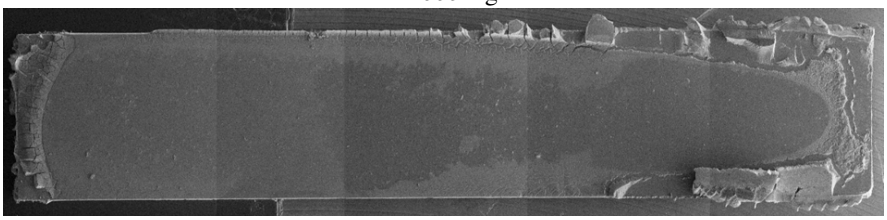


1 000 x g

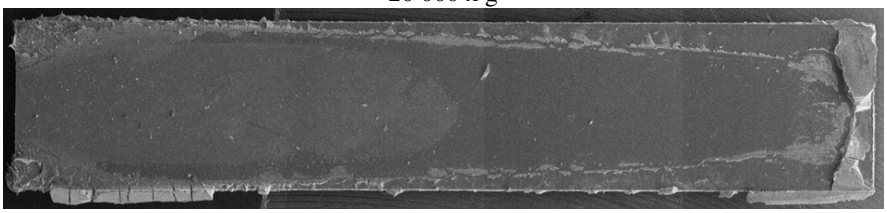


Batch O2 - Centrifugation Temperature 10°C

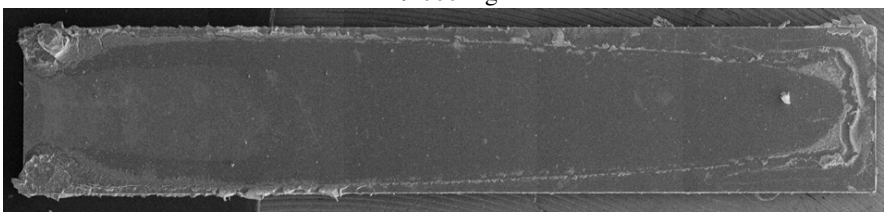
21 000 x g



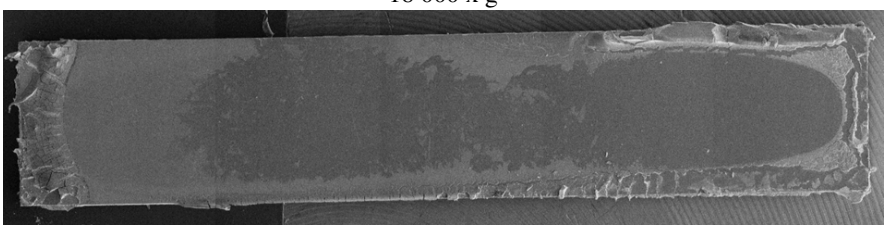
20 000 x g



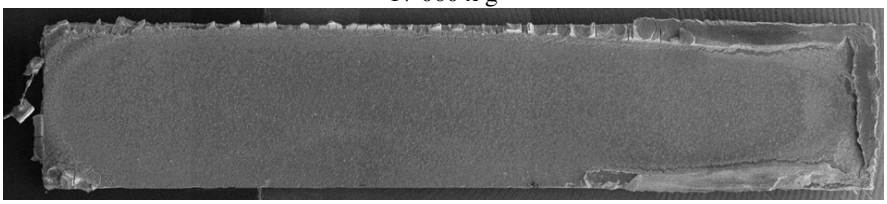
19 000 x g



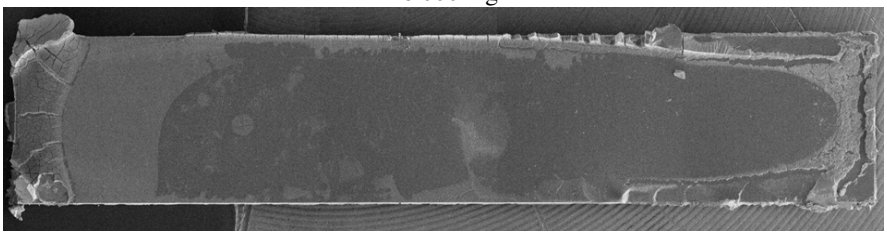
18 000 x g



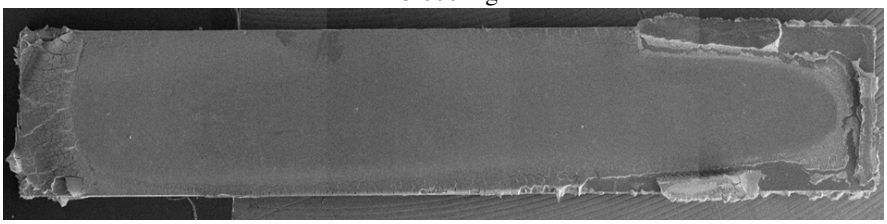
17 000 x g



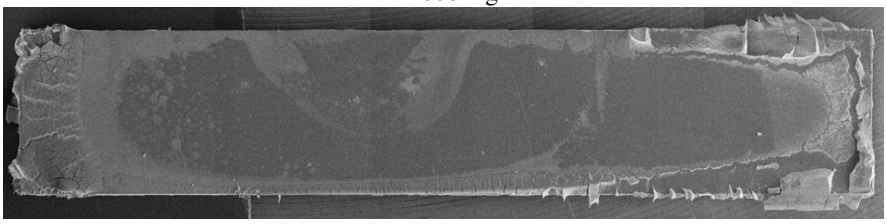
16 000 x g



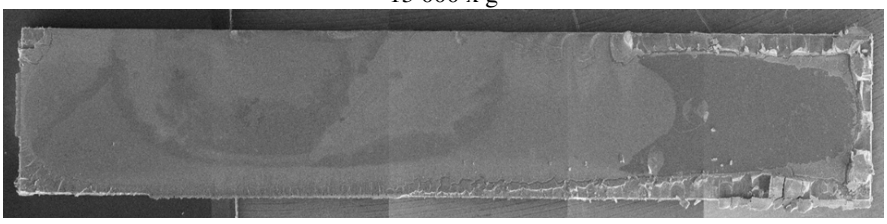
15 000 x g



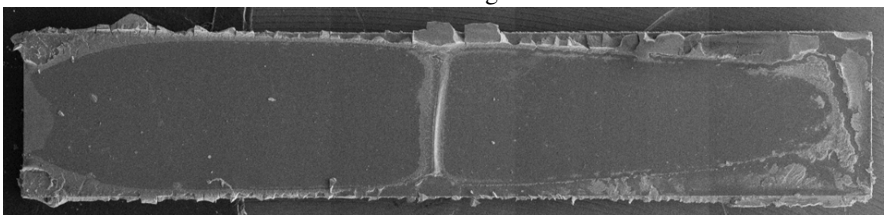
14 000 x g



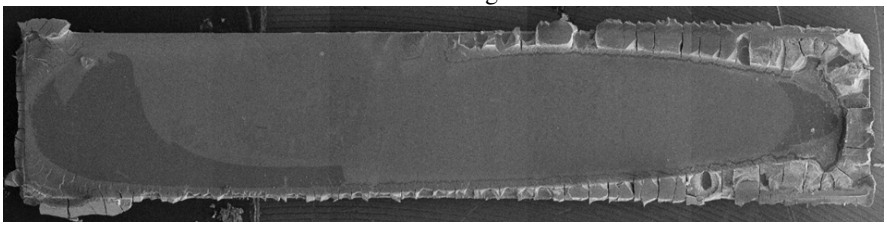
13 000 x g



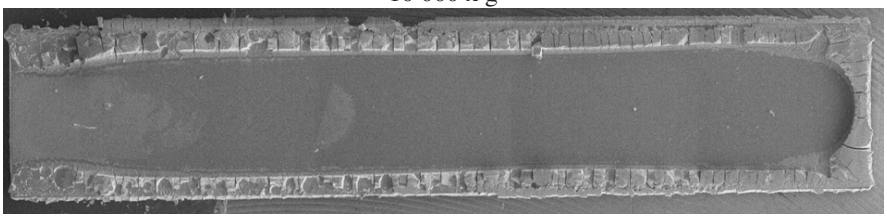
12 000 x g



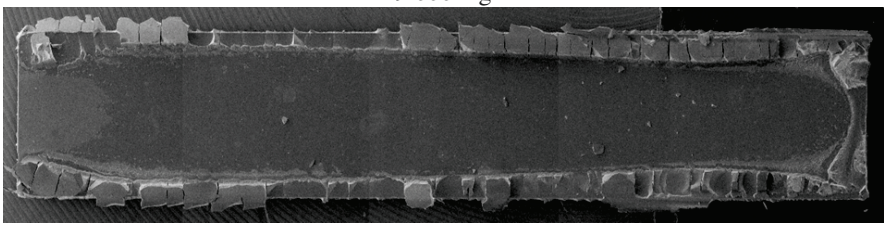
11 000 x g



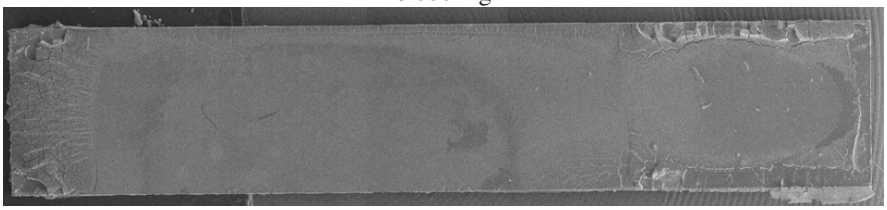
10 000 x g



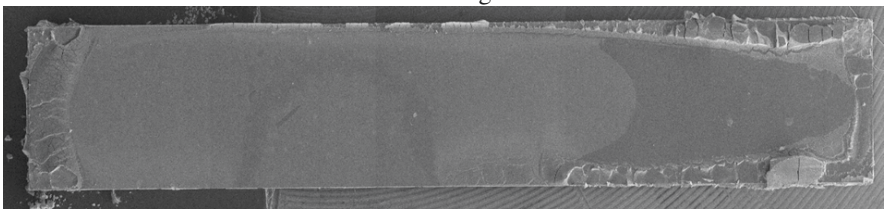
9 000 x g



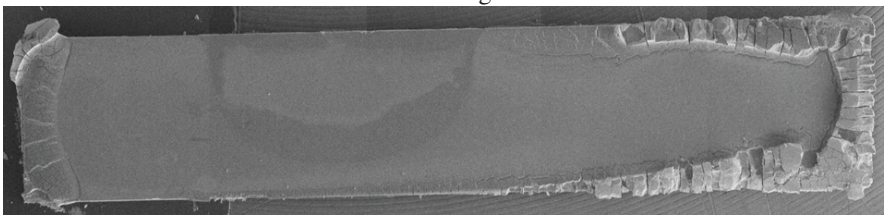
8 000 x g



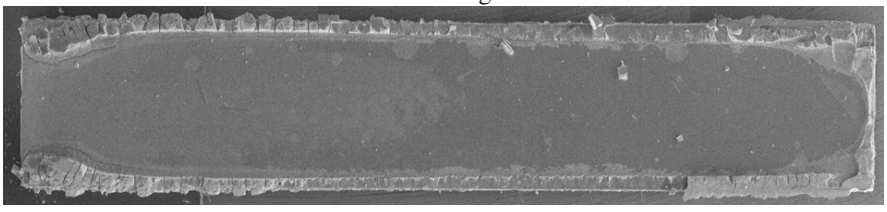
7 000 x g



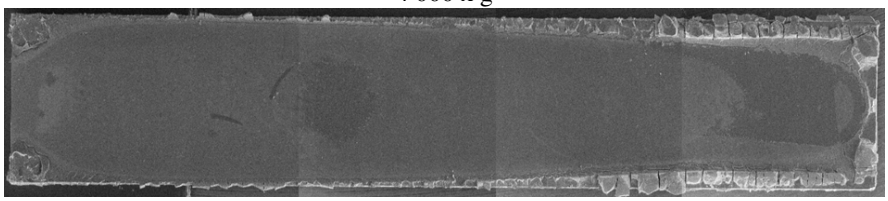
6 000 x g



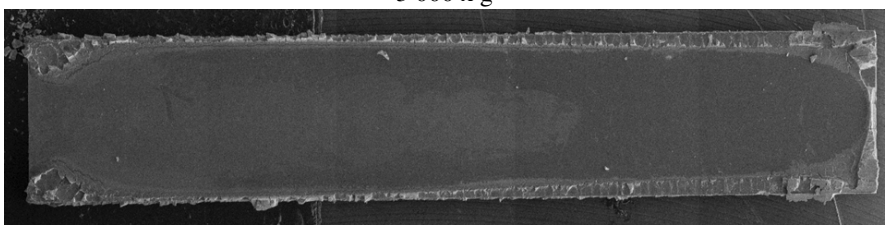
5 000 x g



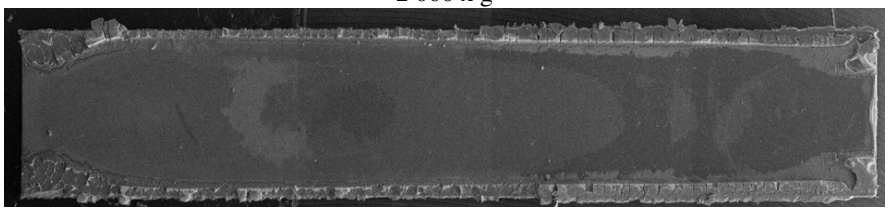
4 000 x g



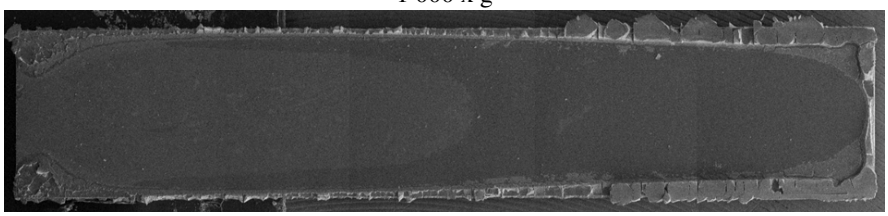
3 000 x g



2 000 x g

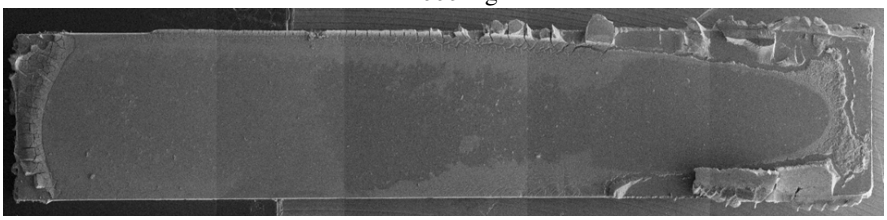


1 000 x g

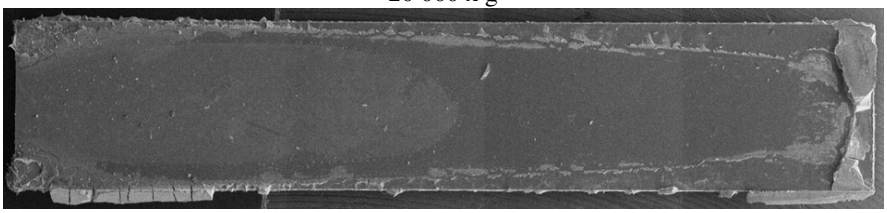


Batch O2 - Centrifugation Temperature 10°C - Reproduced

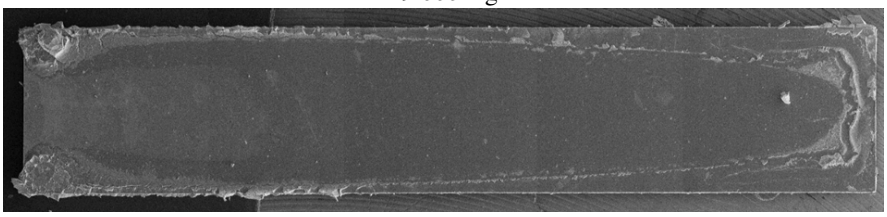
21 000 x g



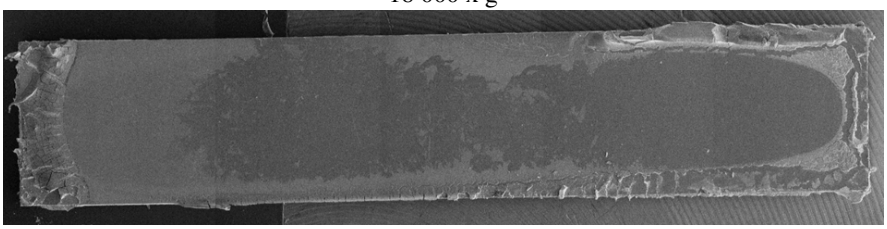
20 000 x g



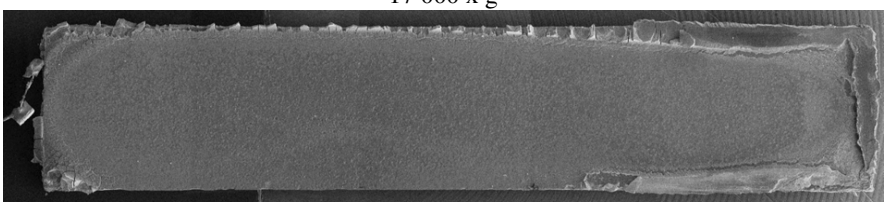
19 000 x g



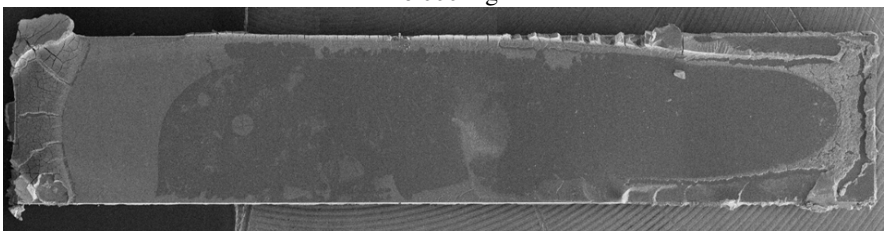
18 000 x g



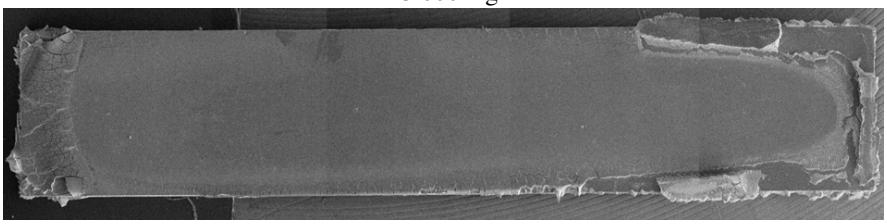
17 000 x g



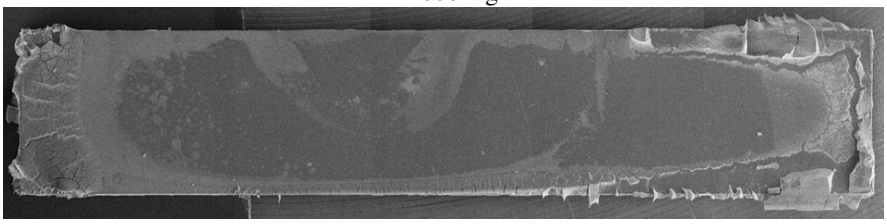
16 000 x g



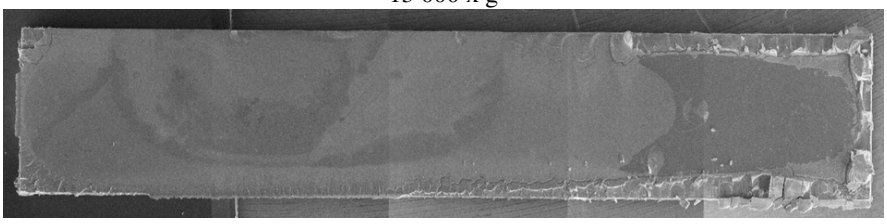
15 000 x g



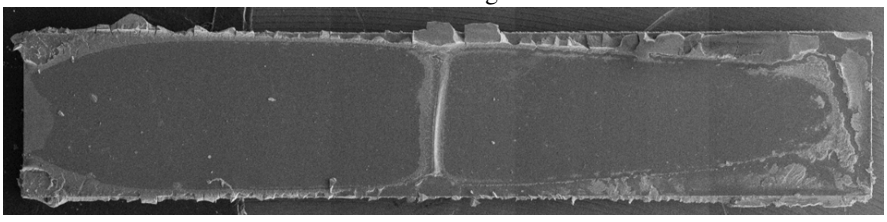
14 000 x g



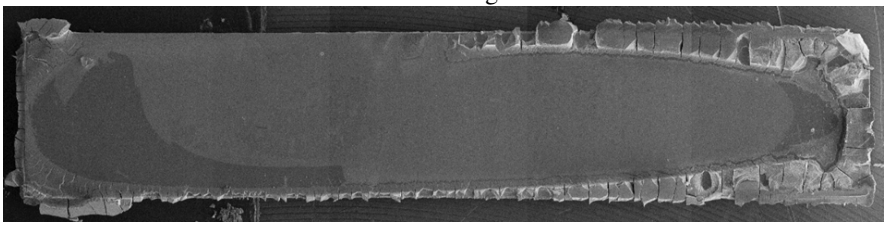
13 000 x g



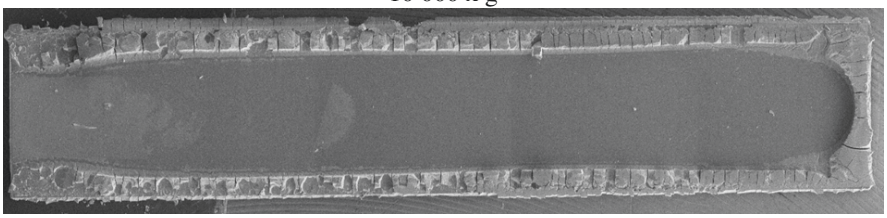
12 000 x g



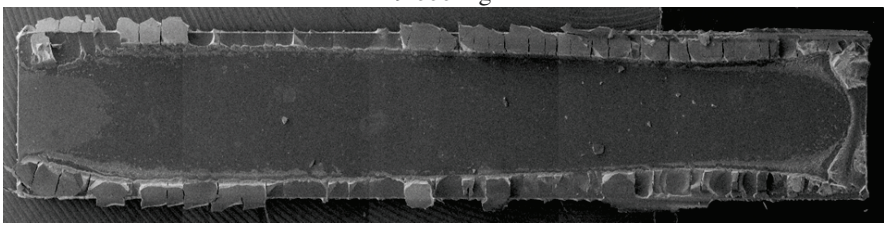
11 000 x g



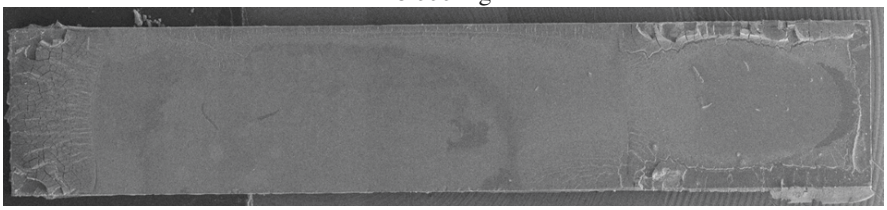
10 000 x g



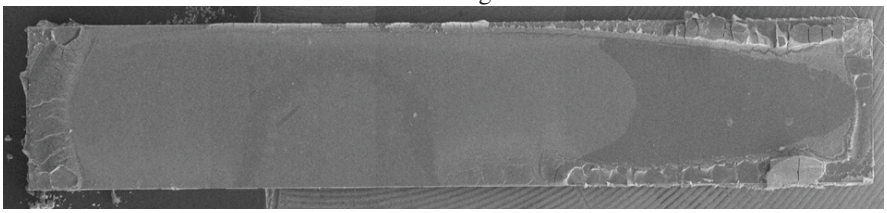
9 000 x g



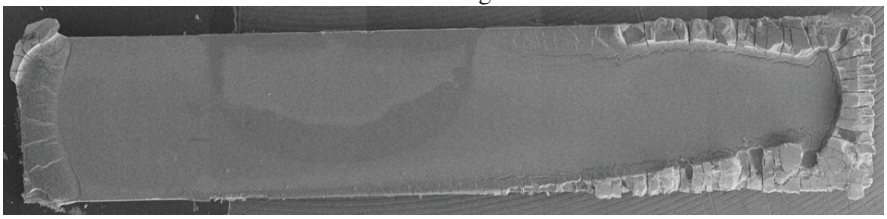
8 000 x g



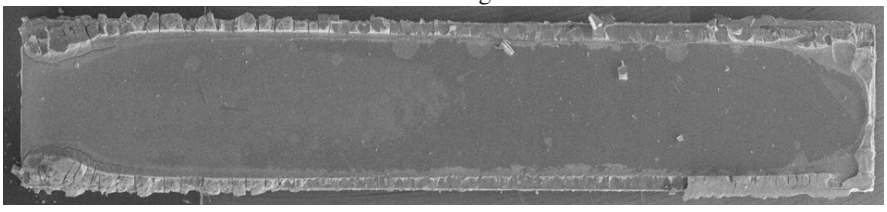
7 000 x g



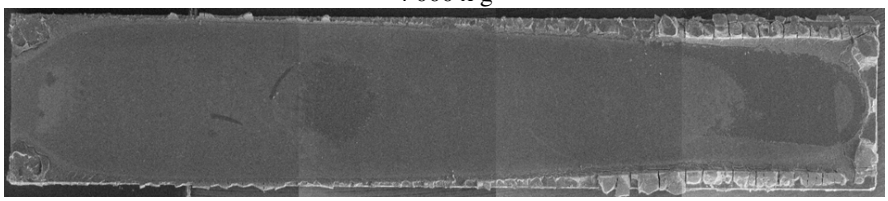
6 000 x g



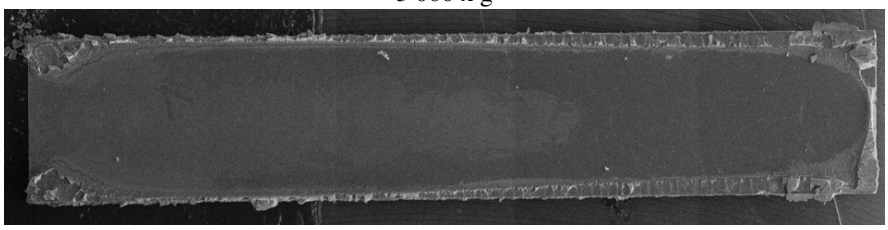
5 000 x g



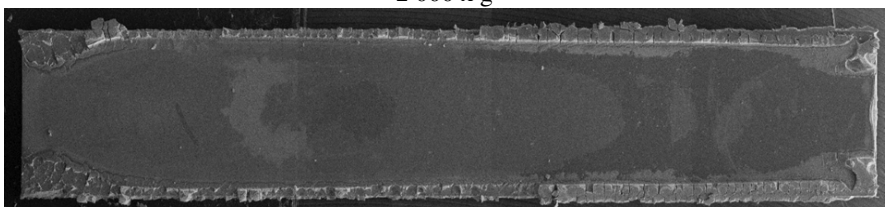
4 000 x g



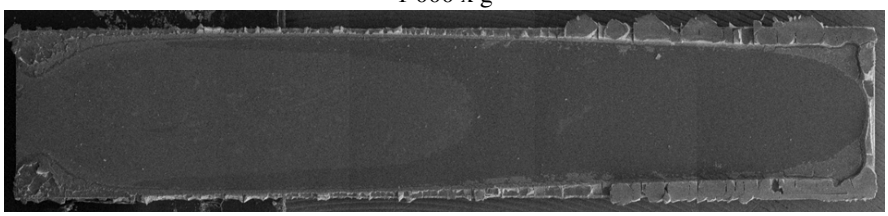
3 000 x g



2 000 x g

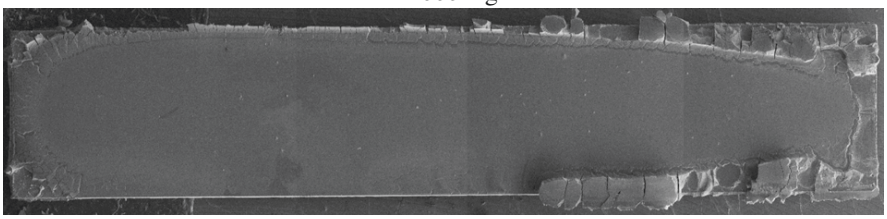


1 000 x g

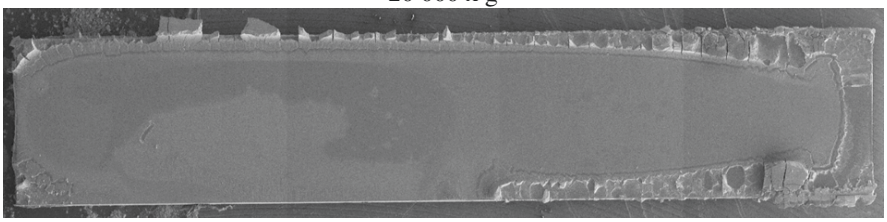


Batch O2 - Centrifugation Temperature 20°C

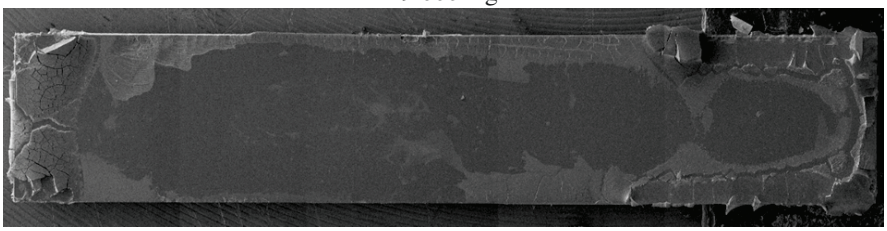
21 000 x g



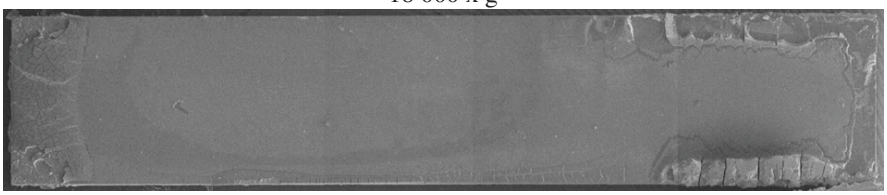
20 000 x g



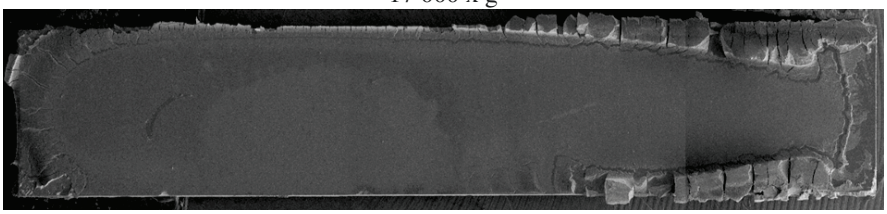
19 000 x g



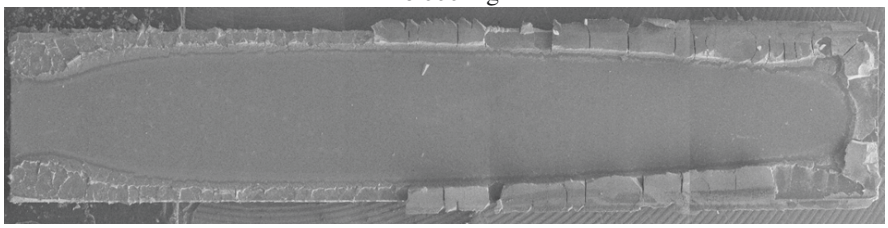
18 000 x g



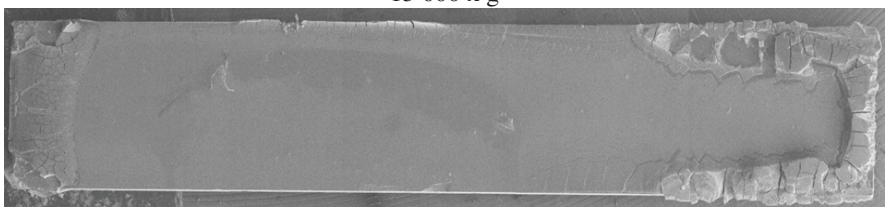
17 000 x g



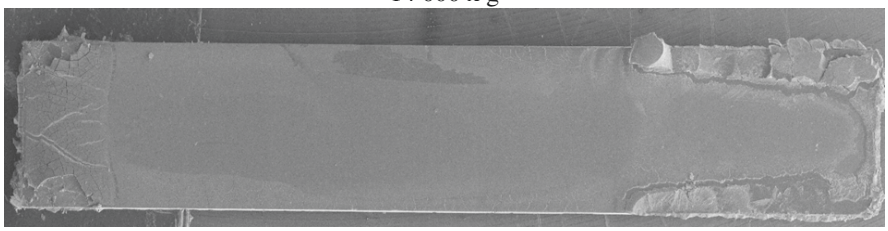
16 000 x g



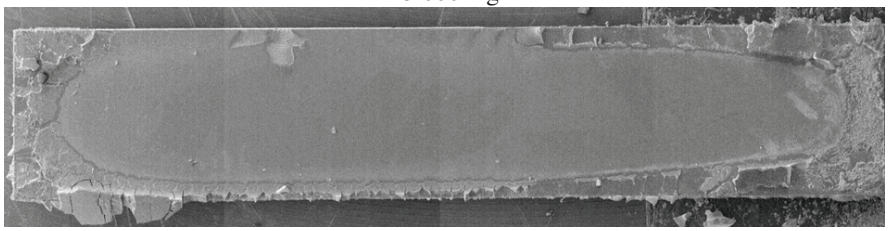
15 000 x g



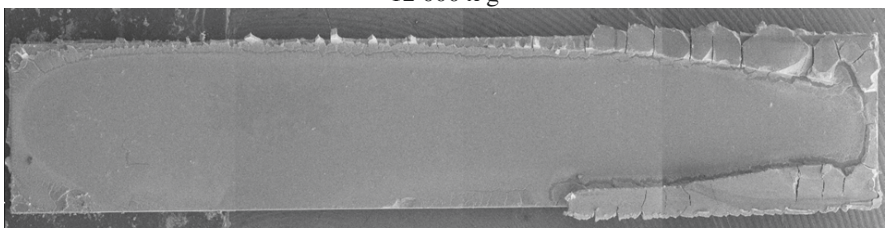
14 000 x g



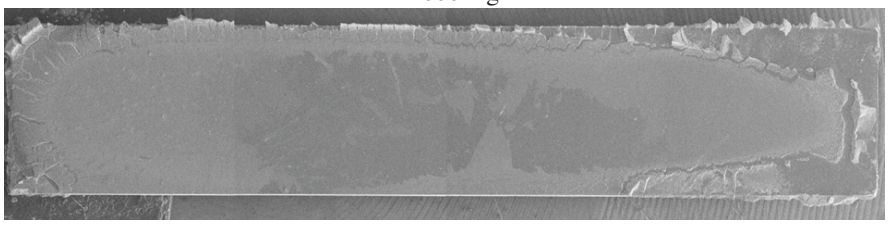
13 000 x g



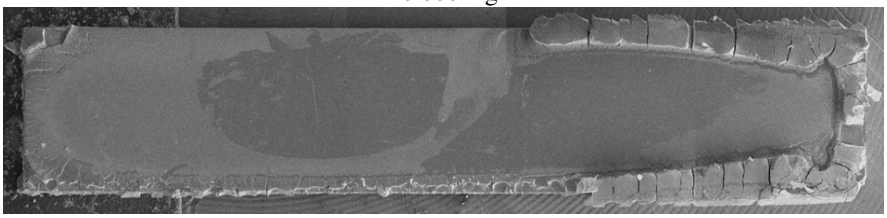
12 000 x g



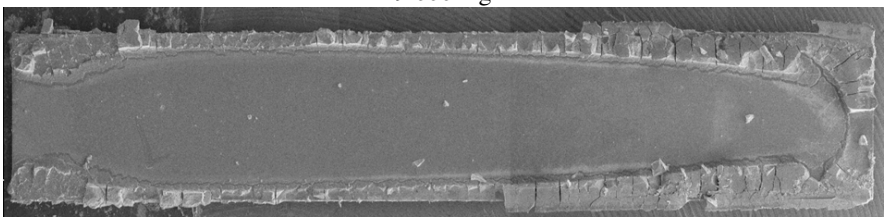
11 000 x g



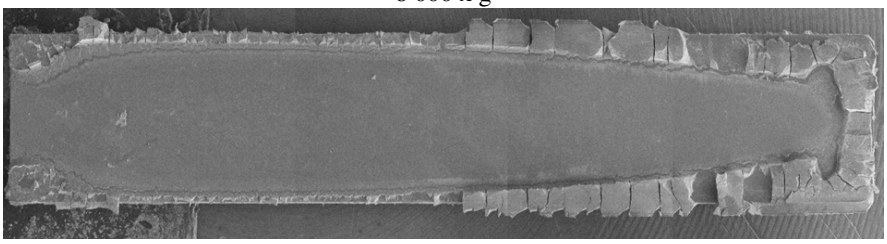
10 000 x g



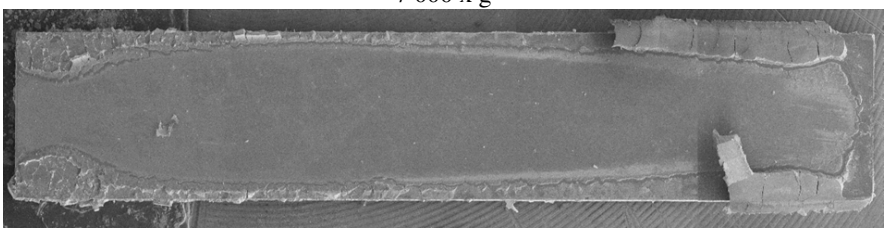
9 000 x g



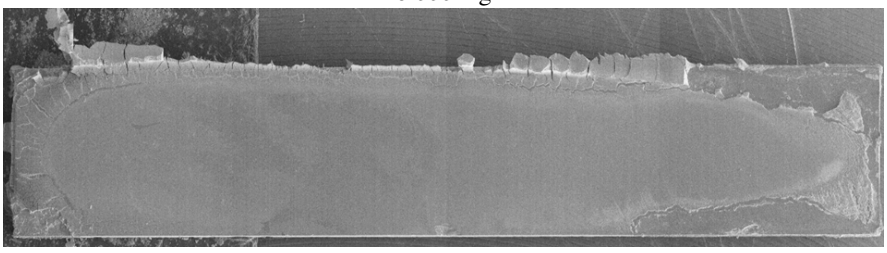
8 000 x g



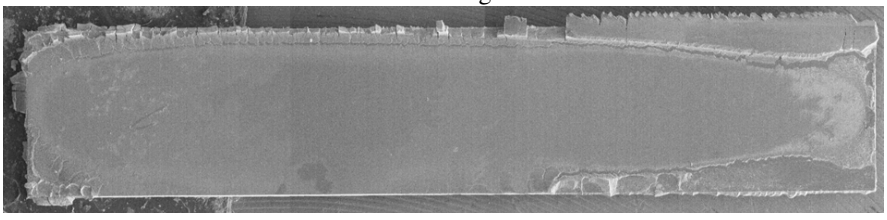
7 000 x g



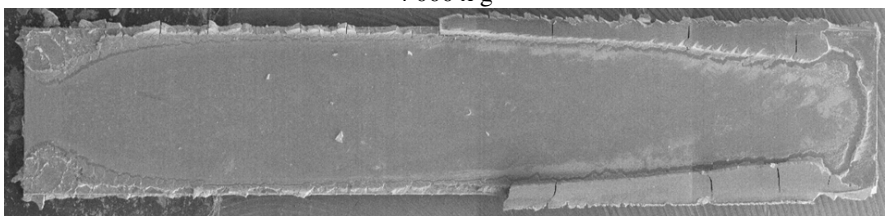
6 000 x g



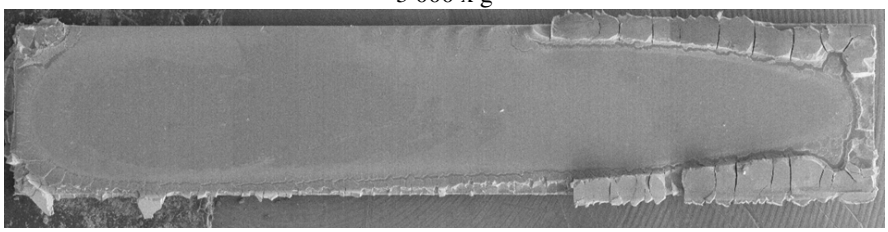
5 000 x g



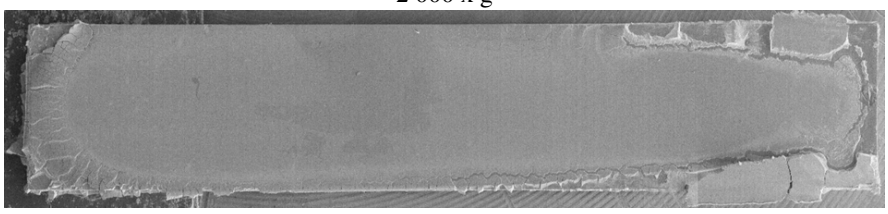
4 000 x g



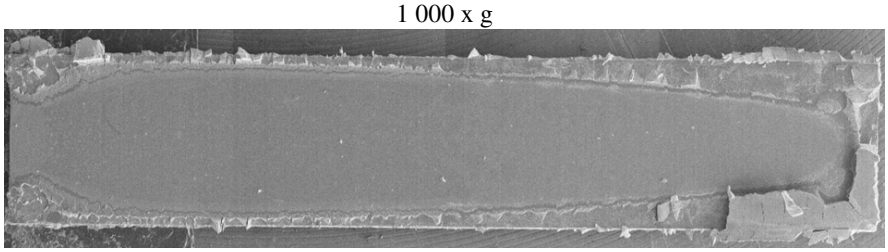
3 000 x g



2 000 x g

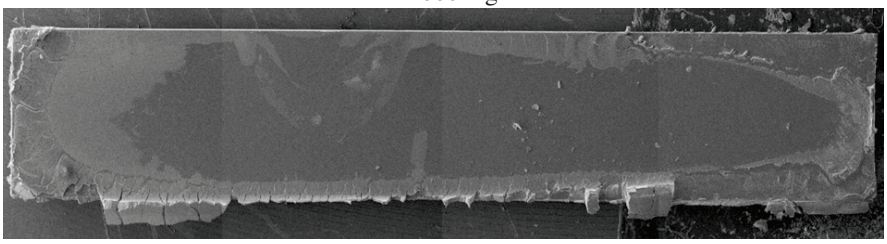


1 000 x g

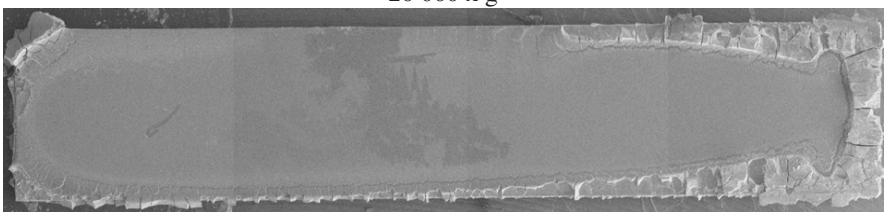


Batch O2 - Centrifugation Temperature 20°C - Reproduced

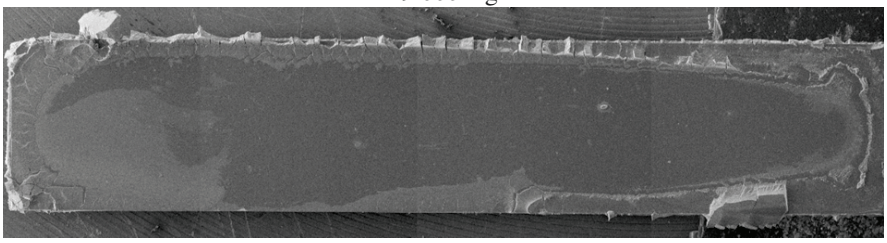
21 000 x g



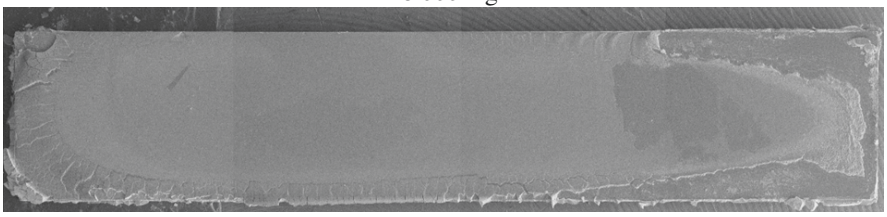
20 000 x g



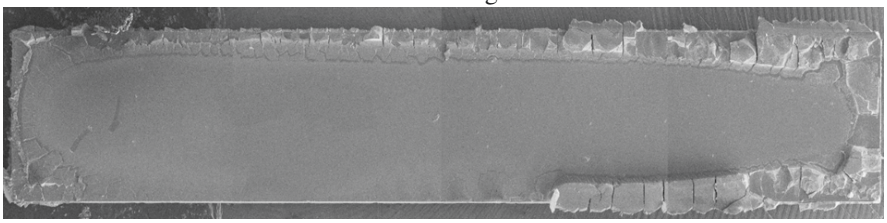
19 000 x g



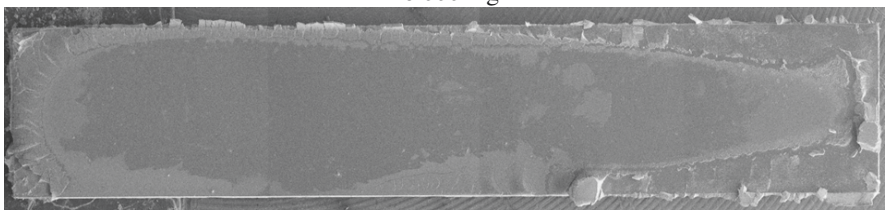
18 000 x g



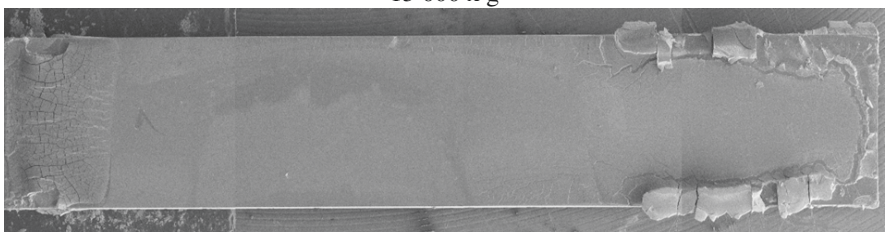
17 000 x g



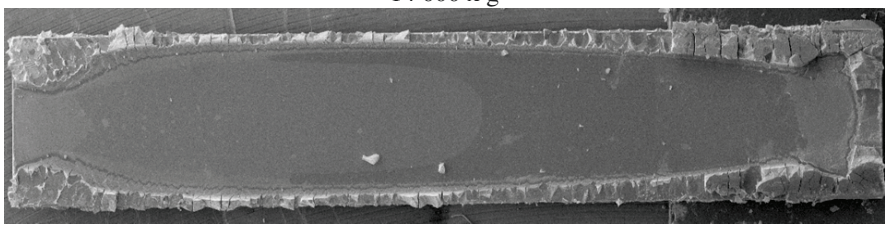
16 000 x g



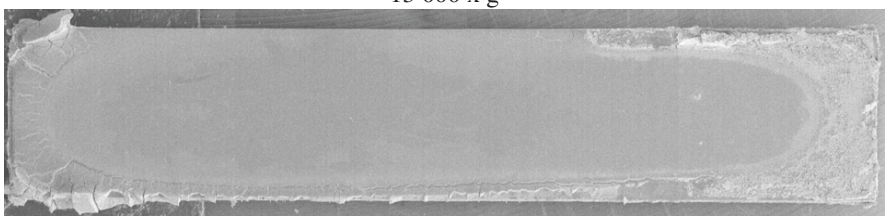
15 000 x g



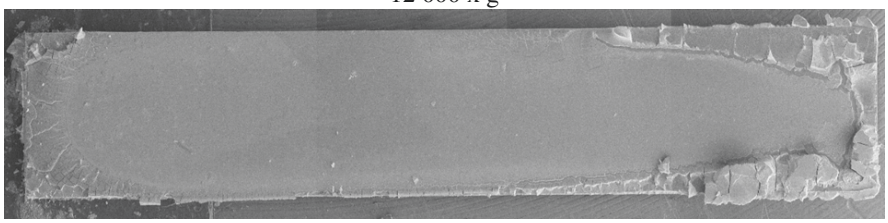
14 000 x g



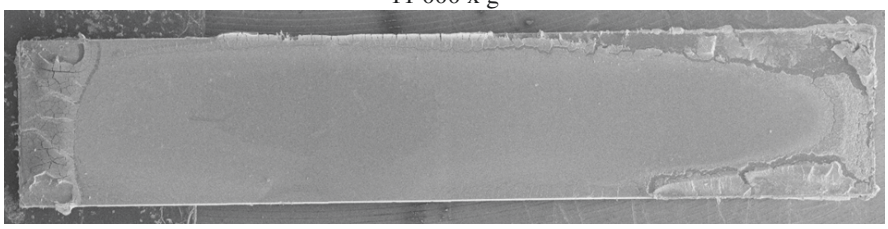
13 000 x g



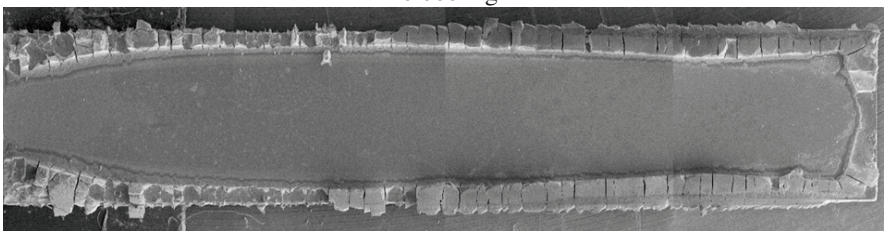
12 000 x g



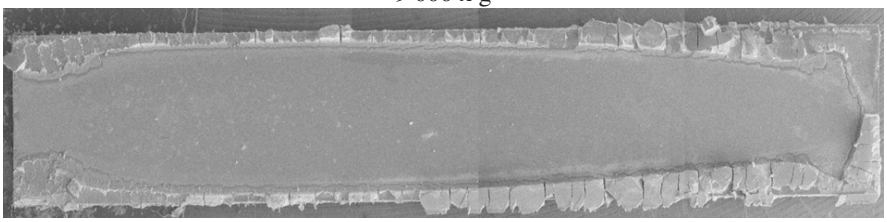
11 000 x g



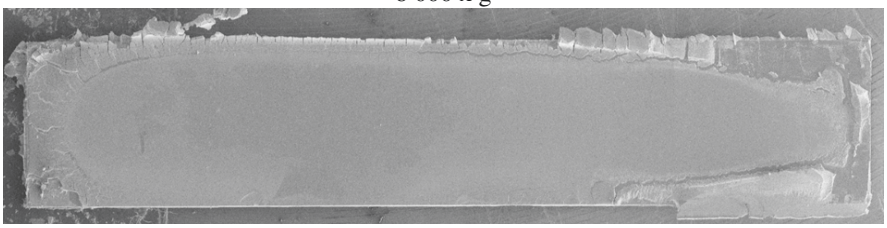
10 000 x g



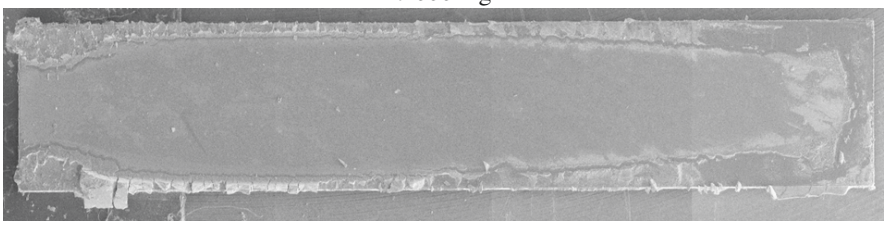
9 000 x g



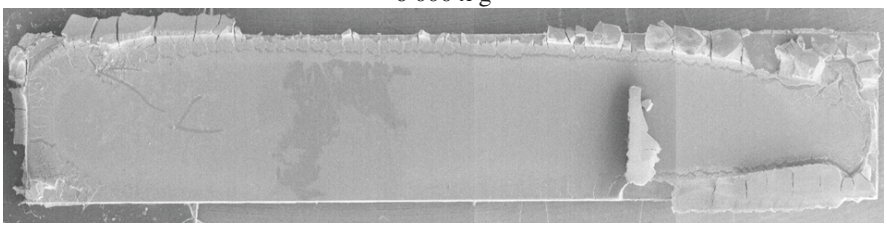
8 000 x g



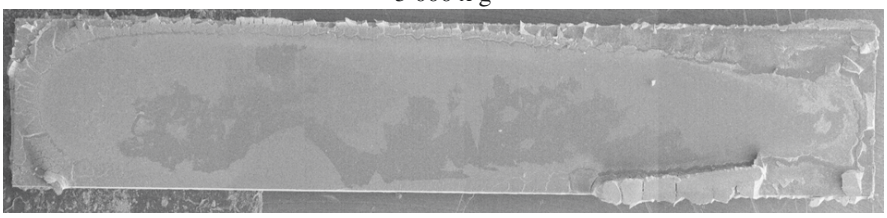
7 000 x g



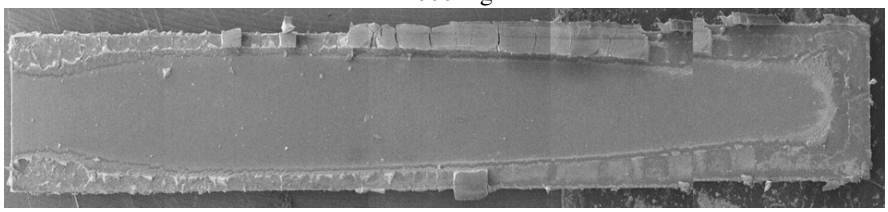
6 000 x g



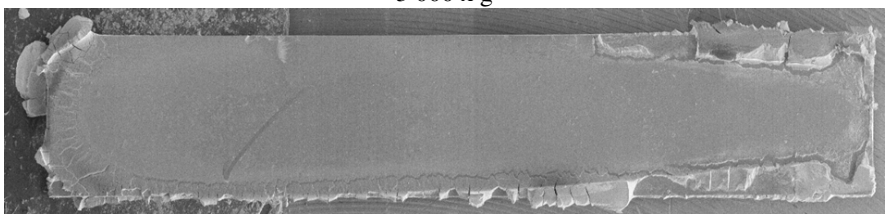
5 000 x g



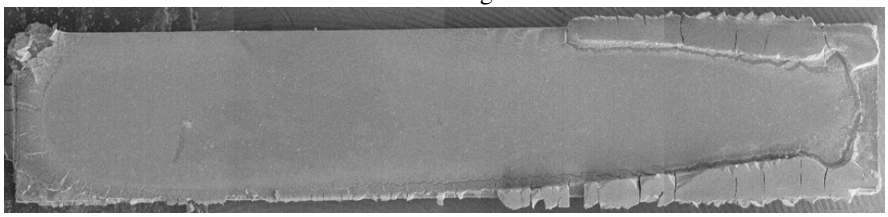
4 000 x g



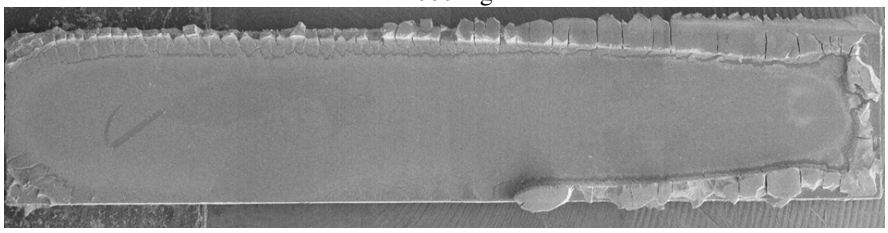
3 000 x g



2 000 x g



1 000 x g



E SAXS on Macrocrystals: Peaks in Azimuthal direction

Positions, FWHM and intesities of peaks identified on the (220) powder ring in the SAXS measurements shown in figures 5.22 and 5.24.

Angle [°]	FWHM [nm^{-1}]	D_{220} [nm]	Intensity [a.u.]	I/I$_{max}$
8	0,000329	17767	30	0,47
18	0,000987	5922	35	0,55
29	0,000658	8884	42	0,66
58	0,000987	5922	64	1,00
83	0,000411	14214	43	0,67
88	0,000411	14214	38	0,59
98	0,001233	4738	38	0,59
111	0,000822	7107	53	0,83
137	0,001151	5076	43	0,67
175	0,000576	10153	39	0,61

Table E.1: Macrocrystal obtained from batch O1, centrifuged at 0°C and 12 000 x g.

Angle [°]	FWHM [nm^{-1}]	D_{220} [nm]	Intensity [a.u.]	I/I_{max}
2	0,000058	101526	560	1,00
5	0,000123	47379	80	0,14
6	0,000082	71068	80	0,14
8	0,000099	59223	115	0,21
10	0,000082	71068	203	0,36
15	0,000164	35534	149	0,27
18	0,000041	142136	102	0,18
19	0,000074	78965	94	0,17
21	0,000156	37404	103	0,18
23	0,000411	14214	80	0,14
30	0,000214	27334	76	0,14
33	0,000156	37404	51	0,09
35	0,000099	59223	52	0,09
42	0,000247	23689	49	0,09
46	0,000156	37404	207	0,37
49	0,000230	25381	98	0,18
61	0,000740	7896	60	0,11
74	0,000238	24506	66	0,12
78	0,000049	118447	228	0,41
81	0,000099	59223	58	0,10
86	0,000255	22925	90	0,16
88	0,000107	54668	114	0,20
90	0,000016	355341	74	0,13
94	0,000296	19741	70	0,13
109	0,000066	88835	145	0,26
111	0,000543	10768	68	0,12
114	0,000189	30899	201	0,36
117	0,000263	22209	353	0,63
119	0,000123	47379	163	0,29
122	0,000173	33842	141	0,25
126	0,000099	59223	62	0,11
128	0,000041	142136	67	0,12
131	0,000049	118447	43	0,08
135	0,000214	27334	107	0,19
145	0,000066	88835	72	0,13
149	0,000354	16527	63	0,11
165	0,000148	39482	24	0,04
175	0,000132	44418	31	0,06

Table E.2: Macrocrystal obtained from batch O1, centrifuged at 0°C and 21 000 x g.

Angle [°]	FWHM [nm^{-1}]	D_{220} [nm]	Intensity [a.u.]	I/I$_{max}$
9	0,000197	29612	11	0,17
14	0,000090	64607	17	0,26
21	0,000247	23689	66	1,00
31	0,000148	39482	17	0,26
35	0,000082	71068	12	0,18
51	0,000090	64607	28	0,42
53	0,000066	88835	13	0,20
78	0,000296	19741	14	0,21
90	0,000099	59223	87	1,32
117	0,000082	71068	25	0,38
122	0,000058	101526	13	0,20
125	0,000214	27334	11	0,17
139	0,000658	8884	13	0,20
175	0,000164	35534	37	0,56

Table E.3: Macrocrystal obtained from batch O1, centrifuged at 10°C and 12 000 x g.

Angle [°]	FWHM [nm^{-1}]	D_{220} [nm]	Intensity [a.u.]	I/I$_{max}$
10	0,002796	2090	9	0,56
18	0,000280	20902	11	0,69
28	0,000534	10934	11	0,69
58	0,000526	11104	16	1,00
67	0,000444	13161	12	0,75
90	0,005838	1001	16	1,00
118	0,000395	14806	14	0,88
133	0,000822	7107	13	0,81
160	0,000822	7107	14	0,88
177	0,000493	11845	13	0,81

Table E.4: Macrocrystal obtained from batch O1, centrifuged at 10°C and 21 000 x g.

Angle [°]	FWHM [nm^{-1}]	D_{220} [nm]	Intensity [a.u.]	I/I$_{max}$
4	0,000411	14214	13	0,65
16	0,000576	10153	10	0,50
32	0,000493	11845	16	0,80
64	0,000329	17767	13	0,65
75	0,001316	4442	11	0,55
79	0,000140	41805	20	1,00
89	0,000740	7896	13	0,65
96	0,000411	14214	14	0,70
115	0,000247	23689	16	0,80
121	0,000740	7896	21	1,05
141	0,000247	23689	11	0,55
145	0,000247	23689	9	0,45
149	0,000058	101526	10	0,50
153	0,000099	59223	12	0,60
160	0,000164	35534	12	0,60
168	0,000658	8884	14	0,70
174	0,000115	50763	15	0,75

Table E.5: Macrocrystal obtained from batch O1, centrifuged at 20°C and 12 000 x g.

Angle [°]	FWHM [nm^{-1}]	D_{220} [nm]	Intensity [a.u.]	I/I$_{max}$
2	0,001151	5076	15	0,36
14	0,000370	15793	14	0,33
16	0,000107	54668	20	0,48
20	0,000576	10153	13	0,31
24	0,000164	35534	14	0,33
30	0,000271	21536	16	0,38
36	0,000197	29612	24	0,57
41	0,000238	24506	19	0,45
48	0,001480	3948	14	0,33
53	0,000247	23689	17	0,40
62	0,000329	17767	33	0,79
67	0,000247	23689	30	0,71
88	0,000214	27334	24	0,57
96	0,000362	16152	31	0,74
102	0,000107	54668	22	0,52
116	0,000576	10153	20	0,48
124	0,000197	29612	22	0,52
132	0,000987	5922	16	0,38
148	0,000222	26322	16	0,38
156	0,000164	35534	42	1,00
162	0,000321	18223	14	0,33
168	0,000230	25381	20	0,48
177	0,000304	19208	14	0,33

Table E.6: Macrocrystal obtained from batch O1, centrifuged at 20°C and 21 000 x g.

Angle [°]	FWHM [nm^{-1}]	D_{220} [nm]	Intensity [a.u.]	I/I$_{max}$
13	0,000247	23689	52	0,40
19	0,000181	32304	57	0,44
29	0,000148	39482	54	0,42
46	0,000230	25381	117	0,91
60	0,000370	15793	83	0,64
72	0,000444	13161	65	0,50
75	0,000082	71068	104	0,81
83	0,000288	20305	63	0,49
98	0,000222	26322	129	1,00
100	0,000140	41805	118	0,91
107	0,000789	7403	95	0,74
111	0,000074	78965	72	0,56
116	0,001480	3948	59	0,46
126	0,000148	39482	56	0,43
132	0,000288	20305	44	0,34
145	0,000206	28427	64	0,50
152	0,000321	18223	45	0,35
158	0,001562	3740	42	0,33
166	0,000773	7560	65	0,50

Table E.7: Macrocrystal obtained from batch O1, centrifuged at 30°C and 12 000 x g.

Angle [°]	FWHM [nm^{-1}]	D_{220} [nm]	Intensity [a.u.]	I/I$_{max}$
8	0,000321	18223	9	1,00
15	0,000115	50763	5	0,56
19	0,000987	5922	4	0,44
23	0,000214	27334	4	0,44
29	0,000740	7896	4	0,44
35	0,000140	41805	4	0,44
43	0,000411	14214	5	0,56
53	0,000238	24506	7	0,78
60	0,000164	35534	4	0,44
65	0,000107	54668	5	0,56
69	0,000066	88835	8	0,89
72	0,000230	25381	9	1,00
83	0,001069	5467	4	0,44
89	0,001398	4180	5	0,56
90	0,000049	118447	8	0,89
98	0,001151	5076	4	0,44
125	0,000493	11845	4	0,44
153	0,000658	8884	8	0,89
164	0,000263	22209	4	0,44
168	0,000411	14214	3	0,33

Table E.8: Macrocrystal obtained from batch O1, centrifuged at 30°C and 21 000 x g.

List of Figures

2.1 Phase diagram of the iron-oxygen system, reprinted with permission from [43]. 3

2.2 a) Inverse spinel (reprinted with permission from [48]) and b) rocksalt structure of wustite. Red and yellow spheres represent tetrahedrally and octahedrally coordinate iron ions, respectively. Green spheres are oxygen ions. 4

2.3 Energy gain due to hopping if a) neighboring lattice sites are both occupied, or b) every lattice site provides two degenerate energy levels and the considered one is empty. Green orbitals allow for electron hopping (darker green corresponds to larger energy gain), red orbitals not. According to [59]. 9

2.4 Super exchange interaction in manganese oxide for different geometries: Depending on the configuration, either antiparallel (a,b) or parallel (c) arrangement is energetically favorable. Yellow (purple) orbitals correspond to an antiparallel (parallel) coupling between oxygen and manganese, according to [59]. 10

2.5 Double exchange interaction in manganese oxide: For parallel arrangement of manganese ions hopping is possible without excitation energy, according to [59]. 10

2.6 a) Domain formation and stray field reduction in ferromagnetic materials. b) Illustration of spin rotation within Bloch and Néel walls. 14

2.7 a) Illustration of the physical origin of ferromagnetic hysteresis loops. b) Barkhausen jumps. 15

2.8 Illustration of antiferromagnetic order by two interpenetrating ferromagnetic sub-lattices. 15

2.9 a) Antiferromagnetic spin canting if a magnetic field is applied perpendicular to the anisotropy axis. b) Spin-flop process for magnetic fields applied parallel to the anisotropy axis. 15

2.10 Examples for magnetization configurations in spherical ferromagnetic nanoparticles. 18

2.11 Illustration of possible magnetization reversal modes in single-domain nanoparticles: a) Coherent rotation occurs if all moments rotate in unison and always point into the same direction. b) For curling the spins are gradually wound up and in c) the buckling mode the spin structure is gradually compressed, according to [64]. 19

2.12 Energy of a single-domain nanoparticle in dependency of the angle θ between the superspin and the anisotropy axis, according to the Stoner-Wohlfarth model for zero applied field (red) and a magnetic field with $h = \frac{\mu_0 H M_s}{2K} = 0.2$ (blue), according to [64]. 20

2.13 Illustration of steric stabilization. 23

2.14 a) Illustration of the contact line for a liquid drop (blue) on a solid surface (gray) surrounded by gas. b) Meniscus formation between two bodies. 25

2.15 Two large spheres approaching each other and thus hindering the small ones to use the space in between. The resulting uncompensated osmotic pressure causes an attractive depletion force. 25

2.16 Phase diagrams for entropy driven crystallization a) without b) with long range and c) with short range interaction. The volume fraction is calculated by dividing the volume occupied by all the particles by the total volume, reprinted with permission from [76]. 26

2.17 Schematic representation of Bragg's law. 28

2.18 Intersection of the Ewald sphere with the reciprocal lattice for a) single crystals and b) polycrystalline powders. 29

2.19 Geometrical construction for the calculation of the phase difference between two beams scattered at different particles separated by $\vec{r}$. The incoming and scattered waves are represented by the wave vectors $\vec{k_i}$ and $\vec{k_s}$, respectively. . . 29

2.20 a) Schematic plot of a typical X-ray spectrum consisting of the continuous Bremsstrahlung and characteristic lines b) Illustration of electron transitions causing characteristic X-ray lines. 31

2.21 Schematic overview on the field dependency of four magnetoresistance effects that are relevant for samples studied in this thesis, taken from [86]. 33

3.1 Schematic illustration of the vibrating sample magnetometer setup. 38

3.2 a) Pickup coil for Quantum Design MPMS systems. b) Example response curve. 39

3.3 Measurement procedures for a) zero field cooling b) field cooling and c) memory effect, where red arrows mark the paths along which the magnetic moment is recorded. 39

3.4 Illustration of measurement procedure for DCD (left) and IRM (right) curves. . 40

3.5 Schematic description of the Kerr rotation θ_K and ellipticity ϵ_K, which can be combined to the complex Kerr angle Φ_K. 41

3.6 Illustration of geometric arrangement for the longitudinal, polar and transversal Kerr effect. 41

3.7 Characteristics of a typical major hysteresis loop. 42

3.8 a) Graphical illustration of a hysteron displaying its threshold reversal fields H_{up}, H_{down} and offset H_u. b) Illustration of the wiping-out and c) congruency property, both reprinted with permission from [112]. 42

3.9 a) Example for a family of FORCs probing the interior of the corresponding major loop. b) Illustration of the relation between the $H_r(H)$ and $H_u(H_c)$ coordinate system. Green dots are representing single hysterons. 43

3.10 Hysterons for the theoretical behavior of an individual nanoparticle for a field applied along the a) easy or b) hard axis. 44

3.11 Theoretical FORC result obtained using easy axis hysterons for a) a normal coercivity distribution without interaction field and without coercivity distribution. b) Interaction field antiparallel to the magnetization direction c) Interaction field parallel to the magnetization direction. 45

3.12 a) Schematical setup of the resistivity option of the Quantum Design PPMS system, taken from [113]. b) Sample geometry for resistivity measurements with a magnetic field applied out-of-plane or c) in-plane. 45

3.13 Geometrical principle of X-ray powder diffraction using the Guinier method in transmission geometry, according to [116]. 46

3.14 Schematic overview on the general measurement setup for (GI)SAXS experiments. 47

3.15 a) Form factors of three monodisperse samples (spherical nanoparticles with a diameter of 1 nm (green) / 2 nm (yellow) / 3 nm (blue)) and their sum (red) representing a polydisperse sample. b) Universal Guinier plot of the particle form factor for spherical (green), rod-like (orange) and lamellar shaped nanoparticles illustrating the domains of information, according to [118]. 49

3.16 Schematical representation of the geometry required for GISAXS experiments, according to [120]. 50

3.17 Determination of the origin of the Q_z axis using the incident beam and the specular reflection. 51

3.18 X-ray absorption spectrum: a) Complete spectrum showing three major transitions and splitting at higher resolution (inset) b) Schematic view of a single edge, according to [123]. 53

3.19 Spin-up ($\sigma = +\frac{1}{2}$) and spin-down ($\sigma = -\frac{1}{2}$) transition probabilities at the L_3 and L_2 edges for left-circular (pink, q=-1), linear (purple, q=0) and right circular polarized X-rays (blue, q=+1), according to [122]. 54

3.20 Schematic setup of the 4-ID-D Beamline at APS for XMCD measurements, inspired by [39]. 56

3.21 Schematical representation of a normalized XAS curve. 57

3.22 Schematical setup for a scanning electron microscope. 58

3.23 Setup illustration for a) Ion Beam Sputtering and b) Molecular Beam Epitaxy. . 59

4.1 a) Chemical structure of oleic acid b) Schematic illustration of an iron oxide nanoparticle, sterically stabilized by oleic acid c) Bidentate interactions of the carboxylic head of oleic acid with iron ions on the surface of the nanoparticle, according to [138]. 61

4.2 Schematic representation of the spin coating process. 62

4.3 Sample 1-01: SEM image in the center of a silicon substrate on which the nanoparticles ($9\mu l$ dispersion with a concentration of 25 mg/ml) are deposited by spincoating (60 s at 3000 rpm). 62

4.4 Sample 1-01: GISAXS measurement performed at GALAXI revealing that the sample is a two dimensional superpowder with a lattice constant of 217 Å. . . . 63

4.5 Sample 1-01: Hysteresis loops at a) 300 K and b) 5 K showing superparamagnetic behavior and exchange bias. c) ZFC (red) and FC (black) curve measured at $\mu_0 H = 0.005$ T revealing a blocking temperature T_B of 245 ± 2 K and a combined ferri- and antiferromagnetic behavior with a Néel temperature T_N of 210 ± 2 K. 64

4.6 X-ray powder diffraction pattern of a nanoparticle multilayer after background subtraction revealing a mixture of wustite with a spinel (maghemite or magnetite). In the lower area of the graph the corresponding XRD patterns are indicated according to the data shown in [141]. 65

4.7 SEM images displaying the influence of variations in a) rotational speed (samples 2-01...2-05) and b) dilution with toluene (samples 2-05...2-10) for the fabrication of a (sub-) monolayer of nanoparticles by spin-coating on silicon substrates. 67

4.8 Sample 2-10: Hysteresis loops at a) 300 K and b) 5 K showing superparamagnetic behavior and exchange bias. c) ZFC (red) and FC (black) curve measured at $\mu_0 H = 0.005$ T revealing a blocking temperature T_B of 237 ± 2 K and a combined ferri- and anitferromagnetic behavior with a Néel temperature T_N of 210 ± 2 K. 69

4.9 Sample 2-10: Raw data of the hysteresis loop measured at 300 K (black) and corresponding Langevin fit (red). 70

4.10 Sample 3-01: a) SEM image and b) ZFC (red) and FC (black) curve measured at $\mu_0 H = 0.005$ T indicating a phase transformation towards maghemite. The hysteresis loops obtained at a) 300 K and b) 5 K reveal superparamagnetic behavior. 71

4.11 Sample 3-02: a) SEM image b) ZFC (red) and FC (black) curve measured at $\mu_0 H = 0.005$ T exhibiting a metastable state during the phase transformation of wustite to maghemite c) Hysteresis loop at 300 K and d) 5 K showing superparamagnetic behavior and exchange bias. 72

4.12 Sample 3-03: a) SEM image b) ZFC (red) and FC (black) curve measured at $\mu_0 H = 0.005$ T displaying a stable, partial phase transition c) Hysteresis loop at 300 K and d) 5 K exhibiting superparamagnetism and a slight exchange bias. 73

4.13 ZFC-FC curves measured at $\mu_0 H = 0.005$ T showing a) the onset (sample 3-04) of phase transition after 30 s of plasma treatment and b) the longest plasma duration possible without phase transition (10 s, sample 3-05). c) Sample 3-06 reveals that hotplate treatment only has almost no influence on the magnetic behavior. 74

4.14 Comparison of ZFC curves (measured at $\mu_0 H = 0.005$ T) for a) a sample treated with oxygen plasma for 11 min (3-07) and b) 12 min (3-08), displaying the necessary duration for phase transition completion. 74

4.15 ZFC (red) and FC (black) curves (measured at 0.005 T) for a) sample 4-01 which is covered with 2 nm platinum and b) sample 4-02 where 5 nm of palladium are applied. Both curves exhibit characteristics similar to the uncovered sample 3-01 (cf. figure 4.10). 76

4.16 Memory effect measurements performed with an aging stop at 140 K for 10000 s on a) the uncovered sample 3-01, b) sample 4-01 which is covered with 2 nm of platinum and c) sample 4-02 on which 5 nm of palladium are applied. 76

4.17 FORC distributions for a,b) sample 4-01 (Pt covered) and sample 4-02 (Pd covered) obtained at a,c) 300 K and b,d) 10 K showing significant changes in the interaction field distribution upon temperature reduction and a negligible coercivity field distribution. 77

4.18 FORC density in dependency of the interaction field at zero coercive field and corresponding Lorentz fit for a) the platinum covered sample 4-01 and b) the palladium covered sample 4-02 at 300 K and 10 K, respectively. The arrows indicate the calculated FWHM. 78

4.19 Hysteresis curves obtained at 5 K for a) the platinum covered sample 4-01 and b) the palladium covered sample 4-02 demonstrating that -1 T are sufficient for negative saturation. 78

4.20 DCD (black), IRM (red) and Delta-M (blue) curves for a) the uncovered sample 3-01, b) sample 4-01 which is covered with 2 nm of platinum and c) sample 4-02 on which 5 nm of palladium showing different strengths of demagnetizing interaction. 79

4.21 Electronic density of states for maghemite. Reprinted with permission from [149]. 80

4.22 XAS measurements for a left and right circularly polarized beam after field-cooling from 300 K to 5 K for a) sample 4-01 with an angle of incidence of 1°and a polarization efficiency of 85% at +3 T and c) -3 T and for b) sample 4-02 with an angle of incidence of 2.2°and a polarization efficiency of 69% at +0.2 T and d) -0.2 T. The corresponding XMCD signals (black) and smoothed curves as guide to the eye (red) are respectively shown in e) for sample 4-01 and f) for sample 4-02. 81

4.23 Sample 5-01 (reference sample, 5 nm palladium only): Resistivity measurements performed at 10 K according to the van der Pauw method with the magnetic field applied a) out-of-plane and b) in plane. For channel I the current flows between a and b and for channel II it flows between b and c. 82

4.24 Sample 5-02 (NPs + 5 nm palladium): Resistivity measurements performed at 10 K according to the van der Pauw method with the magnetic field applied a) out-of-plane and b) in plane. For channel I the current flows between a and b and for channel II it flows between b and c. 83

4.25 Temperature dependency of the resistivity for a) reference sample 5-01 (5 nm palladium only) and b) sample 5-02 (NPs + 5 nm palladium). 84

4.26 Sample 5-02 (NPs + 5 nm palladium): Resistivity measurements performed at 150 K according to the van der Pauw method with the magnetic field applied out-of-plane. The current flows between a and b (channel I). 84

4.27 Overview on the main steps of lithography using either a positive or negative resist, modified [151]. 85

4.28 Sample 5-03: SEM image of the Hall bar structure manufactured by a two step lithography process. The enlarged section on the right shows that the nanoparticles still remain on the surface, covered by a thin, homogeneous Pd film. . . . 86

4.29 Sample 5-03: Magnetic field and temperature dependency of the resistivity for the out-of-plane geometry. 87

4.30 Sample 5-04: a) Magnetic field dependency of the resistivity for the out-of-plane geometry. The lines shown in b) are a guide to the eye to highlight the Lorentz (orange), spin disorder (green) and nanoparticle magnetoresistance effect (blue). 88

4.31 Density of states histograms for platinum and palladium, reprinted with permission from [152]. 89

4.32 Orbital diagrams of a) palladium, b) iron, c) platinum and corresponding ions. . 90

4.33 Sample 4-01: X-ray absorption spectroscopy measurement without normalization performed at the Pt L_3 edge. The edge intensity is indicated by a blue arrow. The green arrow shows the signal intensity in the XANES region. 91

4.34 Spin arrangement for the a) -Pd-O-Pd- b) =Fe-O-Pd- c) -Pt-O-Pt- and d) =Fe-O-Pt- bond. For Pd and Pt ions only the two relevant d orbitals (one d orbital in a lighter, one in a darker shade) are shown. For the oxygen ions in the middle the relevant p orbital is depicted. Fe^{3+} is spherical symmetric as $3d^5$ ion and therefore depicted as sphere. In a crystal field environment the degeneracy of the od-states is lifted but here the nanoparticle surface is considered where the crystal field has no defined symmetry so that the splitting is not well defined. . 92

5.1 Chemical structure of decanoic acid, according to [155]. 93

5.2 SEM images of iron oxide nanoparticles after deposition on a silicon substrate by drop casting, solvent evaporation and oxygen plasma cleaning for a) batch C1, c) batch C2, e) batch C3 and Small Angle X-ray Scattering patterns of 25/30 mg/ml dispersions obtained with GALAXI for b) batch C1, d) batch C2, f) batch C3. 94

5.3 SEM images of iron oxide nanoparticles at the surface of macrocrystals for a) batch O1, c) batch O2 and Small Angle X-ray Scattering patterns of 25/30 mg NP / ml toluene dispersions obtained with GALAXI for b) batch O1, d) batch O2. 95

5.4 X-ray diffraction patterns together with simulated pattern for a spinel structure of a) batch C1, c) batch C2, e) batch C3 and ZFC-FC curves obtained on a nanoparticle (sub-)monolayer deposited on a silicon substrate using b) batch C1, d) batch C2, f) batch C3. 96

5.5 X-ray diffraction patterns together with simulated pattern for a spinel structure of a) batch O1, c) batch O2 and ZFC-FC curves obtained on a single macrocrystal consisting of nanoparticles from b) batch O1, d) batch O2. 97

5.6 Hysteresis curves measured at 300 K (a,c,e,g,i) and 5 K (b,d,f,h,j) for batches C1 (a,b), C2 (c,d), C3 (e,f), O1 (g,h) and O2 (i,j) revealing superparamagnetic behavior. 98

5.7 Schematic overview of the macrocrystal preparation steps. 99

5.8 Nanoparticle sedimentation after 2 h of centrifugation at 10 °C for different accelerations, a) batch O1, b) batch O2. 100

5.9 SEM image of the macrocrystals on top of a 10x2 mm^2 silicon substrate. The left-hand side of the image shows the sample area that was placed in the sample tube bottom for drying. The encircled area shows a thin macrocrystal (height < 100 μm, see below). 101

5.10 Number of macrocrystals per size category for all 21 samples prepared at a centrifugation temperature of 0 °C. 102

5.11 Number of macrocrystals per size category for all samples centrifuged at 0°C, where the dot diameter is proportional to the score value S. 103

5.12 Quality factor for all samples centrifuged at 0°C (black) including a linear fit (red). 103

5.13 Number of macrocrystals per size category for the reproduced samples at a centrifugation temperature of 0°C a) without and b) with illustration of the score value S which corresponds to the dot size. c) Quality factor (black) and linear fit (red). 104

5.14 Number of macrocrystals per size category for all 21 samples centrifuged at 10°C a) without and c) with illustration of the score value S which corresponds to the dot size. e) Quality factor (black) and linear fit (red). b), d) and f) correspond to the reproduced samples. 105

5.15 Number of macrocrystals per size category for all 21 samples centrifuged at 20°C a) without and c) with illustration of the score value S which corresponds to the dot size. e) Quality factor (black) and linear fit (red). b), d) and f) correspond to the reproduced samples. 107

5.16 Number of macrocrystals per size category for all 21 samples centrifuged at 30°C a) without and c) with illustration of the score value S which corresponds to the dot size. e) Quality factor (black) and linear fit (red). b), d) and f) correspond to the reproduced samples. 108

5.17 SEM image of the macrocrystals on top of a 10x2 mm^2 silicon substrate demonstrating how huge macrocrystals at the sample edge break into many small pieces. The left-hand side of the image shows the sample area that was placed in the sample tube bottom for drying. The nanoparticle dispersion used to prepare this sample was centrifuged at 10 000 x g. 109

5.18 Number of macrocrystals per size category for all 21 samples centrifuged at 10°C a) without and c) with illustration of the score value S which corresponds to the dot size. e) Quality factor (black) and linear fit (red). b), d) and f) correspond to the reproduced samples. 111

5.19 Number of macrocrystals per size category for all 21 samples centrifuged at 20°C a) without and c) with illustration of the score value S which corresponds to the dot size. e) Quality factor (black) and linear fit (red). b), d) and f) correspond to the reproduced samples. 112

5.20 a) SAXS pattern of a single macrocrystal removed from the sample centrifuged at 10°C at 21 000 x g using batch O1 and b) radial integrated intensity. 113

5.21 a) SAXS measurements performed on a single macrocrystal removed from the sample centrifuged at 10°C at 21 000 x g using batch O2 and b) radial integrated intensity. The measured (111) peak is labeled in red and further, calculated peak positions for a FCC lattice are shown in black. The specular reflex is highlighted in blue. c) SEM image of an FCC ordered grain at the macrocrystal surface. . . 114

5.22 Batch O1: SAXS measurements performed on single macrocrystals removed from samples that were centrifuged at 12 000 x g (a,c,e,g) and radial integrated intensities (b,d,f,h). The gray area marks the region over which the intensity is integrated for the plots shown in figure 5.23. The centrifugation temperature was a,b) 0°C, c,d) 10°C, e,f) 20°C, g,h) 30°C. 116

5.23 Intensities on the (111) powder ring as function of the azimuthal angle integrated over a ring width of 0.03 $Å^{-1}$ for the SAXS patterns shown in figure 5.22 (batch O1). 117

5.24 Batch O1: SAXS measurements performed on single macrocrystals removed from samples that were centrifuged at 21 000 x g (a,c,e,g) and radial integrated intensities (b,d,f,h). The gray area marks the region over which the intensity is integrated for the plots shown in figure 5.25. The centrifugation temperature was a,b) 0°C, c,d) 10°C, e,f) 20°C, g,h) 30°C. 118

5.25 Intensities on the (111) powder ring as function of the azimuthal angle integrated over a ring width of 0.03 $Å^{-1}$ for the SAXS patterns shown in figure 5.24 (batch O1). 119

5.26 Batch O2: SAXS measurements performed on single macrocrystals removed from samples that were centrifuged at 12 000 x g (a,c,e,g) and radial integrated intensities (b,d,f,h). The measured (111) peak is labeled in red and further, calculated peak positions for a FCC lattice are shown in black. The specular reflex is highlighted in blue. The centrifugation temperature was a,b) 0°C, c,d) 10°C, e,f) 20°C, g,h) 30°C. 120

5.27 Intensities on the (220) powder ring as function of the azimuthal angle integrated over a ring width of 0.01 $Å^{-1}$ for the SAXS patterns shown in figure 5.26 (batch O2). 121

5.28 Batch O2: SAXS measurements performed on single macrocrystals removed from samples that were centrifuged at 21 000 x g (a,c,e,g) and radial integrated intensities (b,d,f,h). The measured (111) peak is labeled in red and further, calculated peak positions for a FCC lattice are shown in black. The specular reflex is highlighted in blue. The centrifugation temperature was a,b) 0°C, c,d) 10°C, e,f) 20°C, g,h) 30°C. 122

5.29 Intensities on the (220) powder ring as function of the azimuthal angle integrated over a ring width of 0.01 $Å^{-1}$ for the SAXS patterns shown in figure 5.28 (batch O2). 123

5.30 Boxplots summarizing the 'mosaic widths' determined from the FWHM of the peaks identified in azimuthal direction on the (220) powder ring for the measurements shown in figures 5.27 and 5.29. The black dots mark the average values and the whiskers indicate minimum and maximum. Bottom and top of the boxes are the first and third quartiles, respectively. The bands inside the boxes show the median values. 126

5.31 Intensities as function of the azimuthal angle integrated over a ring width of 0.04 $Å^{-1}$ for the SAXS patterns shown in figure 5.32. a) Batch C1, b) batch C2, c) batch C3. 127

5.32 a,c,e) SAXS pattern of a single macrocrystal removed from samples centrifuged at 10°C and 21 000 x g using a) batch C1, b) batch C2, c) batch C3 and b,d,f) radial integrated intensities. The gray area marks the region over which the intensity is integrated for the plots shown in figure 5.31. 128

5.33 Memory effect measurements with an aging time of 10 000 s performed on single macrocrystals that were obtained after centrifugation at 10°C at 21 000 x g using a) batch C1, b) batch C2, c) batch O1 and d) batch O2. Hereby the aging stop was performed at 25 K for a) and b) or at 140 K for c) and d). 129

5.34 ZFC-FC measurements performed on single macrocrystals removed from samples prepared using batch O2 by centrifugation at a) 0°C at 21 000 x g, b) 20°C at 21 000 x g, c) 30°C at 21 000 x g and d) 10°C at 12 000 x g. 130

5.35 GISAXS measurement performed at the JCNS GALAXI on the nanoparticle/-palladium multilayer showing only diffuse scattering due to the large scattering length density of palladium. 131

5.36 SEM images of the sample center after each preparation step consisting of nanoparticle deposition, surfactant removal and palladium deposition. 132

5.37 ZFC-FC curves measured on the nanoparticle/palladium multilayer revealing that the nanoparticles still contain wustite remains despite the extensive oxygen plasma treatment. 133

5.38 Hysteresis curves of the nanoparticle/palladium multilayer measured at a) 5 K and b) 300 K, revealing superparamagnetism and exchange bias. 133

5.39 Nanoparticle/palladium multilayer: Memory effect measurement performed with an aging stop at 140 K for 10 000 s demonstrating the superspin glass state of the system. The peak broadening is assigned to the mixed wustite/maghemite iron oxide phase inside the nanoparticles. 134

5.40 Nanoparticle/palladium multilayer: IRM (red), DCD (black) and Delta-M (blue) curves indicating a polarization effect. 134

5.41 Nanoparticle/palladium multilayer: Resistivity in dependency of a magnetic field applied perpendicular to the sample plane, measured at 10 K. 135

List of Tables

2.1 Classification of magnetic effects, where C is the Curie constant and T is the temperature. N is the number of atoms, μ_0 and μ represent the vacuum and magnetic permeability, respectively. V is the volume and k_B the Boltzmann constant. e and m_e give the electronic charge and mass, respectively. Z_a describes the number of electrons and r_a is the ionic radius. μ_B is the Bohr magneton and g_e is the electronic g-factor. E_n and E_0 represent the energy of the excited and ground state, respectively and E_F is the Fermi energy [59]. 13

2.2 Examples for several characteristic length scale ranges, according to [15]. . . . 17

3.1 Assignment of the sample contacts used. 46

4.1 Sample 1-01: Comparison of calculated and measured Q_y values. 63

4.2 Sample overview for section 4.1: The column "sample preparation" provides information about the concentration of the NP dispersion and the rotational speed during spin coating. 66

4.3 Sample overview for section 4.2: The column "sample preparation" provides information about the concentration of the NP dispersion and the rotational speed during spin coating. 68

4.4 Sample overview for section 4.3: The column "sample preparation" provides information about the concentration of the NP dispersion, the rotational speed during spin coating and the plasma process parameters. 75

4.5 Sample overview for section 4.4: The column "sample preparation" provides information about the concentration of the NP dispersion, the rotational speed during spin coating, the plasma process parameters and the matrix material, thickness and deposition method. 80

4.6 Sample overview for section 4.5: The column "sample preparation" provides information about the concentration of the NP dispersion, the rotational speed during spin coating, the plasma process parameters and the matrix material, thickness and deposition method. 88

5.1 Overview of nanoparticle batches used to manufacture macrocrystals. 93

5.2 Overview of sample characteristics at different centrifugation temperatures T, where a_{min} is the minimum acceleration to find macrocrystals longer than 1000 μm, a_{best} is the acceleration of the best sample according to the mean quality factor and M is the arithmetic average of the mean quality values for all samples centrifuged at a specific temperature. 109

5.3 Overview of sample characteristics at different centrifugation temperatures T, where a_{min} is the minimum acceleration to find macrocrystals longer than 1000 μm, a_{best} is the acceleration of the best sample according to the mean quality factor and M is the arithmetic average of the mean quality values for all samples centrifuged at a specific temperature. 110

5.4 Measured Q_y value for the (111) reflex together with calculated positions of further peaks (equation 5.3) for face centered cubic symmetry (cf. equation 5.6) and a lattice constant of 23.2 nm. 115

5.5 Measured Q_y values for the (111) reflex together with the calculated lattice constants (according to equation 5.4) and the calculated positions of further peaks (according to equation 5.3) for face centered cubic symmetry (cf. equation 5.6). 124

5.6 Average sizes of coherently scattering areas D_{220} calculated using the FWHM of the (220) ring integrated in radial direction ΔQ_{220}. T and a are the centrifugation temperature and acceleration, respectively. 125

E.1 Macrocrystal obtained from batch O1, centrifuged at 0°C and 12 000 x g. . . . 193

E.2 Macrocrystal obtained from batch O1, centrifuged at 0°C and 21 000 x g. . . . 194

E.3 Macrocrystal obtained from batch O1, centrifuged at 10°C and 12 000 x g. . . . 195

E.4 Macrocrystal obtained from batch O1, centrifuged at 10°C and 21 000 x g. . . . 195

E.5 Macrocrystal obtained from batch O1, centrifuged at 20°C and 12 000 x g. . . . 196

E.6 Macrocrystal obtained from batch O1, centrifuged at 20°C and 21 000 x g. . . . 197

E.7 Macrocrystal obtained from batch O1, centrifuged at 30°C and 12 000 x g. . . . 198

E.8 Macrocrystal obtained from batch O1, centrifuged at 30°C and 21 000 x g. . . . 198

List of Acronyms

APS	Advanced Photon Source
BA	Born Approximation
BCS	Bardeen-Cooper-Schrieffer
CCP	Cubic Close Packing
CFD	Coercive Field Distribution
CFE	Cold Field Emission
cgs	centimeter-gram-second
CTR	Crystal Truncation Rods
DA	Decoupling Approximation
DCD	DC Demagnetization remanence
DWBA	Distorted Wave Born Approximation
EXAFS	Extened X-ray Absorption Fine Structure
FC	Field Cooled
FORC	First-Order Reversal Curves
FT	Fourier Transform
FWHM	Full Width Half Maximum
GALAXI	Gallium Anode Low-Angle X-ray Instrument
GISAXS	Grazing Incidence Small Angle X-ray Scattering
IBS	Ion Beam Sputtering
ICSD	Inorganic Crystal Structure Database
IFD	Interaction Field Distribution
IRM	Isothermal Remanent Magnetization
JCNS	Jülich Center for Neutron Science
LMA	Local Monodisperse Approximation
LUMO	Lowest Unoccupied Molecular Orbital
MBE	Molecular Beam Epitaxy

MOKE	Magneto-Optical Kerr Effect
MPMS	Magnetic Property Measurement System
NP	nanoparticle
PPMS	Physical Property Measurement System
rpm	Revolutions Per Minute
rps	Revolutions Per Second
SAXS	Small Angle X-ray Scattering
SE	Secondary Electrons
SEM	Scanning Electron Microscopy
SFM	SuperFerroMagnetism
SPM	SuperParaMagnet
SQUID	Superconducting QUantum Interference Device
SSG	SuperSpin Glass
TEM	Transmission Electron Microscopy
UHV	Ultra High Vacuum
VSM	Vibrating Sample Magnetometer
XANES	X-ray Absorption Near Edge Structure
XAS	X-ray Absorption Spectroscopy
XMCD	X-ray Magnetic Circular Dichroism
XRPD	X-Ray Powder Diffraction
ZFC	Zero Field Cooled

List of Symbols

A	amplitude of sample motion / exchange constant / effective area of the coil normal to the magnetic induction
C	Curie constant
E_0	energy of the ground state
E_F	Fermi energy
E_S	energy eigenvalue of the singlet state
E_T	energy eigenvalue of the triplet state
E_n	energy of the excited state
E_{kin}	kinetic energy of electrons
E_{ne}	nuclear-electron attraction (Coulomb) energy
E_{th}	thermal Energy
E_{xc}	electron-electron exchange-correlation
E	energy / eigenvalue of the hamiltonian describing the system without interaction giving the energy
$F(\vec{Q})$	phase factor
F	attractive force between colloidal spheres due to depletion
G	geometric factor of pickup coils
H_0	hamiltonian describing the system without interaction
H_c^{FORC}	FORC coercivity
H_c	coercive field strength
H_{down}	threshold reversal field for negative field strength
H_r	reversal field strength
H_{up}	threshold reversal field for positive field strength
H_u	hysteron offset from origin / interaction field
I	electrical current / beam intensity
J	electron-electron repulsive (Coulomb) energy / exchange integral
K	anisotropy constant / K constant
M_d	normalized DCD curve
M_r	normalized IRM curve
M_s	saturation magnetization
M_{atom}	magnetization averaged over the atomic volume

M	magnetization
$N_{\parallel}$	demagnetization factors parallel to the symmetry axis of the ellipsoid
$N_{\perp}$	demagnetization factors perpendicular to the symmetry axis of the ellipsoid
N_{inc}	number of incoming particles
N_{sc}	number of scattered particles
N	number of turns in a pickup coil / number of atoms / number of monomers in the polymer chain
O	observable
$P(\vec{Q})$	form factor
P_{sc}	scattering probability
P	polarization efficiency / arbitrary point in space / osmotic pressure
Q_y	scattering vector component parallel to the sample surface
Q_z	scattering vector component perpendicular to the sample surface
Q_{Bragg}	position of Bragg peak in Q space
R_G	radius of gyration
R_c	critical radius for monodomain state
R_s	sheet resistance
R	particle radius / gas constant
$S(Q)$	structure factor
$S(\vec{Q_y})$	y component of the structure factor
$S\,(R)$	center of mass movement
T_B	blocking temperature
T_C	Curie temperature
T_G	glass temperature
T_N	Néel temperature
T_V	temperature for Verwey transition
T_c	critical temperature for superconduction
$T_q^{(Q)}$	electric multipole operator
T	temperature
$U_1,\ V_1,\ W_1$	set of integers
$U_2,\ V_2,\ W_2$	set of integers
U_s	repulsive energy between two nanoparticles with steric stabilization

U_{dd}^{fluc}	contribution to the dipolar interaction energy due to thermal fluctuations
U_{dd}^{stat}	static contribution to the dipolar interaction energy
U_{dd}	dipolar interaction energy
U_{dep}	depletion interaction potential
U_{vdW}	van der Waals interaction potential
U	Coulomb energy
$V_{ext}^{\uparrow\downarrow}$	spin density for minority electrons
V_m	molar volume
V_{ov}	overlap volume
$V_{xc}^{\uparrow\downarrow}$	spin density for minority electrons
V	volume / potential energy / electromotive force
W_{l_i,l_k}	coupling energy between orbital angular momenta of single electrons
W_{l_i,s_i}	coupling energy between spin and orbital angular momentum
W_{s_i,s_k}	coupling energy between single spins of electrons
Z_a	number of electrons
ΔE_{KE}	kinetic energy change
ΔE_{PE}	molecular field energy
ΔE	total energy change
ΔH_u	global interaction field
$\Delta\Phi$	total phase difference
Γ	surface densities
Ω	solid angle
Φ_0	magnetic flux quantum
Φ_K	complex Kerr angle
Φ	magnetic flux
Ψ_S	wave function for a two-electron system forming a singlet state
Ψ_T	wave function for a two-electron system forming a triplet state
Ψ	wave function / angle between the superspin moment and the long symmetry axis
Θ	contact angle
α_0	electronic polarizability of a non-polar atom
α_f	angle of scattered beam
α_i	angle of incidence

α	radial quantum number / fine-structure constant / angle between magnetocrystalline anisotropy axis and applied magnetic field
χ	magnetic susceptibility
δ	domain wall width
ϵ_K	Kerr ellipticity
ϵ_r	relative permittivity
ϵ_0	vacuum permittivity
$\frac{\sigma}{2}$	monomer length
γ	magnetic quantum number of core state / gyromagnetic ratio / interfacial tension
$\hbar$	reduced Planck constant
κ	ellipticity
$\|\Phi\rangle$	eigenfunction of the hamiltonian describing the system without interaction
λ	wavelength
$\langle L_z \rangle$	expectation value for orbital operator in Bohr magnetons
$\langle S_z \rangle$	expectation value for spin operator in Bohr magnetons
$\langle T_z \rangle$	expectation value for magnetic dipole operator in Bohr magnetons
μ^+	absorption of right circular polarized light
μ^-	absorption of left circular polarized light
μ_0	integrated isotropic absorption / vacuum permeability
μ_B	Bohr magneton
μ_L	orbital magnetic moment
μ_S	spin magnetic moment
μ_c	integrated dichroic absorption
μ	magnetic permeability
ν	orbiting frequency of the electron
ω	angular frequency of sample motion
π	phase factor
ρ_{FORC}	FORC distribution
ρ	electron density / resistivity
σ_w	energy of a domain wall per unit area
σ	sample moment
σ	spin quantum number / surface tension / scattering cross section

τ_0	elementary spin flip time
τ_m	measurement duration
τ	characteristic relaxation time
θ_K	Kerr rotation
θ	angle of incidence / angle between the superspin moment and the magnetocrystalline anisotropy axis / scattering angle / Weiss temperature
$\vec{B}$	magnetic induction
$\vec{G}$	reciprocal lattice vector
$\vec{H}$	magnetic field
$\vec{J}$	total angular momentum of the whole electron shell
$\vec{L}$	total orbital angular momentum
$\vec{M}$	microscopic magnetic moment / magnetization
$\vec{Q}$	scattering vector
$\vec{S}$	spin vector / total spin of the whole electron shell
$\vec{\mu}$	magnetic dipole moment
$\vec{a},\ \vec{b},\ \vec{c}$	basis vectors
$\vec{a}^*,\ \vec{b}^*,\ \vec{c}^*$	basis vectors of the reciprocal space
$\vec{d_{hkl}}^*$	reciprocal lattice vector
$\vec{d_{hkl}}$	component of $\vec{r_{hkl}}$ parallel to $\vec{d_{hkl}}^*$
$\vec{j}$	total angular momentum of a single electron
$\vec{k_f}$	scattered wave vector
$\vec{k_i}$	wave vector of the incoming beam
$\vec{k_s}$	wave vector of the scattered beam
$\vec{k}$	wave vector
$\vec{l}$	orbital angular momentum of a single electron
$\vec{m}$	macroscopic magnetic moment
$\vec{p_{hkl}}$	component of $\vec{r_{hkl}}$ lying within the plane
$\vec{p}$	momentum
$\vec{r_j}$	origin for the definition of relative particle positions
$\vec{r_{hkl}}$	vector pointing from the origin to any point in a plane
$\vec{r}$	vector from dI to an arbitrary point in space / vector giving the three positional coordinates x, y and z / vector between two particles

$\vec{s}$	spin angular momentum of a single electron
$\vec{t_1}$	vector within a plane
$\vec{t_2}$	vector within a plane
$\vec{x}$	position in space
$\widehat{H}_U$	Hamilton operator for Coulomb energy
$\widehat{H}_t$	Hamilton operator for kinetic energy
$\widehat{H}$	Hamilton operator
$\widehat{O}$	observable
$\widehat{S}$	spin operator
ξ	nanoparticle coherence length
a	lattice constant / nearest neighbor distance / radius / interatomic distance
b	monomer length / scattering parameter
$c_{i\sigma}$	operator that removes an electron with spin σ from lattice site i
$c^+_{j\sigma}$	operator that creates an electron with spin σ at lattice site j
c	orbital quantum number of core state
$d\vec{I}$	infinitesimal conductor element that points towards positive current direction
d_{Bragg}	distance between aligned particles according to Bragg's law
d	distance between planes of atoms
e	electron charge
f_j	form factor / scattering length / X-ray atomic scattering factor
$g(E_F)$	density of states at the Fermi edge
g_e	Landé factor
g	electronic g-factor
$h,\ k,\ l$	Miller indices
h_0	equilibrium height of polymer chains
h	Planck constant
$i\epsilon$	mathematicaly necessary construct without physical origin
j	total angular momentum / incident beam flux
k_0	elastically conserved wave vector modulus
k_B	Boltzmann constant
l	orbital quantum number / azimuthal radius / path length difference
m_l	magnetic quantum number

m_s	spin quantum number
m_K	mass of the nucleus
m_e	electron mass
m	moment density
n_0	electron density for the non-magnetic case
n_B	total number of solutes
n_h	number of holes available in the final states
$n_\downarrow$	spin density for minority electrons
$n_\uparrow$	spin density for majority electrons
$n_{i\sigma}$	operator that counts electrons with spin σ at lattice site i
n_{tar}	target density
n	principal quantum number / electron density / number of particles per second
p_0^k	vapor pressure for a curved surface
p_0	vapor pressure for a flat surface
p	probability for superspin reversal / pressure
q	absolute value of the scattering vector
r_a	ionic radius
r	distance between electron and nucleus / distance between two magnetic dipoles / center to center distance between two particles / principal radius of curvature
s	spin / tangent slope
t_w	waiting time
t	hopping amplitude / sheet thickness
u	polarizability of a dipole
v	molar volume / velocity
z	number of sites in the unit cell (e.g. 1 for simple cubic, 2 for body centered cubic) / distance to the surface

Bibliography

[1] B. D. Terris and T. Thomson, "Nanofabricated and self-assembled magnetic structures as data storage media," *J. Phys. D: Appl. Phys.*, vol. 38, no. 12, p. R199, 2005.

[2] Karmar *Journal of Physics*, vol. 012002, 2011.

[3] R. Saidur, S. N. Kazi, M. S. Hossain, M. M. Rahman, and H. A. Mohammed, "A review on the performance of nanoparticles suspended with refrigerants and lubricating oils in refrigeration systems," *Renewable and Sustainable Energy Reviews*, vol. 15, no. 1, pp. 310 – 323, 2011.

[4] Prasad *Nanostructure, Science and Technology*, vol. 89, 2009.

[5] H. A. Atwater, "The promise of plasmonics," *Sci. Amer.*, vol. 296, no. 4, pp. 56–63, 2007.

[6] D. J. Norris, A. L. Efros, and S. C. Erwin, "Doped nanocrystals," *Science*, vol. 319, no. 5871, pp. 1776–1779, 2008.

[7] O. Petracic, "Superparamagnetic nanoparticle ensembles," *Superlattices and Microstructures*, vol. 47, no. 5, pp. 569 – 578, 2010.

[8] M. J. Benitez, O. Petracic, H. Tüysüz, F. Schüth, and H. Zabel, "Fingerprinting the magnetic behavior of antiferromagnetic nanostructures using remanent magnetization curves," *Phys. Rev. B*, vol. 83, p. 134424, Apr 2011.

[9] C. P. Bean and J. D. Livingston, "Superparamagnetism," *J. Appl. Phys.*, vol. 30, no. 4, pp. S120–S129, 1959.

[10] K. Sato, T. Fukushima, and H. Katayama-Yoshida, "Super-paramagnetic blocking phenomena and room-temperature ferromagnetism in wide band-gap dilute magnetic semiconductor (Ga, Mn)N," *Japanese Journal of Applied Physics*, vol. 46, pp. L682–L684, 2007.

[11] S. Soeya, "Distribution of blocking temperature in bilayered Ni81FE19/NiO films," *Journal of Applied Physics*, vol. 76, no. 5356-5360, 1994.

[12] E. E. Carpenter, "Effects of shell thickness on blocking temperature of nanocomposites of metal particles with gold shells," *Transactions on Magnetics*, vol. 35, pp. 3496–3499, 1999.

[13] J. Dai, J. Q. Wang, C. Sangregorio, J. Fang, E. Carpenter, and J. Tang, "Magnetic coupling induced increase in the blocking temperature of gamma-fe2o3 nanoparticles," *Journal of Applied Physics*, vol. 87, no. 10, pp. 7397–7399, 2000.

[14] C. Radhakrishnamurty and S. D. Likhite, "Hipkinson effect, blocking temperature and curie point in basalts," *Earth and Planetary Science Letters*, vol. 7, pp. 389–396, 1970.

[15] A. P. Guimaraes, *Principles of Nanomagnetism*. Springer, 2009.

[16] S. Bedanta, O. Petracic, X. Chen, J. Rhensius, S. Bedanta, E. Kentzinger, U. Rücker, T. Brückel, A. Doran, A. Scholl, S. Cardoso, P. P. Freitas, and W. Kleemann, "Single-particle blocking and collective magnetic states in discontinuous CoFe/Al 2 O 3 multilayers," *J. Phys. D: Appl. Phys.*, vol. 43, no. 47, p. 474002, 2010.

[17] M. Suzuki, S. I. Fullem, I. S. Suzuki, L. Wang, and C. J. Zhong, "Observation of superspin-glass behavior in Fe3O4 nanoparticles," *Phys. Rev. B*, vol. 79, p. 024418, Jan 2009.

[18] S. A. Majetich and M. Sachan, "Magnetostatic interactions in magnetic nanoparticle assemblies: energy, time and length scales," *J. Phys. D: Appl. Phys.*, vol. 39, no. 21, p. R407, 2006.

[19] O. Petracic, X. Chen, B. S., K. W., S. S., C. S., and F. P. P., "Collective states of interacting ferromagnetic nanoparticles," *Journal of Magnetism and Magnetic Materials*, vol. 300, no. 1, pp. 192 – 197, 2006.

[20] M. Varón, M. Beleggia, T. Kasama, R. J. Harrison, R. E. Dunin-Borkowski, V. F. Puntes, and C. Frandsen, "Dipolar magnetism in ordered and disordered low-dimensional nanoparticle assemblies," *Sci. Rep.*, vol. 3, Feb 2013.

[21] D. L. Leslie-Pelecky and R. D. Rieke, "Magnetic properties of nanostructured materials," *Chemistry of Materials*, vol. 8, no. 8, pp. 1770–1783, 1996.

[22] P. J. Jensen and G. M. Pastor, "Low-energy properties of two-dimensional magnetic nanostructures: interparticle interactions and disorder effects," *New Journal of Physics*, vol. 5, p. 68, 2003.

[23] J. B. Kortright, O. Hellwig, K. Chesnel, S. Sun, and E. E. Fullerton, "Interparticle magnetic correlations in dense co nanoparticle assemblies," *Phys. Rev. B*, vol. 71, p. 012402, 2005.

[24] J. Lopes and Y. G. Pogorelov, "Indirect interactions between magnetic nanoparticles in granular alloys," *Journal of Magnetism and Magnetic Materials*, vol. 272-276, pp. e1249–e1250, 2004.

[25] F. Li, D. P. Josephson, and A. Stein, "Colloidal assembly: The road from particles to colloidal molecules and crystals," *Angewandte Chemie International Edition*, vol. 50, no. 2, pp. 360–388, 2011.

[26] E. Josten, *Long range order in 3D nanoparticle assemblies*. PhD thesis, RWTH Aachen, 2014.

[27] S. A. Sebt, A. Bakhshayeshi, and M. R. Abilhassani, "Magnetic properties of core/shell nanoparticles with magnetic or nonmagnetic shells," p. P09006, 2012.

[28] L. Wang, J. Luo, M. M. Maye, Q. Fan, Q. Rendeng, M. H. Engelhard, C. Wang, Y. Lin, and C.-J. Zhong, "Iron oxide-gold core-shell nanoparticles and thin film assembly," *J. Mater. Chem.*, vol. 15, pp. 1821–1832, 2005.

[29] X. Teng and H. Yang, "Synthesis of face-centered tetragonal fept nanoparticles and granular films from Pt@Fe2O3 core-shell nanoparticles," *Journal of the American Chemical Society*, vol. 125, no. 47, pp. 14559–14563, 2003. PMID: 14624605.

[30] X. Teng and H. Yang, "Synthesis of magnetic nanocomposites and alloys from platinum-iron oxide core-shell nanoparticles," vol. 16, pp. S554–S561, 2005.

[31] X. Teng, D. Black, N. J. Watkins, Y. Gao, and H. Yang, "Platinum-maghemite core-shell nanoparticles using a sequential synthesis," vol. 3, pp. 261–264, 2002.

[32] X. B. Zhang, J. M. Yan, S. Han, H. Shioyama, and Q. Xu, "Magnetically recyclable Fe@Pt core-shell nanoparticles and their use as electrocatalysts for ammonia borane oxidation: The role of crystallinity of the core," vol. 131, pp. 2778–2779, 2009.

[33] L. T. Kuhn, A. Bojesen, L. Timmermann, M. M. Nielsen, and S. Mørup, "Structural and magnetic properties of core-shell iron-iron oxide nanoparticles," *Journal of Physics: Condensed Matter*, vol. 14, no. 49, p. 13551, 2002.

[34] A. Ebbing, O. Hellwig, L. Agudo, G. Eggeler, and O. Petracic, "Tuning the magnetic properties of co nanoparticles by Pt capping," *Phys. Rev. B*, vol. 84, p. 012405, Jul 2011.

[35] A. Uheida, M. Iglesias, C. Fontas, M. Hidalgo, V. Salvado, Y. Zhang, and M. Muhammed, "Sorption of palladium(ii), rhodium(iii), and platinum(iv) on Fe3O4 nanoparticles,," *Colloid and Interface Science*, vol. 301, pp. 402–208, 2006.

[36] P. Gambardella, S. Rusponi, M. Veronese, S. S. Dhesi, C. Grazioli, A. Dallmeyer, I. Cabria, R. Zeller, P. H. Dederichs, K. Kern, C. Carbone, and H. Brune, "Giant magnetic anisotropy of single cobalt atoms and nanoparticles," *Science*, pp. 1130–1133, May 2003.

[37] E. Navarro, Y. Huttel, C. Clavero, A. Cebollada, and G. Armelles, "Magnetic coupling between Fe nanoislands induced by capping-layer magnetic polarization," *Phys. Rev. B*, vol. 69, p. 224419, Jun 2004.

[38] F. Meier, S. Lounis, J. Wiebe, L. Zhou, S. Heers, P. Mavropoulos, P. H. Dederichs, S. Blügel, and R. Wiesendanger, "Spin polarization of platinum (111) induced by the proximity to cobalt nanostripes," *Phys. Rev. B*, vol. 83, p. 075407, Feb 2011.

[39] P. Zakalek, *Magnetic Interface Effects in Thin Film Heterostructures*. PhD thesis, RWTH Aachen, 2015.

[40] J. B. Calvert, "Iron - the metal of mars gives us magnetism and life." University of Denver, Online `http://mysite.du.edu/~jcalvert/phys/iron.htm`, 2015.

[41] G. S. of Australiahmad, "Iron fact-ite." Geological Society of Australia, Online `www.gsa.org.au/resources/factites/factitesIron.pdf`.

[42] U. Schwertmann and R. M. Cornell, *The Iron Oxides: Structure, Properties, Reactions, Occurences and Uses*. Wiley VCH, 2003.

[43] G. Ketteler, W. Weiss, W. Ranke, and R. Schlogl, "Bulk and surface phases of iron oxides in an oxygen and water atmosphere at low pressure," *Phys. Chem. Chem. Phys.*, vol. 3, pp. 1114–1122, 2001.

[44] J. Coey, "Magnetism in future," *Journal of Magnetism and Magnetic Materials*, vol. 226-230, Part 2, no. 0, pp. 2107 – 2112, 2001.

[45] A. P. C. Teixeira, J. C. Tristao, M. H. Araujo, L. C. A. Oliveira, F. C. C. Moura, J. D. Ardisson, C. C. Amorim, and R. M. Lago, "Iron: a versatile element to produce materials for environmental applications," *Journal of the Brazilian Chemical Society*, vol. 23, no. 9, pp. 1579–1593, 2012. Magnetite: Structure, transformation, application.

[46] M. A. Legodi and D. de Waal, "The preparation of magnetite, goethite, hematite and maghemite of pigment quality from mill scale iron waste," *Dyes and Pigments*, vol. 74, no. 1, pp. 161 – 168, 2007. Maghemite / magnetite / hematite: Pigments.

[47] D. Mishra, *Structural and magnetic Characterization of Self-assembled magnetic nanoparticles*. Phd thesis, Ruhr Universität Bochum, 2012.

[48] M. Friák, A. Schindlmayr, and M. Scheffler, "Ab initio study of the half-metal to metal transition in strained magnetite," *New Journal of Physics*, vol. 9, January 2007. Magnetite: Properties.

[49] Spektrum, Online `http://www.spektrum.de/lexikon/geowissenschaften/magnetit/9927`.

[50] M. Aliahmad and N. N. Moghaddam, "Synthesis of maghemite nanoparticles by thermal-decomposition of magnetite nanoparticles," *Materials Science-Poland*, vol. 31, no. 2, pp. 264–268, 2013.

[51] D. Mishra, D. Greving, G. A. Badini Confalonieri, J. Perlich, B. P. Toperverg, H. Zabel, and O. Petracic, "Growth modes of nanoparticle superlattice thin films," *Condensed Matter*, 2013.

[52] Spektrum, Online `http://www.spektrum.de/lexikon/geowissenschaften/maghemit/9871`.

[53] M. Yin, Z. Chen, B. Deegan, and S. O'Brien, "Wüstite nanocrystals: Synthesis, structure and superlattice formation," *Journal of Materials Research*, vol. 22, pp. 1987–1995, 7 2007.

[54] C. McCammon and L. G. Liu, "The effects of pressure and temperature on nonstoichiometric wustite: The iron-rich phase boundary," *Physics and Chemistry of Minerals*, vol. 10, no. 3, pp. 106–113, 1984. Wustite: Properties.

[55] D. S. Tannhauser, "Conductivity in iron oxides," *Journal of Physics and Chemistry of Solids*, vol. 23, no. 23, pp. 25 – 34, 1962. Wustite / magnetite: Structure, conductivity.

[56] H. Schröcke and K.-L. Weiner, *Mineralogie: Ein Lehrbuch auf systematischer Grundlage*. Walter de Gruyter, 1981.

[57] D. Mishra, M. J. Benitez, O. Petracic, G. A. Badini Confalonieri, P. Szary, F. Brüssing, K. Theis-Bröhl, A. Devishvili, A. Vorobiev, O. Konovalov, M. Paulus, C. Sternemann, B. P. Toperverg, and H. Zabel, "Self-assembled iron oxide nanoparticle multilayer: x-ray and polarized neutron reflectivity," *Nanotechnology*, vol. 23, no. 5, p. 055707, 2012.

[58] G. E. Kugel, B. Hennion, and C. Carabatos, "Low-energy magnetic excitations in wustite," *Physical Review B*, vol. 18, pp. 1317–1321, Aug 1978. Wustite: Structure, magnetism.

[59] M. Opel and S. Goennenwein, "Magnetismus." Vorlesungsskript TU München, 2005.

[60] R. Gross, "Physik IV - Atome, Moleküle, Wärmestatistik - Vorlesungsskript zur Vorlesung im SS 2003." Walther-Meissner-Institut Bayerische Akademie der Wissenschaften und Lehrstuhl für Technische Physik, Technische Universität München, 2003.

[61] Permagsoft. Online `http://www.permagsoft.com/english/html/theory.html`.

[62] R. Feynmann, R. Leighton, and M. Sands, *Quantenmechanik*, vol. 3. Oldenbourg Verlag München Wien, 2006.

[63] S. Blundell, *Magnetism in Condensed Matter*. Oxford University Press, 2001.

[64] K. H. J. Buschow, ed., *Handbook of Magnetic Materials*, vol. 23. Elsevier, 2015.

[65] P. Bruno, *Physical origins and theoretical models of magnetic anisotropy*, ch. 24. Forschungszentrum Jülich GmbH, 1993.

[66] S. Feynmann, Leighton, *The Feynmann Lectures on Physics*. Basic Books - A Member of the Perseus Books Group, 2010.

[67] C. Kittel, *Einführung in die Festkörperphysik*. Oldenbourg Wissenschaftsverlag GmbH, 2006.

[68] D. Koelle, "Experimentalphysik V - Festkörperphysik." Vorlesungsmanuskript Universität Tübingen, 2003.

[69] L. Bergmann and C. Schaefer, *Lehrbuch der Experimentalphysik Band 6 - Festkörper*, vol. 6. 2005.

[70] A. Raman, "From interactomic and intermolecular forces to tip-sample interaction forces." Lecture notes Purdue University, 2009.

[71] C. Barrera, A. P. Herrera, and C. Rinaldi, "Colloidal dispersions of monodisperse magnetite nanoparticles modified with poly(ethylene glycol)," no. 329, pp. 107–113, 2008.

[72] H. J. Butt and M. Kappl, *Surface and Interfacial Forces*. Wiley, 2010.

[73] P. Joos, *Dynamic Surface Phenomena*. Ridderprint, 1999.

[74] H. J. Butt, K. Graf, and M. Kappl, *Physics and Chemistry of Interfaces*. Wiley, 2003.

[75] H. N. W. Lekkerkerker and R. Tuinier, *Colloids and the depletion interaction*. Springer-Verlag, 2011.

[76] V. J. Anderson and H. N. W. Lekkerkerker, "Insights into phase transition kinetics from colloid science," *Nature*, vol. 416, pp. 811–815, Apr. 2002.

[77] K. J. M. Bishop, C. E. Wilmer, S. Soh, and B. A. Grzybowski, "Nanoscale forces and their uses in self-assembly," *Small*, vol. 5, no. 14, pp. 1600–1630, 2009.

[78] M. Dove, *Structure and Dynamics*. Oxford University Press, 2003.

[79] M. Winter, *Messung von zeitlichen und räumlichen Strukturen mittels ultrakurzen Elektronenpulsen*. PhD thesis, Universität Kassel, 2008.

[80] S. Disch, *The spin structure of magnetic nanoparticles and in meagnetic nanostructures*. Phd thesis, RWTH Aachen, 2010.

[81] T. Brückel, J. Voigt, G. Heger, G. Roth, H. Frielinghaus, J. Stellbrink, R. P. Hermann, E. Kentzinger, U. Rücker, R. Zorn, M. Angst, and D. Richter, *Laboratory Course Neutron Scattering*. Forschungszentrum Jülich GmbH, 2012.

[82] T. Brückel, M. Angst, D. Richter, and R. Zorn, eds., *Scattering Methods for Condensed Matter Research: Towards Novel Applications at Future Sources*. Forschungszentrum Jülich, 2012.

[83] D. Suter, "Vorlesungsmanuskript Festkörperphysik - Freie Elektronen." Online: `https://e3.physik.uni-dortmund.de/~suter/vorlesung/Festkoerperphysik/5_Freie_Elektronen.pdf.`, 1995.

[84] G. Reiss, E. Hastreiter, H. Brückl, and J. Vancea, "Thickness-dependent thin-film resistivity: Application of quantitative scanning-tunneling-microscopy imaging," *Phys. Rev. B*, vol. 43, pp. 5176–5179, Feb 1991.

[85] I. S. Beloborodov, A. V. Lopatin, V. M. Vinokur, and K. B. Efetov, "Granular electronic systems," *Rev. Mod. Phys.*, vol. 79, pp. 469–518, Apr 2007.

[86] T. F. Moerstedt, "Magnetische und elektrische Eigenschaften selbstorganisierter Nanopartikel," Master's thesis, RWTH Aachen, 2016.

[87] N. Reckers, "Magnetowiderstand von ferromagnetischen elektronenlithographisch hergestellten Leiterbahnen," diplomarbeit, Universität Duisburg-Essen, 2005.

[88] I. Knittel and U. Hartmann, "Lorentz magnetoresistance of thin films in the presence of surface scattering and domain structures," *Journal of Magnetism and Magnetic Materials*, vol. 294, no. 1, pp. 16 – 26, 2005.

[89] J. Nickel, "Magnetoresistance overview." Hewlett Packard - Computer Peripherals Laboratory HPL-95-60, 1995.

[90] A. Wysocki, K. D. Belashchenko, J. P. Velev, and M. Schilfgaarde, "Calculations of spin-disorder resistivity from first principles," *J. Appl. Phys.*, vol. 101, p. 09G506, 2007.

[91] H. Kinder, "Vorlesung Supraleitung und Tieftemperaturphysik." Vorlesungsmanuskript, Online: `http://einrichtungen.ph.tum.de/E10/Dateien/skript.html`, 2000.

[92] J. Pascual, "Vorlesung Experimentalphysik - The Tunnel Magnetoresistance." Online: `http://users.physik.fu-berlin.de/~pascual/Vorlesung/WS05/Slides/WS05-06%20AdMat%20IT%20-%20L4b.PDF`, 2005.

[93] Y. K. Lee, J. Kim, Y. Rhee, and V. V. Kudryavtsev, "Electron transport properties of phase co ti alloy films with various degrees of long range order," *Physics of Condensed Matter*, vol. 15, no. 3, pp. 451–459, 2000.

[94] R. P. Guertin and S. Foner, *Magnetometry*. John Wiley & Sons, Inc., 2002.

[95] Quantum Design, *Vibrating Sample Magnetometer PPMS Quantum Design Manual*.

[96] CAU, "Basic laboratory materials science an engineering vibrating sample magnetometry." Christian-Albrechts-Universität zu Kiel, 2011.

[97] E. Britannica, "BCS theory." Online `http://www.britannica.com/science/BCS-theory`, Sep 2015.

[98] H. Ohanian, *Classical Electrodynamics*, vol. 2. Jones & Bartlett Learning, LLC, 2006.

[99] J. Clarke, "SQUIDs," *Scientific American*, vol. 271, p. 46, 1994.

[100] NIST, "National institute of standards and technology." Online, http://physics.nist.gov/cgi-bin/cuu/Value?flxquhs2e.

[101] R. Simon and A. Smith, *Superconductors - Conquering Technology s New Frontier*. Springer-Verlag, 1988.

[102] A. Ebbing, "Magnetische eigenschaften von Co/Pt und Co/Pd nanostrukturen und nanopartikeln," Master's thesis, Ruhr-Universität Bochum, 2010.

[103] M. McElfresh, "Fundamentals of magnetism and magnetic measurements featuring quantum design's magnetic measurement system," *Primer: Purdue University, USA*, 1994.

[104] S. Wang, A. Khapikov, S. Brown, and J. Harrell, "Thermal effects on delta-m measurements in magnetic thin films," *IEEE Trans. Magn.*, vol. 37, pp. 1518–1520, Jul 2001.

[105] J. W. Harrell, S. Wang, and H. Fujiwara, "Field step dependence of delta-m curves," *J. Appl. Phys.*, vol. 91, pp. 8605–8607, Mai 2002.

[106] P. E. Kelly, K. O'Grady, P. I. Mayo, and R. W. Chantrell, "Switching mechanisms in cobalt-phosphorus thin films," *IEEE Trans. Magn.*, vol. 25, pp. 3881–3883, Sep 1989.

[107] "Magneto-optic kerr effect magnetometry and microscopy." AG Magnetismus Fachbereich Physik, Online: `https://www.physik.uni-kl.de/hillebrands/research/methods/magneto-optic-kerr-effect-magnetometry-and-microscopy/`, 2016.

[108] *Magneto-optischer Kerr-Effekt, Fortgeschrittenen-Praktikum II im Bereich angewandte Physik*. Universität Kaiserslautern, 2014.

[109] F. Béron, L.-P. Carignan, D. Ménard, and A. Yelon, *Extracting Individual Properties from Global Behaviour: First-order Reversal Curve Method Applied to Magnetic Nanowire Arrays*. 2010.

[110] J. Gräfe, M. Schmidt, P. Audehm, G. Schütz, and E. Goering, "Application of magneto-optical kerr effect to first-order reversal curve measurements," *Rev. Sci. Instrum.*, vol. 85, no. 2, p. 023901, 2014.

[111] D. Lonormand, *Characterization of Magnetic Nanostructured Materials by First Order Reversal Curve Method*. Master thesis, University of New Orleans, 2012.

[112] T. G. Sorop, C. Untiedt, F. Luis, M. Kröll, M. Rasa, and L. J. de Jongh, "Magenetization reversal of ferromagnetic nanowires studied by magnetic force microscopy," *Phys. Rev. B*, vol. 67, p. 014402, 2003.

[113] Quantum Design, *Quantum Design: Physical Property Measurement System Hardware Manual*, 2008.

[114] Quantum Design, *Quantum Design: Performing van der Pauw Resistivity Measurement, Application Note 1076-304, 2007*.

[115] Universität Augsburg, *Pulverdiffraktometrie - Praktikumsmanuskript FP26 der Universität Augsburg, Institut für Physik, Lehrstuhl für Festkörperchemie*, 2014.

[116] L. A. Aslanov, G. V. Fetisov, and J. A. K. Howard, *Crystallographic Instrumentation*. Oxford University Press, 1998.

[117] L. A. Feigin and D. I. Svergun, *Structure Analysis by Small-Angle X-Ray and Neutron Scattering*. Plenum Press - New York and London, 1987.

[118] H. Schnablegger and S. Y., *A Practical Guide to SAXS*. Anton Paar GmbH, 2006.

[119] E. Kentzinger, M. Krutyeva, and U. Rücker, "Galaxi: Gallium anode low-angle x-ray instrument," *Journal of large-scale research facilities*, vol. 2, no. A61, 2016.

[120] G. Renaud, R. Lazzari, and F. Leroy, "Probing surface and interface morphology with grazing incidence small angle x-ray scattering," *Surface Science Reports*, vol. 64, no. 8, pp. 255 – 380, 2009.

[121] H. Murayama, "221b lecture notes on scattering theory ii, berkeley university." Online `hitoshi.berkeley.edu/221b/scattering2.pdf`, 2005.

[122] G. van der Laan and A. I. Figueroa, "X-ray magnetic circular dichroism - a versatile tool to study magnetism," *Coordination Chemistry Reviews*, vol. 277-278, pp. 95 – 129, 2014. Following Chemical Structures using Synchrotron Radiation.

[123] J. E. Penner-Hahn, *X-ray Absorption Spectroscopy*. John Wiley & Sons, Ltd, 2001.

[124] J. Yano and V. K. Yachandra, "X-ray absorption spectroscopy," *Photosynthesis Research*, vol. 102, no. 2-3, pp. 241–254, 2009.

[125] B. T. Thole, G. van der Laan, and G. A. Sawatzky, "Strong magnetic dichroism predicted in the m4,5 x-ray absorption spectra of magnetic rare-earth materials," *Phys. Rev. Lett.*, vol. 55, pp. 2086–2088, Nov 1985.

[126] G. van der Laan, B. T. Thole, G. A. Sawatzky, J. B. Goedkoop, J. C. Fuggle, J.-M. Esteva, R. Karnatak, J. P. Remeika, and H. A. Dabkowska, "Experimental proof of magnetic x-ray dichroism," *Phys. Rev. B*, vol. 34, pp. 6529–6531, Nov 1986.

[127] J. C. Lang, *X-ray Magnetic Circular Dichroism*. John Wiley & Sons, Inc., 2002.

[128] C. T. Chen, Y. U. Idzerda, H.-J. Lin, N. V. Smith, G. Meigs, E. Chaban, G. H. Ho, E. Pellegrin, and F. Sette, "Experimental confirmation of the x-ray magnetic circular dichroism sum rules for iron and cobalt," *Phys. Rev. Lett.*, vol. 75, pp. 152–155, Jul 1995.

[129] W. Kuch, *Abbildende magnetische Mikrospektroskopie*. Habilitation, ULB Sachsen-Anhalt, 2002.

[130] W. Daumann, *InP-Kurzkanal-Heterostruktur-Feldeffekttransistoren mit elektronenstrahldefinerten Gate-Kontakten*. Phd thesis, Universität Duisburg-Essen, 2000.

[131] A. E. Vladar and M. T. Postek, *Handbook of Charged Particle Optics*. CRC Press, 2009.

[132] H. Reingruber, *Rasterelektronenmikroskopie - Vorbereitungsunterlagen zur Praktikumsübung im Rahmen des Praktikums für Fortgeschrittene im SS2010 im Forschungsinstitut für Elektronenmikroskopie (FELMI)*, 2010.

[133] I. South Bay Technology, "Ion beam sputtering: Practical applications to electron microscopy." Applications Laboratory Report 91.

[134] B. A. Joyce, "Molecular beam epitaxy," *Reports on Progress in Physics*, vol. 48, no. 12, p. 1637, 1985.

[135] "Pva tepla 300 microwave plasma system useres manual published by the center for nanoscale science & technology."

[136] A. Pizzi and K. L. Mittal, *Handbook of Adhesive Technology, Revised and Expanded*. CRC Press, 2003.

[137] S. Laurent, D. Forge, M. Port, A. Roch, C. Robic, L. V. Elst, and R. N. Muller, "Magnetic iron oxide nanoparticles: Synthesis, stabilization, vectorization, physicochemical characterizations, and biological applications," *Chem. Rev.*, vol. 108, no. 6, pp. 2064–2110, 2008.

[138] P. Burnham, N. Dollahon, C. H. Li, A. J. Viescas, and G. C. Papaefthymiou, "Magnetization and specific absorption rate studies of ball-milled iron oxide nanoparticles for biomedicine," *Journal of Nanoparticles*, vol. 2013, p. 13, 2013.

[139] Ocean NanoTec LLC, Online `https://www.oceannanotech.com/spec.php?cid=71&pid=160&s_id=872`.

[140] M. P. Morales, S. Veintemillas-Verdaguer, M. I. Montero, , C. J. Serna, A. Roig, L. I. Casas, B. Martinez, , and F. Sandiumenge, "Surface and internal spin canting in gamma-Fe2O3 nanoparticles," *Chemistry of Materials*, vol. 11, no. 11, pp. 3058–3064, 1999.

[141] C.-J. Chen, H.-Y. Lai, C.-C. Lin, J.-S. Wang, and R.-K. Chiang, "Preparation of monodisperse iron oxide nanoparticles via the synthesis and decomposition of iron fatty acid complexes," *Nanoscale Research Letters*, vol. 4, no. 11, pp. 1343–1350, 2009.

[142] F. Walz, "The Verwey transition - a topical review," *Journal of Physics: Condensed Matter*, vol. 14, no. 12, p. R285, 2002.

[143] A. Hevroni, M. Bapna, S. Piotrowski, S. A. A. Majetich, and S. Majetich, "Tracking the verwey transition in single magnetite nanocrystals by variable-temperature scanning tunneling microscopy," *The Journal of Physical Chemistry Letters*, vol. 7, no. 9, pp. 1661–1666, 2016. PMID: 27088645.

[144] A. Trunova, *Ferromagnetische Resonanz an oxidfreien magnetischen Fe und FeRh Nanopartikeln*. Phd thesis, Universität Duisburg-Essen, 2009.

[145] J. Nogués and I. K. Schuller, "Exchange bias," *Journal of Magnetism and Magnetic Materials*, vol. 192, no. 2, pp. 203 – 232, 1999.

[146] O. Gunnarsson, "Band model for magnetism of transition metals in the spin-density-functional formalism," *Journal of Physics F: Metal Physics*, vol. 6, no. 4, p. 587, 1976.

[147] J. F. Janak, "Uniform susceptibilities of metallic elements," *Phys. Rev. B*, vol. 16, pp. 255–262, Jul 1977.

[148] J. Vogel, A. Fontaine, V. Cros, F. Petroff, J.-P. Kappler, G. Krill, A. Rogalev, and J. Goulon, "Palladium magnetism in Pd/Fe multilayers studied by xmcd at the Pd L2,3 edges," *J. Magn. Magn. Mater.*, vol. 165, no. 1, pp. 96 – 99, 1997.

[149] G. S. Parkinson, "Iron oxide surfaces," *Surf. Sci. Rep.*, vol. 71, pp. 272–365, March 2016.

[150] W. C. McGinnis, M. J. Burns, R. W. Simon, G. Deutscher, and P. M. Chaikin, "Magnetoresistance in thin palladium films," *Physica B: Condensed Matter*, vol. 107, pp. 5–6, 1981.

[151] G. Wilbs, "Kontaktierung von GaN Nanodrähten," bachelor thesis, Universität Duisburg-Essen, 2011.

[152] N. V. Smith, G. K. Wertheim, S. Hüfner, and M. M. Traum, "Photoemission spectra and band structures of d-band metals. iv. x-ray photoemission spectra and densities of states in rh, pd, ag, ir, pt, and au," *Phys. Rev. B*, vol. 10, pp. 3197–3206, Oct 1974.

[153] M. D. Hall, G. J. Foran, M. Zhang, P. J. Beale, and T. W. Hambley, "Xanes determination of the platinum oxidation state distribution in cancer cells treated with platinum(iv) anticancer agents," *J. Am. Chem. Soc.*, vol. 125, no. 25, pp. 7524–7525, 2003. PMID: 12812486.

[154] C. Jiang, C. W. Leung, and P. W. T. Pong, "Magnetic-field-assisted assembly of anisotropic superstructures by iron oxide nanoparticles and their enhanced magnetism," *Nanoscale Research Letters*, vol. 11:189, 2016.

[155] PubChem, "Open chemistry database - decanoic acid, pubchem cid 2969." Online: `https://pubchem.ncbi.nlm.nih.gov/compound/Decanoic_acid`.

[156] R. D. Deegan, O. Bakajin, T. F. Dupont, G. Huber, S. R. Nagel, and T. A. Witten, "Capillary flow as the cause of ring stains from dried liquid drops," *Nature*, vol. 389, pp. 827–829, Oct 1997.

[157] D. R. Lide, *Handbook of Chemistry and Physics*. CRC Press, 2005.

[158] "Laboratory module 1: Indexing x-ray diffraction patterns." ResearchGate, Online `https://www.google.de/url?sa=t&rct=j&q=&esrc=s&source=web&cd=1&cad=rja&uact=8&ved=0ahUKEwivg4LwlfrOAhUEChoKHTbfCU0QFggeMAA&url=https%3A%2F%2Fwww.researchgate.net%2Ffile.PostFileLoader.html%3Fid%3D55dab51f5f7f71b92c8b45fc%26assetKey%3DAS%253A273837705367552%2540144229940490 9&usg=AFQjCNEX1JzyWf5zlYYSNMwOK4ZGnS-G2A`.

[159] D.-M. Smilgies, "Scherrer grain-size analysis adapted to grazingincidence scattering with area detectors," *Applied Crystallography*, vol. 42, pp. 1030–1034, 2009.

Acknowledgement

It is a great pleasure for me to express my sincere gratitude to all members of the JCNS-2 for their warm welcome in this group and the comfortable working environment as well as their support throughout the whole time I was allowed to spend here. Additionally I want to thank several people in particular:

Prof. Dr. Thomas Brückel for offering me the opportunity to work in this very interesting field and for his support. I could profit from a rich pool of methods and knowledge within this group.

Prof. Dr. Rainer Waser from PGI-7 for agreeing to be the second reviewer and helping me in overcoming bureaucratic obstacles.

PD Dr. Oleg Petracic for his extremely well mentoring. I deeply appreciate his patient guidance, enthusiastic encouragement and useful critiques of this work throughout the whole development process as supervisor.

Dr. Emmanuel Kentzinger and Markus Waschk for performing the XMCD measurements that evolved to be a key issue of this thesis.

Dr. Yongseong Choi from the Advanced Photon Source at Argonne National Laboratory, Dr. Paul Zakalek and Alice Klapper for their extensive support in data evaluation.

PD Dr. Eberhard Göring and Dr. Joachim Gräfe from the Max-Planck-Institute for Intelligent Systems for performing several valuable FORC measurements and supporting me in data evaluation.

Dr. Emmanuel Kentzinger and Michael Smik for enabling easy access to the GALAXI device and their support in data evaluation.

Dr. Wolfgang Albrecht and Dr. Jürgen Moers from HNF for the preparation of Hall bar structures on my samples by lithography.

Chengpeng Jiang from the Magnetism and Nano-Bio Technology Center at the University of Hong Kong, department of Electrical and Electronic Engineering in China for preparing several nanoparticle batches.

Thomas Jansen from PGI-6 for depositing various metal films on my samples.

Stephany Bunte for sample slicing.

René Borowski from PGI-7 for the cooperation that gave me access to the cleanroom.

Jochen Friedrich from PGI-7 for the cooperation that gave me access to a SEM.

Finally I wish to thank my family and especially my husband Martin: thank you so much for your support, encouragement and understanding not only during this thesis but ever since we met, I love you.

Band / Volume 128
Self-purifying $La_{2/3}Sr_{1/3}MnO_3$ epitaxial films: Observation of surface precipitation of Mn_3O_4 particles for excess Mn ratios
A. Steffen (2016), 154 pp
ISBN: 978-3-95806-162-0

Band / Volume 129
Strain and electric field mediated manipulation of magnetism in $La_{(1-x)}Sr_xMnO_3/BaTiO_3$ heterostructures
M. Schmitz (2016), VI, 141 pp
ISBN: 978-3-95806-164-4

Band / Volume 130
High-Throughput Live-Cell Imaging for Investigations of Cellular Heterogeneity in *Corynebacterium glutamicum*
S. Helfrich (2016), xvi, 217 pp
ISBN: 978-3-95806-167-5

Band / Volume 131
Laser-Induced Ultrafast Electron- and Spin-Dynamics in the Electronic Band Structure of Co(001)
M. A. Plötzing (2016), ii, 109, XXXIV pp
ISBN: 978-3-95806-168-2

Band / Volume 132
Robot-Assisted Phenotyping of Genome-Reduced *Corynebacterium glutamicum* Strain Libraries to Draft a Chassis Organism
S. Unthan (2016), 122 pp
ISBN: 978-3-95806-169-9

Band / Volume 133
Characterization of amino acid ammonia lyases & aminomutases for the production of chiral α- and β-amino acids
A. Dreßen (2016), ix, 112 pp
ISBN: 978-3-95806-176-7

Band/Volume 134
7th Georgian-German School and Workshop in Basic Science
Kacharava, A. (Ed.) erscheint nur als CD (2016)
ISBN 978-3-95806-179-8

Band / Volume 135
Crystal growth and scattering studies on two ferrites
S. Adiga (2016), iv, 150 pp
ISBN: 978-3-95806-183-5

Band / Volume 136
Manipulating the Structural and Electronic Properties of Epitaxial $NaNbO_3$ Films via Strain and Stoichiometry
B. Cai (2016), VI, 114 pp
ISBN: 978-3-95806-185-9

Band / Volume 137
Surface Potential of Metallic Surfaces and Self-Assembling Organic Monolayers in Various Electrolytes
J. Wang (2016), ii, 58 pp
ISBN: 978-3-95806-188-0

Band / Volume 138
Ab initio investigation of hybrid molecular-metallic interfaces as a tool to design surface magnetic properties for molecular spintronics
R. Friedrich (2016), 277 pp
ISBN: 978-3-95806-194-1

Band / Volume 139
Topological Matter – Topological Insulators, Skyrmions and Majoranas
Lecture Notes of the 48th IFF Spring School 2017
27 March – 07 April 2017, Jülich, Germany
ed. by S. Blügel, Y. Mokrousov, T. Schäpers, Y. Ando (2017), ca 1000 pp
ISBN: 978-3-95806-202-3

Band / Volume 140
In situ studies of the growth and oxidation of complex metal oxides by pulsed laser deposition
C. Xu (2017), iv, 159 pp
ISBN: 978-3-95806-204-7

Band / Volume 141
Intrinsic and extrinsic spin-orbit torques from first principles
G. Géranton (2017), 122 pp
ISBN: 978-3-95806-213-9

Band / Volume 142
Magnetic Proximity Effects in Nanoparticle Composite Systems and Macrocrystals
G. Wilbs (2017), III, 230 pp
ISBN: 978-3-95806-233-7

Weitere ***Schriften des Verlags im Forschungszentrum Jülich*** unter
http://wwwzb1.fz-juelich.de/verlagextern1/index.asp

Schlüsseltechnologien /
Key Technologies
Band / Volume 142
ISBN 978-3-95806-233-7

